Design, Fabrication, and Characterization of an Ultra-Low Cost Inductively-Coupled Plasma Chemical Vapor Deposition Tool for Micro- and Nanofabrication

by

Parker Andrew Gould

B.Eng., Electrical Engineering, Vanderbilt University (2011)
M.Phil., Micro- and Nanotechnology Enterprise, University of Cambridge (2012)
S.M., Electrical Engineering, Massachusetts Institute of Technology (2014)

Submitted to the Department of Electrical Engineering and Computer Science
in Partial Fulfillment of the Requirements for the Degree of

Doctor of Philosophy

at the

MASSACHUSETTS INSTITUTE OF TECHNOLOGY

February 2019

© 2019 Massachusetts Institute of Technology. All rights reserved.

Signature redacted

Signature of Author..
Department of Electrical Engineering and Computer Science
January 15, 2019

Certified by.. Signature redacted
Martin A. Schmidt
Professor of Electrical Engineering and Computer Science
Thesis Supervisor

Accepted by.................................... Signature redacted
Leslie A. Kolodziejski
Professor of Electrical Engineering and Computer Science
Chair, Department Committee on Graduate Students

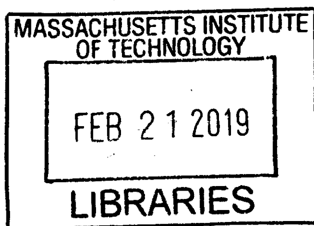

ARCHIVES

Design, Fabrication, and Characterization of an Ultra-Low Cost Inductively-Coupled Plasma Chemical Vapor Deposition Tool for Micro- and Nanofabrication

by

Parker Andrew Gould

Submitted to the Department of Electrical Engineering and Computer Science on January 15, 2019 in partial fulfillment of the requirements for the degree of Doctor of Philosophy

Abstract

The high cost of semiconductor fabrication equipment has traditionally represented a large barrier to entry for groups seeking to develop or commercialize novel micro- and nanoscale devices. Much of the cost barrier stems from the large size of the substrates processed in this equipment, and the associated complexity of maintaining consistent operation across the full substrate area. By scaling the substrate size down from the 150-300 mm diameter sizes commonly seen in today's production environments, the capital cost and physical footprint of tools for micro- and nanoscale fabrication can be dramatically decreased, while still retaining a similarly high level of performance.

In this work, an ultra-low cost inductively-coupled plasma chemical vapor deposition (ICP-CVD) system for processing substrates up to 50.8 mm (2") in diameter is presented. The ICP-CVD system is built within a modular vacuum tool architecture that allows sections of the full tool to be easily and inexpensively replaced to adapt to new processing conditions or provide additional functionality. The system uses a non-pyrophoric mixture of silane (1.5% in helium) and low substrate temperatures ($\leq$ 150°C) to deposit uniform silicon-based films with a high quality comparable to films deposited in research-grade commercial tools. Using response surface methods, the performance of the ICP-CVD system has been characterized for both silicon dioxide and silicon nitride films, and repeatable control of the deposited film properties, including deposition rate, index of refraction, film stress, and density, has been demonstrated.

Thesis Supervisor: Martin A. Schmidt

Title: Professor of Electrical Engineering and Computer Science

Acknowledgements

For the last several years, I have had the good fortune of working on a project that, while routinely challenging, has consistently remained engaging and enjoyable. This has been largely due to an amazing network of people who have provided both academic and personal support and made it so much easier to come in to work, even when it is absurdly cold outside.

First off, I would like to thank my advisor and mentor, Prof. Marty Schmidt, who for the entirety of my time at MIT has been nothing but supportive of my work and has given me the freedom to pursue the types of problems I found interesting, while still being there to ask the hard questions and steer me back on course when I drifted off. Your experiences and counsel in not just academia, but also industry and entrepreneurship have been invaluable.

To my other committee members, Prof. Tayo Akinwande and Prof. Karen Gleason, I have been very lucky to interact and learn from you both for many years prior to this thesis, and the guidance you have provided over library sessions and one-on-one meetings has been instrumental in not only constructing this thesis, but in also building who I am as a scientist and engineer.

The completion of this work and much of everything else I have done at MIT would not have been possible without Mitchell Hsing, my friend and research partner in the Inch Fab initiative. Sharing an office and many spirited "discussions" has been a pleasure and undoubtedly led to markedly better ideas and designs. I look forward to our continued work in making the Inch Fab a reality.

I would also like to thank the other members of the Schmidt research group: Carson Teale, Dr. Hanqing Li, and former group members Dr. Eric Newton and Dr. Eric Lam. Your openness in providing a new perspective on a problem or sharing pieces of your vast amount of micro- and nanofabrication knowledge continues to be enormously helpful.

Another member of the MIT community that has made my time here immensely more productive and enjoyable is Mark Belanger, the manager of the Edgerton Student Shop. In addition to entrusting me with the opportunity to teach students how to use machine tools, you have always been willing to let me exceed my three questions per day quota, and provided me with the skills and facilities to make much of the work in this thesis a reality. Significant thanks also go out to the MIT Hobby Shop and Prof. Marty Culpepper, who have also assisted greatly in the fabrication of Inch Fab tools.

Tremendous thanks are also due to the MTL community, especially Kurt, Dennis, Bob, Eric, Donal, Gary, Bernard, Vicky, Whitney, Jim, Kris, Dave, and Paul, who have all been extremely generous with their time, advice, and patience in helping me both use and understand a wide array of fabrication equipment.

To all my friends in Cambridge (and throughout the rest of the world), especially Alex, Dan, Joel, Michael, Austin, Philipp, the ever-evolving Muddy crew, and the GAME softball team, thank you so much for providing countless good times, listening to me gripe, and keeping me grounded.

Finally, thank you to my parents Paul and Patsy, and my brother Patrick, for your relentless support in everything I have done, and for instilling in me the values that have made it all possible. I hope the best is yet to come.

Table of Contents

Chapter 1: Introduction and Background 19

1.1 Motivation 19

1.2 Background 21

1.2.1 Theory of Operation 21

1.2.2 Atmospheric Pressure CVD (APCVD) 24

1.2.3 Low Pressure CVD (LPCVD) 25

1.2.4 Plasma-enhanced CVD (PECVD) 26

1.2.5 Inductively-Coupled Plasma CVD (ICP-CVD) 27

1.2.6 Comparison of CVD Techniques 29

1.3 Objectives 30

1.4 Outline of Thesis 31

Chapter 2: System Design 33

2.1 Tool Design Overview 34

2.2 Vacuum Tool Design Concepts 35

2.2.1 Materials Selection 36

2.2.2 Seals and Leaks 37

2.2.3 Design for "X" 41

2.3 IFIC Modular Tool Architecture 42

2.3.1 Lower Chamber Assembly (LCA) 44

2.3.2 Upper Chamber Assembly (UCA) 52

2.3.3 Substrate Chuck Assembly (SCA) 58

2.3.4 Load Lock Assembly (LLA) 67
2.4 Supplementary Equipment Systems 73
2.4.1 Process Gas Delivery 74
2.4.2 Vacuum Generation and Management 78
2.4.3 RF Power Delivery 80
2.4.4 Control System and User Interface 81
2.5 System Cost Analysis 83
2.5.1 Cost Breakdown 84
2.5.2 Cost Reduction 86
2.5.3 Quantity Discounts 87
Chapter 3: Experimental Methods 89
3.1 Methods for System Characterization 89
3.1.1 Leak rate and rate-of-rise 89
3.1.2 Base pressure and pump-down times 92
3.1.3 Pumping Speed 95
3.1.4 Sample Loading and Unloading 96
3.1.5 SCA Heater Performance 98
3.1.6 Control Electronics 102
3.2 Methods for Film Characterization 103
3.2.1 Response Surface Methodology 103
3.2.2 Film Thickness and Index of Refraction 106
3.2.3 Average Film Stress 109
3.2.4 Film Uniformity 113

3.2.5 Wet Etch Rate 117

3.2.6 Chemical Composition 119

3.2.7 Electrical Properties 120

3.2.8 Surface Morphology 121

3.3 Standard Operating Protocols 121

3.3.1 Running Samples 122

3.3.2 Characterization sequence for samples 125

3.4 Conclusions 127

Chapter 4: Silicon Dioxide Deposition 129

4.1 Early Testing 129

4.1.1 Stabilizing Deposition Parameters 130

4.1.2 Chasing Uniformity 131

4.2 Establishing a Process Window 139

4.3 Response Surface Testing 140

4.3.1 RSM Parameter Selection 140

4.3.2 RSM Results 145

4.3.3 Validation of RSM results 163

4.4 Additional Tests 168

4.4.1 FTIR 168

4.4.2 Electrical Breakdown 170

4.4.3 Surface Morphology 172

4.5 Summary of Results 173

Chapter 5: Silicon Nitride Deposition 177

5.1 Early Testing ... 178
5.1.1 Chamber Spacing ... 178
5.1.2 Stress Reduction ... 180
5.2 Establishing a Process Window ... 181
5.3 Response Surface Testing ... 186
5.3.1 RSM Parameter Selection ... 186
5.3.2 RSM Results ... 189
5.3.3 Validation of RSM Results ... 206
5.4 Additional Testing ... 210
5.4.1 Substrate Temperature ... 210
5.4.2 FTIR ... 212
5.4.3 Surface Properties ... 215
5.5 Summary of Results ... 216
Chapter 6: Conclusions and Future Efforts ... 217
References ... 223
Appendix A: Standard Cleaning Protocol ... 233
Appendix B: Gas Delivery and Vacuum Generation System ... 235

List of Figures

Figure 1.1: Visual step-by-step of the CVD process. 23

Figure 1.2: Schematic diagram of a hot wall APCVD reactor. 24

Figure 1.3: Schematic diagram of an LPCVD reactor. 25

Figure 1.4: Schematic diagram of a PECVD reactor with a separate low-frequency bias power source connected to the substrate electrode. 27

Figure 1.5: Schematic diagram of an ICP-CVD system. 29

Figure 2.1: IFIC Block Diagram 35

Figure 2.2: Examples of seals (red arrows) and virtual leak mitigation (blue arrows) in the UCA. 40

Figure 2.3: Differentially pumped linear and rotary motion feedthrough. 41

Figure 2.4: Labeled cross-sectional view of the four modular assemblies of the IFIC 43

Figure 2.5: Exploded view of the four modular assemblies. The dotted lines indicate how the assembly mate with one another 44

Figure 2.6: Renderings showing the assembled LCA, connection information, and naming conventions 45

Figure 2.7: Exploded view of the LCA with labels for the major components. Not shown are the support legs, which attach to the support plate and lift assembly. 46

Figure 2.8: Comparison of (a) spider flanges used to connect CF 6" gate valve to LCA and LLA, and (b) the new, more compact insertable gate valve and plate flange design. 51

Figure 2.9: Renderings of the UCA. (a) The assembled UCA; (b) Cross-sectional view showing both gas entry paths; (c) Exploded view with labels for key components. 53

Figure 2.10: Exploded and cross-section views of the upper flange of UCA. The dotted line indicates the gas flow path. 56

Figure 2.11: Renderings of the SCA. (a) The assembled SCA and substrate puck; (b) Cross-sectional view of SCA and puck showing the positions of the spring plungers and mating grooves; (c) Exploded view with labels for key components. 59

Figure 2.12: (a) Spring-loaded thermocouple assembly; (b) Cross-sectional view of SCA showing thermocouple position. 62

Figure 2.13: Cross-section view showing substrate puck mated onto the chuck receiver at the top of the receiver. The spring plungers are held in place by the grooves in the stainless steel ring on the outside of the receiver. 64

Figure 2.14: Loading and unloading of substrate pucks from the SCA. The green arrows show the loading process and the red arrows shows the unload process. The SCA is rotated ~20 degrees at the position of (b) to lock or unlock the puck. 65

Figure 2.15: (a) 2" wafer alignment jig for loading onto substrate pucks; (b) a 2" wafer loaded into a substrate puck. 66

Figure 2.16: Renderings of the LLA. (a) Exploded and labeled view of LLA components; (b) Assembled LLA view with wafer transfer arm extended. 69

Figure 2.17: Block diagram of RF connections in the IFIC. 81

Figure 2.18: Screenshots from the operation tab (left) and recipe tab (right) of the PARC software used to monitor and control the IFIC. 83

Figure 3.1: Load lock pressure vs. pump-down time. Time needed to fall below 0.01 torr noted for each curve. 93

Figure 3.2: Process chamber pumping performance with throttle valve fully open. The green circles refer to simulation data provided by Leybold. 96

Figure 3.3: Temperature of the SCA measured by the integrated thermocouple and the substrate measured by an external IR camera during heat-up. 100

Figure 3.4: Temperature line scan across the substrate from external IR camera at equilibrium. The added lines delineate between the alumina clamp and substrate regions of the scan... 100

Figure 3.5: LWIR images of the substrate and surrounding puck. (a) shows the image used to generate the line scan in Figure 3.4. The orange-to-red rings at the center of the substrate are reflecations from the LWIR camera lens; (b) shows an image taken at a slightly oblique angle to illustrate the reflections from the camera lens. 101

Figure 3.6: Graphical representation of test locations in circumscribed CCD designs for (a) two factors; (b) three factors. 105

Figure 3.7: Schematic view of the ellipsometry process. Image courtesy of [61]. 107

Figure 3.8: J.A. Woollam M-2000S VASE. Shown on the stages is 2" sample centered within a custom alignment plate. 108

Figure 3.9: (a) FLX-2320 in the MTL cleanroom; (b) the custom alignment plate created for measuring 2" wafers. 111

Figure 3.10: (a) UV1250SE Thin Film Measurement System; (b) Wafer handling robot for the UV1250. The handle wafer with alignment plate and 2" wafer can be seen at the top left. 115

Figure 3.11: Standard UV1250 pattern used for uniformity measurements. The pattern has 25 points and a 4 mm edge exclusion. 116

Figure 3.12: (a) ThermoFisher Nicolet iS50 FTIR system; (b) 2" wafer with IFIC-deposited SiO_2 film mounted in transmission mode. 120

Figure 4.1: (a) SiO_2 deposition without mechanical clamp; (b) SiO_2 deposition with mechanical clamp (1.75" (44.5 mm) diameter aperture) 132

Figure 4.2: (a) SiO_2 deposition on wafer centered on large thermal mass; (b) SiO_2 deposition of wafer placed off-center on large thermal mass. 132

Figure 4.3: Demonstration of the effect of MMC on the ion saturation current (which is proportional to the plasma density [78]). Both the density and uniformity are improved. Figure reproduced from [80]. 134

Figure 4.4: Aperture plates with varying center diameters. (a) AP0.75; (b) AP1.25. 136

Figure 4.5: Percent deviation from the mean film thickness across the wafer as a function of the central dimension of the aperture plate. The edge exclusion is 4 mm in each scans.......... 137

Figure 4.6: Percent deviation from the mean film thickness across the wafer as a function of the spacing between the wafer and aperture plate (AP1.25, 1.25" center diameter). The edge exclusion is 4 mm in each scan. 137

Figure 4.7: Contour plots showing deposition rate vs. pairs of input factors. Each graph is evaluated at the center point values of the factors not shown. Contours are equal across all plots. 147

Figure 4.8: Index of Refraction vs. O_2/SiH_4 ratio. Included are data from both the RSM sequence and follow-up testing (Section 4.3.3.1), containing tests at several different pressures, temperatures, and bias powers. The error bars show the standard deviation. 150

Figure 4.9: Contour plots showing average film stress vs. pairs of input factors. The dotted line marks the -300 MPa contour. Each graph is evaluated at the center point values of the factors not shown. 152

Figure 4.10: Contour plots of average film stress vs. pressure and temperature. (a) Evaluated at 5 sccm O_2, 1.5 W; (b) Evaluated at 5 sccm O_2, 0 W; (c) Evaluated at 4 sccm O_2, 0 W. The -300 MPa threshold for "low-stress" SiO_2 films is denoted with a dotted black line. 154

Figure 4.11: Contour plots of film uniformity (percent deviation from the mean). (a) Test #1 from the cube block; (b) Center point test (overall test #15); (c) Test #30 from the star block. The black lines indicate the mean film thickness, while the white lines show one standard deviation. 156

Figure 4.12: CV and Uniformity as a function of edge exclusion distance for three different samples. A 4 mm edge exclusion was used for the RSM test sequence. 158

Figure 4.13: Contour plots showing the normalized BOE etch rate vs. pairs of input factors. Each graph is evaluated at the center point values of the factors not shown. 161

Figure 4.14: RSM center point deviation from the mean for each measured parameter.......... 167

Figure 4.15: FTIR spectra for 2 RSM center point samples. The spectra are offset for clarity. The observable peaks are labeled. The faint C-H peaks are likely from surface contamination, and were not observed in other IFIC samples. 169

Figure 4.16: J-E plot for SiO_2 sample deposited at 100°C and 1.5 W bias power. 170

Figure 4.17: J-E plot for SiO_2 sample deposited at 150°C and 3 W bias power. 171

Figure 4.18: Surface roughness maps. (a-b) Center point tests; (c) Film with low compressive stress; (d) Film with high compressive stress. 172

Figure 4.19: Overlay plots for the two film scenarios described in Table 4.16. The white region indicates the remaining available process window. The black Xs show the locations of actual tests. The plot in (a) was evaluated at 75°C and 0 W bias power. The plot in (b) was evaluated at 4 sccm O_2 and 0 W bias power. 174

Figure 5.1: Percent deviation from the mean SiN_x film thickness across the wafer as a function of the spacing between the wafer and aperture plate (AP1.25, 1.25" center diameter). The edge exclusion is 4 mm in each scan. 179

Figure 5.2: Bias power effects on film characteristics. Non-uniformity increases slightly with increasing base power (3.2% to 3.5%). Error bars for 0 W points indicate one standard deviation. Constant parameter values: 300W ICP Power, 2 sccm N_2, 8 sccm Ar, 75 mTorr, 100°C substrate temperature. 185

Figure 5.3: Contour plots showing the RSM model-predicted SiN_x deposition rate vs. pairs of input factors. Each graph is evaluated at the center point value of the factor not shown. Contours are equal across all plots. 192

Figure 5.4: Contour plots showing the RSM model-predicted SiN_x index of refraction vs. pairs of input factors. Each graph is evaluated at the center point value of the factor not shown. Contours are equal across all plots. 194

Figure 5.5: Estimated Si:N ratio vs. N2 flow (at 8 sccm Ar and 75 mTorr). The error bar barely visible on the 2 sccm N_2 point represents one standard deviation. 196

Figure 5.6: Contour plots showing the RSM model-predicted SiN_x average film stress vs. pairs of input factors. Each graph is evaluated at the center point value of the factor not shown. Contours are equal across all plots. 197

Figure 5.7: Evolution of pressure effect on film stress for several scenarios. Dots indicate data from a measured test. 198

Figure 5.8: Contour plots of film uniformity (percent deviation from the mean). The black lines indicate the mean film thickness, while the white lines show one standard deviation. (a) CV: 1.64%, Uniformity: ±3.10%; (b) CV: 1.66%, Uniformity: ±3.36%; (c) CV: 1.20%, Uniformity: ±2.32%; (d) CV: 2.19%, Uniformity: ±3.78%; 200

Figure 5.9: Sample contour plot of film uniformity with AP1.25 aperture plate overlaid in the same orientation used in the IFIC during the SiN_x tests. 202

Figure 5.10: Contour plots showing the RSM model-predicted SiN_x BOE etch rate ratio vs. pairs of input factors. Each graph is evaluated at the center point value of the factor not shown. Contours are equal across all plots. 204

Figure 5.11: SiN_x center point deviation from the mean for each measured parameter........ 209

Figure 5.12: Results from single-factor temperature testing. (a) Deposition rate and index of refraction; (b) Average film stress and BOE etch rate ratio. The error bars on the 100°C data points represent one standard deviation. 211

Figure 5.13: FTIR scans of three SiN_x RSM center point tests. 212

Figure 5.14: FTIR scans of three SiN_x samples deposited with increasing N_2 flow levels. All other parameters were kept at the RSM center point values. 213

Figure 5.15: FTIR scans of three SiN_x samples deposited at different substrate temperatures. All other parameters were kept at the RSM center point values........ 214

Figure 5.16: Surface roughness maps. (a-b) Center point tests; (c) Film with high tensile stress; (d) Film with high compressive stress........ 215

Figure 6.1: Cross-sectional images of ~200 nm of SiN_x deposited at 75°C on top of ~1 µm of patterned photoresist. The SiN_x films show good conformality. 219

List of Tables

Table 1.1: Basic deposition reactions for SiO_2 and SiN_x. 23

Table 1.2: Deposition conditions and performance of four common CVD types. 29

Table 1.3: Deposition characteristics of four common CVD techniques. 30

Table 2.1: Cost breakdown of the IFIC (quantity of one). 85

Table 3.1: Repeatability test results for the J.A. Woollam M-2000S VASE. 109

Table 3.2: Repeatability test results for the Tencor FLX-2320. All values shown have units of MPa. 113

Table 3.3: Repeatability test results for the KLA-Tencor UV1250SE. 116

Table 3.4: Repeatability test results for the 7:1 BOE etch rate process. 119

Table 4.1: The effect of increasing input parameters on output SiO_2 film characteristics. A dash indicates a small or negligible effect over the range tested. 139

Table 4.2: Process window for stable SiO_2 depositions. 140

Table 4.3: Number of experiments needed and α values for CCD RSM sequences of various sizes. 141

Table 4.4: Constant parameters used for the SiO_2 RSM test sequence. 142

Table 4.5: RSM test sequence for SiO_2. Also shown are the equations and valued needed to convert factors from coded to actual units. 143

Table 4.6: Raw results for each sample in the SiO_2 RSM test sequence. 145

Table 4.7: Fit coefficients for second-order model for deposition rate. 146

Table 4.8: Fit coefficients for second-order model for average film stress. 151

Table 4.9: Published Uniformity values for SiO_2 depositons in commercial ICP-CVD systems. The average Uniformity from the SiO_2 RSM sequence is included in green for reference. 159

Table 4.10: Fit coefficients for second-order model for normalized etch rate. 160

Table 4.11: Input parameters for the RSM follow-up tests. 163

Table 4.12: Measured results for the RSM follow-up tests. 163

Table 4.13: Comparison of RSM follow-up results to model predictions 164

Table 4.14: Summary of the model fits for the 14 qualified pre-RSM experiments. 165

Table 4.15: Summary of results from center point repeatability tests 167

Table 4.16: Desired film properties for two sample scenarios 173

Table 5.1: The effect of increasing input parameters on output SiN_x film characteristics. A dash indicates a small or negligible effect over the range tested 182

Table 5.2: Process window for quality SiN_x depositions 183

Table 5.3: RSM test sequence for SiN_x. Also shown are the equations and valued needed to convert factors from coded to actual units. 188

Table 5.4: Constant parameters used for the SiN_x RSM test sequence 189

Table 5.5: Raw results for each sample in the SiN_x RSM test sequence 190

Table 5.6: Fit coefficients for second-order IFIC SiN_x deposition rate model. 191

Table 5.7: Fit coefficients for second-order IFIC SiN_x index of refraction model 194

Table 5.8: Fit coefficients for simple third-order IFIC SiN_x average film stress model. 197

Table 5.9: Published Uniformity values for SiN_x depositions in commercial ICP-CVD systems. The average Uniformity from the SiN_x RSM sequence is included in green for comparison. 201

Table 5.10: Fit coefficients for second-order IFIC SiN_x BOE etch rate ratio model. 204

Table 5.11: Published BOE etch rate values for ICP-CVD and PECVD SiN_x depositions. The average etch rate range from the SiN_x RSM sequence is included for comparison. 205

Table 5.12: Input factor values for the SiN_x RSM follow-up tests. 207

Table 5.13: Measured results for the SiN_x RSM follow-up tests 207

Table 5.14: Comparison of SiN_x RSM follow-up results to model predictions. 207

Table 5.15: Summary of results from SiN_x repeatability tests 209

Table 6.1: Range of film properties achievable for SiO_2 and SiN_x films deposited in the IFIC. The values provided are based on the process windows used for the RSM test sequences for each film type 217

Chapter 1: Introduction and Background

1.1 Motivation

A general rule of thumb for new semiconductor fabrication facilities (fabs) is that revenues from the first year of production must match the capital cost of building the fab itself. With modern fabs routinely exceeding 1 billion USD to build and equip [1], this rule serves as a nearly insurmountable barrier to entry for groups seeking to commercialize new semiconductor devices aimed at smaller market segments which require a dedicated process. The foundry fab model has arisen partially to overcome this inefficiency, but to remain profitable, these foundries typically offer only a few standardized processes that allow customer customization through unique lithography masks. The limited diversity afforded by these foundries can make some devices with smaller market sizes economically viable, but many devices (particularly in the micro-electromechanical systems (MEMS) sector) require process customization beyond the lithography level. A (market) for smaller-volume, "research-grade" fabrication tools does exist and is made use of in many academic and government facilities, but the capital cost for this equipment is still large enough that it presents a significant barrier for even well-endowed organizations.

To address these problems, a research initiative was established to explore the possibility of building radically cheaper tools for micro- and nanoscale fabrication. The idea at the root of this initiative has been that if the size of the substrate being processed is scaled down from the 150-300 mm sizes commonly seen in larger scale production environments today, the capital cost and physical footprint of the tools for processing those substrates will also scale down dramatically.

A substrate size target of 1-2" (25.4-50.8 mm) has been used for each of the tools created thus far within this initiative, and 2" silicon wafers are used as the substrate material throughout this work. The full suite of tools for processing these 1-2" substrates is colloquially referred to as the "Inch Fab", and utilizes almost exclusively the same type of fabrication processes used in large scale fabs today. This has been a specific design choice to maintain process compatibility and

translatability between Inch Fab tools, which are targeted at R&D and low-volume production use cases, and large scale tools, which require larger volumes and utilization percentages to remain economically viable.

The Inch Fab initiative has a cumulative capital cost target of below 1 million USD for the complete toolset needed to fabricate functional devices, and a space goal of less than 100 ft^2 (9.3 m^2) for the processing tools themselves, with another sub-100 ft^2 (9.3 m^2) for all required back-end equipment. It has been envisioned that the very small physical footprint of Inch Fab tools will allow them to reside inside large laminar flow hoods that provide the clean and low-turbulence atmosphere needed for micro- and nanoscale processing, and eliminate the need for a full clean room environment. This substantial reduction in equipment size and required clean space will also greatly decrease energy and materials costs, and minimize the environmental impact of running fabrication processes.

The initial efforts of the Inch Fab initiative have been directed at developing tools that enable the development and small-scale production of microelectromechanical systems (MEMS) devices, which are among the device types that are currently the most underserved by the existing fabrication infrastructure. The inductively-coupled plasma chemical vapor deposition (ICP-CVD) tool developed in this work fits well with this strategy, as many novel MEMS devices use non-standard substrate or layer materials with have low thermal budgets, which make them difficult to integrate into standard fabrication architectures.

The first tool developed in the Inch Fab line of tools was an ultra-low cost deep reactive ion etching (DRIE) system [2], [3]. DRIE tools are used to create highly anisotropic, high aspect-ratio trenches in silicon—an essential aspect of many MEMS processes. In addition to this, the Bosch-style, time-multiplexed DRIE process [4], [5] performed in the Inch Fab DRIE involves a carefully controlled combination of reactive ion etching, physical sputtering, and chemical vapor deposition, three very important fabrication techniques in their own right. This made the development of this tool extremely useful from a learning perspective. Many of the insights and design principles gained from the development of this tool were utilized in the ICP-CVD tool

design discussed in the next chapter. The current iteration of the Inch Fab DRIE tool costs less than 32,000 USD to produce in quantities of one, and has demonstrated performance levels on par with or better than commercial tools with price tags 10-50 times higher. A selection of these performance metrics include etch rates of up to 7 µm/min, aspect ratios greater than 10:1, etch selectivity to photoresist greater than 50:1, and an etch depth uniformity better than 2% across the substrate. Since the DRIE development, other smaller prototype tools and tool modules have also been designed for the Inch Fab initiative, but the ICP-CVD tool described throughout this work (routinely abbreviated as the IFIC for Inch Fab ICP-CVD) represents the second major tool (along with a magnetron sputtering system being concurrently developed) in the Inch Fab portfolio.

1.2 Background

Like the previously mentioned Bosch process technique for DRIE, the ICP-CVD method for thin film deposition is a relatively recent development, with the early rounds of commercial ICP-CVD systems debuting in the late 1990s [6], [7]). ICP-CVD features many advantages over older CVD techniques, including significantly lower deposition temperatures, higher quality films, and reduced usage of toxic and corrosive gases. ICP-CVD tools can be used to deposit a large variety of materials, most commonly the silicon dioxide (SiO_2) and silicon nitride (SiN_x) dielectrics focused on in this thesis, but also amorphous silicon, silicon carbide, and several others [8].

1.2.1 Theory of Operation

Chemical vapor deposition (CVD) is the process of depositing a thin film of solid material by way of decomposing a gaseous chemical using an energy source (commonly heat or plasma). It is one of several techniques used in micro- and nanoscale fabrication for depositing thin films. Other common techniques include evaporation and sputtering, which are often grouped together under the heading of physical vapor deposition (PVD). In evaporation, heat or a focused beam of electrons are used to evaporate or sublimate the desired film material (the "target") in a high vacuum environment. The vapor then condenses on the substrate temperature, creating the thin

film. In sputtering, atoms of the target material are physically removed via bombardment with high-energy ions and travel to the surface of the substrate, forming a film. The ion bombardment can be generated using DC or RF voltages, and magnets can be used to confine the bombardment to the target material. Atomic layer deposition (ALD) is another deposition technique that operates by sequentially exposing a substrate to gaseous precursors which adsorb to the surface and undergo a self-limiting chemical reaction. In the ideal case, each cycle deposits a single atomic layer of the desired material on the substrate, producing a very high quality film, but at a very slow rate.

CVD processes were first documented in the 1850s [9], and grew in use in the late 1800s for the development and improvement of incandescent light bulb filaments (including in patents by Thomas Edison [10]). In the early 1900s, CVD processes were used to deposit metals like nickel and aluminum, and in the 1960s were adapted for depositing hard coatings for manufacturing tools. CVD processes for depositing silicon and silicon compounds date from the early 1900s as well, and became widespread in the late 1940s [11]. CVD processes can now be found within many different industries, including machine tool and die production, food packaging, chemical processing equipment, and fine jewelry manufacturing, and it remains a crucial component in creating micro- and nanoscale devices [12].

CVD processes begin by identifying the material to be deposited and then selecting a precursor gas chemistry that is compatible with the requirements of the process chamber and the substrate material. These requirements include temperature limits, operating pressures, and cross-process contamination. The material deposition process begins with the injection of the precursor gas molecule(s) into the process chamber, followed by the transport and adsorption of these molecules (which may have been dissociated to due to gas-phase reactions induced by applied heat or plasma) onto the substrate surface. Once on the surface, gas-solid reactions occur (again potentially assisted by heat or plasma) and the desired deposition material begins to nucleate on the substrate. Gaseous products of these reactions then desorb from the substrate and are removed from the chamber. This process is shown graphically in **Figure 1.1**.

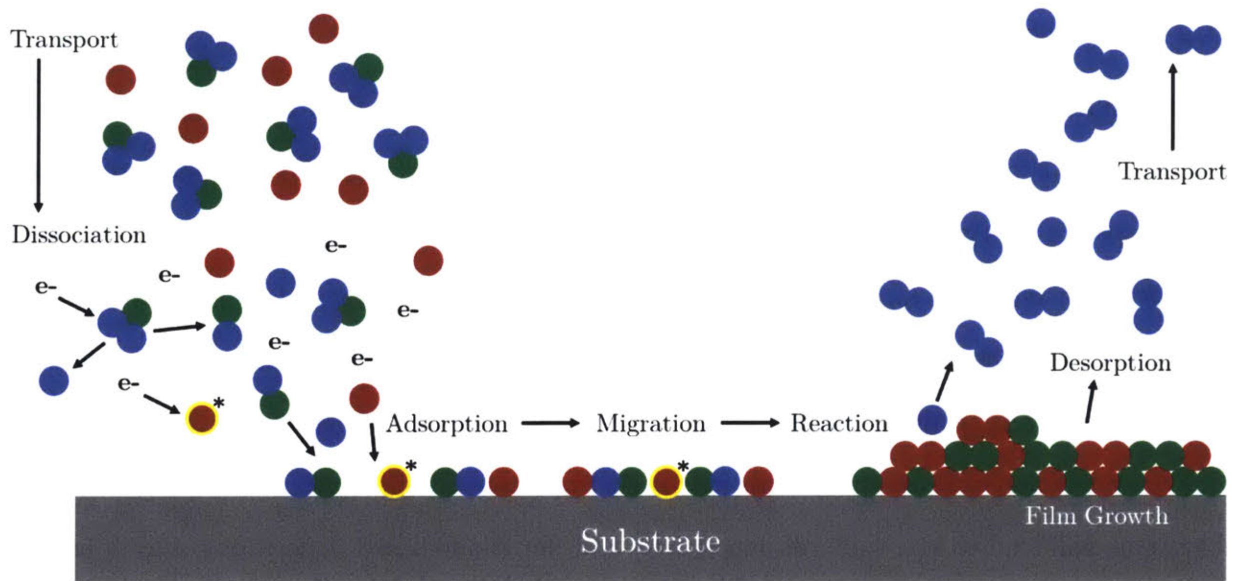

Figure 1.1: Visual step-by-step of the CVD process.

The basic reactions for the most common gas chemistries used to deposit the silicon-containing dielectric materials explored in this work are shown below. The reactions in green denote the chemistries used in this work.

Silicon Dioxide	O_2-based:	$SiH_4 + O_2 \rightarrow SiO_2 + 2H_2$
	N_2O-based:	$SiH_4 + 2N_2O \rightarrow SiO_2 + 2N_2 + 2H_2$
	TEOS-based:	$Si(OC_2H_5)_4 + 2H_2O \rightarrow SiO_2 + 4\ C_2H_5OH$
Silicon Nitride	N_2-based:	$3SiH_4 + 2N_2 \rightarrow Si_3N_4 + 6H_2$
	NH_3-based:	$3SiH_4 + 4NH_3 \rightarrow Si_3N_4 + 12H_2$

Table 1.1: Basic deposition reactions for SiO_2 and SiN_x.

In the mainstream semiconductor industry, there are four main classes of CVD processes in widespread use: atmospheric pressure CVD (APCVD), low pressure CVD (LPCVD), plasma-enhanced CVD (PECVD), and inductively-coupled plasma CVD (ICP-CVD). All of these processes can be used to deposit the materials listed above, but each have their own strengths and weaknesses. A brief description of each technique, along with a table comparing several key attributes are contained in the following sections.

1.2.2 Atmospheric Pressure CVD (APCVD)

Atmospheric pressure CVD (APCVD) is a deposition process that occurs at atmospheric pressures, with substrate heaters used to help initiate the gas and gas-solid deposition reactions. APCVD systems are generally fairly simple with just two process tuning variables: gas transport rate (the input flow rate and the exhaust flow rate) and temperature. This simplicity however, means that fine tuning of film parameters, such as stress and index of refraction, is difficult. APCVD films are typically deposited under a mass-transport limited regime, making the design of the gas entry and exhaust subsystems extremely important. Deficiencies in the designs of these subsystems will lead to non-uniform depositions and, for silane-based depositions, excess powder formation from premature reactions. As many APCVD systems are designed for batch-processing, it can become increasingly more difficult for these gas entry and exhaust systems to attain uniformity. In some commercial systems, better uniformity is achieved through the use of multiple reaction chambers or deposition regions. In the Applied Materials 2100 series of APCVD tools, wafers travel along a belt under a series of independent gas injectors, and in APCVD systems from Quester Technology, five separate chambers are used in sequence to each deposit 20% of the desired thickness. The spatial variability from each of the deposition sites in these configurations are effectively averaged out by the end of the deposition [13]. **Figure 1.2** shows another APCVD geometry, known as hot wall APCVD, where wafers rest on a heated and tilted susceptor plate that helps maintain a constant gas boundary layer thickness [14].

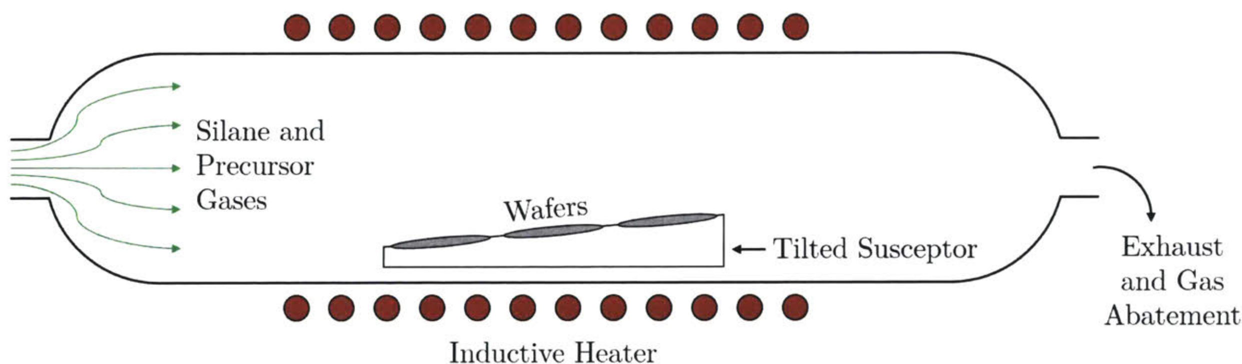

Figure 1.2: Schematic diagram of a hot wall APCVD reactor.

1.2.3 Low Pressure CVD (LPCVD)

Low pressure CVD (LPCVD), as the name implies, takes the APCVD concept of thermally dissociating precursor molecules on a substrate to produce a film, but performs it at significantly lower pressures (typically 0.1-1 torr). By reducing the operating pressure, the reaction rate falls below the rate at which reactant species reach the substrate (gas diffusivity increases with decreasing pressure), thereby shifting the deposition regime from mass-transport limited to reaction-rate limited. This reduces the overall deposition rate, but improves many other film characteristics. Compared to APCVD reactors, LPCVD systems produce denser films with better thickness uniformity, step coverage, and reduced H_2 content, and minimize the production of particles or powder by reducing the amount of gas-phase reactions [15]. One way in which LPCVD's low deposition rates are overcome in production environments is through the use of batch processing. With good temperature control, thickness uniformity can maintained even with close wafer-to-wafer spacing (typically vertically in holder "boats") due to the reaction-rate limited deposition regime, permitting large numbers of wafers (as many as 150 at a time [16]) to be processed simultaneously. Thermal decomposition is the dominant deposition reaction type in LPCVD, which requires temperatures of 600°C or greater to achieve viable deposition rates. These high operating temperatures make LPCVD incompatible with many materials (e.g. polymers and low melting-point metals) and process flows (e.g. diffusion-sensitive wafers with tight doping profiles) [15], [16]. **Figure 1.3** shows a schematic diagram of an LPCVD reactor.

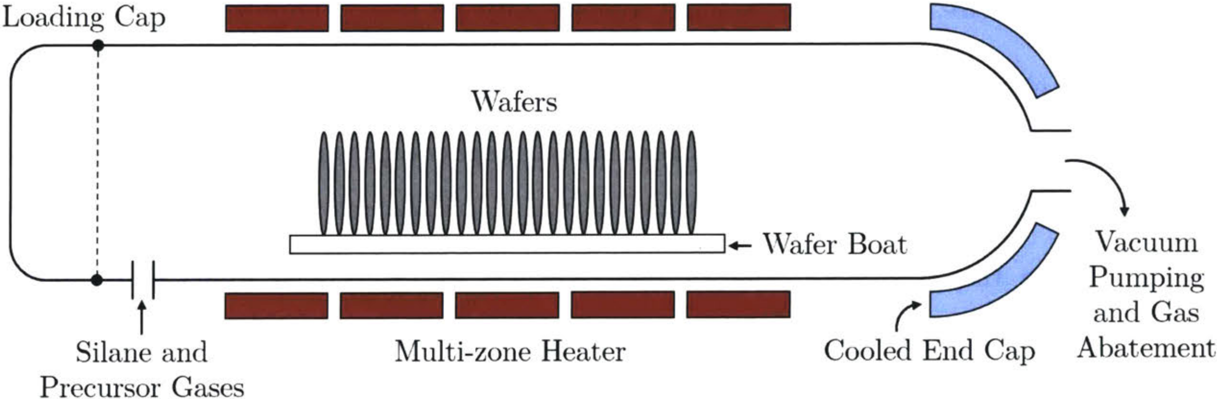

Figure 1.3: Schematic diagram of an LPCVD reactor.

1.2.4 Plasma-enhanced CVD (PECVD)

CVD tools that use plasma to enhance the deposition process fall broadly into two categories: systems with a low-density, capacitively-coupled plasma source and systems with high-density, inductively-coupled (ICP) or electron cyclotron resonance (ECR) sources. The capacitively-coupled systems were the first to be successfully reduced to practice, and are commonly referred to by the broad name "plasma-enhanced CVD" (PECVD). PECVD tools have appreciable differences from APCVD and LPCVD tools, and offer distinct capabilities, notably much lower deposition temperatures (as low as 100°C, although typically ≥200°C) and fast, conformal deposition rates (as high as 400 nm/min for SiO_2 [17] and 300 nm/min for SiN_x [18]).

To achieve these low temperature depositions, PECVD systems apply strong RF (typically 13.56MHz) electric fields between two parallel plates within the process chamber to generate a plasma from the precursor gases. This parallel plate configuration is commonly referred to as a capacitively coupled plasma (CCP) generation system, because the two plates (the electrodes of the capacitor) capacitively couple energy into the precursor gas, which leads to the plasma ignition. The substrate resides on the lower of the two parallel plates, where an additional, usually lower frequency RF power source (100-500 kHz) can be connected to add further control over incident ion energies (affecting film stress, density, and conformality). The dissociated precursor gas atoms and molecules from the plasma adsorb and react readily on the substrate surface, without the need for as much substrate heating as in APCVD and LPCVD. By lowering the deposition temperature, process and material compatibility are greatly improved [11], [13].

In order to produce an environment conducive to plasma generation and maintenance, PECVD systems, like LPCVD systems, also operate at sub-atmospheric pressures (typically from 0.1-2 torr), which leads to fewer particulate-forming gas phase reactions [19], [20] compared to APCVD systems. While they are more complex than APCVD or LPCVD in terms of equipment requirements, PECVD systems have become very widespread due to their versatility in terms of controlling the properties of the deposited film (notably the stress and index of refraction) [16]. **Figure 1.4** shows the major components of a PECVD system.

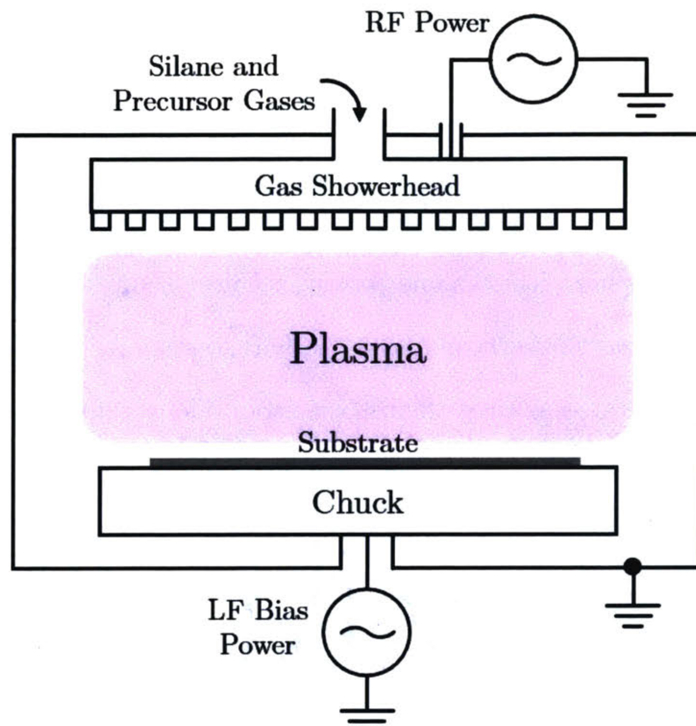

Figure 1.4: Schematic diagram of a PECVD reactor with a separate low-frequency bias power source connected to the substrate electrode.

1.2.5 Inductively-Coupled Plasma CVD (ICP-CVD)

In the late 1980s and early 1990s, significant research was done to develop alternative, high density plasma (HDP) generation systems for semiconductor processes. Electron cyclotron resonance (ECR) and inductively-coupled plasma (ICP) sources were the two main contenders in this space, and HDP-CVD systems featuring both types of sources can be found in the early literature (ECR: [19], [21]–[23], ICP: [6], [7], [24]–[26]). ICP sources eventually became the choice for most HDP-CVD systems, due to their simpler physical structure and ease of scaling [27].

ICP sources generate significantly higher densities of reactive species than parallel-plate CCP sources, giving ICP-CVD tools many advantages over traditional PECVD tools. These advantages include even lower substrate temperature requirements (as low as 20°C), lower hydrogen incorporation in the deposited films, and safer precursor gases (N_2 can be used instead of the corrosive NH_3 for SiN_x depositions). Furthermore, the plasma density from ICP sources is decoupled from the ion energy and flux seen by the substrate (unlike CCP sources), which can be used to decrease the level of ion bombardment and thus minimize surface damage to the film

(which can degrade the performance of sensitive electronic devices like HEMTs [28], [29]). The energy and flux are instead controlled through the application of RF power (resulting in an induced negative DC bias voltage[1]) to an electrode in the substrate chuck, which can be tuned to adjust the deposited film's stress, density, and index of refraction [7], [27].

In a typical ICP-CVD system like the one shown in **Figure 1.5**, the precursor gases (except silane) are flown through a gas showerhead above the ICP source. As the gases pass through the ICP region, a plasma is generated as they are dissociated into ions, radicals, and neutrals. Argon, a relatively heavy atom with a large collisional cross section, is often included to increase the plasma density, particularly during SiN_x and a-Si deposition [25], [30]. The silane is flown into the chamber using a separate "gas ring" located radially just above the substrate to avoid excess unwanted gas phase reactions. When the dissociated precursor gas meets the silane at the substrate surface (typically held between 25°C and 150°C), the standard adsorption, reaction, desorption process occurs and the desired film is deposited. Unlike CCP sources, ICP sources can generate plasmas at pressures of just a few mTorr due to their greater ionization efficiency. This means that ICP-CVD processes can be run at pressures much lower than PECVD processes (5-100 mTorr vs 0.5-2 torr). This large decrease in operating pressure is accompanied by lower deposition rates (~2-5 times slower than PECVD), but these lower rates can actually be useful for precisely controlling deposited film thicknesses. The lower process pressure also means fewer impurities are incorporated into films, in particular less hydrogen, which improves film density and dielectric characteristics [27], [31], [32].

---

[1] Compared to electrons, the larger (relative) mass of ions makes them unable to follow the oscillating electric field from the applied RF power. Lightweight electrons can follow this field though and impact the substrate electrode, causing it to become net negatively charged.

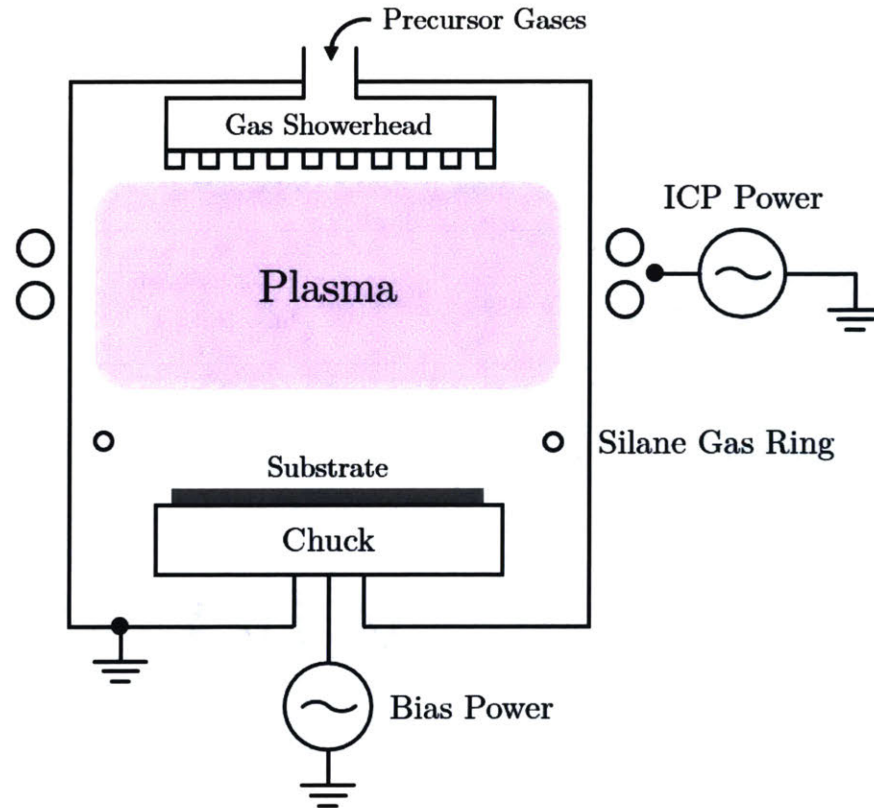

Figure 1.5: Schematic diagram of an ICP-CVD system.

1.2.6 Comparison of CVD Techniques

The following two tables summarize the processing conditions and resulting film characteristics for each of the four CVD types described above.

	Substrate Temperature [°C]	Chamber Pressure [torr]	Dep. Rate [nm/min]		Batch Processing
			SiO_2	SiN_x	
APCVD	~300-500	760	50-500	100-300	Yes, usually 5-10 wafers at a time
LPCVD	~600-800	0.1-1	2-10	2-10	Yes, as many as 150 wafers at a time
PECVD	~200-400	0.5-2	50-400	20-300	No
ICP-CVD	~25-150	0.005-0.1	10-150	10-100	No

Table 1.2: Deposition conditions and performance of four common CVD types.

	Average Film Stress	Conformality	Film Density	Index of Refraction	Film Characteristics
APCVD	Tensile	Poor, "bread-loafing" effect	Average	SiO_2: 1.40-1.45 SiN_x: 1.90-2.15	Significant H_2 content, less uniform than other CVD techniques.
LPCVD	Tensile to compressive	Very good	Excellent	SiO_2: 1.44-1.47 SiN_x: 2.0-2.1	Dense (pinhole-free), minimal impurities, stoichiometric
PECVD	Tunable, primarily compressive	Average, improved with TEOS for SiO_2	Good	SiO_2: 1.45-1.50 SiN_x: 1.90-2.10	Controllable stress, some H_2 content and ion damage, particle-inclusion and pinholes without consistent cleaning
ICP-CVD	Tunable, primarily compressive	Good, requires parameter tuning	Good	SiO_2: 1.40-1.60 SiN_x: 1.90-2.30	Controllable stress, less H_2 content Independent bias on substrate can better control density and conformality

Table 1.3: Deposition characteristics of four common CVD techniques.

1.3 Objectives

Before beginning work on the IFIC system, several project objectives were established to guide the design process. These objectives are listed below and will be addressed throughout the thesis:

- Design a system that fits within the existing Inch Fab tool architecture
- Maintain a low overall system capital cost
- Avoid the use of hazardous process gases
  - Use 1.5% SiH_4/He mixture to avoid pyrophoricity.
  - Use N_2 instead of NH_3 for SiN_x depositions.
- Achieve high quality SiO_2 and SiN_x film depositions
  - Comparable to existing research-grade commercial equipment
- Establish the reliable operation of the tool over time
- Understand the relationship between each input parameter and the output film characteristics
  - Develop models to predict film properties from inputs

1.4 Outline of Thesis

The remainder of this thesis is divided into 5 chapters. **Chapter 2** dissects the design of each of the major assemblies in the IFIC system, discusses the other back-end components in the system, and analyzes the total cost of the tool. **Chapter 3** examines the performance of several (non-deposition) aspects of the system, and provides information and assessments of the measurement techniques used to characterize the deposited films. **Chapter 4** and **Chapter 5** describe the deposition of SiO_2 and SiN_x, respectively, compare the results to those seen in existing tools, and generate models for predicting the output properties of these films. **Chapter 6** summarizes the results of the previous chapters and provides a future outlook for the IFIC and the Inch Fab initiative.

Chapter 2: System Design

One of the overarching goals of the Inch Fab initiative for high-performance, ultra-low cost semiconductor processing tools is to produce modular designs that can easily adapted to perform the exact fabrication processes needed by the end user. To this end, a modular vacuum tool architecture was established during the development of the first Inch Fab tools (etching systems designed to perform reactive ion etching (RIE) and Bosch-process style deep reactive ion etching (DRIE)) that could be used to aid in the development of future tools and processes. The modularity and interchangeability within this architecture allows new fabrication techniques to be brought on line in less time, and makes the tools themselves more flexible in the types of processes they can support.

The idea of tool modularity is not unprecedented, as several currently available commercial tools use common subsystems (e.g. an ICP plasma source or a substrate temperature control system [8], [33]) across different tool types. "Cluster" tools, where multiple process chambers are connected to a single, centralized wafer-handling chamber, can also be considered as modular from an inter-tool perspective. The concept of SMIF (Standard Mechanical Interface) pods or FOUPs (Front Opening Unified Pods), which are standardized wafer carriers used to transfer and interface cassettes of wafers between processing tools in high-volume production, provide a measure of modularity through the path of standardization. The Inch Fab architecture builds on these ideas of modularity by splitting the tool design into four sections: the upper chamber assembly (UCA), the lower chamber assembly (LCA), the substrate chuck assembly (SCA), and the load lock assembly (LLA). The four assemblies work together to achieve the desired process goal, but each have specific and largely independent roles, such that if a new process requires slightly different functionality, a more appropriate version of the relevant assembly can be easily swapped in, rather than redesigning the entire tool.

The Inch Fab ICP-CVD (IFIC) system utilizes this four-part modular architecture, and through its design has provided several refinements and upgrades to each of the assemblies. This

chapter begins with an overview of the full tool, then moves to a discussion of some of the basics of vacuum tool design that underpin each of the four assemblies, and then transitions to a description of the design of each assembly. Sections on the selection and integration of the required peripheral equipment systems follows, and the chapter concludes with a cost analysis of the full IFIC system.

2.1 Tool Design Overview

The design process for the IFIC began with an enumeration of the high-level goals for the tool. These goals are listed below.

- Maintain an ultra-low system cost (ideally a sticker price < 50,000 USD[2])
- Deposit silicon-based dielectrics (SiO_2, SiN_x)
- Use an ICP plasma source to reduce the deposition temperature
- Utilize a dilute silane mixture (1.5% SiH_4/He) to avoid SiH_4 pyrophoricity
- Use N_2 instead of corrosive NH_3 for SiN_x deposition
- Achieve comparable performance to commercially available research-grade tools
- Preserve compatibility with Inch Fab modular vacuum tool architecture
- Minimize the overall footprint of the tool where possible
- Provide a user-friendly operating experience

Some of these goals are related to the specific process of ICP-CVD, while others stem from the goals of the Inch Fab initiative. This section will provide an overview of the tool design that resulted from these goals, and serve as a map to the following sections and chapters where further information relating to the achievement of each goal can be found.

As mentioned at the beginning of this chapter, the IFIC system utilizes the Inch Fab four-piece modular vacuum tool architecture. While these are the crucial sub-systems that make up

[2] In keeping with the Inch Fab initiative's goal of scaling the capital cost of the tool with the area processed. Research-grade 150 mm ICP-CVD tools have a sticker price of ~500,000 USD, and have a processable area 9-10 times larger than the IFIC.

the face of the system, there are many other essential pieces of peripheral equipment that make up the full system. These include the sources of the process gas and RF power, the vacuum pumps, and the control system. **Figure 2.1** shows a block diagram identifying how the primary peripherals and modular assemblies are connected together.

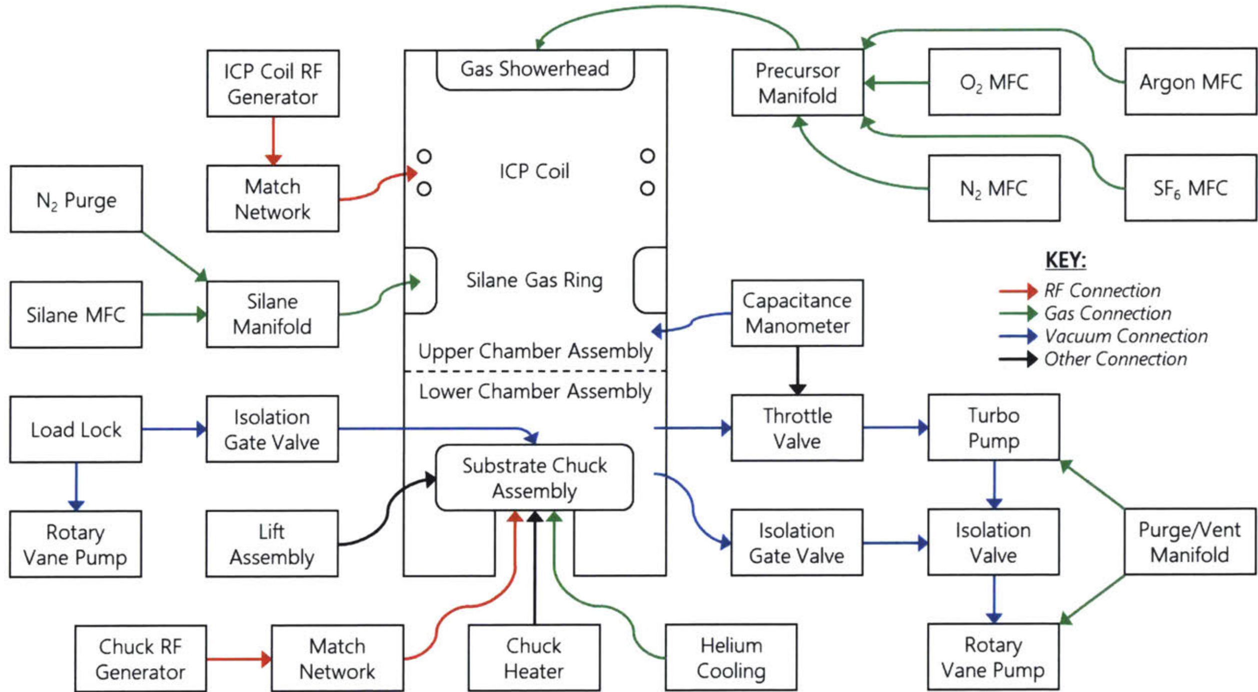

Figure 2.1: IFIC Block Diagram

As seen in **Figure 2.1**, in addition to the four main assemblies, the IFIC features two separate RF power delivery systems, two separate pumping systems, and two separate process gas delivery systems. Each of these serve an important role in producing high quality depositions, and have been carefully selected or designed to meet both cost and performance requirements.

2.2 Vacuum Tool Design Concepts

Before moving on to discuss the IFIC's assemblies and sub-systems, several principles of vacuum tool design are worth noting. These principles were used throughout the design process, and provide context to the design decisions discussed in the following sections.

2.2.1 Materials Selection

In addition to the traditional parameters considered during material selection for machine design (such as strength, weight, cost, and temperature stability), materials to be used in a vacuum environment must be "vacuum-compatible". In general, vacuum-compatible materials must have low outgassing rates, low gas permeability, and low vapor pressure. Many materials that would ordinarily be good candidates for pieces of a non-vacuum tool may not be suitable for high-vacuum applications (e.g. nylon – high outgassing rate, neoprene rubber – high gas permeability, and brass or galvanized steel – high vapor pressure) [34]. Commonly used metals for vacuum tools include 6061 aluminum, 304/304L stainless steel, and nickel. Commonly used plastics include polytetrafluoroethylene (PTFE), polyether ether ketone (PEEK), and polyimide. Quartz, alumina, and borosilicate glass are good choices when ceramic materials are required. Elastomers generally offer lower vacuum performance than the materials listed above, but due to their high compressibility are extremely useful as O-rings or gaskets for sealing components together. Fluoroelastomers such as Viton are widely used for this purpose. All of these materials must, of course, be free of surface contaminants such as dirt or grease in order retain their vacuum compatibility. In addition to thorough cleaning prior to installation in a tool, the vacuum performance of materials can nearly always be improved after installation with exposure to elevated temperature (known as "baking out") and certain plasma discharges. The specific cleaning and baking process used for fabricated parts installed in the IFIC is included in **Appendix A**.

Material selection for the IFIC required careful consideration of the specific conditions a part would be exposed to. Certain characteristics, like vacuum compatibility and chemical compatibility with each of the process gases (specifically SiH_4 and SF_6) were considered universally, but the requirements for properties like temperature resistance or conductivity vary widely depending on the part. For instance, the substrate chuck assembly (SCA) was designed to be heatable up to 200°C during operation. This temperature means that certain wire insulation materials like PVC or polyolefin could not be used, nor could nitrile O-rings. Large RF powers

and voltages are also an unavoidable aspect of the IFIC, and so proper insulation and isolation of powered components also played an important role in the material selection process.

2.2.2 Seals and Leaks

One of the most important aspects of vacuum tool design is sealing. Seals not only isolate the vacuum environment inside the tool from the outside atmosphere, but also serve to isolate sections of the tool from one another, preventing fluid communication unless it is specifically desired. There are several different seal materials and types of seals used in the IFIC. The choice of a particular material or type depends on a variety of factors, including the materials and geometry of the components being sealed together, the frequency of unsealing/resealing (if at all), and the forces available to make the seal.

When a seal is imperfectly made, a leak point is created. The leak resulting from this imperfect seal is known as a "residual leak", and will allow gas to be exchanged between the two sides of the seal. When there is a pressure difference between the two sides of the seal (e.g. atmospheric pressure and vacuum), gas will flow into the low pressure side, raising the pressure and potentially disrupt any balance of other gas flows on the low pressure side. Residual leaks can be detected using the methods discussed in **Section 3.1.1**, but can largely be eliminated by choosing an appropriate type of seal for the interface and being meticulous during the installation process.

A second type of leak, known as "virtual leaks", can occur when gas is trapped in pockets or adsorbed on surfaces within the evacuated region of a vacuum chamber. The first virtual leak case (gas trapped in pockets) can be seen as a sort of sub-category of residual leaks, where the gas is trapped in the pockets during installation at atmospheric pressure and slowly leaks out into the chamber via a residual leak path. The leak path can be through an intended seal like an O-ring or gasket, but is often through a low-conductance pathway like the area between the threads of a screw and a tapped hole. The pressure difference between the virtual leak source and the chamber will slowly dissipate as the source is evacuated, but this process can take days or even longer depending on the conductance between the source and chamber. To combat this, parts

can be designed to minimize the volume of gas trapped during the assembly process or higher-conductance relief paths can be added to speed the removal of the trapped gas. A classic example of this tactic (and one used several times in the IFIC) is to minimize virtual leaks from gas trapped under screws by replacing the solid screws with "vented" screws. Vented screws have holes drilled through their long axis (center-vented) or slots milled along the threads and under the screw head (slot-vented), which allows the trapped gas pocket to be removed quicker via the higher-conductance vent path at the cost of a small reduction in the screw's holding strength. An example of the use of vented screws in the IFIC is shown as part of **Figure 2.2**.

The second virtual leak case, gas adsorbed on the surfaces of a vacuum chamber, also originates from exposure to atmospheric pressure during installation or after venting the chamber. While exposed to this high pressure, gas molecules (most commonly water vapor) adsorb to all accessible surfaces and are very slowly desorbed upon pump-down. To alleviate this virtual leak case, chamber surfaces can be heated up ("baked out"), which increases the rate of desorption. Care must be taken however, to not heat any of the materials in the chamber past their thermal limits during this process. Baking parts in a vacuum oven immediately prior to installation can also help to reduce virtual leaks, particularly in the case of permeable materials like O-rings, which can absorb water or other volatile compounds into their bulk while at atmospheric pressure. Adsorbed gas can also be removed to some degree via Ar or O_2 plasma cleaning [35], [36], the latter of which is also very effective at removing any organic contaminants on surfaces in the chamber. In the IFIC, all parts were vacuum baked for at least 12 hours at 90°C prior to installation in the system and then cleaned in situ after installation using both Ar and O_2 plasmas.

Transitioning back to seals, the most basic and widespread seal type used in the IFIC is the static face seal. This type of seal can be used to seal flanges or certain fitting types together, and is enacted by deforming a gasket material between two surfaces. If the face seal is not meant to be regularly unsealed, a common sealing method is to compress a one-time-use gasket made from soft or annealed metal between two (metal) edges that sit proud from the surface of the flange or fitting. This is the type of seal used most often in Swagelok VCR fittings and ConFlat (CF)

flange seals. These seals are very leak-tight, and since they are an all-metal seal can be baked to high temperatures to reduce outgassing. Another type of semi-permanent face seals are tapered pipe thread seals. National Pipe Taper (NPT) and British Standard Pipe Taper (BSPT) threaded fittings can be used to create a vacuum-tight seals by applying a thin layer of PTFE tape or sealing compound to the threads and firmly tightening. Tapered pipe seals require patience and some experience to correctly install, but depending on the situation can be the most economical sealing method from both a cost and required-space perspective. Untapered threaded fittings that use elastomeric O-rings located under the head of the fitting to create a seal also exist and can be situationally useful[3].

If a face seal needs to be routinely unsealed and resealed during operation of the tool, or metal gaskets cannot be used (as is the case with most parts with aluminum sealing faces), a reusable elastomer seal can be used instead. Most commonly, this involves using a circular cross-section O-ring and a rectangular or trapezoidal groove cut into one of the two surfaces being sealed together. Depending on the magnitude and direction of the pressure differential during sealing (inside or outside of the O-ring), the dimensions of the groove can be adjusted to provide the correct amount of stretch and compression to ensure a leak-tight seal. Many different guides are available to help determine the exact dimensions needed for a good seal [37], but a good rule of thumb is rectangular O-ring grooves should be ~75% of the O-ring's cross-section deep, and ~125% of the cross-section wide, and cause 1-3% of diametrical stretch in the O-ring once installed. **Figure 2.2** shows a partial cross-section of the upper portion of the UCA, which features several different seal types.

[3] A list of many different threaded seal types can be found in [129].

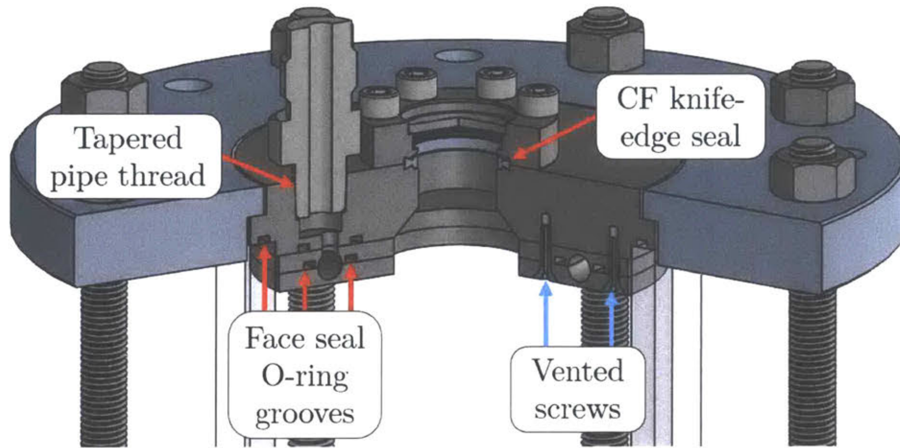

Figure 2.2: Examples of seals (red arrows) and virtual leak mitigation (blue arrows) in the UCA.

Another type of seal used in the IFIC is the dynamic axial seal. This seal type is used to seal a rod within a cylindrical bore, and allows the rod to be translated and rotated while maintaining vacuum-tightness. The seal is created by an O-ring placed in a groove cut into the bore. Like the face seal grooves, many design guides exist to assist in sizing the groove [37]. In vacuum tools, where this type of seal is routinely used for feedthroughs, two grooves separated by a port (such as a threaded female NPT hole) are often used instead of a single groove. If the port between the two grooves is pumped to a low pressure (between atmosphere and the vacuum pressure, typically < 1 torr), it creates what is known as a differentially pumped seal. This type of seal is much more robust against the small leaks that can occur as the rod slides over the O-rings, as the pressure differential between the vacuum chamber and the small intermediate volume between the grooves is much smaller than the atmosphere-vacuum differential and is easily maintained through the small pump port. **Figure 2.3** shows a cross-section view of this configuration, as used for the sample transfer arm feedthrough in the LLA.

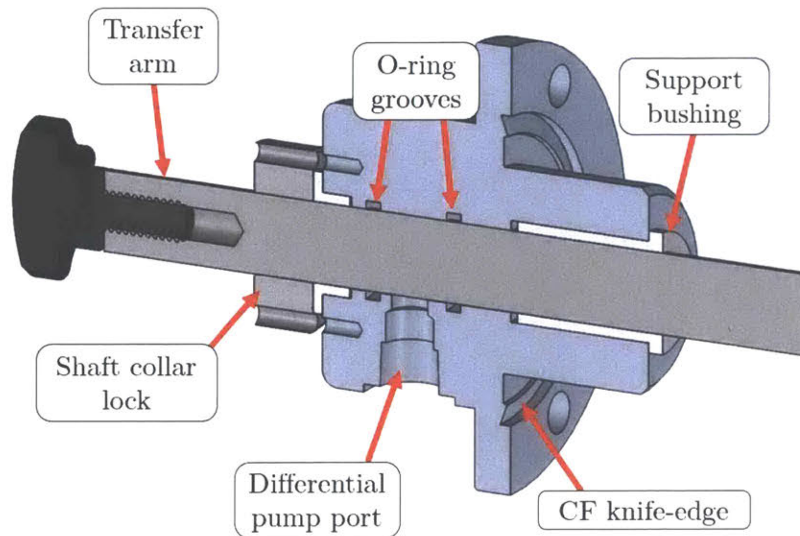

Figure 2.3: Differentially pumped linear and rotary motion feedthrough.

2.2.3 Design for "X"

The final topic in this discussion of vacuum tool design revolves around the idea that when designing parts or systems, attention should be paid to more than just the part's end use or function, but also to how easily it can be manufactured, assembled, or tested, all of which also play a role in how much the part will ultimately cost. For the Inch Fab initiative, which is centered around the development of ultra-low cost processing tools, keeping these principles in mind while designing a new tool is essential. A design that may improve performance by 5% but also cost by 5% needs to be carefully evaluated before it is integrated into the system.

Design for manufacturability (DFM) from a vacuum tool perspective often begins with the choice of material for a part. For example, from a raw material cost standpoint, 6061 aluminum and 304 stainless steel are similar, but 6061 is much easier and faster to machine. If the superior weldability and slightly better UHV performance of 304 are not required (and they were not for much of the IFIC design), 6061 offers a significant DFM advantage. Considering the specific fabrication steps and processes needed to produce a part during its design phase and then optimizing the design to require less time, fewer operations, or wider tolerances are canonical examples of DFM that were routinely used in the IFIC design process, particularly for parts fabricated using CNC machining techniques.

Design for assembly (DFA) in the context of vacuum tool design corresponds not only to the initial assembly, but also to potential disassembly, which will inevitably be needed for cleaning or servicing operations. Galling or seizing of parts (fasteners are particularly susceptible), which may only be discovered during the disassembly process, is an important example of the consequences of failing to consider DFA concepts. Galling and seizing can nearly always be avoided through proper material selection (dissimilar metals or silver-plated fasteners) or the use of specific lubricants, but these decisions must be made before the assembly process. During the actual assembly process for vacuum-based tools, one of the biggest sources of contamination that can affect a tool's future performance is the person actually assembling the system. Design choices that reduce the amount of part handling needed to assemble a part or system are good examples of DFA. For the IFIC, DFA was also important to consider during applications like printed circuit board (PCB) design, where the size and relative placement of components drastically affects the yield and how much effort is required to populate a board.

Design for test (TFT) in vacuum tool design can involve adding features like grooves that increase the conductance into the atmospheric side of seals, which makes checking for leaks in that seal much more effective, or adding valves (temporarily or permanently) into gas or vacuum lines to help isolate problems or test certain sub-sections of a tool. From the software control perspective, the implementation of DFT in the IFIC has led to the development and refinement of the data logging, debugging, and direct hardware communication interfaces now included in the Process and Recipe Control (PARC) software.

Each of these "Design for X" principles have been used throughout the design of the IFIC, and specific examples will be highlighted in the following sections.

2.3 IFIC Modular Tool Architecture

In this section, the design of the four modular assemblies that make up the IFIC are described. The functional requirements for each assembly will be provided, and the design choices that fulfilled those requirements will be explained. How each of the four assemblies interface with one

another will be discussed throughout the section. To provide some visual context for this interfacing, **Figure 2.4** shows a labeled cross-sectional rendering of the IFIC, and **Figure 2.5** shows an exploded view depicting how each of the four assemblies connect together.

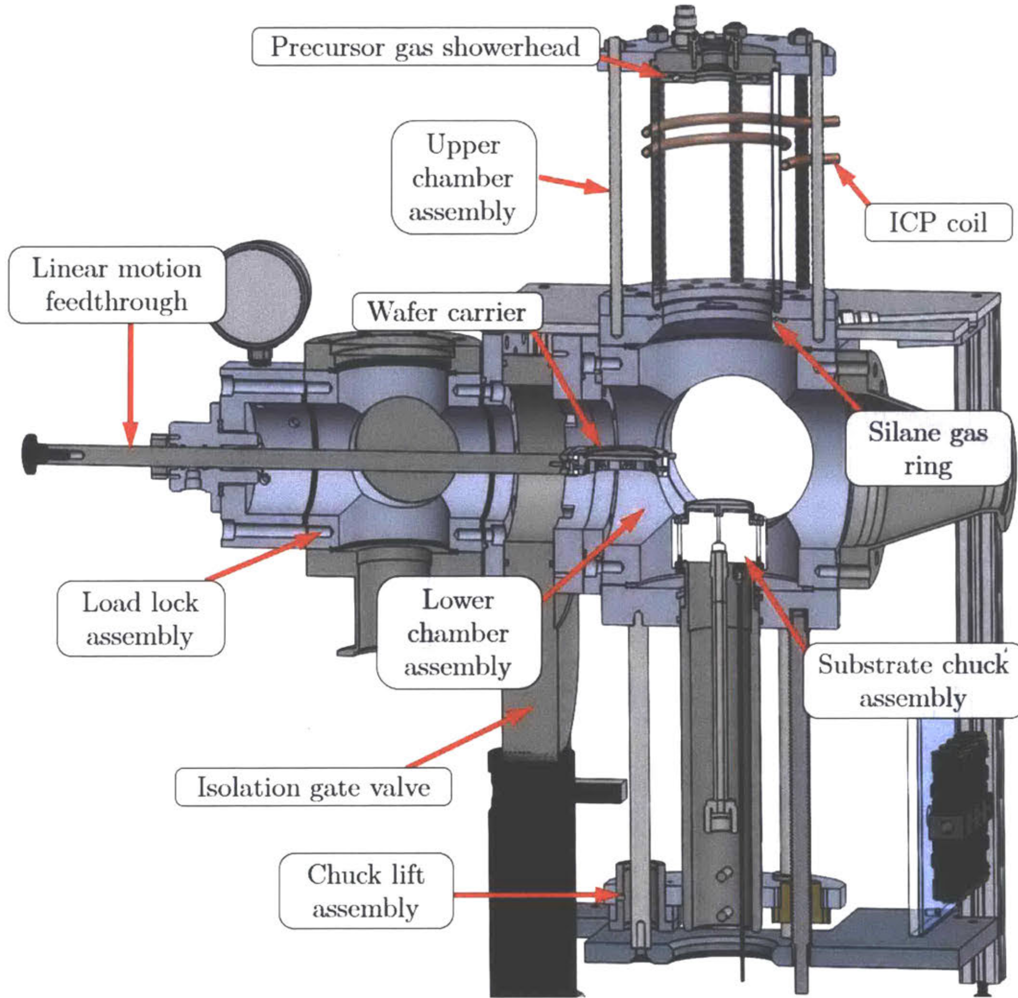

Figure 2.4: Labeled cross-sectional view of the four modular assemblies of the IFIC

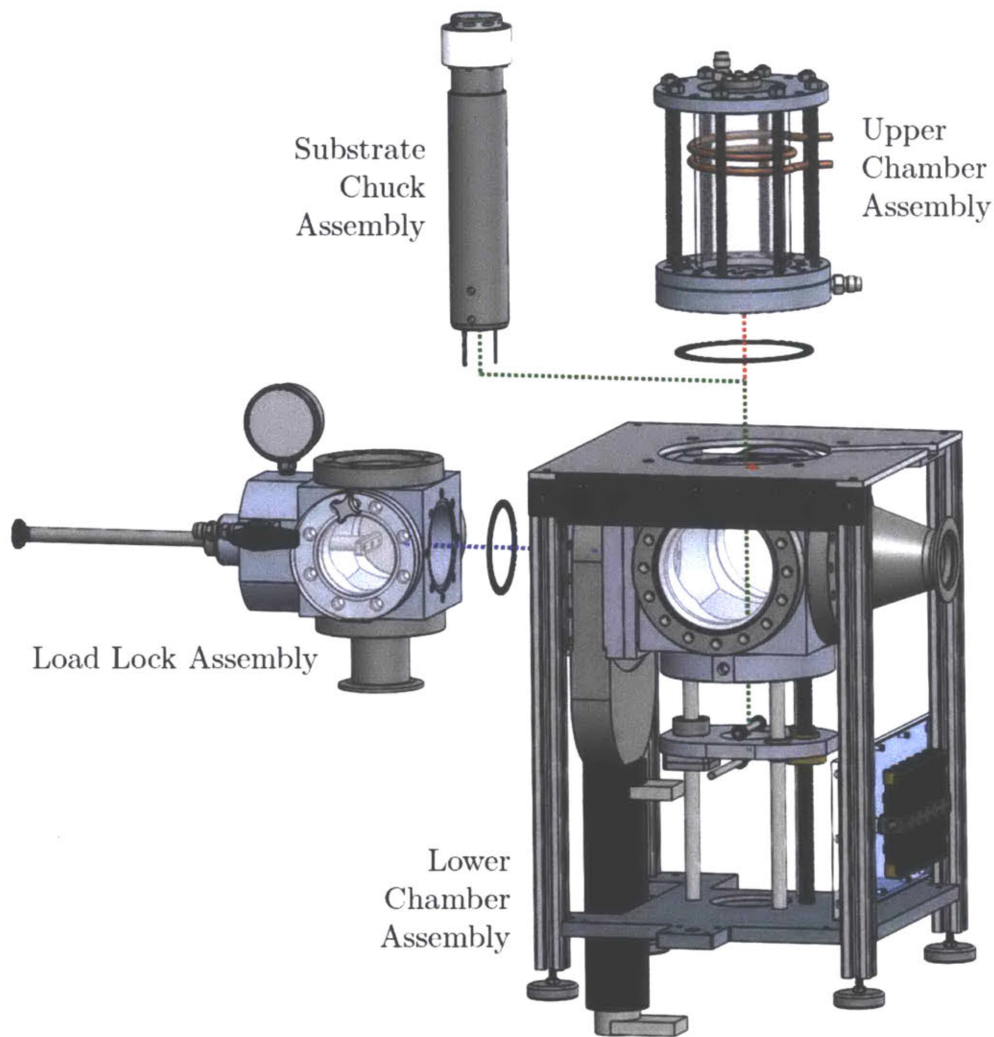

Figure 2.5: Exploded view of the four modular assemblies. The dotted lines indicate how the assembly mate with one another.

2.3.1 Lower Chamber Assembly (LCA)

In the Inch Fab modular vacuum tool architecture, the lower chamber assembly (LCA) operates as the backbone of the processing tool. The primary functional requirements for the LCA are to:

- Serve as a stable mechanical base for the rest of the tool
- Provide mechanical support and registration for the upper chamber assembly (UCA)
- Provide a connection interface and sample transfer pathway for the load lock assembly (LLA)

- Provide a rotary and linear motion vacuum feedthrough that can support the substrate chuck assembly (SCA) and translate it between the sample loading and processing positions
- Connect to the conductance control (throttle) valve and primary (turbomolecular pump) vacuum foreline
- Connect to the auxiliary (roughing) vacuum foreline

The resulting design that meets these requirements is shown below in both assembled and exploded renderings.

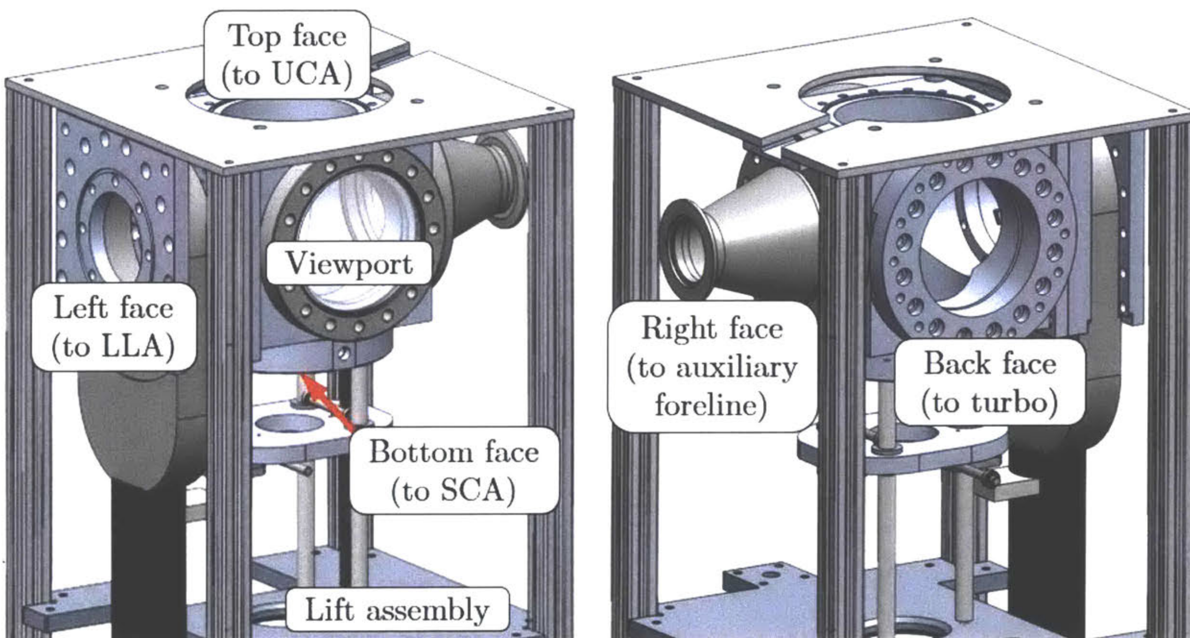

Figure 2.6: Renderings showing the assembled LCA, connection information, and naming conventions.

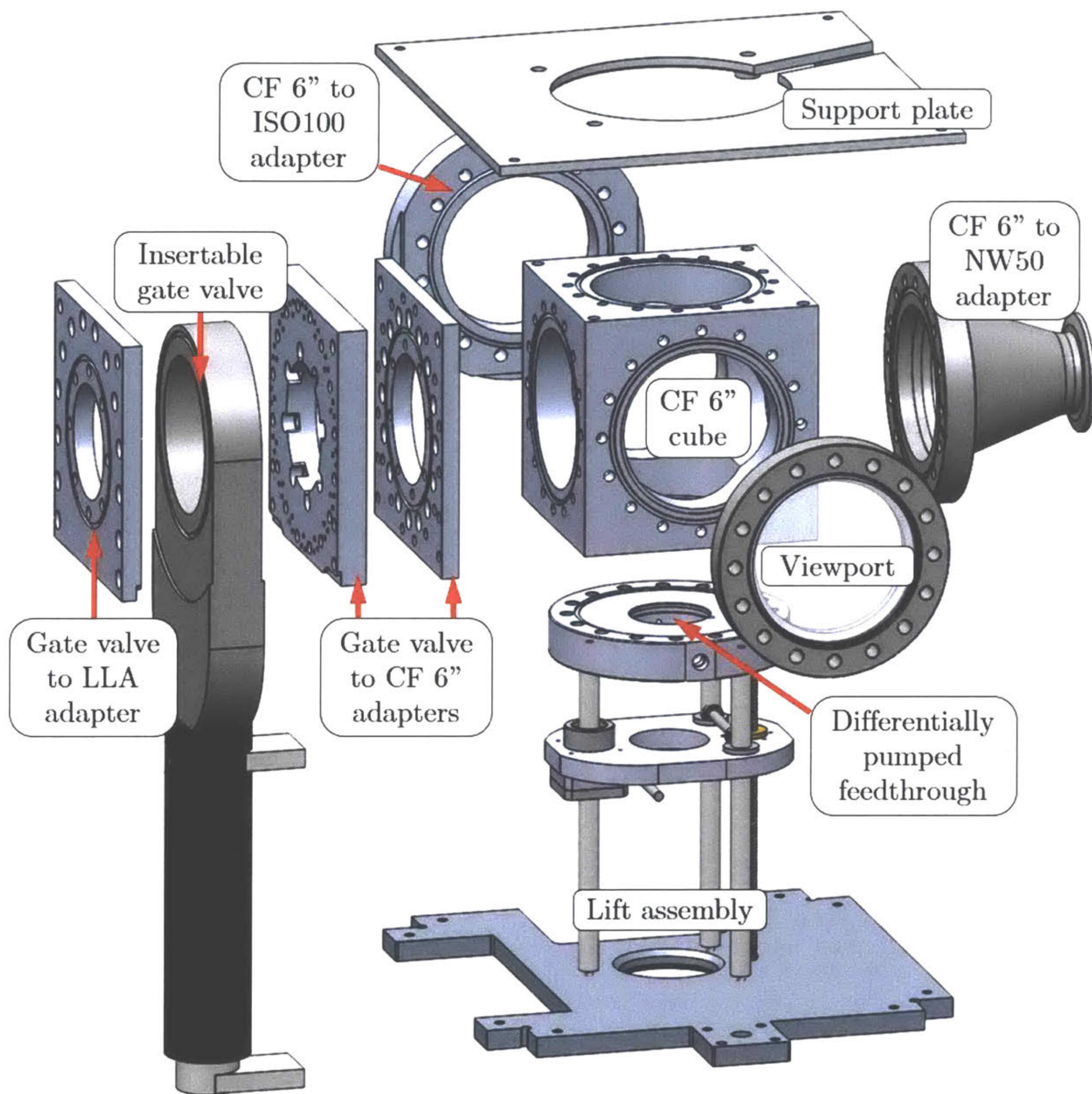

Figure 2.7: Exploded view of the LCA with labels for the major components. Not shown are the support legs, which attach to the support plate and lift assembly.

At the core of the LCA is a 6" (152.4 mm) cube with CF-style knife-edges and bolt patterns on each face. Four tapped holes on the top face are used to connect to a 12" (305.4 mm) square support plate, which itself is connected at each corner to 18" (457 mm) long legs. Another support plate is attached at the bottom of the legs to provide stability. This bottom plate also serves as the base for the SCA lift assembly, which will be discussed shortly.

The UCA mates with the LCA on the top face of this cube using a molded Viton gasket specifically designed to make a reusable face seal across the CF knife-edge. The force provided by the weight of the UCA is enough to initiate a vacuum-tight seal once pump-down begins, and the added downward force from the ~760 torr (~14.7 psi or ~0.1 MPa) atmosphere-to-vacuum pressure differential completes the seal. Proper registration between the UCA and LCA knife-edges is achieved using chamfered plastic alignment pins that are screwed in along the bolt circle of the CF flange.

The front face of the cube is outfitted with a large viewport (~100 mm viewing area), which was included to allow the sample loading/unloading process to be monitored, and also serves as an easy way to monitor the internal conditions in the chamber. The viewport window material is borosilicate glass, which was chosen because it is significantly cheaper than other viewport materials at the 6" CF size. Borosilicate, like other SiO_2-based glasses is susceptible to etching via fluorine-based dry etch chemistries (including the SF_6 used for chamber cleans in the IFIC), but no cloudiness has been observed on the window after cleans, suggesting that its placement below the primary plasma discharge region and opposite the turbo pump limits the amount of both deposition and etching species that it encounters. If these circumstances change, the window could be replaced with a more etch-resistant window material like sapphire, but these windows are much more expensive, even at smaller viewing areas.

The back face of the cube provides the connection to the throttle valve and turbo pump foreline. In order to maximize the conductance between the chamber and the turbo pump inlet, the overall foreline length must be kept very short. The turbo pump and throttle valve for the IFIC were specified with ISO NW100 flanges (ISO flanges were the only flange type offered on both the throttle valve and turbo pump for the size needed) and so an adapter flange converting from ISO100 to 6" CF was needed to connect these items to the LCA. The shortest normally stocked adapter for this flange-pair is 6" (152.4 mm) long (e.g. KJLC part number F0600XQF100), which would have doubled the length of foreline and complicated the assembly process

appreciably[4]. To avoid this, a custom, "zero-length" adapter plate was designed and fabricated. This plate is only 0.75" (19.1 mm) long, and makes the installation process very straightforward. The adapter plate is first installed alone on the LCA cube, and then the throttle valve, spacer plate (1.75" (44.5 mm) long—to prevent the throttle valve flapper from hitting the turbo pump rotors), and turbo pump can be connected as a stack to the adapter plate using a single set of bolts. This reduced the full length of the turbo pump foreline from 10" (254 mm) down to 4.75" (120.7 mm), drastically improving the conductance[5] between the chamber and pump inlet. Further discussion of the turbo pump selection and performance can be found in **Section 2.4.2** and **Section 3.1.2-3.1.3**.

The auxiliary foreline, which connects the processing chamber to the main roughing pump, is connected to the right face of the LCA cube. During normal operation, this foreline is closed off using an NW50 gate valve, and the main roughing pump serves as the backing pump for the turbo pump, but it can be used to quickly evacuate the chamber after it has been vented, or keep the chamber pumped down if the turbo must be isolated or removed from the system. The section of this foreline between the LCA cube and the gate valve is also where the main pressure measurement devices are installed. In the IFIC, a capacitance manometer (0.1 torr full scale) is used to measure the chamber pressure and provide the feedback signal to the throttle valve. An additional port (normally blanked off) is also included in this foreline section that can be outfitted with a higher or lower pressure range sensor, or another type of sensor altogether.

The left face of the LCA cube connects the LLA to the main chamber. The two assemblies are normally kept isolated from one another using a gate valve, which is connected to both assemblies using a set of custom adapter plates. Like the turbo foreline case, these adapter plates were designed to both reduce the path length and installation complexity between assemblies. In

---

[4] This adapter type would have required installing bolts in both directions in a tight space and, due to these adapters using the ISO-K clamp style rather than the ISO-F bolt hole style, would have required an external part or jig to properly align the throttle valve to the rest of the chamber.

[5] Using formulas from [41], molecular flow conductance was increased by ~50% and viscous flow conductance increased by ~100%.

this instance however, the path length reduction was sought out in order to reduce the physical dimensions of the IFIC system, rather than maximize the flow conductance. As will be discussed in greater detail in **Section 2.3.3**, the transfer of samples from the LLA, into the LCA, and onto the SCA is accomplished using a linear feedthrough rod. The minimum length of this rod is determined by the distance it must extend into the chamber, and so reducing the transition length between the LCA and LLA will reduce the required length of the rod. Taken together, this reduction of the transition length and the rod length means that the maximum system dimension in this axis is reduced by twice the amount removed by adapter plates (since the fully retracted rod will extend a shorter distance out from the feedthrough, and the body of the system will itself be shorter). This is quite positive and certainly in line with the Inch Fab design ethos, but perhaps the greater advantage of the adapter plates comes from how they drastically improve the process of installing the LLA and isolation gate valve.

In previous iterations of Inch Fab tools, which used the same 6" CF cube base for the LCA and 4.5" CF cube base for the LLA, a gate valve with either 6" CF or NW100 flanges was used to provide a large enough aperture for the wafer carrier to pass through. Both of these flange options for the gate valve have female threads on the flanges, as do the cubes they need to mate with. Thus, an intermediate adapter flange was needed to connect each cube to the gate valve. If the overall length between the LLA and LCA were not an issue, these adapters would be very simple parts, and could be installed with relative ease. As established earlier however, every unit of length added to the transition region between the assemblies results in two units of length added to the overall system, and compactness is a design goal. Therefore, minimal length "spider flanges" were designed to keep the transition region short. A rendering of these spider flanges is included in **Figure 2.8**. Fabricating these spider flanges is not simple, and installing them is very tedious work, and actually required the use of a custom, extra narrow 12-point wrench made using a waterjet cutter. Furthermore, many of the flanges on the gate valves are simply welded on to the valve body without a tight angular alignment specification for the bolt holes, meaning

that the faces of LLA and LCA may not end up parallel to one another, and the amount of this skew may not be consistent.

The gate valve and adapter plate combination designed for the IFIC represents a much better solution for this interface. The crux of this design is the use of an "insertable" gate valve rather than a flange gate valve. Insertable gate valves[6] have integral O-rings just outside of their apertures on both sides of the valve. By compressing the valve between two plates or flanges, a vacuum seal can be made and the valve itself can be supported (via friction). As the sealing flanges are now separate from the gate valve itself, they can be designed to directly connect to adjacent parts rather than needing a transitional adapter like the spider flange. In addition to producing a more compact part stack (3" (76.2 mm)) than the previous design (5" (127 mm))[7], which reduces the length of the system by a total of 4 inches (the additional 2 inches coming from a reduction in the required transfer arm length), the installation process for this new design is also much simpler and substantially faster. **Figure 2.8** shows a comparison between the spider flange design and the insertable gate valve design for connecting the LCA and LLA assemblies.

[6] The specific type of insertable gate valve used in the IFIC can be found in [130].

[7] In fact, the first iteration of this design was so compact that the door to the load lock would not fully open. An extra 0.25" (6.35 mm) therefore had to be added to the middle adapter plate.

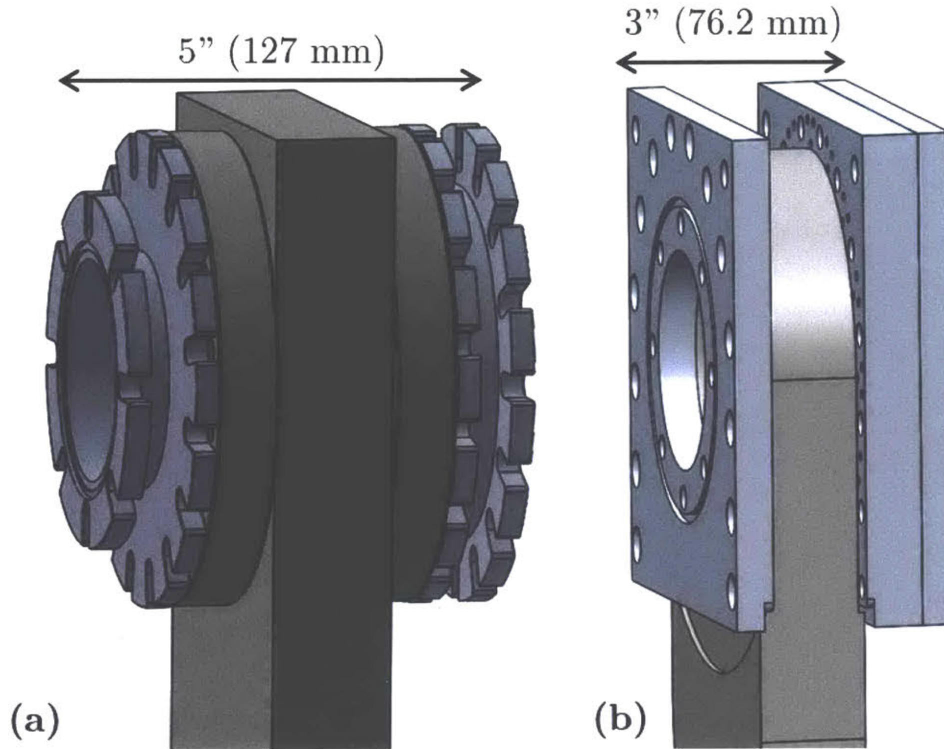

Figure 2.8: Comparison of (a) spider flanges used to connect CF 6" gate valve to LCA and LLA, and (b) the new, more compact insertable gate valve and plate flange design.

The last side of the LCA cube, the bottom face, connects to a differentially-pumped feedthrough (like the one shown in **Figure 2.3**) through which the SCA can be translated and rotated within the chamber while maintaining vacuum. The feedthrough allows the substrate to be loaded near the middle of the LCA cube and then raised into the processing position. The specific position of the SCA can be controlled precisely using a lift mechanism that drives a plate coupled to the bottom of the SCA up and down using a lead screw connected to a timing belt system. The rods that couple the SCA to the lift mechanism also allow it to be rotated, which is essential for the sample loading and unloading process, which will be discussed in **Section 2.3.3**. Rigidly coupling the SCA to the lift mechanism also prevents the atmosphere-to-vacuum pressure differential (~200 N of force given the SCA dimensions) from pulling the SCA into the chamber. The lift mechanism is currently manually operated, and shaft collars on the mechanism's support arms provide hard stops to reliably set the processing and sample load/unload heights. Proof-of-

concept testing has been done to show how this mechanism could easily be automated using motors and limit switches, but this has not been implemented in the IFIC.

2.3.2 Upper Chamber Assembly (UCA)

In the Inch Fab modular vacuum tool architecture, the upper chamber assembly (UCA) is the section of the tool where the desired process originates. In plasma-based systems like the Inch Fab DRIE and the IFIC, the UCA is where the process gases are introduced to the chamber and the plasma discharge is created. Insofar as functional requirements, the IFIC UCA needs to:

- Create a stable, high-density inductively-coupled plasma (ICP) discharge
- Distribute the process gas at a location upstream of the ICP generation region
- Distribute the SiH_4/He mixture at a location downstream of the ICP discharge but upstream of the substrate
- Contain a central utility port that can be used for deposition monitoring or diagnostic purposes
- Be easily cleanable, both in situ and ex situ
- Include a safe barrier between the user and the high RF power and high temperature chamber components

Figure 2.9 shows renderings of the UCA design used in the IFIC and labels some of the critical components.

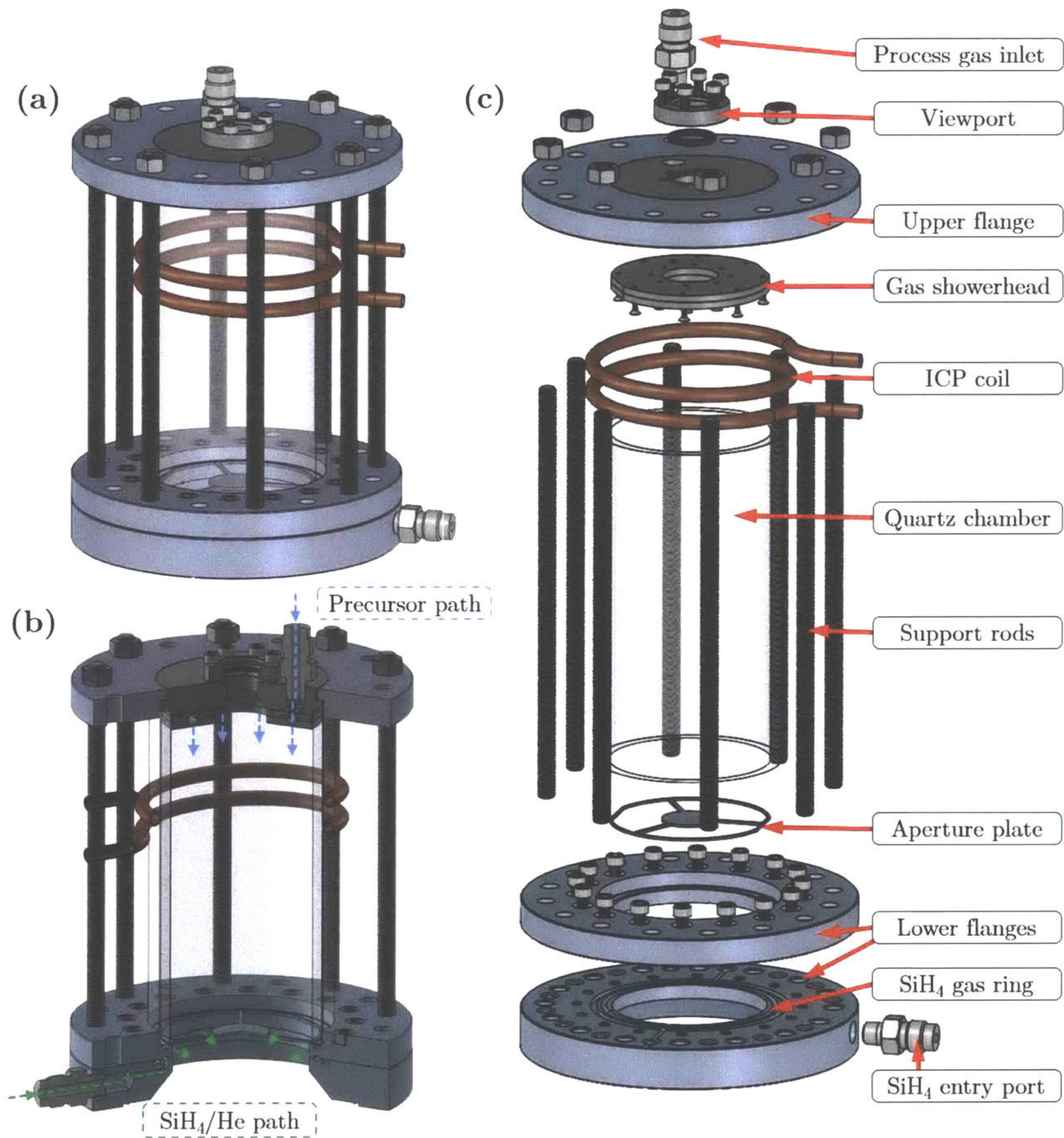

Figure 2.9: Renderings of the UCA. (a) The assembled UCA; (b) Cross-sectional view showing both gas entry paths; (c) Exploded view with labels for key components.

The basic design of the UCA seen in the figure above originated during the design of the Inch Fab DRIE system, which also featured a two-turn helical ICP source, an upper gas showerhead, and a central utility port [2]. The IFIC version has several new features and design improvements. Unlike traditional PECVD or RIE/DRIE systems, ICP-CVD systems utilize two separate gas

distribution networks to deliver process gases into the chamber. These networks are labeled in **Figure 2.9b**. The upper showerhead, which handles all the precursor gases except for the SiH_4/He mixture, is connected to the upper flange of the UCA, above the ICP coil.

The second gas distribution network (typically referred to as the "gas ring" in the literature, and also in this work), delivers the SiH_4/He mixture the chamber below the plasma generation region and just above the substrate. In large commercial tools, a welded torus forms this ring, with a series of apertures drilled along the inside diameter providing the entry point into the chamber. Such an assembly is both difficult and expensive to manufacture, and would be very challenging to integrate in the tighter chamber dimensions of Inch Fab-scale tools. The solution devised for the IFIC was to incorporate the gas ring into the wall of bottommost flange of the UCA, effectively creating a side-entry and -exhaust version of the upper showerhead. To achieve this, the bottom flange of the UCA, which was previously used to provide seals against the LCA and the insulating chamber cylinder, was split into two halves, with hemispherical grooves machined in each near the inner diameter (leaving just a 0.050" wall thickness to the chamber). Along this inner "wall" several grooves were cut, providing apertures for the silane to enter the chamber. As was also done in the upper showerhead, the size and spacing of the grooves were optimized using network analysis techniques to provide spatially uniform gas streams [38]–[40]. A key aspect of this design is that, although there is not an actual seal along on the inner wall (in the non-groove sections), the close thickness and flatness tolerances (< 0.002" (~0.05mm)) specified for the two flange halves makes any unintentional gap between them small enough that, compared to the grooves, it will appear to have virtually no conductance (i.e. near infinite flow resistance).

In the previous section's discussion of the seal between the LCA and UCA it was noted that tightening bolts around the 6" CF flange bolt circle was not required to attain or maintain sufficient compression for a leak tight seal. This bolt circle is still very useful, and as was also mentioned in the previous section, chamfered plastic alignment pins are used in the some of the holes to register the two assemblies to one another. Another way in the bolt circle can be utilized

is as a means to implement a passive over-pressure relief valve for the IFIC. In the rare event that the IFIC chamber becomes pressurized (above atmospheric pressure), the otherwise unattached UCA will lift up from its seal to the LCA and exhaust the excess pressure if the force from that pressure exceeds the gravity force acting on the UCA. Roughly speaking, this will occur if there is more than 1.5 psi (~0.01 MPa) of over-pressure based on the UCA's weight and the area inside the 6" CF seal. By inserting screws through 1-3 bolt holes in both sections of the bottom flange and partially tightening the screws until ~0.2" (5 mm) remains between the bottom of the heads and the top of the bottom flange, the partially engaged screws will prevent the UCA from popping off the LCA in there is a sudden over-pressure event. These screws can easily and quickly be removed if the UCA needs to be removed from the system.

The top flange of the IFIC UCA is similar to the designs from previous the Inch Fab DRIE, but includes one key design change that increases its modularity. This change involved splitting the top flange of the UCA into two pieces, a central cylinder cap section that contains the upper gas showerhead and the central utility port and seals to the top of the chamber walls, and an outer clamping rim section that provides downward sealing force on the central section using a threaded rod and nut connection to the lower flange and additional mechanical stability. **Figure 2.10** provides a labeled rendering of the configuration. The cylinder cap section has an outermost diameter that matches the outer diameter of the chamber and raised features on the top and bottom faces for alignment. The raised feature on the top face centers the clamping rim section of the flange over the cylinder cap, and the raised portion on the bottom face ensures that the cap stays concentric with the cylindrical chamber tube.

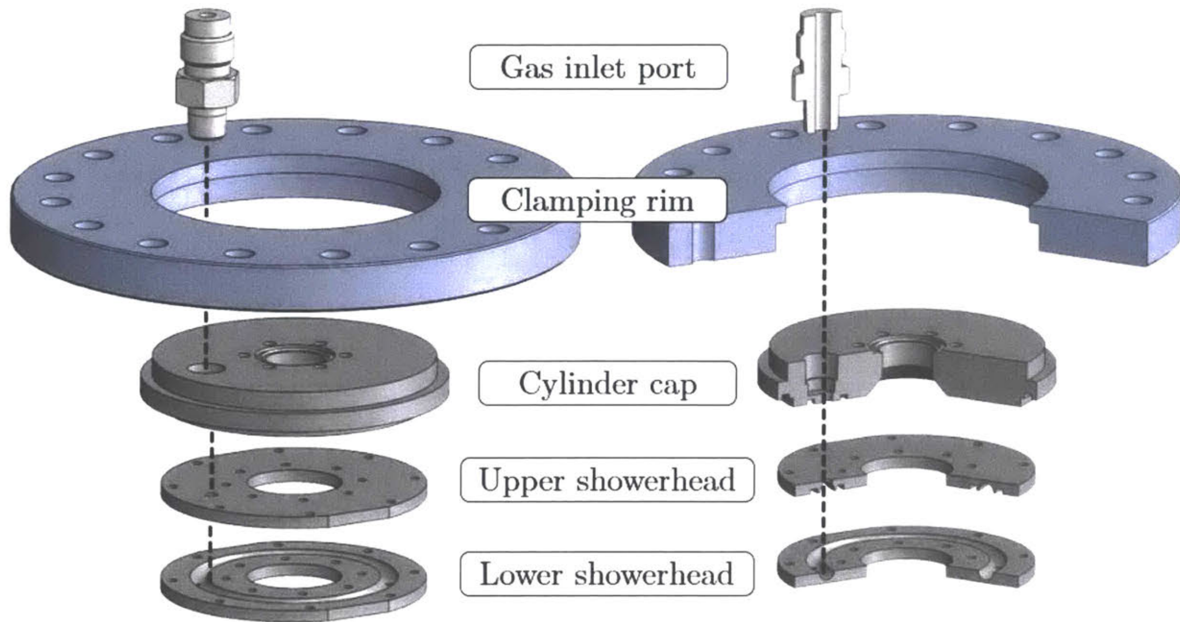

Figure 2.10: Exploded and cross-section views of the upper flange of UCA. The dotted line indicates the gas flow path.

The gas showerhead attaches to this bottom face using vented screws. The showerhead consists of two plates with hemispherical grooves that mate together to form a torus. Process gas is flown into the central flange section through an eccentric port and enters the showerhead at a single point on the top of the torus. The gas then exits into the chamber through a set of six evenly spaced apertures along the torus floor. The size of the torus and the apertures have been optimized using gas flow theory [39]–[41] and circuit network analysis techniques [38] to provide six uniform, spatially distributed gas streams to the ICP plasma generation region. Using an eccentric entry point for the process gas allows the utility port (a 1.33" CF knife edge) to be located at the exact center of the upper flange. This standardized flange size allows a wide variety of different instrumentation to be easily installed. Examples include Langmuir probes for measuring plasma parameters, spectrometers for optical emission spectroscopy or actinometry, or vacuum pressure sensors. In the IFIC, the default installed item is a sapphire viewport (0.59" (15 mm) viewing area).

When the system is pumped down to vacuum, the pressure differential across the central flange section becomes sufficient for a leak-tight seal, meaning that the outer rim section can be

fully removed without needing to vent the system. During normal operation, this is not something that needs to be done, but what is does allow is much easier experimentation with the ICP coil, or plasma density and uniformity add-ons (see **Section 4.1.2**), or other ideas that require adding components around the rim of the chamber tube. With this upper flange design, new coil configurations can be tested in just a few minutes, rather than the hours it would take to vent, disassemble, and pump down the system with the old flange design.

The actual ICP coil used in the IFIC is the same design as is used in the Inch Fab DRIE system. The two-turn coil is made of 0.25" (6.35 mm) outer diameter hollow copper tubing, with a turn-to-turn spacing of 0.5" (12.7 mm). To maintain a cool coil during operation, the ends of the coil are connected to a chilled water source, which is kept at 15°C. RF power is connected to one end of the coil using copper strap, which itself is connected to a type HN bulkhead fitting for interfacing with the RF supply. The other end of coil in connected to a low-inductance ground strap that also provides grounding to the rest of IFIC system components. These coil connections are made in a small enclosure that is designed to slide over two of the threaded rods that connect the upper and lower flanges in the UCA. This geometry centers the coil around the chamber tube. Hex nuts on the threaded rods allow the height of the coil to be adjusted and then locked into place. The electron and ion densities achievable with this coil design were tested using a Langmuir probe inserted through the central utility port during the previous characterization of the Inch Fab DRIE system and are discussed in [2]. For the SiO_2 and SiN_x depositions characterized in **Chapter 4** and **Chapter 5**, the transition from the low-density capacitively-coupled plasma discharge (known as E-mode) to the high-density, inductively-coupled plasma discharge (H-mode) was found to occur around 160 W for the $O_2/SiH_4/He$ plasma used to deposit SiO_2, and at ~210 W for the $N_2/Ar/SiH_4/He$ plasma used in SiN_x depositions.

To provide a safe barrier around the ICP coil and the high RF powers it handles during operation, a perforated sheet of aluminum was cut and rolled to form a protective shield around the whole UCA body. The holes in this shield are ~2 mm in diameter and effectively suppress any stray RF radiation from the powered ICP coil (as confirmed with EMF testing). They also

reduce the intensity of the light that emanates from the quartz chamber tube during an inductively-coupled discharge. The porosity also helps dissipate heat generates during processing. As mentioned previously, the entire IFIC system is also grounded using low-inductance copper strap, which is also connected to the RF sources and is ultimately terminated at a ground bus connected directly to earth ground.

2.3.3 Substrate Chuck Assembly (SCA)

The substrate chuck assembly (SCA) holds the substrate during processing, and provides several external stimuli that can enhance the deposition process. The SCA developed for the IFIC was designed to be able to meet the following functional requirements:

- Heat the substrate to at least 150°C
- Provide backside helium pressure for improved heat transfer between the substrate and SCA
- Measure the temperature of the SCA (and by proxy the substrate)
- Apply RF bias power (up to 10 W) to the substrate
- Utilize a simple and reliable mechanism for loading and unloading substrates
- Be no larger than 2.4" (61.0 mm) in diameter at the level of the substrate.
- Maintain a 2" (50.8 mm) column diameter to fit the linear and rotary feedthrough at the bottom of the LCA.

There are many advantages stemming from the reduced size of the Inch Fab initiative's micro- and nanoscale fabrication tools, but one area where this reduced size presents a real challenge is in the design of substrate chucks. The SCA modules for tools like the IFIC require many different components, which all need to fit in a very tight geometry. As seen from the functional requirements above, the IFIC SCA requires a heating element, temperature measurement, a helium conduit, and an RF bias connection all within a 2.4" (61.0 mm) diameter package that still provides appropriate electrical and thermal isolation for the components and can also survive in the vacuum and plasma processing environment of the IFIC chamber. Additionally, the design needs to be able to reliably accept substrates and provide thermal and electrical coupling to them.

The SCA design resulting from this challenging set of requirements is shown and labeled in **Figure 2.11** and discussed in detail below.

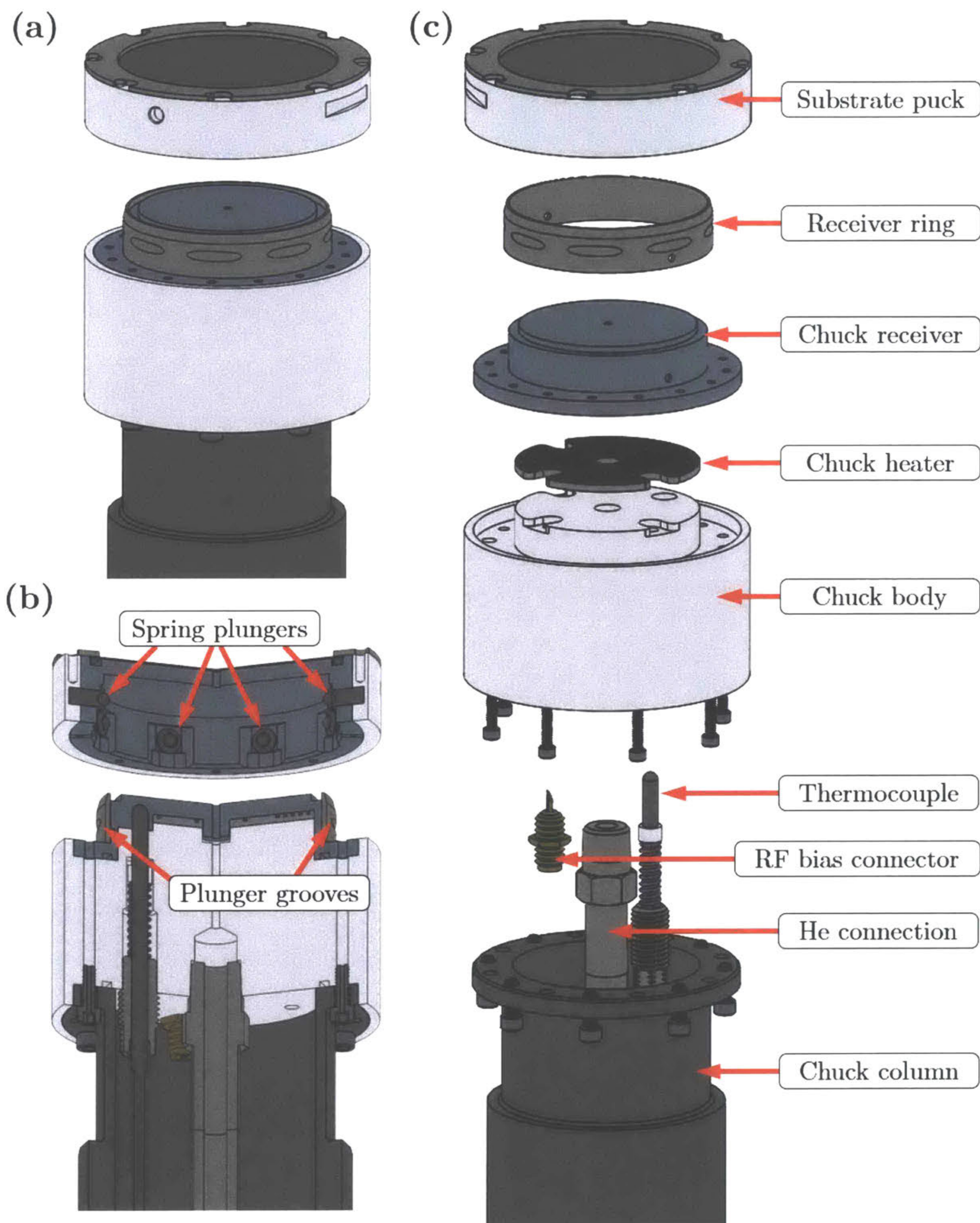

Figure 2.11: Renderings of the SCA. (a) The assembled SCA and substrate puck; (b) Cross-sectional view of SCA and puck showing the positions of the spring plungers and mating grooves; (c) Exploded view with labels for key components.

The SCA has four main sub-assemblies: (1) the 304 stainless steel chuck column, which slides up and down through the feedthrough at the bottom of the LCA; (2) the PEEK chuck body, which contains the connection points for the substrate heater, thermocouple, backside helium, and RF bias power, and provides both thermal and electrical isolation; (3) the 304 stainless steel and 6061 aluminum chuck receiver, which couples to the substrate puck, and has the end connection points for the RF bias power and thermocouple measurement; and (4) the multi-material substrate puck assembly, which holds the substrate to be processed and locks onto the chuck receiver to provide thermal and electrical connections for processing. The first three sub-assemblies are sealed together during the install process using O-rings, and the substrate puck forms a leak-tight seal with the O-ring on top of the chuck receiver as soon it is locked in place for processing. The design of and relationship between the components within these assemblies is discussed in the following sections.

As discussed in **Section 1.2.5**, one of the biggest advantages of ICP-CVD compared to other CVD techniques is its ability to produce high quality depositions at low substrate temperatures. Literature examples can be found for the depositions at temperatures as low as 20°C, but improvements in film qualities are generally always seen as temperature increases. To allow the effect of substrate temperature on films deposited in the IFIC to be explored over a wide range, a temperature target of 150°C was set for a substrate heater installed in the SCA. This value was heavily informed by published literature ICP-CVD results, which seldom exceed the 150°C threshold. In order to raise the chuck temperature, which was specifically designed to have a small thermal mass, from room temperature to 150°C in a reasonable amount of time (5 minutes), it was estimated that 13 W (~3900 joules) would be needed [42]. Given the low thermal conductivity of the surrounding PEEK material and very low thermal conductivity of the vacuum outside the SCA and substrate, it was assumed that conduction and convection losses would be small, and that the radiation losses at 150°C would not exceed the warmup power requirement (meaning that the power needed to maintain a temperature of 150°C would be less than 13W) [42], [43]. The space available in the SCA body for a heating element was 1.7 in^2 (1100 mm^2),

meaning that a power density of at least ~7.5 W/in^2 (0.012 W/mm^2) was needed for the heater. There are several heater options available at this power density and temperature range. Thin-film polyimide and thick-film silicone rubber heaters are very compact, typically offer power densities up to 10 W/in^2 (0.016 W/mm^2), and can operate at temperatures up to 200°C (230°C for silicone). These heater types use either an etched foil or a wire-wound resistive heating element laminated between layers of insulating material. While they can be very inexpensive if a standardized geometry is used, they are not cost effective to purchase commercially in small quantities if a custom layout is needed. Modifying the design of the SCA to accommodate a standard size was strongly considered but ultimately it was decided that an in-house-designed, bespoke wire-wound heater could provide the largest heating area while not impeding the placement or operation of the rest of the components. The designed heater uses a serpentine resistance wire pattern embedded in a PTFE base and covered with a layer of 0.0025" (0.064 mm) polyimide tape[8]. The entire heater is 0.065" thick, and the materials used are all rated to 260°C (although the heater has not been tested past 200°C). The serpentine pattern is just under 24" (610 mm) long (plus another 1.5" (38.1 mm) for connections), which lead to a resistance of ~20.4 ohms. At a 24 V drive voltage, this produces a heater power density of ~16.6 W/in^2 (0.026 W/mm^2), which gives a safety factor of 2.2 over the estimated power density requirement. Electrical connections to the resistance wire are made using crimp-style connectors covered in PTFE-based heat-shrink, and the heater is driven using a commercial PID controller with a pulse-width modulation (PWM) output connected to a DC-DC solid-state relay. Test results for the heater are provided in **Section 3.1.5**.

To measure temperature and provide feedback for the substrate heater, an ungrounded (for RF-isolation), hollow tube-style, K-type thermocouple was used. Rather than permanently potting the thermocouple into the top of the chuck receiver which would prevent any later modification (or even disassembly) of the SCA, a custom, spring-loaded retainer for the

[8] The surface of the PTFE sheet used for the heater base had a factory-provided etched texture that allowed it better accept the adhesive of the tape.

thermocouple was designed. These spring-loaded mechanisms exist commercially, but are either inexpensive and far too large, or very expensive and barely small enough to fit in the limited dimensions of the SCA. **Figure 2.12** shows the full spring loaded assembly. A retaining ring is press-fit over the thermocouple body, which confines one end of a simple compression spring. The other end of the spring is confined by a hollow piece of threaded rod (a 5/16"-24 thread was used) that has a hex-pattern milled into its far end to allow for easy tightening with a wrench. Upon installation and compression of the spring, the tip of the thermocouple will be kept in good thermal contact with the chuck receiver. This is very important because poor thermal contact is very difficult to diagnose or compensate for once the SCA is installed in the system, and this can lead to inconsistent temperature readings that will negatively affect deposition results.

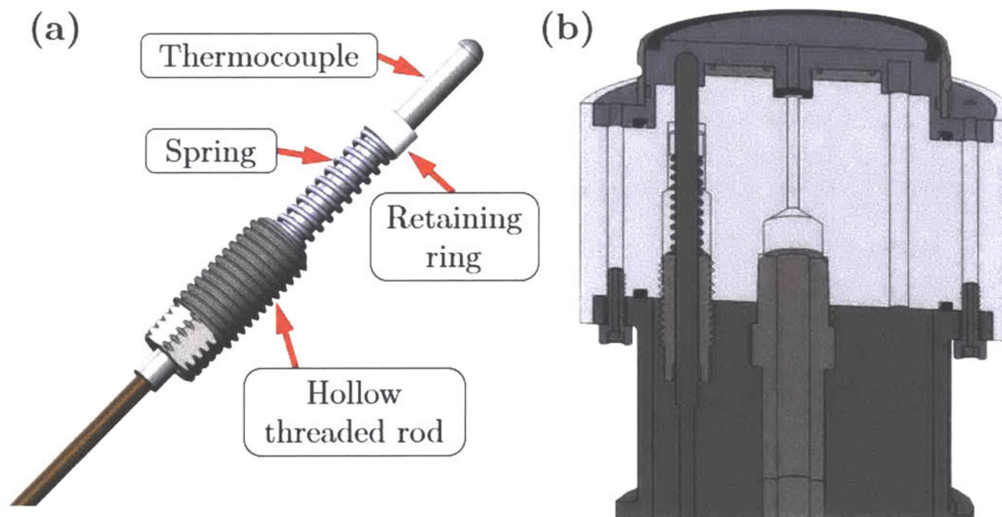

Figure 2.12: (a) Spring-loaded thermocouple assembly; (b) Cross-sectional view of SCA showing thermocouple position.

The third aspect of the substrate heating system is the backside helium pressure. As a gas, helium is inexpensive and has a thermal conductivity bested only by hydrogen [44], which makes it a good choice as a non-contact heat transfer medium. Because the substrates being processed may have delicate features on their backside, direct thermal contact with the heated chuck is not advisable, and additionally may not provide sufficient heat transfer due to asperities on one or both of the surfaces. In the IFIC SCA, a controlled pressure of helium is flown from a pressure controller (see **Section 2.4.1**) to the central port on the bottom face of the PEEK SCA body. It

exits from an aperture on top of the chuck receiver and fills the thin cavities between the receiver, substrate puck, and substrate. Helium that leaks through the O-ring seals and into the chamber is detectable by a rise of chamber pressure, but such leaks have not been observed after the initial testing and refinement of the SCA design. The normal pressure setpoint used for the backside helium is 20 torr, which, coupled with the designed cavity spacings of ~0.004" (0.1 mm) provides a thermal conductivity of ~0.1 $W/(m \cdot K)$ [45]. This pressure and geometry has been experimentally found to offer consistent substrate heat transfer. Test results for this design are presented in **Section 3.1.5**.

To make a reliable RF bias power connection to the SCA, SMA pin and socket connectors were used. The socket was press fit into the underside of the chuck receiver and the pin was soldered to a ~1" (25.4 mm) piece of solid-core 22 AWG wire which was then soldered to a standard bulkhead SMA connector. The 22 AWG wire connections were given stress relief via heat-shrink and then encased in a piece of 0.25" (6.35 mm) outer diameter PTFE tubing for structural rigidity during installation and further electrical insulation. To monitor the DC-self bias voltage induced from the plasma and or any bias power applied to the SCA, a high-impedance low-pass filter circuit was connected using a T-adapter to the RF bias power line (between the impedance matching network and the SCA). By varying the relative phase between the ICP coil and substrate bias power RF generators, the negative self-bias voltage was maximized for depositions with non-zero bias power setpoints.

The final aspect of the SCA design is the substrate loading and unloading mechanism, which is a new design developed and tested first on the IFIC SCA. Previous substrate loading mechanisms used in Inch Fab tools were effective, but required complicated fabrication procedures and usually some amount of custom fitting and modification after initial fabrication to get the sealing and unsealing procedure reliably working. The new design uses a substrate puck fitted with spring plungers (essentially spring loaded bearing balls retained in cylindrical cavities) that mate to detents radially located around the rim of the chuck receiver. When mated, the holding force provided by the spring plungers in the detents is sufficient to form the seal needed to prevent

the backside helium pressure from escaping into the chamber. A sectioned view of the substrate puck and chuck receiver mated together is shown in **Figure 2.13**.

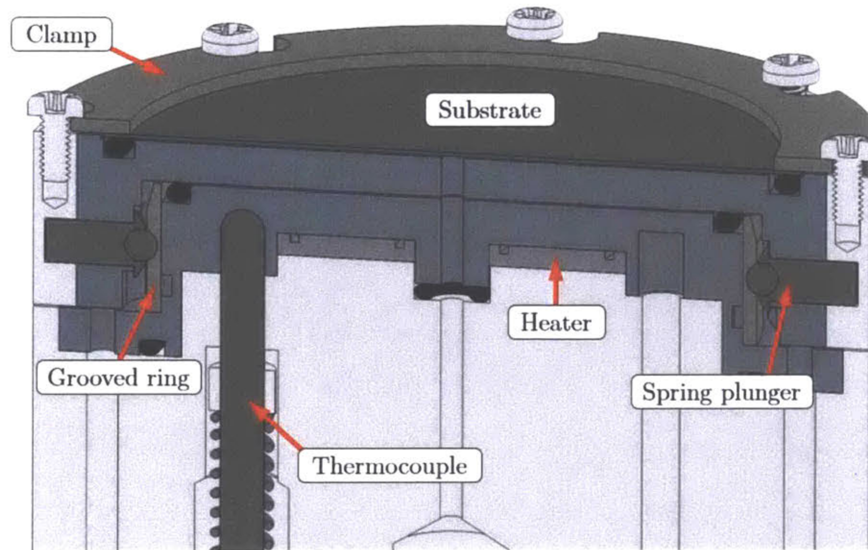

Figure 2.13: Cross-section view showing substrate puck mated onto the chuck receiver at the top of the receiver. The spring plungers are held in place by the grooves in the stainless steel ring on the outside of the receiver.

During the load process, the substrate puck is positioned over the chuck receiver (this exact position is preset with a hard stop connected to the wafer transfer arm), and the receiver is then raised until the spring plungers depress and the puck slides onto the receiver. If the plungers are then aligned with the detents on the receiver by rotating the SCA, that puck is locked into place and the O-ring seal is formed. The detents prevent the puck from detaching or the seal from breaking until processing is complete. To unlock the puck, the wafer transfer arm is inserted into the puck to lock its rotation and the SCA is rotated ~20 degrees in either direction, causing the plungers to exit the detent. From this position, the SCA can be lowered and the puck is free to be retracted into the load lock. **Figure 2.14** features a series of pictures showing this load and unload process.

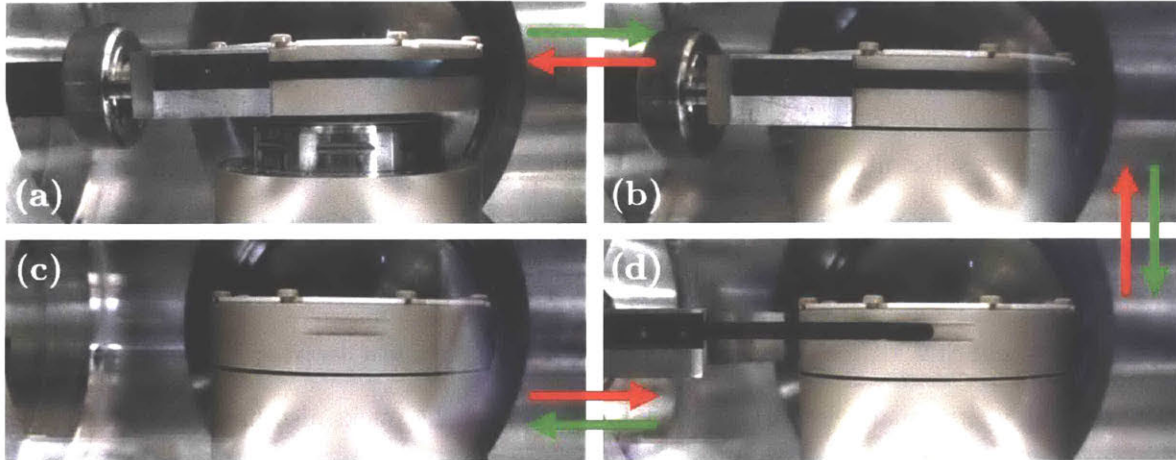

Figure 2.14: Loading and unloading of substrate pucks from the SCA. The green arrows show the loading process and the red arrows shows the unload process. The SCA is rotated ~20 degrees at the position of (b) to lock or unlock the puck.

The spring plungers at the core of this idea are very inexpensive and come in a wide variety of sizes, materials, and spring forces. The choice of a specific spring force, along with the geometry of the receiver and detents used, allow the force needed to lock or unlock the substrate puck to be controlled at the design phase. For the design used here, four evenly spaced spring plungers with spring constants of ~15 N/mm and initial compression forces of ~9 N were used in each substrate puck. Eight evenly spaced detents were included on the receiver (to increase the number of angular positions available for locking and also as a way to reduce wear on the detents), and placed at a height such that the puck would compress the O-ring at least 10% when locked into place. The depth of the detents was chosen so that ~50 N of force would be needed to dislodge the spring plunger ball from the detent. With four plungers the total force needed to dislodge the puck is ~200 N, which is approximately three times more force than the puck would be expected to withstand while compressing the trade size 029, Durometer D60A Viton O-ring down 10% (~54.5 N)[9] and sealing against 20 torr of backside helium pressure (~3.4 N). This holding force was verified during the tests described in **Section 3.1.4**. The amount of force needed to lower the puck onto the chuck itself is ~23 N (test results also discussed in **Section 3.1.4**), which is

[9] Full parameters used in the calculation: trade size: 029, diameter: ~4.9", cross-section: 0.070", hardness: Durometer 60A, compression: 10%, compression force: 1-2.5 lbf / linear inch [37].

small enough to prevent significant deflection in the extended sample transfer arm (and thus avoid creating a large angular mismatch between the puck and receiver).

The top of the substrate puck, where the actual substrate is clamped, can be machined to accommodate any substrate size (below a maximum diameter of 2.15" (54.6 mm)). This recess can enable precise alignment of common substrate sizes (such as the 2" (50.8 mm) wafers used during the SiO_2 and SiN_x depositions described in **Chapter 4** and **Chapter 5**), or can be left out to allow loading of irregularly sized pieces. The top face of the pucks also have an O-ring groove (ideally near the edge of the substrate being processed) to provide a seal to the backside of the substrate (to prevent helium leakage). Substrates are clamped onto the O-ring and puck using a thin (~0.040" (1 mm) thick) alumina clamp which also sets the area exposed for deposition. The most common aperture sizes used for 2" (50.8 mm) wafers was 1.75" (44.5 mm). The clamps are held in place by eight 2-56 PEEK screws. To minimize the amount of time needed to add or remove a substrate from the puck, the clamps feature a new "twist-lock" design that allows them to be inserted over the screw heads, rotated 5 degrees, and then tightened into place with ~2 turns of the screws. Further time savings have been realized through the use of a wafer alignment jig, which works in conjunction with the puck recess to help align the 2" wafers on the puck before clamping. **Figure 2.15** shows this jig and a substrate puck with a clamped 2" wafer.

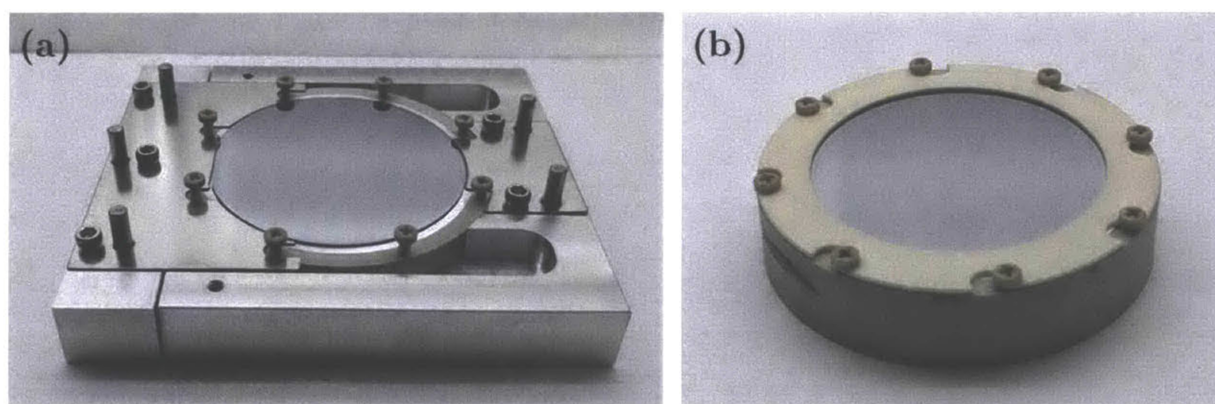

Figure 2.15: (a) 2" wafer alignment jig for loading onto substrate pucks; (b) a 2" wafer loaded into a substrate puck.

Having at least two substrate pucks was also found to be an important timesaver, particular for the long sequences of deposition experiments carried out in the following chapters, as it allowed

the next substrate to be loaded and clamped while the previous sample was being processed. This also allowed the transition time between removing a sample from the load lock and inserting a new sample to be reduced, which in turn reduced the time needed for the load lock to pump-down (see **Section 3.1.2**). The following section takes a close look at the design of the load lock assembly, the last of the four assemblies in the Inch Fab modular vacuum tool architecture.

2.3.4 Load Lock Assembly (LLA)

Load locks are critical in maintaining consistent, clean conditions in vacuum-based fabrication tools because they allow samples to be loaded and unloaded from a tool without venting the processing chamber. Once a sample is loaded into a tool's load lock, the load lock is evacuated until a predefined pressure setpoint is reached (10 mTorr was used in the IFIC). When this pressure is achieved, the valve isolating the load lock and processing chamber can be opened and the sample transferred inside the tool for processing. Once the processing is finished, the sample is returned to the load lock where it can be retrieved for the next process step (after venting the load lock). In the IFIC, the load lock assembly (LLA) connects to the rest of the tool via a gate valve connected to the left face of the LCA. A linear substrate transfer arm is used to move the substrate from the load lock into the chamber and then onto the SCA. The primary functional requirements for the LLA are to:

- Pump-down to $<$ 10 mTorr quickly
- Permit simple loading and unloading of substrates via a vacuum-sealing door
- Transfer substrate pucks to and from the SCA reliably
- Allow inspection of the substrate without venting
- Facilitate ancillary pumping requirements (backside helium cooling and differentially pumped feedthroughs)

Like the LCA, the main body of the LLA is cube with CF knife-edges machined into each of the six faces. These cubes are very versatile and can be purchased quite economically given the complexity and density of their features. The LLA used the next standard size down from 6" size

used in the LCA, which has a side length of 4.5" (114 mm). Connected to the six faces are a viewport, a "fast-access" door, a blank flange, the vacuum foreline, the chamber isolation gate valve (connecting to the LCA), and lastly, a 2" (50.8 mm) spacer flange (to which the sample transfer arm feedthrough, vent valve and pressure gauges are affixed). **Figure 2.16** shows renderings of the IFIC LLA.

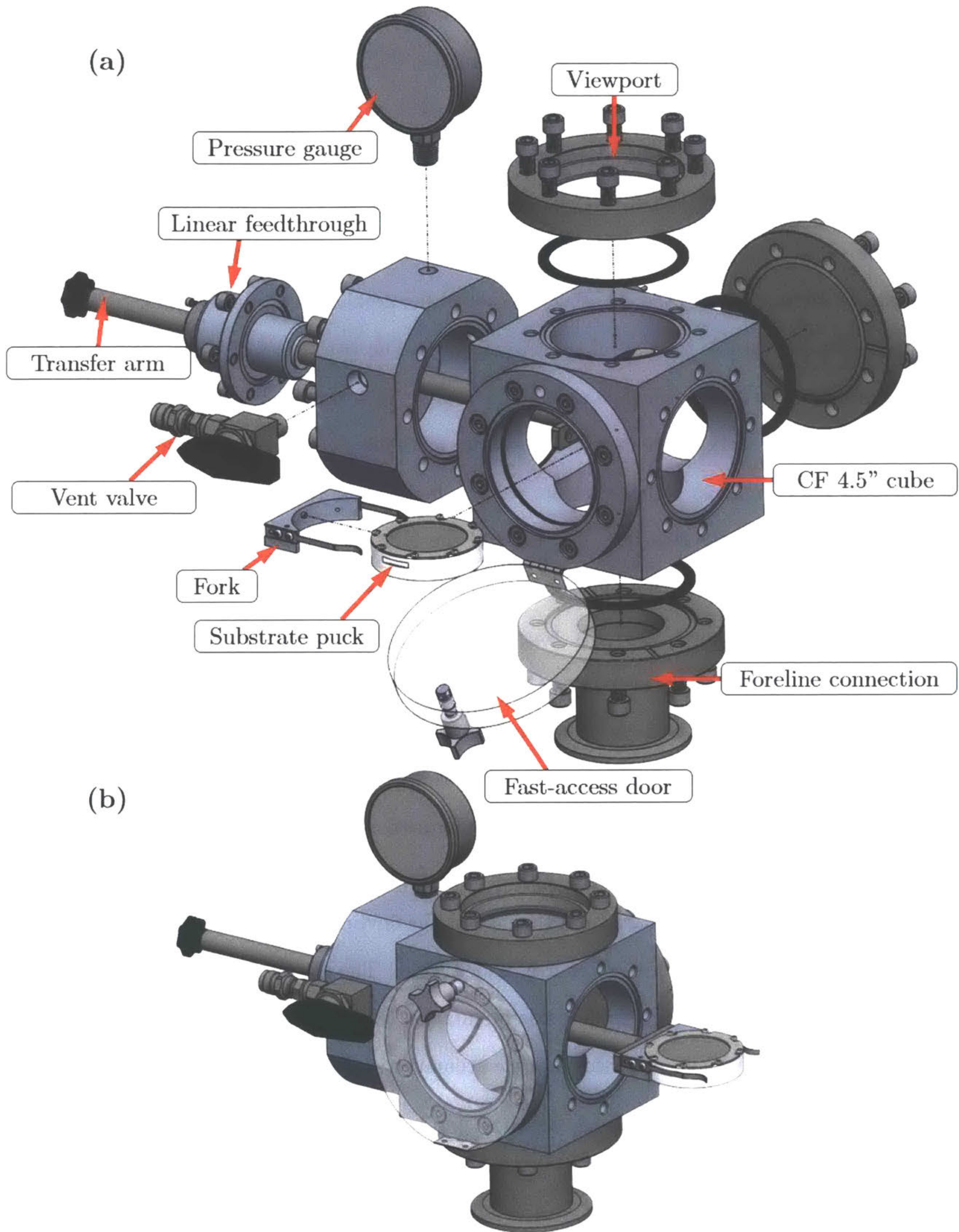

Figure 2.16: Renderings of the LLA. (a) Exploded and labeled view of LLA components; (b) Assembled LLA view with wafer transfer arm extended.

The LLA installed in the IFIC system includes several new design features. The first deals with the manner in which samples are loaded into the LLA. The small size of the IFIC LLA provides a great advantage in terms of the time it takes to pump-down, but the small dimensions also make it difficult to maneuver a substrate into the load lock and onto the sample transfer arm. Unlike systems that support larger wafers, the hand of an average operator cannot fit through the ~2.8" (71.1 mm) aperture provided by the LLA's 4.5" CF flanges to precisely position the substrate for loading into the chamber. To solve this problem, a two-piece puck grabber was developed that attaches to the end of the transfer arm. The two pieces of the grabber, the fork and receiver, mate together using magnets and a dovetail groove. The beginning of the pin (receiver) and socket (fork) sections of the dovetail each have a generous taper that make it very easy to align the two pieces. The substrate puck is loaded onto the fork outside LLA, and then the fork is pushed onto the receiver. The arms of the fork are made from spring steel and hold the puck tightly against a locating pin which prevents the puck from rotating. The fork arms are extremely cheap to produce (using a waterjet cutter), and easily be replaced if they are inadvertently bent past their yield point. Once the two grabber pieces are pushed together, the magnets catch and the fork is securely held on the receiver. As **Figure 2.16** shows, substrates enter the LLA from the door on the front face. This is in contrast to many commercial single-wafer processing tools, which use a top-loading configuration because the wafers are large and it is difficult to orient them on a transfer arm or fork from the side. This orientation provides opportunities for particulate matter from the user or the environment to fall downward onto the substrate during loading, which is, of course, undesirable. The two-piece grabber system makes it easy to load and unload wafers from a side orientation (although it would operate just as well in a top-load system), which averts this particle accumulation scenario.

In order to load the substrate puck onto the grabber, the LLA must be vented and a port opened to access the interior. The typical way this is accomplished is using a hinged "fast-access" door that can be swung open or sealed vacuum-tight with just a few turns of a single thumbscrew. Unfortunately, these doors are rather expensive (> 700 USD for a 4.5" CF version) and so a low-

cost version that could be used on other Inch Fab tools (which all currently use load locks based on 4.5" CF cubes) was designed. The first half of the door design consists of an aluminum flange with a 4.5" CF knife edge on one side and a basic O-ring groove just larger than the central 2.8" (71.1 mm) aperture on the other side. The bolt holes for connecting this flange to the LLA were counterbored to allow the second half of the door, a window made from scratch-resistant polycarbonate, to sit flush against it when the door is closed. The window and flange are connected using a simple butt-hinge, and the O-ring seal between the two is completed by tightening a captive machine screw (held in the window) into threads contained in the aluminum flange. Sealing directly to the polycarbonate window greatly simplifies the design and achieves the maximum possible viewing diameter. All together this design requires only ~40 USD worth of material and about 1.5 hours of fabrication time using basic CNC machining equipment, providing a much greater value than the existing commercial options.

The actual venting of the chamber that must be completed before this door can be opened is accomplished using a pair of series-connected Swagelok valves positioned immediately to the left of the door on the short spacer flange connected to the back face of the LLA. The first valve is a simple 90°-pattern ball valve in fluid connection with the LLA. The second valve is purge valve that has been adjusted to slowly vent the load lock to atmospheric pressure over ~20 seconds. By using an on-off valve connected to the purge valve, the venting rate can be kept consistent, rather than fluctuating with differences in the degree of openness in the purge valve. The placement of the valves is significant because it provides a physical interlock that keeps the load lock door from being opened or closed while the ball valve handle is in the vent position. This acts as a way of preventing an attempted pump-down while the LLA is still open to venting (i.e. the ball must be closed after the LLA is vented in order to open or reclose the door). The "venting orientation" of this valve can be seen in **Figure 2.16b**. This configuration does vent the load lock using air from the surrounding environment and not a dry gas like N_2 or Ar. Venting and/or flushing the load lock using a dry gas was considered, but ultimately the short pump-down time of the load

lock (test results provided in **Section 3.1.2**) and the lack of any observable negative effects from the air purge led to the adoption of the lower cost and complexity two-valve design.

A cost barrier similar to that of the fast-access door led to the design of the custom linear and rotary motion feedthrough used for the sample transfer rod. Differentially pumped vacuum feedthroughs (described in **Section 2.2.2**) for linear and rotary motion exist as stock products from several different vendors, but they have several drawbacks, in addition to being quite expensive (700-800 USD). The biggest drawback from the IFIC perspective is that these feedthroughs use very small shafts (typically ~0.25" (6.35 mm)). Given the long throw needed for the transfer arm (~10" (254 mm)), and the force needed to insert the substrate puck on the SCA, these small shafts are simply not stiff enough. Another feature lacking from the commercial feedthroughs is a way to lock the travel or rotation of the arm at an arbitrary position. Given the pressure differential across the feedthrough, the arm wants to be pulled into the vacuum chamber, which can lead to serious problems if not closely monitored (e.g. if the arm drifts through the gate valve aperture and the gate is then closed). It is very simple to integrate a lock mechanism at the design stage, but much more cumbersome to retrofit a commercial product with one. The feedthrough design developed for the IFIC LLA (shown in **Figure 2.3**) accommodates a 0.5" (12.7 mm) diameter shaft and supports it over a length of 2.25" (57.2 mm) using a pair of bushings. Differential pumping is available through an NPT port between the two axial O-ring seals, and a thumb-screw actuated shaft collar is rigidly connected to the end of the atmosphere side of the feedthrough. As implemented in the IFIC, the feedthrough attaches via a 2.75" CF fitting to the LLA, but the design is easily modifiable to use larger CF sizes or any NW40 or larger flange size. The flange material, bushings, shaft collar, and fasteners together cost about 25 USD, and the part takes ~2 hours of basic CNC machining to fabricate and assemble. Additional shaft collars were added onto the transfer arm to provide hard stops at desired positions (such as directly over the SCA and in with the load lock door).

The pumping system for the LLA is powered by a small 2-stage rotary vane pump. A soft-pump-enabled isolation valve separates the LLA from this pump (and an otherwise unused

butterfly valve stands as a manual isolation backup). The soft-pump feature prevents excessive turbulent flow and particle generation during a pump-down from atmosphere by first opening a lower conductance pathway between the two sides of the valve and letting this path provide the initial pump-down (typically to around 10 torr, which takes just a few seconds in the IFIC LLA), and then opening the primary, larger conductance flow path to complete the pump-down process. Below this isolation valve, the backside helium cooling exhaust line and the pump lines for the differentially pumped feedthroughs are connected. The feedthrough pump lines are simple sections of PTFE tubing that require little conductance and contribute minimally to the gas load. A shutoff valve in series with the lines does allow them to be isolated if needed. The helium exhaust line is closed off from the foreline while the system is idle, but during processing, a control valve in the manifold connected to the helium controller opens to allow a continuous flow of helium to the substrate. The amount of flow can be adjusted using a needle valve, but is not normally changed in practice. At the 20 torr setpoint normally used for the backside helium cooling, the helium flow raises the foreline pressure to ~150 mTorr, so the isolation valve to the LLA is kept shut during processing. Once the processing is completely, a purge process gives the helium 60 seconds to be exhausted from the SCA and this foreline, after which the exhaust valve and the isolation valve states are reversed to keep the LLA pumped down and the helium exhaust closed.

The LLA described provides a highly functional yet inexpensive way to greatly improve the efficiency and cleanliness of the IFIC as a fabrication tool. Taken together with the other three modular assemblies described in this section, they comprise the most visible and unique portions of the full IFIC system. However, without the carefully selected and integrated "back-end" or equipment described in the following section, the encouraging deposition results presented in the later chapters would not be possible.

2.4 Supplementary Equipment Systems

In addition to design of the core four modular assemblies described in the previous section, much of the "back-end" equipment that drives the IFIC also required a careful design process and substantial background research. This equipment can be separated into four categories: process

gas delivery, vacuum generation and management, RF power delivery, and control systems. The equipment selection and important design elements for each of these categories are described in the following sections.

2.4.1 Process Gas Delivery

The process gas delivery system for the IFIC uses a similar overall configuration to the one originally designed for use in the Inch Fab DRIE system. Process gas flows are set using mass flow controllers (MFCs) and routed using electronic solenoid valves installed in manifolds. The specific process gases installed in the IFIC as described here are O_2, N_2, Ar, SF_6, and the 1.5% SiH_4/He mixture. The non-silane gases are grouped together in a single manifold, and the silane mixture is controlled in a separate manifold. Prior to the MFCs for each gas, the supply line from the gas cylinder is routed through a filter with a 7 µm pore size to prevent debris from clogging the sensor elements. The outlets of the MFCs connect straight to the solenoid valve manifolds, and the outlets of the manifolds are directly routed to the appropriate input on the UCA (the gas ring for silane and process gas showerhead for all other gases).

2.4.1.1 Mass Flow Controllers

The specific MFCs used are made by Alicat Scientific, Inc. [46], and have been chosen due their excellent balance of performance and cost. Unlike most MFCs, which measure the amount of flow thermally using heaters and temperature sensors along the flow path, Alicat MFCs measure flow by routing a portion of the gas flow through a "laminar flow element" (LFE), and measuring the pressure drop across a defined section of the resulting laminarized (low Reynolds number) flow stream. From this measured pressure drop, the dimensions of the flow path, and the viscosity of the input gas, the volumetric flow rate can be calculated using the Hagen-Poiseuille equation, and then converted into a mass flow using the density of the gas (which is a function of its temperature and pressure, which are also measured). Compared to traditional thermal methods[10],

---

[10] Some of the latest thermal MFC models use specially designed MEMS or CMOS-based sensors that substantially increase their performance, but also substantially increase their price.

this LFE method for flow control permits faster response times, larger dynamic range, and requires no warm-up time. Furthermore, the Alicat MFCs are cheaper than most of the other thermal options (1100-1600 USD per unit depending on the full scale flow and gas type), making them an easy choice for inclusion in the IFIC (and as the MFC of choice in the other Inch Fab tools).

2.4.1.2 Helium Pressure Controller

Alicat Scientific also makes the pressure controller used to control the helium pressure applied to the backside of the substrates to facilitate good thermal contact. The pressure is measured using a small capacitance manometer inside the unit and used to set the position of a proportional valve, which controls the amount of helium admitted into the volume under measurement. This is what is referred to as an upstream pressure control, as compared to the downstream pressure control method used by the throttle valve to augment the pressure in the process chamber (which is discussed in the following section). These controllers also use the same interface as the MFCs, making them easy to integrate into the control system, and from a cost perspective are less than half the price of a widely used alternative from MKS Instruments.

2.4.1.3 Flow Control Valves

The electronic solenoid valves used in the manifolds (and also for controlling several of the larger pneumatic vacuum valves discussed in **Section 2.4.2**) are made by Clippard Instrument Laboratory, Inc. The specific series used are the EV "Mouse" valves, which have several advantages over the traditional pneumatically actuated bellows- or diaphragm-sealed valves used in most commercial tools. The first and biggest advantage is cost. For the process gas and silane manifolds, Clippard's high-end "analytical series" EV valves [47] (each analytical series valve is cleaned, assembled and tested in a cleanroom) were used, which cost ~44 USD each. First-hand testing has shown these valves to be leak-tight to better than 1×10^{-7} atm $\cdot$ cm^3/sec. The least

expensive pneumatic valve from a common vendor like Swagelok still exceeds 200 USD[11]. The next advantage is that the EV series valves are actuated electronically using low-voltage DC solenoid coils (the 24 V variety were used in the IFIC, which require only 0.67 W to open). In pneumatic valves, an additional external valve (often a small solenoid valve like a Clippard EV...) is required to provide and exhaust the compressed air used for actuation. The last notable advantage of the EV valves is their compact form factor (< 1" (25.4 mm) in diameter, < 2" (50.8 mm) in height), which allows them to be tightly spaced in manifolds. The compact size of the EV values does mean that the maximum flow they can support (~2500 sccm at 10 psid) is smaller than the least expensive pneumatic valve, but the flows required for the IFIC are also very small (< 20 sccm for non-silane gases, and < 300 sccm for SiH_4/He), so this parameter is not applicable. EV valves have been used extensively and without issue on all the Inch Fab initiative tools designed thus far, and will continue to be moving forward.

2.4.1.4 Special Considerations for Silane

The inclusion of silane as a process gas (even in the dilute 1.5%-in-He form) means that extra safeguards were taken to prevent both accidental leaks of silane to the surrounding atmosphere (potential pyrophoric combustion risk) and the unintentional mixing of the silane feed supply with any oxidizing process gas supply (namely O_2).

The first of these safeguards was to fully isolate the silane delivery system from the rest of the process gases (up until the process chamber). This is very important from a safety perspective, but not altogether inconvenient, as the silane enters the process chamber (through the gas ring) separate from the rest of the process gases anyway. The silane gas lines (at both positive pressures prior to the MFC and at vacuum pressures after) are fully purgeable using a combination of alternating vacuum suction and inert gas flow from an independent N_2 cylinder (separate from

[11] These valves have leak rates of ~1-4×10^{-9} atm · cm^3/sec, which is certainly better than the EV valves, but altogether unnecessary given the process pressures and gas flows (~0.15-4 atm · cm^3/sec equivalent) used in the IFIC.

the N_2 supply used for SiN_x depositions). The second safeguard was the addition of an excess flow valve (made by Parker Veriflo), which was configured to trip if the flow of the SiH_4/He mixture exceeded ~300 sccm (at the 20 psig supply pressure set by the regulator on the SiH_4/He cylinder)[12]. The full scale flow of the silane MFC used is 300 sccm, so a flow value above that threshold indicates that a leak likely exists, which will cause the excess flow valve to trip. A normally closed valve was also added to the silane supply line just prior to the filter on the MFC inlet and connected into the IFIC system's emergency stop bottom. In the event of an emergency, pushing this button will cut off the supply of silane to the MFC (as well as turning off both RF supplies and sending an emergency stop signal to the control system, which will initiate a purge of all other process gases).

To minimize the chance of a leak, all the process connections and piping for the silane delivery line were made using VCR-style fittings, which are very robust and have a small port at each connection point that simplifies the leak checking process. These process connections were thoroughly leak checked (see **Section 3.1.2**) before operation to ensure that all the connections were sound. To mitigate any potential downstream problems from the IFIC system's exhaust, which will contain a combination of unreacted silane, process gases, and reaction products during deposition runs, the exhaust port from the roughing pump backing the system was routed through non-combustible piping to a dedicated exhaust duct and a valve for adding additional N_2 as a further diluent was installed near the pump exhaust port.

The final safeguard implemented was a series of visual labels that were produced that indicate the status of the silane gas line (similar to the labeling used on gas cabinets in larger fabrication facilities), along with the status of several other critical system components (the state of the turbo pump, the chilled water supply, and the process gases). When not in use, the silane cylinder and

---

[12] The trip point can also be changed by varying the regulator's output pressure (higher pressures lead to higher trip point flows) if needed. Large supply pressures are not needed for the SiH_4/He MFC, which requires just a 5-10 psi differential between the inlet and outlet pressure to stably operate.

the valve on its pressure regulator were closed, and the card was updated to indicate this status to other users in the area.

Appendix B contains a full schematic with connection information for the complete process gas delivery system as well as the vacuum generation system, which is outlined in the following section.

2.4.2 Vacuum Generation and Management

Vacuum pressures in the IFIC process chamber are generated and maintained using a combination of a two-stage PFPE-oil-sealed rotary vane pump (rough to medium vacuum) and a turbomolecular pump (high vacuum). The low process pressures (~10-100 mTorr) and the high process gas flows (~100-220 sccm, of which $> 90\%$ is the silane mixture) used for depositions are not possible to achieve using only a rotary vane pump as was possible in the Inch Fab DRIE system, and so the additional pumping capacity of a turbo pump is required. The chamber pressure during deposition processes is controlled using a butterfly-style conductance-control throttle valve located just in front of the turbo pump inlet. This type of valve actively reads in measurements of the chamber pressure provided by the capacitance manometer installed in the LCA and varies the conductance of the turbo foreline (by varying the degree of openness of the butterfly valve) in order to maintain the desired pressure setpoint. The turbo pump is configured with a N_2 purge system that is activated during processing and chamber cleaning to minimize the contaminants seen by the mechanical bearing assembly. The N_2 for this purge is sourced from the same dedicated N_2 cylinder used for silane purging.

The turbo pump used in the IFIC is a Leybold T 350iX [48], which was chosen after researching several vendors and running many performance simulations. The iX series of turbo pumps feature a controller included directly on the body of the pump, and several digital interfacing options for integration into the IFIC's overall control system. The controller also has three relay outputs that can be configured to automatically control external elements like turning on the cooling fan whenever the turbo is spinning, or activating a vent valve to control the deceleration of the pump during shut-down, which are important safety features that help prevent damage from being done

to the what is the single most expensive component in the IFIC system. The iX series of pumps also features a hybrid bearing system that does not require periodic re-lubrication, which is advantageous as this would require demounting the pump from the LCA. This was seen as a good compromise between basic turbo pumps that require routine lubrication or replacement of the bearings and pumps with magnetically-levitated bearings, which are significantly more expensive (usually > 50% more than an equivalent size mechanical bearing pump).

The decision on the particular size and configuration (the "T 350") was based primarily on this model's high pumping speed for helium and the larger throughput limit (the maximum volumetric flow rate of gas that can be passed through a pump at a given pressure). The "T" series pumps have only turbomolecular stages, which use rotors with many angled blades spinning at high speeds (60,000 RPM in the T 350iX) to progressively direct gas molecules away from the pump inlet. Multiple levels of rotors are combined to progressively compress the evacuated gas, increasing its pressure with each rotor stage, until it is finally exhausted via using the backing pump. The non-T series pumps include a Holweck stage (also known as turbo-drag stage) after several turbomolecular stages. Holweck stages use a cylindrical rotor spaced very closely to a stator with a helically spiraled channels to impart momentum to gas molecules, driving them further away from the pump inlet [49]. This type of stage allows a higher backing pressure to be used (often meaning a smaller or less expensive backing pump can be used), but with a tradeoff of decreased throughput. Simulations using the dimensions of the foreline connected to the LCA showed that a (non-T) 350iX would be nearing its performance limit at 200 sccm of flow, compared to an upper bound of 450 sccm when using T 350iX. As will be shown in **Chapter 5**, the standard recipe converged upon for SiN_x depositions includes 200 sccm of the SiH_4/He, which ultimate validated the decision to go with the higher throughput T 350iX pump.

In addition to the pumps and pressure control devices, the vacuum system in the IFIC also requires the use of several isolation valves. The biggest of these is the gate valve that connects the LLA to the LCA and facilitates the transfer of substrates in and out of the processing chamber. The advantages of using the insertable type gate valve from a system design perspective were

described in **Section 2.3.1**. Isolation valves are also used to separate the rotary vane pumps from their upstream connections (the turbo pump and the load lock). Unlike the gate valve, which has a double-acting actuation mechanism (meaning that pressurized air is required to both close and open the valve), the pump isolation valves were specifically chosen to be single-acting, with a normally closed, spring return mechanism. The rationale behind this is to provide protection for the system in the event of a loss of power or compressed air. In either of these situations, the pump isolation valve will close, protecting the upstream components from potential contamination from back-streamed oil. Valve position indicators are another safeguard included on all of the valves used in the IFIC. These position indicators provide relay closures or magnetic reed switch actuation that indicates the actual position of the valve. This position information is used to inform the control system of the real status of the valve, rather than solely relying on the control signal or mechanical switch state to infer the position. Pneumatic valves like the gate valve can take up to 5 seconds to fully open or close, which can potentially cause problems with interlock protections (for example, if the load lock is vented immediately after closing the gate valve, the chamber will also be unintentionally vented until the gate valve has to fully close).

2.4.3 RF Power Delivery

As originally designed, the RF power delivery system for the IFIC was identical to that of the DRIE system. A pair of 600 W 13.56MHz RF generators made by Advanced Energy (Cesar 136 models) provide power to the ICP coil and the substrate electrode. These generators were chosen because they are air-cooled, compact (2U rackmount size), can have the phase of their output signal externally adjusted (using the standardized common exciter (CEX) interface), and have a history of reliability and wide use in the semiconductor industry. Conveniently, they are also priced very competitively. Impedance matching is achieved using an automatic impedance matching network connected to the ICP coil (T&C Power Conversion model AIT-600-06), and a manual matching network connected to the substrate electrode. Several additional items are also included in the substrate electrode path. The first is a 10 dB attenuator rated for 75 W. The 600 W RF generator connected to this section cannot stably provide the 0-5 W needed for the

depositions. The attenuator serves to bias the generator into a more stable operating regime (a factor of 10 higher for the 10 dB attenuator), and dissipates the remaining power as heat. The lack of economical low power RF generators that would eliminate the need for this practice has been a consistent struggle for Inch Fab initiative tools, as will be discussed more in **Section 2.5**. The second item connected to the substrate bias line is a 500 pF, 5 kV RF capacitor connected in series between the manual matching network and the substrate electrode. This capacitor allows the applied RF bias power to induce a negative DC bias voltage (on top of the RF signal) on the substrate electrode. This serves to further accelerate the dissociated positive ions towards the substrate, which can be advantageous depending on the process requirements. The capacitor also prevents the DC voltage from being transmitted back to the matching network or RF generator. To measure the DC bias induced on the substrate electrode, a high-impedance low-pass filter circuit is connected in between the DC blocking capacitor and RF input on the SCA. A block diagram of the RF connections is included below.

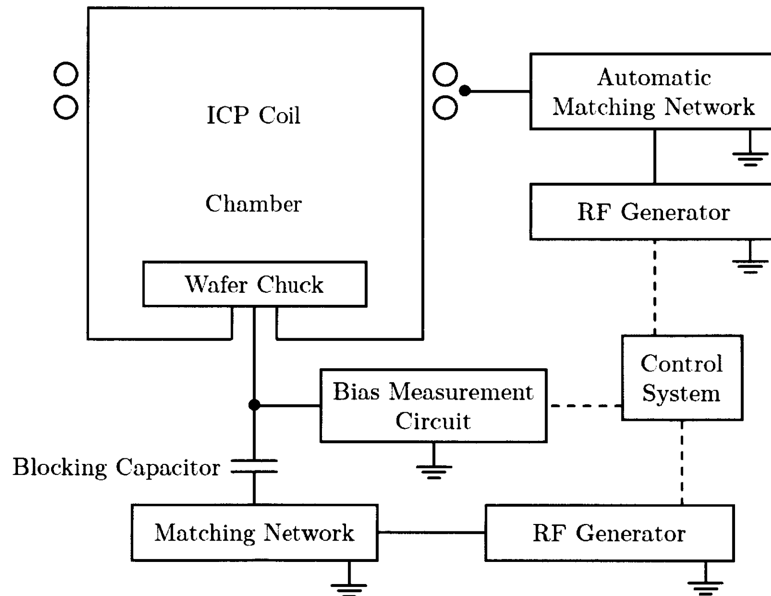

Figure 2.17: Block diagram of RF connections in the IFIC.

2.4.4 Control System and User Interface

To integrate and manage all of the different pumps, flow controllers, pressure controllers, power sources, and process monitoring equipment, a centralized control system is required. Rather than rely on expensive PLCs or sluggish LabVIEW-style VIs, the control system for the IFIC has

been designed and built around inexpensive, yet powerful microcontrollers. Early iterations of this system were used to control the Inch Fab DRIE system, but the design has since undergone major revisions to improve its functionality and evolve into a general purpose fabrication tool control system that can be used to control a wide variety of equipment including CVD, etch, evaporation, and sputtering systems. At the core of the control system are pair of 72MHz 32-bit ARM Cortex-M4 microcontrollers, one of which is used to control and monitor the essential aspects of a process, and the other of which provides ancillary support and controls elements like data logging and user interface tasks. These microcontrollers, along with several custom PCBs, a power distribution system, and all the connections needed to interface with the RF generators, MFCs, pressure measurement devices, valves, and other components are housed in a shielded 1U rackmountable enclosure. Users can access information about the current state of the IFIC system from an LCD screen located on the front panel of this enclosure. The control system itself runs off of a 24VDC supply, which it also filters and then distributes to power or actuate each of the other components in the system using either switches on the front panel of the enclosure or choices made via the software interface. The full bill of materials for the control system, including the enclosure and connectors is just under 650 USD.

The user interacts with this control system using the Process and Recipe Control (PARC) software, which provides the graphical user interface and is compatible with Windows, Mac, and Linux. From this GUI, users can build, save, and recall process recipes, monitor chamber characteristics and process progress during runs, and debug equipment as needed. Both the hardware and the software have been built to be modular in nature so that different brands or even types of equipment can easily be integrated into a system with minimal effort (and often even with little to no coding required). Screenshots from the operation and recipe tab of the PARC software are shown below in **Figure 2.18**.

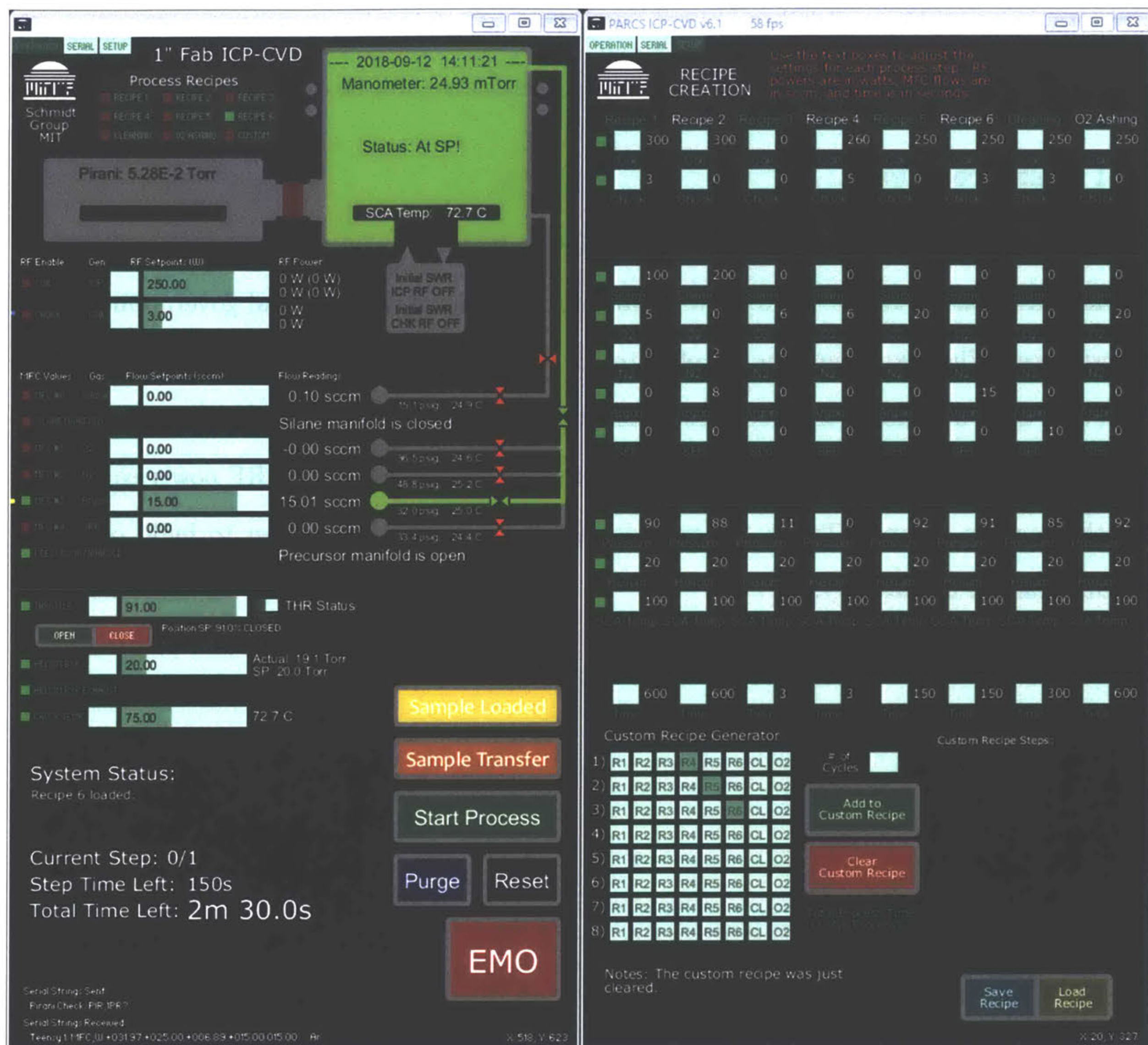

Figure 2.18: Screenshots from the operation tab (left) and recipe tab (right) of the PARC software used to monitor and control the IFIC.

2.5 System Cost Analysis

The primary goal of the Inch Fab initiative is to produce micro- and nanofabrication tools that are far less expensive than existing commercial options while still maintaining a similarly high level of performance. The IFIC was designed around this goal, and through the process of its construction and characterization, several cost-related insights related have been gained. This section will begin with an examination of how the cost of the system is distributed across the many sub-systems and assemblies discussed in the previous sections. Following this, several ideas

for further reducing the cost will be considered, and the potential impact of volume discounts will be addressed. Finally, the costs of operation and maintenance will be examined.

2.5.1 Cost Breakdown

In the previous sections of this chapter, significant attention was paid to the design of the four modular assemblies that are the most forward facing aspects of the IFIC and govern much of its performance. When examining the bill of materials for the full system however, it quickly becomes clear, that these assemblies only represent a minor portion of the overall capital cost of the system. The majority of the cost is instead concentrated in just two categories: the RF power equipment and the vacuum pumps. **Table 2.1** provides a full breakdown of the cost to build one IFIC system arranged by category.

Category	System Component	Price [USD]	Category Cost	% of Total Cost
Process Chamber	Upper Chamber Assembly	800	3,450	7.2%
	Lower Chamber Assembly	1,500		
	Substrate Chuck Assembly	450		
	Load Lock Assembly	700		
RF Power	ICP Coil RF Generator	5,500	14,850	31.1%
	ICP Coil Matching Network	3,000		
	Substrate Bias RF Generator	5,500		
	Substrate Bias Matching Network	500		
	Substrate Bias Attenuator	200		
	RF Cabling	150		
Vacuum Generation	Turbomolecular Pump	6,700	10,400	21.8%
	Rotary Vane Pump (Backing)	2,500		
	Rotary Vane Pump (LLA)	1,200		
Vacuum Management	LCA/LLA Gate Valve	1,500	2,900	6.1%
	Backing Pump Isolation Valve	500		
	LLA Pump Isolation Valve	400		
	Ancillary Valves	500		
Process Gas Control	Precursor Gas MFCs (×4)	4,600	6,650	13.9%
	SiH_4/He MFC	1,600		
	Flow Control Valves	450		
Pressure Control	Throttle Valve	3,200	4,900	10.3%
	Backside He Pressure Controller	1,700		
Pressure Measurement	Capacitance Manometer	1,600	2,800	5.9%
	Pirani Gauge (×2)	1,200		
Control System	Rackmount Controller	650	800	1.7%
	I/O Cabling	150		
Plumbing	Vacuum Hose and Fittings	500	950	2.0%
	Process Gas Hose and Fittings	450		
	Total System Cost	**$47,700**		

Table 2.1: Cost breakdown of the IFIC (quantity of one).

As the numbers show, more than 90% of the cost of the IFIC comes from the supporting equipment, with just under two-thirds coming from the RF power, vacuum generation, and process gas control categories. These are of course, extremely important components that the IFIC could

not function without (with one exception to be discussed shortly), but it illustrates just how unbalanced the cost distribution is. This is not exclusively a negative observation however, as it does illustrate that the four modular assemblies are relatively inexpensive compared to the total system cost, which opens up some unique possibilities for tool expansion or experimentation. For example, a multi-user facility like an academic fab could purchase a single IFIC system and then add additional UCAs that could be rotated in and out of the system depending on the type of film being deposited or substrate material being used. Despite this, the total cost estimate of $47,700, is certainly higher than what is desired. Fortunately, though, there are several ways in which this cost can be appreciably reduced, which are discussed next.

2.5.2 Cost Reduction

The design of the IFIC system already incorporates many cost-saving features, several of which were discussed in the preceding sections. The results of the characterization tests, presented in the following chapters, uncovered a few additional avenues for reducing the IFIC price tag. From a cost perspective, by far the largest of these findings is that the substrate bias power, despite being proven to have a substantial impact on stress levels in both SiO_2 and SiN_x films, may not, in fact, be needed as input parameter because its effects can largely be subsumed by appropriate value selections in other parameters. Without substrate bias, the IFIC would operate in pure ICP mode, which is a configuration actually used in several commercial systems [29], [32], [50]. The cost savings of making this change are dramatic, reducing the system price by more than 6,000 USD to 41,450 USD, a drop of more than 13%. Additional savings in the RF section could one day also be realized by replacing the automatic matching network used for the ICP coil with a new type of ICP coil and passive matching network developed by collaborators during the early stage of this work [51]. Based on cost estimates for this new configuration, as much as 2,000 USD could be further removed from the price. Another significant way in which costs could be reduced is through the sharing of some of the peripheral equipment. This is particularly applicable in situations where multiple Inch Fab tools are being used together in the same space (or eventually in the full Inch Fab fabrication platform). High cost items like RF generators can be routed

through switch boxes to multiple systems, or large banks of MFCs can be used to supply compatible gases to different systems. This could effectively reduce the price of the IFIC by thousands of USD.

2.5.3 Quantity Discounts

The costs presented above in **Table 2.1** reflect the price of purchasing just enough components to produce a single IFIC system. To explore how these prices change with increasing quantities, vendors for each of the components were contacted and asked to provide pricing information for enough components to complete a small production run of 10 IFIC systems. The median price break available at this relatively low quantity was between 8 and 10%, but some of the larger breaks were actually for some of the more expensive items, including the turbo pump system (45% off at 10 units) and the precursor gas mass flow controllers (15% off for quantities above 25 units—40 total are needed for 10 systems). Taking all of the discounts together, the per-system cost drops nearly 20% to 38,600 USD, or to just 32,935 USD if the substrate bias RF power is removed. This is a much more palatable price point for the IFIC, and approaching a low enough value to make a sticker price of $<$ 50,000 USD a reality.

Chapter 3: Experimental Methods

The characterization of the Inch Fab ICP-CVD (IFIC) system required the use of a wide variety of measurement and analysis techniques. In this chapter, each of the techniques employed will be described and discussed through the lens of what information they provide about the system or films produced by the system. The first section explains several of the techniques used to verify the performance of the IFIC system design as described in the previous chapter from a mechanical, electrical, and vacuum integrity perspective. Data and insights gathered using these techniques will also be presented. The second section will focus on the measurement methods used to assess the quality of the films produced by the IFIC. Special attention will be given to the reliability and potential error sources within these methods. The final section of the chapter will outline the standard procedure used when depositing films and the standard sequence of measurement methods utilized to characterize those films. The data generated from these methods will be dissected in **Chapter 4** and **Chapter 5**.

3.1 Methods for System Characterization

Before depositions could begin in the IFIC, several aspects of the system itself required testing. The types of experiments used to test the system include both quantitative assessments of the absolute performance of the system and more qualitative measures relating to the usability and intuitiveness. The methods used for these experiments are discussed in the following sections, and the results of the quantitative tests are presented.

3.1.1 Leak rate and rate-of-rise

Arguably the most important characteristic of a vacuum system is, not surprisingly, how well it holds vacuum. To assess vacuum tightness in systems like the IFIC, two different measures, leak rate and rate-of-rise, are commonly measured. The leak rate of a system is the cumulative total of all the leaks from the individual components and connections within the system. Leak

rates are reported like mass flow rates, with units of atm $\cdot$ cm^3/s or equivalent. Leaks most often occur at seals between components, where small gaps or defects create a pathway to the outside atmosphere. These leaks are known as "residual leaks". A different class of leaks, known as "virtual leaks", occur when gas is trapped in pockets or adsorbed on surfaces (adsorbed water vapor is a particularly pernicious virtual leak source) within the evacuated region of the chamber. Virtual leaks can often be eliminated or minimized with careful design choices or post-assembly heat treatment, both of which are discussed in **Section 2.2.2**, but if a virtual leak is detected (generally by the observation of a longer than normal pump-down time coupled with the eventual attainment of the normal ultimate base pressure), pinpointing the exact source can be very difficult.

Leak rates of individual components or sub-sections of a system are typically measured directly using a piece of equipment known as a He leak detector, while the full system leak rate is calculated indirectly using the measured rate-of-rise. The rate-of-rise of a system refers to the rate at which the actual pressure rises in the system if it is isolated from pumping sources. Measuring rate-of-rise is relatively simple, requiring only the pressure gauges installed on the system, and the ability to isolate the vacuum chamber from any pumping elements (e.g. using isolation valves).

When assembling the IFIC, a Varian 979 He leak detector was used to check for large leaks in the chamber and the region between the SiH_4/He cylinder and the SiH_4/He MFC. Helium leak detectors integrate a mass spectrometer specifically tuned for detecting helium with a turbo pump system, which is used to evacuate the system or components being tested. Once evacuated, an external source of helium can be sprayed on and around potential leak points and if a residual leak exists, the mass spectrometer will detect it as a spike in the measured He concentration. As there can be an appreciable time lag between spraying the helium and the potential detection downstream (if the leak path is small or tortuous, the conductance of the He will be very low), it is important to be very patient and systematic when leak-checking a system, starting with components that are physically higher off the ground (since helium rises) and closer to the leak detector inlet whenever possible.

After probing the system and tightening a few fittings, the maximum observed He leak rate was reduced to 2.6×10^{-9} atm $\cdot$ cm^3/s for the chamber, and 1.9×10^{-9} atm $\cdot$ cm^3/s for the SiH_4/He inlet line, which are both very good (the typical specification for leak tightness of vacuum welded components is 10^{-9} to 10^{-8} atm $\cdot$ cm^3/s [52]). It should be noted however, that these numbers are not the definitive leak rates for the system. Since the components could not be totally immersed in a helium ambient, it cannot be stated with certainty that all the possible leak points were probed or detected. For the SiH_4/He line the quoted number is likely a reasonably accurate estimation, as each connection point in the line was easily accessible and thoroughly probed (and nearly all of the connections are made with Swagelok VCR-style connectors that are virtually virtual leak-free). This was important to confirm, as even though the 1.5% SiH_4 mixture used in the IFIC is not pyrophoric, it is still flammable, and should not be leaked at any level into the environment.

In the processing chamber, however, there are many more connection points and not all are easily accessible. The lack of a large He leak rate value suggests that no significant residual leaks are present, but the chamber also has much more surface area and geometry that can contribute to the virtual leak rate, which the He leak detector cannot measure. The data provided next for the rate-of-rise of the chamber shows that the value measured by the He leak detector is, in fact, an underestimate.

After He leak checking, the IFIC system was allowed to pump down for 24 hours and then isolated. The rate-of-rise was then monitored using the capacitance manometer gauge for one hour and found to be 7.7×10^{-5} torr/min. This value can then be coupled with the interior volume of the chamber, estimated at 1.5 L, to give a leak rate of $\sim2.5\times10^{-6}$ atm $\cdot$ cm^3/s, which is certainly larger than the He leak rate value, but for vacuum processing chambers is within the acceptable range of $< 1\times10^{-5}$ atm $\cdot$ cm^3/s [53]. As a frame of reference, this leak rate means that it would take ~4.6 days for a single cubic centimeter of atmospheric air to infiltrate the system, and this intrusion would only raise the system pressure by ~0.5 torr. Even still, better results could almost certainly be achieved if the chamber were allowed to pump down longer or heated up to help

remove the virtual leaks from adsorbed water vapor or other volatile compounds, but these steps were not deemed necessary.

3.1.2 Base pressure and pump-down times

The base pressure and pump-down times of the IFIC system were measured for both the processing chamber and the load lock using the pressure gauges installed in each. In the load lock, the installed pressure gauge for the low pressure range is an MKS 901P Pirani-style gauge which can measure pressures down to 1×10^{-5} torr with an accuracy of $\pm10\%$ [54]. Pirani gauges measure pressure by measuring the change in resistance of a heated section of wire exposed to the environment being measured. As the pressure decreases, the thermal conductivity of the environment decreases, reducing the amount of heat loss and increasing the temperature of the wire, thereby changing its resistance. The thermal conductivity of a gas varies depends on its composition, which can make Pirani gauges unsuitable for applications where they will be exposed to different streams of gases or gases for which there are not suitable calibration curves. For a load lock, however, air or dry gases like N_2 or Ar are the only gas types that will be seen, and these are included in user-selectable calibrations preprogrammed into the 901P (which is actually marketed specifically for use in vacuum load locks).

To test the base pressure, the load lock was allowed to pump down for 24 hours, after which the Pirani pressure had settled to 2.1×10^{-3} torr. Additional, informal tests where the load lock was allowed to pump down over several days did not improve this pressure, implying that this is the ultimate base pressure for the load lock. Given that the load lock is pumped only by a 2-stage rotary vane pump (an Ulvac GLD-040), this pressure is fully in line with expectations. The pump-down time for the load lock was logged using the PARC software and is plotted in **Figure 3.1**. The time needed for the pressure to fall below 0.01 torr is the relevant number in this situation, as that is the threshold pressure at which the sample can be loaded into the processing chamber. This pump-down time is of great practical importance, as the load lock is cycled from atmospheric pressure to vacuum each time a sample is loaded or unloaded, and longer pump-down times reduce the total possible throughput. Two main factors were observed that affect this

pump-down time: the length of time the load lock is open, and the relative humidity of the outside environment. This is to be expected, as the longer the load lock is exposed to atmospheric pressure, the more water vapor is allowed to adsorb onto the walls and foreline of the load lock. In humid conditions, this water vapor adsorption is only increased. **Figure 3.1** also includes a series plotting the pump-down time after the load lock was left exposed to the atmosphere for 5 minutes, showing that the pump-down time increases by more than 70%. To avoid this extra pump-down time, the next sample puck was always prepared prior to venting the load lock to minimize the time spent at atmospheric pressure.

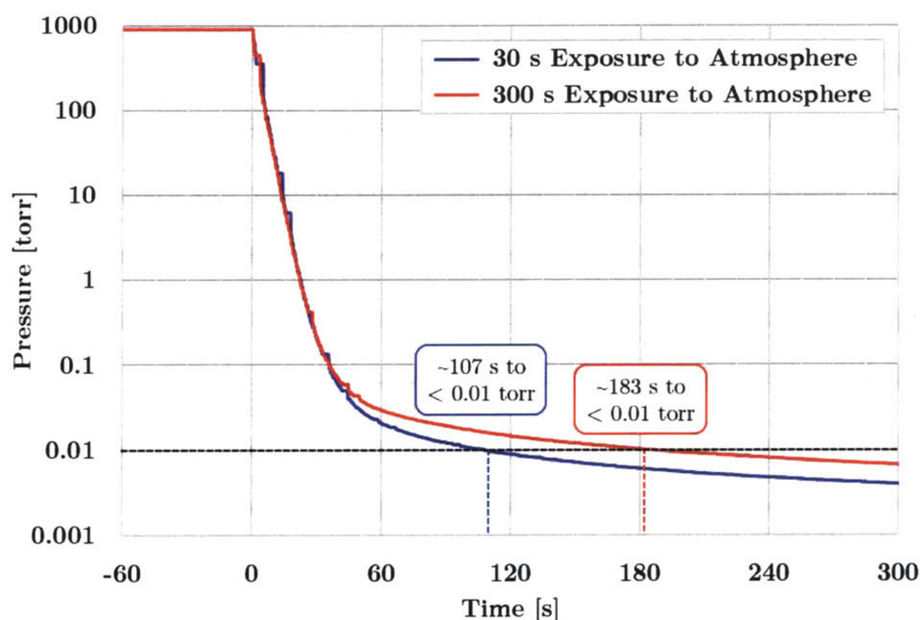

Figure 3.1: Load lock pressure vs. pump-down time. Time needed to fall below 0.01 torr noted for each curve.

Given the typical processing time and other factors like the thermal equilibration time (discussed in **Section 3.1.5**), this pump-down time of < 2 minutes was deemed satisfactory. If improvements are desired, the conductance path to the load lock pump could be shortened or widened, or a dry gas like N_2 or Ar could be used to vent and/or flush the load lock, reducing the amount of water vapor adsorbed during sample transfers.

In the processing chamber, the installed pressure gauge is a capacitance manometer (Inficon CDG045D) with a full scale pressure reading of 0.1 torr, and 4 decades of measuring precision,

meaning that the lowest pressure it can measure is 1×10^{-5} torr, with a stated accuracy of ±0.15% [55]. Capacitance manometers operate by measuring the capacitance between a mechanically fixed reference electrode and thin diaphragm which deflects based on the pressure in the measured environment. As the diaphragm deflects, the capacitance between it and the reference electrode changes and the change is converted to a voltage by a simple bridge circuit. This method of measuring pressure is fully independent of the gas composition and is therefore very commonly used in process chambers. It also has a very fast response time, which makes it the sensor of choice for pressure control applications (including the IFIC, where it serves as the pressure measurement input for the throttle valve). Capacitance manometers are also often heated (to 45°C in the IFIC) to discourage interaction with the gas species in the processing environment. To determine the base pressure in the processing chamber, the IFIC was allowed to pump down for 24 hours, after which the pressure in the installed manometer was found to be bottomed out (0 V of signal). This means that the base pressure is below 1×10^{-5} torr. Unlike other deposition processes like sputtering or evaporation, which rely on achieving ultra-low pressures either before or during the deposition process, the ICP-CVD process does not explicitly require the ability to monitor such low pressures, other than to know the chamber's exact base pressure. If the exact base pressure were required to be known, a different type of gauge, such as a cold cathode or hot filament ionization gauge could be added. Unfortunately, these gauges have several disadvantages (they are not gas type independent, have lower response times, and require protection from atmospheric pressure) and could not be used as a replacement for the capacitance manometer, so their added cost to the IFIC was determined to be unnecessary (although a blanked off port was added to the foreline design in case this changes).

The pump-down time of the processing chamber is a bit more complicated to measure than the load lock because of the turbo pump. The turbo pump (Leybold T350iX) requires an inlet pressure below ~0.4 torr to turn on, and then requires ~4 minutes to accelerate to the normal 60,000 RPM operating speed. By the time the turbo reaches this speed, the chamber pressure is typically around 8×10^{-5} torr, and pumping down to below 1×10^{-5} takes another 2-4 hours,

depending on if the chamber was fully vented to atmosphere or the turbo was just powered off and the backing pump allowed to continue evacuating the chamber through the static pump rotors. Since the processing chamber is very rarely vented, this time is not a critical factor. A more relevant pump-down time is perhaps the time it takes to pump the system from the process setpoint pressure back down to a near base pressure. This is essentially the time needed to exhaust all of the process gas in the system, such that the processed substrate can be safely removed. After each deposition recipe, a 60 second purge cycle is run to exhaust the process gases, as well as the backside helium. Just 10 seconds into this cycle, the chamber pressure, which can as high as 0.1 torr during a process, is reduced to 5×10^{-5} torr, and after the full 60 seconds, which are needed to fully pump the backside helium from the SCA, the chamber pressure is further reduced to just 2-3×10^{-5} torr, very near the resolution limit of the manometer.

A characteristic of the pumping system that is of critical importance is the overall pumping speed or throughput, which is discussed in the following section.

3.1.3 Pumping Speed

One of the consequences of using a very dilute silane mixture as is done in the IFIC is the need to pump much larger quantities of gas during depositions. This concern was addressed in **Section 2.4.2**, which discusses the design of the pumping system and the eventual choice of the Leybold T350iX turbomolecular pump for the primary system pump. Once the turbo pump was received and installed, tests of its pumping capabilities were undertaken. To do this, various mass flow rates of the SiH_4/He mixture were introduced into the system and the resulting system pressure (with the throttle valve fully open) was logged and compared to the simulation data provided by Leybold. These measurements were also converted to an effective pumping speed. The data is plotted in **Figure 3.2**.

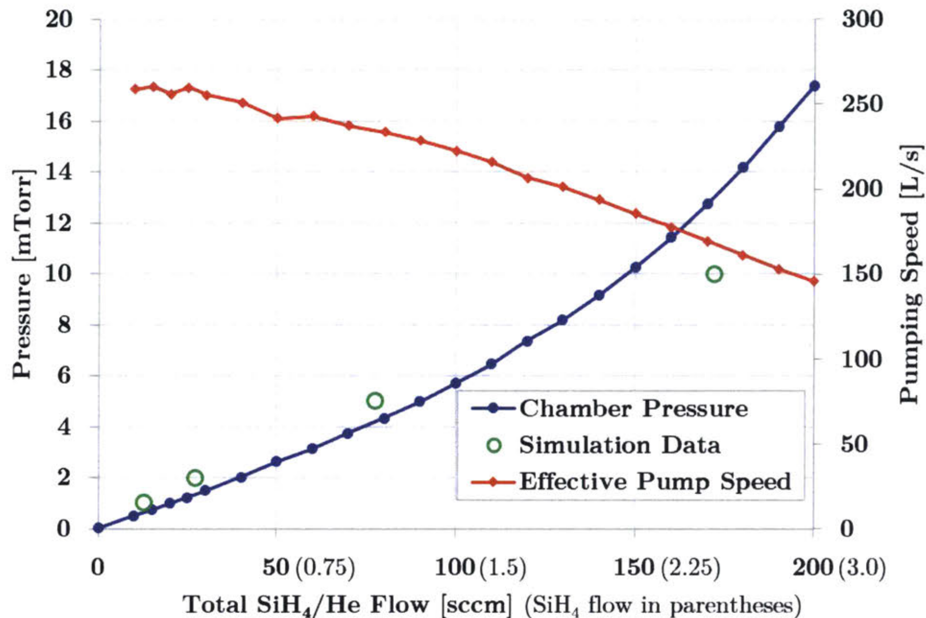

Figure 3.2: Process chamber pumping performance with throttle valve fully open. The green circles refer to simulation data provided by Leybold.

This was a very straightforward test to carry out, but it provided some important information about the minimum process pressures that could be achieved vs. the input SiH_4/He flow (which dominates the total flow during depositions). Ultimately it was found that quality depositions were best achieved at pressures appreciably higher than these minimums, so the throttle valve was always used to control the deposition pressure. This potentially means that future iterations of the IFIC could use a slightly smaller turbo pump, such as the Turbovac 350iX, but unfortunately this drop in pumping speed and throughput does not come with a substantial drop in price (a difference of about 5% in list price at the time of this writing), and the next smaller size (the Turbovac 250iX, about 20% less inexpensive) would likely not provide sufficient pumping speed. Additional information on the cost of pumping can be found in **Section 2.5.1**.

3.1.4 Sample Loading and Unloading

The next aspect of the IFIC tested was the sample loading and unloading procedure using the substrate puck, transfer arm, and substrate chuck assembly (SCA) receiver (see **Section 2.3.3** and **2.3.4** for more information on these designs). Testing this procedure began by first testing the spring plunger-based locking mechanism outside of the system. With four of the possible eight

spring plungers installed in the substrate puck, the force needed to lower the puck onto the SCA receiver was found to be ~65 N (compared to the estimate of 71.2 N calculated from the stated spring plunger strength and the SCA receiver geometry. With a 0.5" (12.7 mm) diameter, 304 stainless steel rod serving as the transfer arm and reaching a maximum extension into the chamber of ~10" (254 mm) during loading, the transfer arm stiffness is ~27 N/mm. This suggested that the transfer would deflect ~2.4 mm during the loading process. This is a relatively small amount, but would cause the puck and receiver axes to be off-parallel, so to be safe, the chamfer angle at the top of the SCA receiver was decreased from 45° to 15°, which reduced the lowering force to ~23 N (compared to the calculated estimate of 19 N) and the transfer arm deflection to < 1 mm. Additionally, a chamfer was added to the bottom of the substrate puck, to help guide it onto the receiver. Overall, this resulted in a much smoother load and unload process.

Once the puck was loaded and locked into place on the SCA receiver, the holding force was found using spring scales to exceed the design specification of 200 N, which is more than 3 times the estimated force of ~60 N that would be provided by the backside helium pressure (~3.4 N at 20 torr) and the restoring force from the O-ring (~54.5 N at 10% compression[13]). The torque needed to rotate the puck between the locked and unlocked positions was also found to be very small, and easily handled by the alignment pin in the fork assembly.

With the forces confirmed, the SCA and wafer transfer arm were installed into the lower chamber assembly (LCA) and load lock assembly (LLA), respectively. Loading and unloading the substrate puck was first tested with the system vented, and the procedure was confirmed to work smoothly. Shaft collars were added on both the exterior and interior of the transfer arm to serve as hard location stops for when the substrate puck was exactly centered over the SCA, and for when the puck was directly lined up with the load lock door. In a fully automated system, these stop positions could be easily implemented through limit switches.

[13] Full parameters used in the calculation: trade size: 029, diameter: ~4.9", cross-section: 0.070", hardness: Durometer 60A, compression: 10%, compression force: 1-2.5 lbf / linear inch [37] .

Lastly, with the system under vacuum, the sample loading and unloading sequence was tested several times and the leak-tightness against the backside helium pressure was tested. No leaks were detected (as measured by monitoring the chamber pressure), providing a final validation of the spring plunger-based design. In the subsequent testing of the IFIC, more than 300 load/unload cycles (> 600 interactions) have been completed with no dropped, damaged, or stuck pucks. From the extension of the transfer arm into the chamber to its retraction after locking the substrate puck in place, loading a sample takes about 10 seconds, with a similar amount of time needed to remove the puck after processing. As a pleasant surprise, there remains a good deal of tactile feedback in the load/unload processes, and it is easy to feel when the puck locks onto or disengages from the grooves in the SCA receiver. Coupled with viewing the process through the viewport on the LCA, this makes the load/unload process very user-friendly and requires almost no practice to master. Continued testing in the IFIC will determine the long-term durability of this substrate handling system, but so far there are no indications to suggest it will falter.

3.1.5 SCA Heater Performance

Even though ICP-CVD offers the ability to deposit films at temperatures as low as room temperature, the quality of these films is undoubtedly improved with increased temperature (this will be discussed in more detail in **Chapter 4** and **Chapter 5**). To heat the substrate, a custom NiCr wire heater was integrated into the SCA and controlled using a PID controller and a DC-DC solid-state relay with an ungrounded thermocouple providing feedback (see **Section 2.3.3** for more design details). In order to test both the response time and the uniformity of this heater set-up a FLIR E6 handheld IR camera was used. The FLIR camera uses long-wave infrared (LWIR, 7.5-13 µm) radiation to measure the heat signature of the wafer. Unfortunately, none of the standard optical viewport materials are transmissive at this wavelength range, and so a custom LWIR-transmissive viewport was constructed using a 1" (25.4 mm) diameter AR-coated ZnSe window (Thorlabs Item #WG71050-G). This viewport was connected to a CF flange adapter and attached to the top of the LCA in place of the normal upper chamber assembly (UCA). The chamber was then pumped down and a substrate was loaded onto the SCA. The heater was then

activated with a 75°C setpoint and thermal images were taken every 15 seconds to monitor the heat-up process. The wafer temperature reached a steady state after ~7.5 minutes. The temperature reported by the thermocouple attached to the PID controller was recorded along with this test, and is shown along with the progression of the IR-measured temperature for a point near the center of the wafer in **Figure 3.3**. From these data it is apparent that the thermocouple measurement is outpacing the wafer temperature, reaching its steady state ~5.5 minutes after the heater was turned on[14]. This is not particularly surprising, as even though the backside helium is flowing, the thermal conductivity of He at 20 torr and a gap of ~100 µm is ~0.1 $W/(m \cdot K)$ [45], which is far less than the thermal conductivity of the thermocouple to SCA connection (made using a solid, spring-loaded contact plus thermal grease with $k = 2.3\ W/(m \cdot K)$). Nevertheless, the lag time of ~2 minutes between the thermocouple reading (which is always available in the system, unlike the IR measurement) reaching the setpoint value and the IR camera showing a steady-state temperature is the important value to note, and was used to create the 5 minute thermal equilibration period guideline used in subsequent processing.

[14] The warm-up time could be accelerated by using more aggressive PID parameters. As the waviness in the data in **Figure 3.3** shows, the tuner currently cycles the heater signal on and off even during the earliest stages of warm-up. When performing multiple depositions, the heater is kept on in between samples, which reduces the time it takes to reach the setpoint temperature appreciably.

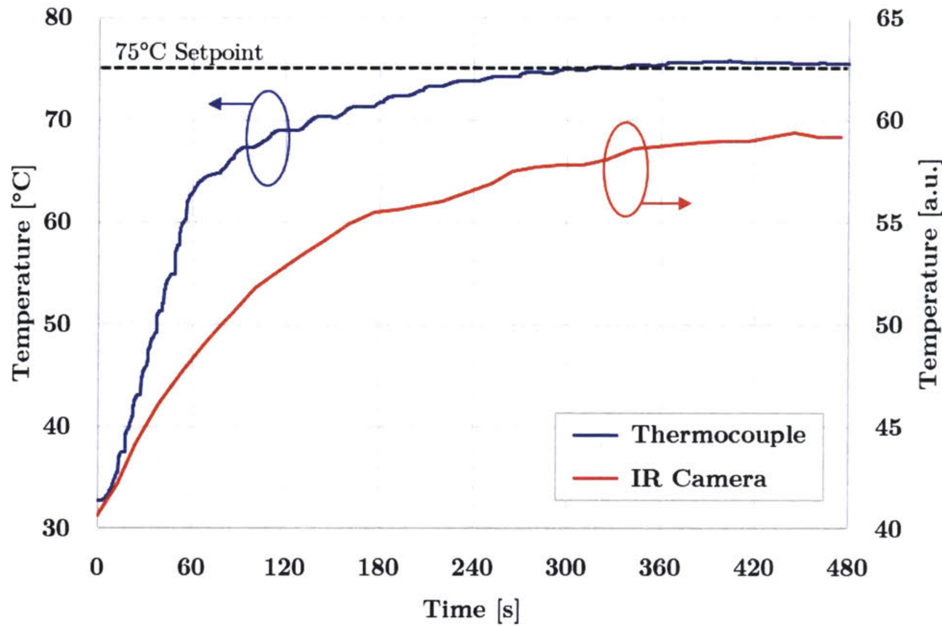

Figure 3.3: Temperature of the SCA measured by the integrated thermocouple and the substrate measured by an external IR camera during heat-up.

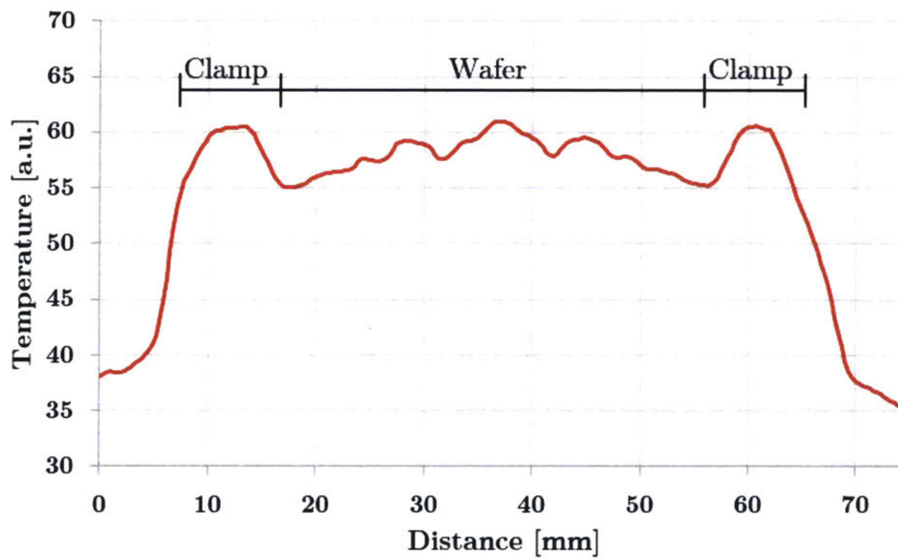

Figure 3.4: Temperature line scan across the substrate from external IR camera at equilibrium. The added lines delineate between the alumina clamp and substrate regions of the scan.

A line scan showing the temperature across the wafer was taken from the final image of this warm-up sequence and is plotted in **Figure 3.4**. The right-side temperature axis in **Figure 3.3** left-side temperature axis in **Figure 3.4** are labeled as arbitrary units because the actual temperature measured is very dependent on the emissivity and reflected temperature values selected in the IR camera. The emissivity value used is applied to all the pixels across the image

frame, but in reality emissivity is very material dependent, so relative temperature across different materials (e.g. the silicon wafer and the alumina clamp ring) can be difficult to interpret. Measuring through a ZnSe window versus through air also affects the values seen. Within a single material however, the values can be compared in a relative sense, but the absolute values may be shifted. All that is to say, the data in **Figure 3.4** shows that the wafer temperature appears to relatively consistent, which is corroborated by examining the colors in the raw thermal image (shown as **Figure 3.5a**). Unfortunately the three local maxima seen at the 29, 37, and 45 mm marks on **Figure 3.4**, and as the orange-to-red rings in **Figure 3.5a** are due to reflections from the FLIR camera lens, confirmed afterwards by testing images taken at slightly oblique angles (see **Figure 3.5b**). The small viewing area of the constructed viewport (~23 mm) did not allow images to taken at enough of angle to remove this effect, but future revisions of the viewport design will place the window off-center and potentially slightly tilted to avoid these reflections.

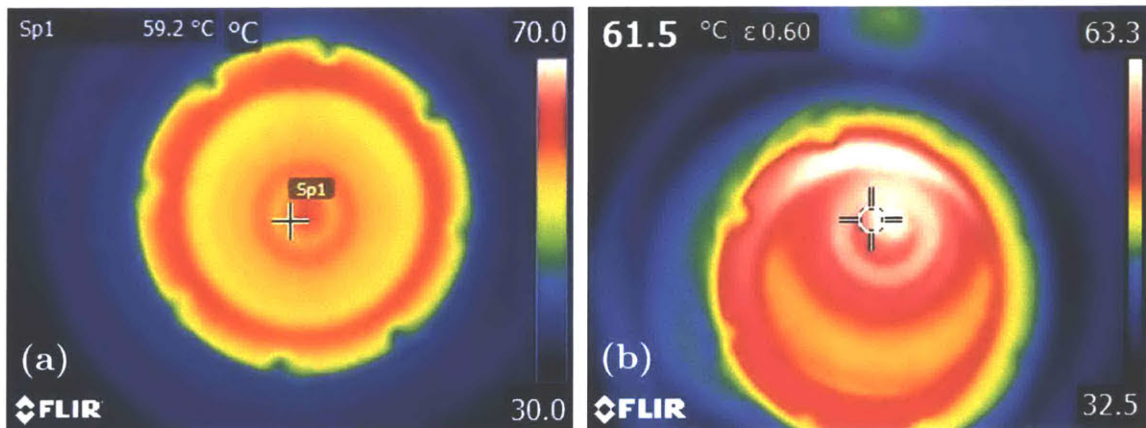

Figure 3.5: LWIR images of the substrate and surrounding puck. (a) shows the image used to generate the line scan in Figure 3.4. The orange-to-red rings at the center of the substrate are reflecations from the LWIR camera lens; (b) shows an image taken at a slightly oblique angle to illustrate the reflections from the camera lens.

The key takeaways from this test were that (1) the SCA heater functions as designed and appears to produce a spatially uniform temperature profile across the substrate and (2) the time it takes for a substrate to heat up is roughly correlated with the temperature displayed on the PID controller, but an additional 3-5 minutes should be added to ensure that the desired substrate temperature is reached.

3.1.6 Control Electronics

As outlined in **Section 2.4.4**, the IFIC is operated using a custom control system designed and built in-house. The control system was originally designed to control the Inch Fab DRIE system, but since has been upgraded and adapted to operate as a general purpose vacuum processing tool control center. Compared to the rapid switching requirements of Bosch process-based DRIE, the control requirements for a CVD process are much less stringent, with recipes usually consisting of just one step and the desired run time. The process logging and monitoring requirements however, are just as important in CVD (and have been used to identify problems such as out-of-calibration MFCs and prevent mistakes in process set-up) and have been greatly improved during the IFIC development process.

In order to test the limits of this functionality, several experiments were carried out in which the communication interfaces between the control system and each connected peripheral were sped up until errors or missed commands began to appear. Each interface was then returned to the last stable speed, and the overall sampling rate of the control system (the rate at which at one least data packet from each of the connected peripherals could be received, processed, and logged) was noted. By completing this exercise, the sampling rate was improved from ~1.2 full samples per second to ~4.9 samples per second. Interestingly, it was determined that actual process of saving the captured data to the log file was a performance bottleneck in this process. Future improvements by more experienced software engineers may be able to alleviate this. If logging is disabled, the sampling rate increases to ~11 samples per second, and the limiting factors become the actual response times of the peripherals themselves (that is to say, although the peripherals continue to respond to requests for new data, the data they provide is not from new measurements—this is particularly true for the RF generators).

The second test of the control system was an informal test of its long-term stability, as measured by the total "up-time" without needing a reset. At the time of this writing, the IFIC

control system has been running without a reset for nearly four months[15], as measured by a counter on the front screen of the control box. In production facilities, tools are often run 24/7/365, so the robustness of a tool's control system is crucial.

3.2 Methods for Film Characterization

In this section, the methods used to understand the properties of films deposited in the IFIC are described, beginning with the statistical design-of-experiments (DOE) method used to generate the test sequences and predictive models used extensively in Chapter 4 and 5.

For the experimental measurement techniques that follow this, an overview of the operating principles behind the measurement will be provided, and for the most widely used techniques, an analysis of the reliability and potential error sources will also be provided.

3.2.1 Response Surface Methodology

RSM testing is a particularly useful form of DOE that is often employed in scenarios where the outcome of interest (the "response") may be influenced by several different variables ("factors"), and where the objective is to learn how to optimize that response [56]. Response surface designs are an extension of factorial designs. In factorial designs, all of the factors are tested using a "crossed" pattern, in which each factor is set to one of the possible levels (generally two (-1 or +1) or three (-1, 0, +1) levels are used) for every test, and all possible combinations of the levels are tested. For a factorial design with k factors and n levels, this means that n^k tests are needed. For a simple 2 factor, 2 level factorial design (known as a 2^2 design), the tests would be [(-1, -1), (+1, -1), (-1, +1), (+1, +1)]. This factorial methodology is in contrast to a one-factor-at-a-time testing methodology, in which each factor is individually tested at several levels while keeping all of the other factors at a central value. This methodology can be very useful in

[15] The previous reset was to apply a firmware update, and so the stable up-time has actually been even longer.

early explorations of a process window, but lacks the ability to uncover any interaction between parameters, as well as being less efficient in the number of tests needed to estimate responses [56].

Response surface designs extend the concept of factorial designs by adding additional tests at particular factor values that will allow the estimation of not only the linear effects of factor changes on a system, but also any curvature from higher-order and multi-factor interaction effects. For second-order modelling, the two most commonly used response surface designs are the Box-Wilson central composite design (CCD) [57] and the Box-Behnken design [58]. The former was chosen for the SiO_2 and SiN_x depositions since it provides a wider range of factor levels (5 vs. 3). There are three sub-types of CCD designs, circumscribed, inscribed, and face-centered, which differ in the way the tests added to the base two-level factorial design are spaced. There were no major restrictions in the factor levels for the SiO_2 or SiN_x RSM, so a circumscribed CCD design, where the added tests (known as "star" or "axial" tests) are placed at levels outside the factorial tests (known as "cube" tests in the RSM lexicon). Additional "center point" tests are also placed at the exact center of the design (i.e. the factor levels are all set at the midpoint between the two levels of the factorial design). These center point tests are repeated multiple times, which helps provide an estimate of the repeatability and/or error in the measurements, and also helps to stabilize the variance in the responses predicted by a generated RSM model. **Figure 3.6** shows a graphical representation of 2 and 3 factor circumscribed CCD designs, where each axis in the graphs correspond to a factor being tested. Each point on the graph represents an individual experiment, and the coordinates of that point indicate the level of each factor in that experiment. The standard practice is to the code these levels in order to compensate for scale differences between the real values used for each factor.

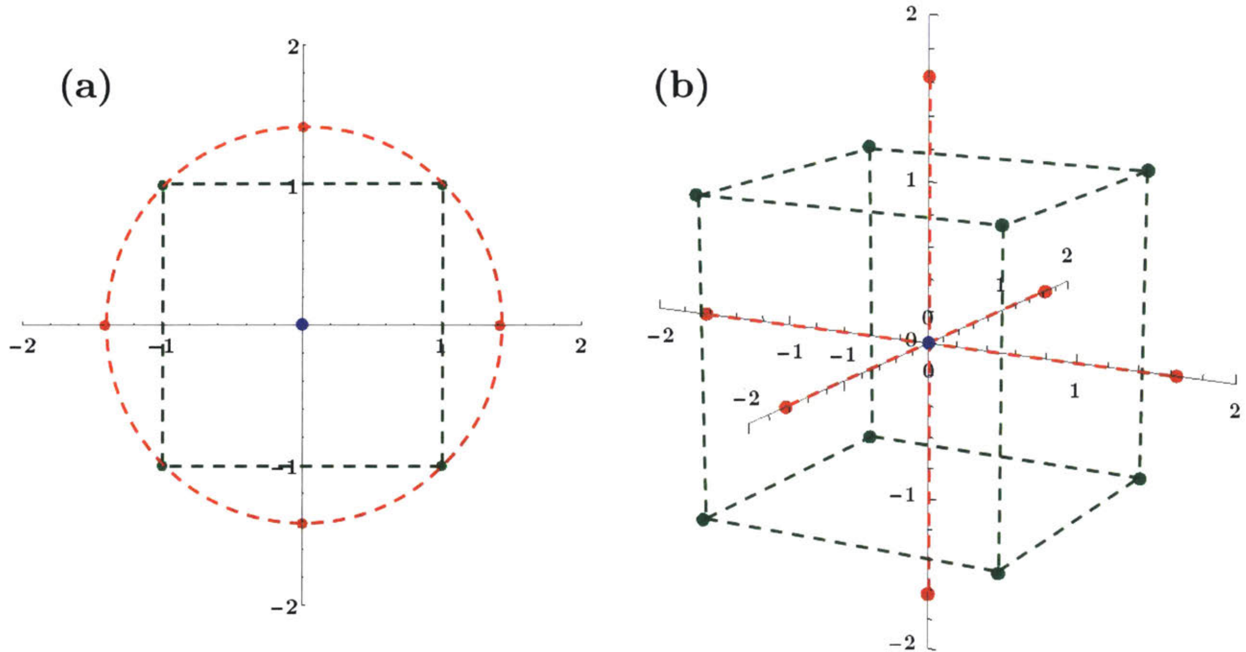

Figure 3.6: Graphical representation of test locations in circumscribed CCD designs for (a) two factors; (b) three factors.

The three types of experiments in circumscribed CCD designs are represented by the colors used for the points in the **Figure 3.6**. The blue point represents the center (or zero) point of the design, and is coded as [0, 0, 0] (for the three factor case in **Figure 3.6b**). The green points represent the factorial or cube tests, which are coded as [±1 ,±1, ±1]. The red points represent the star tests, which are coded [$\pm\alpha$, 0, 0], [0, $\pm\alpha$, 0], and [0, 0, $\pm\alpha$]. The value of α is chosen to give the design certain properties, such as rotatability or orthogonality. A rotatable design means that the variance of the response predicted by the generated model will only depend on the distance away from the design center point (it is independent of its direction or orientation along any of the factor axes). For a rotatable design, α = (number of factors)$^{1/4}$. Orthogonality in a design means that the effect of blocking the design does not affect the calculation of the coefficients for the response surface model [59]. Blocking is used to eliminate nuisance variables such as the effect of running tests over multiple days or using multiple bottles of a reagent. In the analysis of a blocked design, a blocking factor is produced which compensates for any block-specific differences. The formulas for calculating α for rotatable and orthogonal designs are below [60].

$$\alpha_{rotatability} = k^{1/4}$$

$$\alpha_{orthogonality} = \sqrt{\frac{k(1 + n_{s0}/n_s)}{1 + n_{c0}/n_c}}$$

Where: k is the number of factors in the design.
n_{s0} and n_s are the number of center points and non-center points in star block, respectively.
n_{c0} and n_c are the number of center points and non-center points in cube block, respectively.

3.2.2 Film Thickness and Index of Refraction

Immediately after a film was deposited in the IFIC, the first measurement performed was to examine the film's color. The color of the film results from thin film interference, a phenomenon whereby broadband light is selectively attenuated or amplified due to destructive and constructive interference, resulting in a dominant, visible color. The color seen depends on three things, the viewing angle, the thickness of the film, and its index of refraction (n). For thin SiO_2 and Si_3N_4 films, color charts are widely available that match colors to film thicknesses[16]. This rough measurement was a good way to estimate the thickness of a film and compare thicknesses across films.

For a more quantitative assessment of the thickness and index of refraction, a technique known as ellipsometry was used. Ellipsometry operates by shining a beam of linearly-polarized light at an angle across the sample, and measuring the change in polarization of that light after it reflects off the sample. As the incident light interacts with the sample, the polarization become elliptical (the source of the "ellipsometry" name), and using a detector, the ratio of the amplitudes (ψ) of the parallel (p) and perpendicular (s) components of this elliptically polarized light is captured along with the phase shift (Δ) between the p and s components. **Figure 3.7** provides a schematic view of the ellipsometry process, courtesy of J.A. Woollam [61].

[16] Usually assuming the stoichiometric refractive indexes of ~1.46 for SiO_2 and ~2.0 for Si_3N_4.

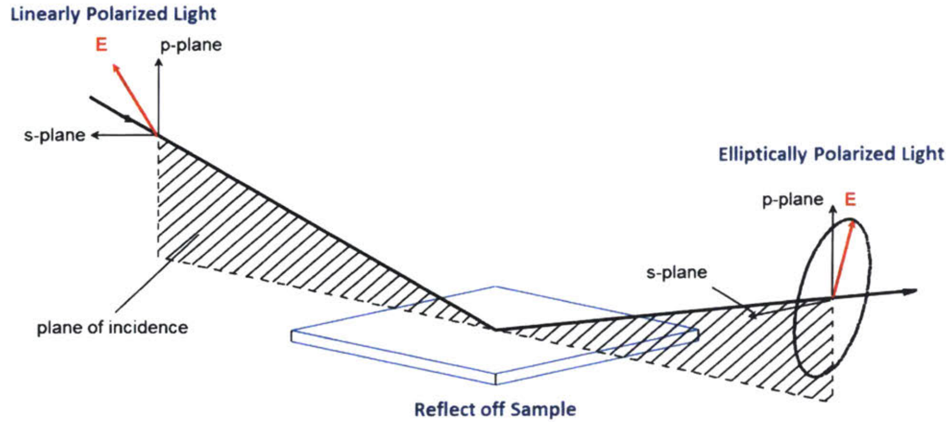

Figure 3.7: Schematic view of the ellipsometry process. Image courtesy of [61].

These values are related to the complex reflectance ratio (ρ), which is the ratio of the parallel (R_p) Fresnel reflection coefficient to the perpendicular (R_s) coefficient. The equation relating this values is commonly referred to as the ellipsometry equation, and is shown below.

$$\rho = \frac{R_p}{R_s} = \tan(\psi)\, e^{i\Delta}$$

In basic ellipsometry, ψ and Δ are collected using a single wavelength of light (632.8 nm light from a HeNe laser is very common) and a single incident angle. This information is typically not enough to provide concrete measurements about a film's thickness and index of refraction because the ψ and Δ measured are periodic, and for thick films, it will be unknown how many times the signal has "wrapped around". To get around this problem, spectroscopic ellipsometry captures ψ and Δ at many different wavelengths, which increases sensitivity. Further increases in sensitivity can also be obtained by taking measurements at different beam angles, which provides a different optical path length for the beam to interact with the sample [62]. This is known as variable-angle spectroscopic ellipsometry. Once a measurement is made, all of the ψ and Δ values are then used to fit a material model that can provide information about the film's thickness and index of refraction. Some pre-existing knowledge about the range of possible values for the thickness and index make this process much easier, but accurate results can be achieved iteratively by monitoring how the parameters used to generate the models are varying.

A J.A. Woollam M-2000S variable angle spectroscopic ellipsometer (VASE) was used to measure the films deposited in the IFIC. The data was gathered at 150 wavelengths from ~400-700 nm, and at incident angles of 65 and 75 degrees. A Cauchy model was used to fit the gathered data, with the fitted model providing the film's thickness and the index of refraction (as a function of wavelength), along with error estimates (which were typically 0.1-0.15% of the fitted value). To ensure that samples were measured under consistent conditions, the system was calibrated before each measurement session using a reference silicon wafer with 25.0 nm of thermal oxide on the surface. Furthermore, thin alignment plates were created and coupled to the measurement stage using dowel pins to ensure that samples could be repeatedly measured in the same locations. An example of one of these sheets can be seen in the photo of the M-2000S VASE shown as **Figure 3.8**.

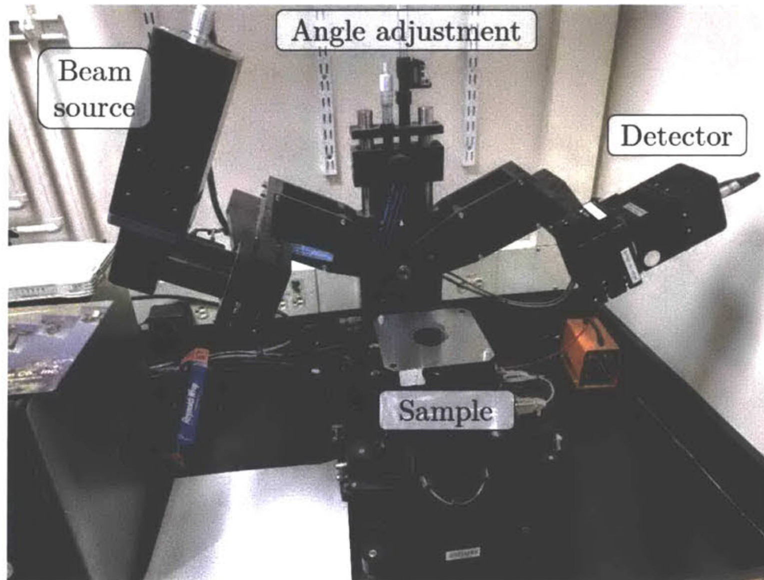

Figure 3.8: J.A. Woollam M-2000S VASE. Shown on the stages is 2" sample centered within a custom alignment plate.

Ellipsometry is known to be an extremely accurate measurement technique, but to be confident that the results gathered using this specific VASE could be trusted, two tests were performed. The first test simply compared the thickness value found using the VASE to the thickness measured from a cross-sectional view in a scanning electron microscope (SEM). This was done for both SiO_2 and SiN_x films, and the measurements were found to agree within 1-2% (~2-4 nm of

variation for the samples measured). Difficulties in determining the exact position on a SEM image to place a measurement bar can account for this small level of error, and it was not explored further. A second confirmation of the accuracy of the VASE system came from the uniformity measurements taken using the UV1250SE system discussed in **Section 3.2.4**. The thickness measurements taken by this system were found to agree very well with the VASE system, usually with less than a 1% difference in values for SiO_2, and less than 2% for SiN_x.

The second test of the VASE measurements involved measuring the same five samples in three different measurement sessions and comparing the results. The results for this test are shown below in **Table 3.1**. The MSE value shown is the mean squared error, and is an indication of how well the generated model fits the gathered data.

	Sample 1		**Sample 2**		**Sample 3**		**Sample 4**		**Sample 5**	
	Thickness [nm]	n_{632nm}	**Thickness [nm]**	n_{632nm}	**Thickness [nm]**	n_{632nm}	**Thickness [nm]**	n_{632nm}	**Thickness [nm]**	n_{632nm}
Mean	354.67	1.463	354.87	1.463	351.67	1.464	350.33	1.465	352.47	1.467
Range	0.60	0.0014	0.10	0.0005	0.40	0.0011	0.30	0.0009	0.30	0.0007
Standard Deviation	0.32	0.0007	0.06	0.0003	0.21	0.0006	0.15	0.0005	0.15	0.0004
Average Fit MSE	2.204		2.335		2.172		2.356		2.349	

Table 3.1: Repeatability test results for the J.A. Woollam M-2000S VASE.

As the data show, the VASE is very precise and repeatable, showing sub-nanometer variation even across several measurement sessions. Combined with the verification from the SEM and spectral reflectance measurements, it can be safely asserted that the measurements made using the VASE provide an accurate view of the film thickness and index of refraction for films deposited in the IFIC.

3.2.3 Average Film Stress

The average stress of a film deposited on a substrate is determined by measuring the change in the radius of the substrate before and after the film is deposited. A film with compressive

stress deposited on top of a perfectly flat substrate will cause that substrate to bend away from the film (concave down), with the opposite occurring for tensile films. Most substrates however, have some intrinsic stress and are not perfectly flat. Therefore, it is necessary to measure the curvature of the substrate before deposition to have an accurate reference to compare with after the film is deposited. In some cases, the pre-deposition curvature measurement would reveal the substrate to have a very unique profile (rather than the "bowl", "mound", or "saddle" shapes seen on most wafers) that would make calculating an accurate radius of curvature not possible. These wafers were not included in any datasets that measured average film stress.

To actually measure the pre- and post-deposition curvature, a Tencor FLX-2320 Thin Film Stress Measurement System (FLX) was used. The FLX measures curvature by scanning a laser across the surface of a wafer at a constant angle, and measuring the position of the reflected beam with a position-sensitive detector. The FLX makes this measurement with two different wavelength laser sources (670 nm and 750 nm) to avoid potential problems with destructive interference from films on the substrate. Curvature within a wafer is very often orientation-dependent, and so three pins equally spaced 120° apart along the edge of the table (where the wafer rests) allow alignment plates for wafers of different diameters to be locked into place at various orientations. For IFIC film tests, four scans (at angles of 0°, 45°, 90°, and 135° relative to the wafer flat) were taken for each sample both before and after deposition. The FLX table also features three raised points at a diameter of ~75 mm which prevent the wafers being measured from resting directly on and potentially conforming to the table surface.

The FLX was not originally designed to measure wafers with diameters below 100 mm, and so a custom alignment plate was machined to reliably orient the 2" wafers in the path of the laser scans and interface with the angle-alignment pins. The design of the stock alignment plates for larger substrates are fully open in the middle section, allow the wafers to rest on the three raised points. For the measuring curvature at more than one orientation, this is a very inconvenient set-up, requiring that both the wafer and the alignment plate be picked up separately and re-oriented with the table and each other for each new measurement. For a single set of

measurements for a wafer, this is perhaps not too much of an imposition, but when a new cassette of 25 wafers needs curvature measurement, that leads to a lot of extra wafer handling (more than 1,100 curvature measurements have been made over the course of this thesis), which is both time very consuming and has the potential to introduce contaminants. To alleviate this, the custom alignment plate for the 2" wafers has an alignment recess rather than an opening, allowing the plate and wafer to be moved at the same time, as well as two screws partially threaded into the edge of the plate, which make lifting and rotating the plate much easier than the stock design. To prevent the wafers from resting on the floor of the recess, three tapered holes holding captive bearing balls are included. The diameter of the balls is greater than the thickness of the material below the wafer recess, meaning that when the plate is in contact with the table, the bottom of the balls are also in contact with the table, allowing the wafer to sit freely while still remaining in the desired angular orientation. A picture of the FLX system along with the custom alignment plate are shown in **Figure 3.9**.

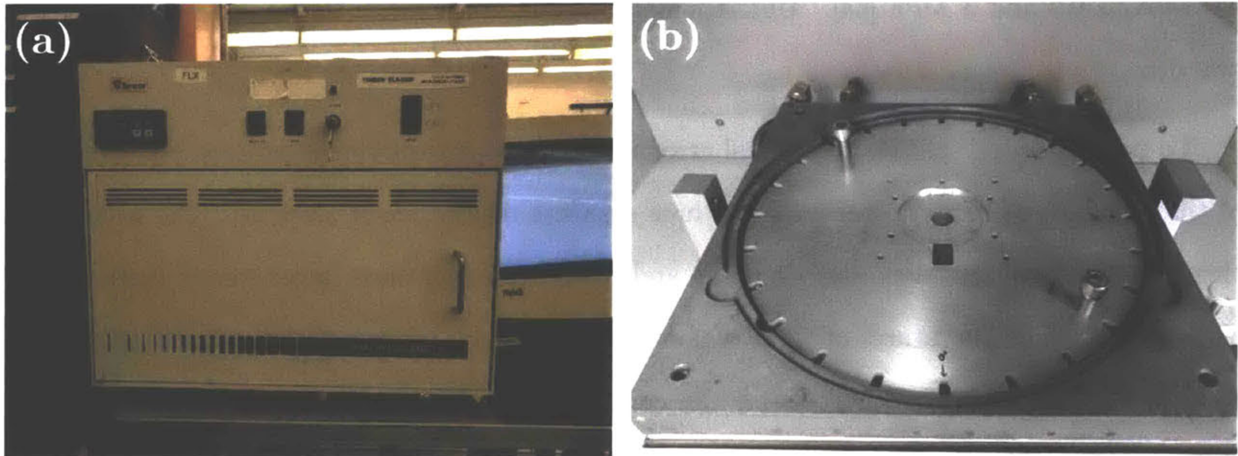

Figure 3.9: (a) FLX-2320 in the MTL cleanroom; (b) the custom alignment plate created for measuring 2" wafers.

Once the curvature of a wafer with a deposited film has been measured, the average stress in the film can be calculated using Stoney's equation [63], which is reproduced below. In addition to the two radius of curvature values (R_{before} and R_{after}), the biaxial elastic modulus ($E/(1-\nu)$), substrate thickness (h), and film thickness (t) are needed to compute the average stress (σ). For 2" diameter, (100) silicon wafers used throughout this work, the biaxial elastic modulus was taken

to be 180.5 GPa, the substrate thickness was 270 μm (measured using a calibrated optical microscope), and the film thickness was the value measured by the VASE system described in **Section 3.2.2**.

$$\sigma = \frac{h^2}{6t}\left(\frac{E}{1-\nu}\right)\left(\frac{1}{R_{after}} - \frac{1}{R_{before}}\right)$$

After computing the stress for each of the orientation in a wafer, the values were averaged to give the average film stress in the wafer. The range in values between the orientations was typically less than 50 MPa, and did not appear to scale with the average film stress. Some of this variation is likely due to actual differences in the film stress along the different measurement orientation, but another portion is almost certainly due to error inherent to the measurement process. The FLX-2320 manual provides 1σ repeatability estimates for a variety of substrate and film thickness combinations. Interpolating from these values would suggest that with a 270 μm substrate and films thicknesses between 100 nm and 1 μm, the measurement repeatability should be between 0.3 and 3 MPa [64]. Unfortunately, this is much lower that what was observed in practice.

To provide an estimation of the real error in the stress measurement process, the curvatures of three blank wafers were measured in three separate measurement sessions. The wafers each then had a layer of SiN_x deposited on them, and the thickness of those layers were measured using ellipsometry. The curvatures of these wafers were then each measured three times, providing a total of 9 different pre- and post-deposition combinations for each of the four angle orientations on each wafer. The results from this test are shown in **Table 3.2**.

Sample 1	0° Scans	45° Scans	90° Scans	135° Scans	All Scans
Mean	-61.66	-59.26	-63.92	-43.25	-57.02
Range	20.07	21.87	13.85	55.70	55.70
Standard Deviation	6.91	6.29	4.49	16.62	12.54

Sample 2	0° Scans	45° Scans	90° Scans	135° Scans	All Scans
Mean	-29.50	-22.19	-47.51	-38.81	-34.50
Range	48.60	48.02	25.58	68.18	80.26
Standard Deviation	15.43	15.98	8.21	19.57	17.72

Sample 3	0° Scans	45° Scans	90° Scans	135° Scans	All Scans
Mean	-302.02	-288.09	-290.84	-312.94	-298.47
Range	37.82	42.57	25.85	19.16	56.83
Standard Deviation	11.86	11.97	8.26	5.84	13.76

Table 3.2: Repeatability test results for the Tencor FLX-2320. All values shown have units of MPa.

Examining the data, it is clear that the average film stress measurement features a non-negligible amount of error inherent to the either the machine, the operator, or some other unknown factor. The average 1σ repeatability observed is ~15 MPa, appreciably larger than 0.3-3 MPa value suggested by the FLX manual. This larger than expected error does not significantly reduce this experimental method's usefulness, but it is very important to know and consider in the analysis of the data presented in **Chapter 4** and **Chapter 5**.

3.2.4 Film Uniformity

The uniformity of a deposited film's thickness can be measured in several ways. Measuring the film in several locations using the ellipsometry method described in **Section 3.2.2** is one option, but these measurements take at least 60 seconds (not including model-fitting), and the variable-angle adjustment is a manual process. Measuring the thickness across the wafer using a stylus or optical profilometer is another option, but this requires a very precise measurement of

the curvature of the underlying substrate (much more precise than the FLX-2320 scans discussed in the previous section can provide) to process the actual film height. What is needed is a method that can rapidly measure thickness and do so at multiple locations across the wafer. In order to fairly compare these measurements across samples, the ability to measure samples at the same locations every time is also needed. The method used to achieve this is known as spectral reflectance or reflectometry, and was performed using a KLA-Tencor UV1250SE Thin Film Measurement System (shown in **Figure 3.10a**). The UV1250 features an automated wafer handler and stage that orients and positions samples is a very repeatable. It can also be programmed to automatically measure a sample at a pattern of predefined points, making it an ideal tool for measuring uniformity. The measurement technique it uses, reflectometry, operates by measuring the fraction of light reflected from a film (or film stacks). The reflectance is measured over a range of wavelengths (~400-700nm were used in the UV1250) at perpendicular incidence, and using the index of refraction for the film at those wavelengths (from a built-in material model or from data from another measurement like ellipsometry), the thickness can be calculated.

The UV1250, like the FLX-2320 from the previous section, was not designed to measure wafers below 100 mm in diameter. In order to adapt it for use with the 2" wafers used in the IFIC, a thin (~250 µm) alignment plate was created that could precisely position and align a 2" wafer to the center of a 150 mm wafer. The alignment plate was then affixed to this "handle" wafer, allowing 2" wafers to be loaded into the UV1250 like a normal wafer. This alignment plate setup can be seen in **Figure 3.10b** passing the wafer-flat-alignment section of the UV1250.

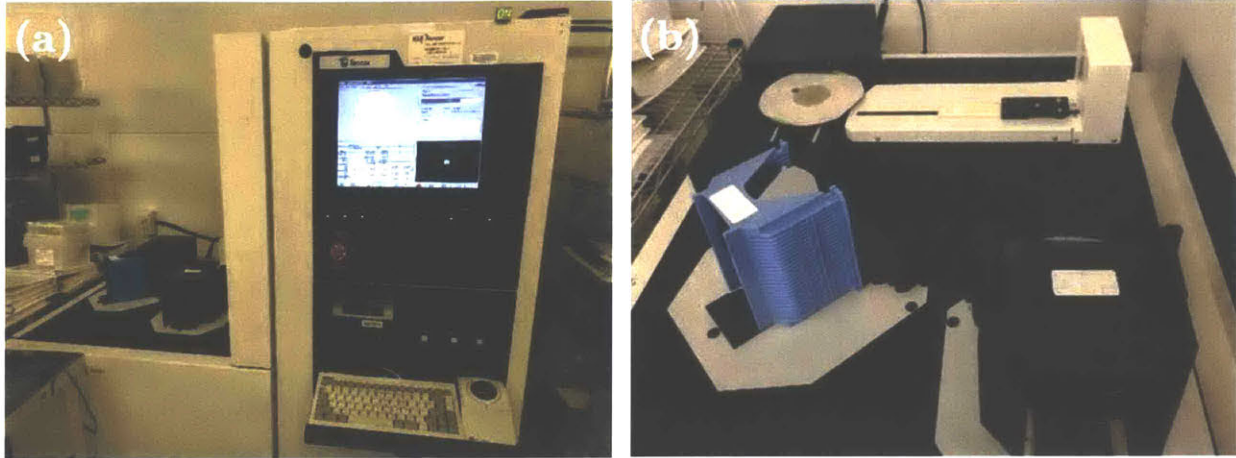

Figure 3.10: (a) UV1250SE Thin Film Measurement System; (b) Wafer handling robot for the UV1250. The handle wafer with alignment plate and 2" wafer can be seen at the top left.

To measure just the 2" wafer section instead of the full 6" handle wafer, measurement patterns were designed for 150 mm wafers using a minimum edge exclusion distance of 50 mm. The most common edge exclusion used for IFIC samples is 57 mm, which represents a ~4 mm exclusion from the edge of the 1.75" (44.45 mm) deposition region. The most commonly used pattern for measuring film uniformity has 25 points spread across the wafer in three concentric rings and a middle point. This pattern is shown in **Figure 3.11**.

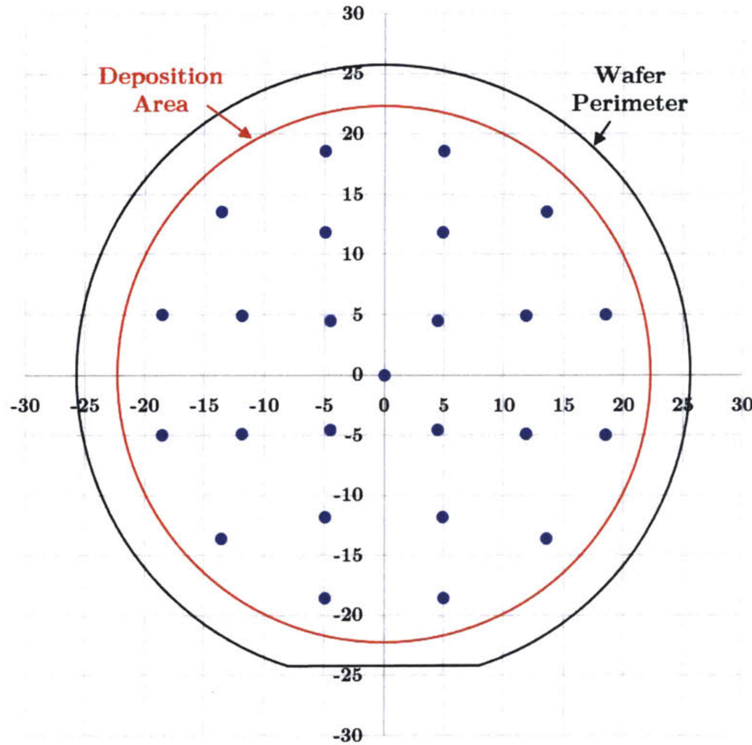

Figure 3.11: Standard UV1250 pattern used for uniformity measurements. The pattern has 25 points and a 4 mm edge exclusion.

In addition to calculating single-number uniformity values from these point patterns, contour surfaces were also fitted to the generated data, which were used to analyze the spatial nature of the film thickness variations. This was used in addition to the uniformity numbers when making changes to the spacing and sizes of components in the IFIC (see **Section 4.1.2** and **4.3.2.4**).

To assess the reliability of the data produced by reflectometry measurements in the UV1250, the same test used to probe the VASE (measuring the same five samples in three different measurement sessions) was carried out. The data from this test is shown in **Table 3.3**.

	Sample 1		Sample 2		Sample 3		Sample 4		Sample 5	
	CV	Unif.	CV	Unif.	CV	Unif.	CV	Unif.	CV	Unif.
Mean	1.48%	2.44%	1.43%	2.49%	1.34%	2.29%	1.36%	2.34%	1.45%	2.52%
Range	0.07%	0.07%	0.06%	0.12%	0.02%	0.08%	0.06%	0.16%	0.03%	0.08%
Standard Deviation	0.03%	0.04%	0.03%	0.06%	0.01%	0.05%	0.03%	0.08%	0.02%	0.04%

Table 3.3: Repeatability test results for the KLA-Tencor UV1250SE.

The precision seen in the data shown above indicate that measurements in the UV1250 are very repeatable and the measurement error is minimal. The accuracy of the actual thickness measurements made by the tool was assessed by comparing to thickness data taken using the Woollam VASE (which itself had its accuracy confirmed by comparison to SEM data). It was found that when the goodness-of-fit (GOF) values, which are taken for each point measurement, were above 0.98 (1.0 being a perfect fit to the chosen material model), the measured thickness values agree within 1% for SiO_2 and 2% for SiN_x. For the SiN_x samples measured as part of **Chapter 5**, the use of sample-specific index of refraction information from the earlier ellipsometry measurements was critical to achieving this level of accuracy, as the range of index values for those samples ($n \approx$ 1.9-2.4) was much higher than seen in the SiO_2 measurements.

3.2.5 Wet Etch Rate

The etch rate of deposited films was measured to indirectly make conclusions about their density and chemical quality. Rather than measuring the overall time it takes to for an etchant to remove a given film, deposited films were instead exposed to the etchant for a specific amount of time (less than what it would take to remove the film), and the amount of material removed was measured and the etch rate calculated. To make measuring the amount of the film removed as easy as possible, a section of the deposited film was masked using a thin layer of positive photoresist. This was done to create a well-defined interface between the etched and un-etched sections of the film. The actual etch was carried out for both SiO_2 and SiN_x using a 7:1 BOE (7 parts 40% ammonium fluoride in water, 1 part 49% hydrofluoric acid in water) solution. The substrates being etched were immersed into a plastic beaker of this solution for a fixed time (15-60s, depending on the thickness of the film), and then immediately transferred to a large beaker of deionized water to stop the etching. The substrates were then dried and the masking photoresist was removed. Using a Veeco Dektak stylus profilometer, the height difference across the interface between the masked and unmasked regions was measured, and the etch rate was then calculated. Even though the wafers being etched in this process are known to have non-zero curvature, the use of a profilometer to measure the step height is okay because the lateral

measurement distance needed is very small (0.5 mm was used) compared to the 2" (50.8 mm) diameter of the wafer itself, and therefore the error from the curvature is small.

Unlike the other measurement methods discussed so far, this process is very sensitive to its environment, particularly the ambient temperature. The etch of rate of SiO_2 in BOE solutions is known to double for each 10°C increase in temperature [65], and temperature in the acid hood where the etches were performed varied by as much as 5°C depending on external conditions. To control for this variation, a piece of silicon with 0.5 µm of thermally-grown oxide (cleaved from a single 150mm wafer) was included with each etch test. This silicon piece was masked in the same way as the other samples being etched. The measured etch rates were then normalized to the etch rate of thermal oxide control piece. This method of controlling for differences in experimental conditions is common in etch rate tests, and the data is often presented in the normalized form [66]–[69]. Many investigators use BOE ratios other than 7:1 (or use simply use diluted HF) for their etchant, and so reporting normalized etch rates normalized to a more standardized material like thermal oxide can make it easier to compare values across publications.

The etch rate of silicon-containing films in BOE is also known to be very sensitive to agitation [65], which is more difficult to control for. Multiple samples were often etched at the same time using cassette-style PTFE wafer carriers in order to minimize errors from etch time differences across samples, but a sample's position in the carrier could cause it to experience more turbulent flow during etching or in the insertion or removal from the etch dish. Due to these and other potential sources of variation, other investigators have estimated a ±10% error for timed etch tests [32], [67], which is much higher than the experimental error seen in the other measurement methods.

To estimate the repeatability and experimental error for the BOE etch rate process, a single sample of thermal oxide, IFIC-deposited SiO_2, and IFIC-deposited SiN_x were each taken and cleaved into smaller pieces and then etched in 7:1 BOE in three different sessions. The etch rates for all 9 samples were measured in a single session at three different points per sample, and then compiled to give the data shown in **Table 3.4**. Every effort was taken to maintain the same

experimental conditions for these tests, including using the same carriers for the wafers and the same dishes for the BOE and rinse wafer. The samples from the three sessions were measured in a single session using the profilometer and 3 measurements were taken on each etched piece.

	Thermal SiO_2	IFIC SiO_2		IFIC SiN_x	
	Etch Rate	ER	Ratio	ER	Ratio
Session 1	875	4631	5.29	202	0.231
Session 2	1053	4641	4.41	222	0.211
Session 3	898	4165	4.64	225	0.250
Mean	942	—	4.78	—	0.231
Range	158	—	0.88	—	0.039
Standard Deviation	96.7	—	0.46	—	0.020
Percent Deviation	7.8%	—	7.1%	—	5.7%

Table 3.4: Repeatability test results for the 7:1 BOE etch rate process.

As can be seen in the data, compared to the measurement methods outlined in the previous sections, the BOE etch rate measurement process unfortunately has a much larger window for experimental error. Steps were taken to minimize this error, like normalizing etch rates to the rates of simultaneously etched thermal oxide samples, but a portion of the variation still remains. The level of uncertainty for each film type was considered when analyzing the results from these tests for SiO_2 and SiN_x depositions.

3.2.6 Chemical Composition

Aspects of the chemical composition of films deposited by the IFIC were explored through the use of Fourier-transform infrared spectroscopy (FTIR). In brief, FTIR operates by shining infrared radiation at many different wavelengths (2.5-25 µm in the system used here) onto a sample and measuring the amount of the radiation absorbed and transmitted at each wavelength. The presence of different elements, molecules, and bonds cause radiation at specific wavelengths to be absorbed, and so by identifying the peaks of absorbance in the measured FTIR spectrum, a picture of the chemical composition can be obtained.

Lightly-doped silicon is largely transmissive in the IR range, which conveniently allows films deposited on Si to be measured using the simple FTIR transmission mode. First a blank silicon wafer (with the same properties as the substrate with the film to be measured) was measured to provide a background spectrum, and then the substrate with the deposited film was measured. The background spectrum was then subtracted from this new spectrum, leaving just the absorbance spectrum from the deposited film. Additional corrections relating to the measurement environment were applied to this spectrum, and then the peaks were identified using information found in the literature. The presence or absence of certain peaks, as well as their relative size could then be used to assess the film's chemical make-up. **Figure 3.12** shows the ThermoFisher Nicolet iS50 FTIR system used for these measurements and a look at how samples from the IFIC were mounted for transmission mode measurements.

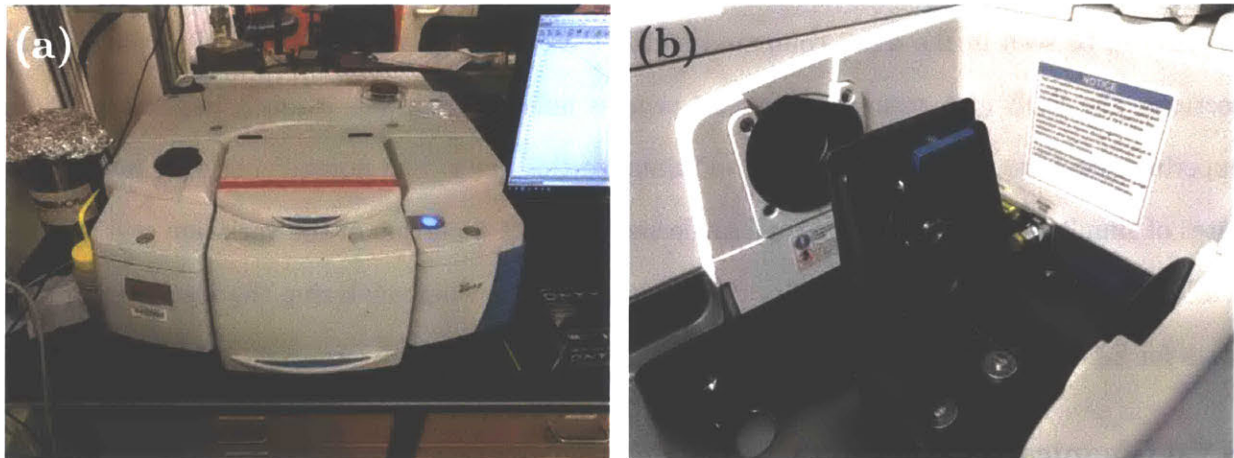

Figure 3.12: (a) ThermoFisher Nicolet iS50 FTIR system; (b) 2" wafer with IFIC-deposited SiO_2 film mounted in transmission mode.

3.2.7 Electrical Properties

The electrical characteristics of the SiO_2 films deposited by the IFIC were investigated using measurements of their electrical breakdown. Additional sample preparation was required to make these measurements, starting with the use of highly-doped P-type wafers (0.001-0.005 $\Omega\cdot$cm) as the substrates, instead of the lightly-doped P- and N-type wafers normally used. After the desired film was deposited, the wafer was then cleaved in half, and half of the sample was then annealed in a furnace at 900°C under N_2 flow for 30 minutes. After annealing, 200nm of aluminum was

evaporated through a shadow mask onto both halves of the sample. The shadow mask left a pattern of contact pads ranging in size from 50 µm to 200 µm on the samples, with each forming an MIS capacitor. It was important that this pad size be kept small to minimize the chance for contaminants to be incorporated between the pad and the film, which can unduly reduce the breakdown field [28], [50]. The samples were then moved to a probe station and connected to a high voltage SMU. The bottom side of the wafer was used as the ground electrode, and a negative voltage (negative because of the P-type doping of the wafers) was applied to the Al contact pads using a probe tip to induce breakdown. Control of the SMU and recording of the voltage and current values were handled by a custom Matlab script communicating over GPIB.

3.2.8 Surface Morphology

The surface morphology of samples was measured using a Wyko NT9800 white light interferometry system. White light interferometry uses a broadband, short coherence length light source to provide a fast and effective alternative to other scanning probe techniques with comparable vertical accuracy for optically transparent samples. The height variations across a scanned region are obtained by precisely modulating the optical path length difference between the sample arm and reference arm of the interferometer and measuring the positions on the sample where the interference contrast is maximized. Relatively large areas (800 µm × 800 µm scan sizes were used for the data reported in the following chapters) can be quickly profiled in this way. Scans were taken at three positions and for each of the samples measured in this work and the roughness statistics reported indicate the average value observed. Data analysis was performed using Gwyddion, an open source, software suite originally designed for analyzing scanning probe microscopy data [70]. Before plotting, the background wafer curvature was removed using 2nd order polynomials in both axes, and the data was zeroed to the lowest measured point.

3.3 Standard Operating Protocols

In the following section, the standard operating protocols (SOPs) for depositing films in the IFIC system and then characterizing those films are discussed. The SOP for depositing films was

crucial to define and adhere to so that sources of error stemming from variations in experimental conditions could be minimized. It was also important to define because the process is not (as of yet) fully automated, and the failure to execute a particular step in the sequence could result in an unusable sample or in the most extreme case, damage to the system itself. The SOP for characterization of the films is less susceptible to mistakes, but it does require careful thought about the order of the measurements, as several require information gained from previous steps, and some transform or destroy portions of the sample such that certain measurements are no longer possible.

3.3.1 Running Samples

The standard operating protocol for depositing films using the IFIC begins with checking to make sure that each of the always-on sub-systems are operating correctly. These checks are especially important at the beginning of a deposition session. The checks that should be made are:

1. The chilled water supply. Is the chiller on, set to 15°C, and reading 15 ± 1°C? Do the chilled water lines feeding the coil feel cold[17]?
2. The turbo pump status. Is the turbo pump spinning at full speed? Is the purge flow to the turbo running?
3. The base pressure in the chamber and the load lock. Is the chamber base pressure below 1×10^{-5} torr? Is the load lock pressure below 5×10^{-3} torr?
4. The supply pressures of process gases. Are the supply pressures of the gases within a reasonable range (40 ± 5 psia)? Is the SiH_4/He gas cylinder open? Is the SiH_4/He isolation valve open?

[17] The presence of excessive condensation on the chilled water lines is a good indicator of high humidity in the environment, which can lead to longer pump-down times and potential problems processing samples with thick coats of photoresist.

5. The RF generators and impedance matching networks. Are the RF generators and the ICP coil matching network turned on and in remote control mode?

Once these checks have been made, the chamber, if it has been at rest for more than two hours, needs to be warmed up before processing. Warming the chamber reduces the amount of process gas molecules adsorbing to the walls, which in turn reduces the amount of deposition on the walls, which then reduces the frequency at which cleaning processes are needed. The warming procedure consists of running an Argon plasma for 7 minutes, which warms the chamber from room temperature to ~40°C. This process is stored as a default recipe in the PARC software, so it can be easily retrieved and run upon startup. The warm-up recipe should be run with a dummy wafer loaded onto the SCA whenever possible, to minimize the amount of ion bombardment damage to the backside He-sealing O-ring.

Once the chamber is warm (or during the warm-up recipe), the substrate being processed can be prepared. Depending on the size of the substrate, the appropriate clamping puck should be selected and the substrate placed in an orientation that covers the entire sealing O-ring. In the case of the most commonly used 2" diameter wafers, the wafer alignment jig (see **Figure 2.15** in **Section 2.3.3**) can be used to easily center and orient the wafer. The alumina clamping ring can then be placed over the PEEK 2-56 clamping screws in the puck and rotated 5 degrees to lock its orientation in place. The screws can then be tightened, completing the substrate preparation.

To load the new substrate into the load lock, the previously processed sample (or dummy wafer) must first be removed. To remove the sample, the "sample loading/unloading" button in the PARC software should be pushed, which will double-check to ensure that no process gas or backside helium is flowing, close the relevant isolation valves (including the main load lock valve), and position the throttle valve at 90% closed (as a safeguard to protect the turbo pump inlet). Next, the gate valve separating the LLA and the LCA can be opened. This valve should only be opened if the pressure difference between the two is $<$ 10 mTorr to prevent the introduction of a

large pressure gradient to either chamber[18]. The transfer arm should then be slid into the chamber, and the fork arms aligned with the slots on the installed puck. With the fork arms engaged, the SCA can be rotated ~20 degrees (either direction, using the guide marks on the lift assembly) to disengage the puck. The puck can then be retracted back into the load lock and the gate valve closed. Once the gate valve is closed, the load lock can be vented by opening the vent valve. Once the load lock is vented, the vent valve can be closed and the load lock door can be opened[19].

The processed substrate puck can be easily removed from the load lock by pulling on the fork assembly, which is coupled magnetically to the transfer arm. The fork assembly can then be attached to the newly prepared puck using the fork arms and alignment pin and reinserted into the load lock. The tapered dovetail groove and the magnets on the fork assembly align the puck to the correct position. The load lock door can now be shut and the pump-down can begin. The pump-down takes 2-3 minutes depending on atmospheric conditions. If it was disabled or not active, the "sample loading/unloading" mode in the PARC software can now be reactivated to ensure that all of the valves and flows are appropriately set. Once the load lock pressure falls below 10 mTorr, the gate valve can be opened and the sample puck loaded and locked onto the SCA.

With the transfer arm retracted and the load lock door closed, the "sample loaded" button can be pressed to engage the backside helium flow and the substrate heater. The chamber pressure should be briefly monitored after this step to ensure there are no helium leaks from the SCA or puck, which would cause the pressure to rise. With the helium flowing, the heat transfer to the puck and substrate is drastically improved, but time is still needed to reach thermal equilibrium. After five minutes of the equilibration time (during which the wafer temperature can be monitored using the software or the display on the PID heater unit), the SCA can be raised to the processing

[18] In normal operation this means that the load lock pressure should be below 10 mTorr, as the pressure in the chamber will quickly return to < 0.1 mTorr after the previous process and purge cycle are concluded.

[19] The position of the vent valve serves as a mechanical interlock, preventing the load lock door from opening or closing if the vent is open. This is to prevent the accidental pump-down of the load lock with the vent valve open.

height. The desired process recipe can be built using the recipe creator tab in the PARC software (or recalled from a saved recipe), and then loaded on the operation tab. Loading a recipe starts the gas flows, sets the RF power setpoints, and configures the throttle valve to control to the correct pressure. After one minute, the gas flows and pressures will have stabilized and the deposition process can be started.

Once the recipe has completed, the IFIC will automatically run a 60 second purge sequence that allows the process gas to be fully removed from the chamber and the helium to be pumped away from the backside of the substrate. The processed substrate and puck can now be removed from the chamber and load lock using the same process described above for removing a dummy wafer. If another deposition is needed, the next substrate can be added at this time, otherwise the dummy wafer should be reloaded into the chamber and both the chamber and load lock should be left pumping down. As a safeguard, the SiH_4/He cylinder and isolation valve should also be closed if the deposition session is finished.

3.3.2 Characterization sequence for samples

The characterization protocol described in this section was developed so that a complete and accurate representation of a film's properties could be obtained in a reasonable amount of time. As many of the measurements rely on information gained in previous steps and some of the measurements involve cleaving or etching the substrate, the particular order of measurements is important.

The characterization sequence for films deposited by the IFIC system actually begins prior to the deposition itself. The first step in this sequence is measuring the curvature of the pre-deposition substrate using the Tencor FLX-2320 as described in **Section 3.2.3**. As mentioned in that section, this measurement may actually lead to some wafers being removed from further testing due to unusual curvatures that make stress calculations unreliable. Once a wafer is measured and approved, it can be processed using the SOP described in the previous section.

The first characterization test carried out after the deposition is ellipsometry, using the J.A. Woollam M-2000S VASE (**Section 3.2.2**). Ellipsometry provides the film's thickness and index of refraction. These numbers give a good first indication of the properties of the film, and in the case of the initial testing of a deposition process, can determine whether further characterization is warranted.

The thickness information gained from ellipsometry is then used as an input to the average film stress measurement, again using the FLX-2320. The curvature of the film-deposited wafer is measured, and using Stoney's formula the average film stress is calculated.

After the stress measurement, the uniformity of the deposition is measured using the KLA-Tencor UV1250SE in its reflectometry mode. The index of refraction information gathered from ellipsometry is used to create a material model in the UV1250SE, and using that model the thickness is measured at a variety of points using an automated X-Y stage. The standard recipe used for this step measures the film thickness at 25 points distributed across the wafer, and uses a 4 mm edge exclusion distance. The pattern can be seen in **Figure 3.11** in **Section 3.2.4**. The gathered thickness data can then be used to calculate various uniformity metrics (most commonly Uniformity and coefficient of variation) and construct contour maps. Additional measurements using different patterns or edge exclusions may also be run at this time if needed.

After the UV1250 measurements, any non-destructive supplementary measurements can be performed. These include FTIR and surface profiling techniques like AFM and white light interferometry that were performed on select samples. SEM imaging can also be done at this stage as long as cleaving the wafer is not required for sample preparation. Breakdown field measurements, which require additional sample preparation steps (see **Section 3.2.7**), can also be carried out at this time[20].

---

[20] Breakdown field measurements require using highly-doped wafers and depositing aluminum as a contact material, making the wafers prepared for this measurement incompatible with BOE etching [131] without further processing (which was not done for the data presented here).

Following these supplementary measurements, the samples were etched in a 7:1 BOE solution and the etch rate was measured at several points using a Veeco Dektak stylus profilometer. This is, of course, a destructive process, and also requires the application and removal of photoresist so any sensitive surface or chemical measurements should be performed before this step to avoid including spurious signals from the etch sequence (see **Section 3.2.5** for more details).

3.4 Conclusions

The experimental methods and analysis techniques described in this chapter allow the performance of the Inch Fab ICP-CVD to be reliably characterized and benchmarked against commercial systems. Test results on some of the critical aspects of the systems gained by using these methods were presented, and the details and reliability of the major film deposition measurement methods were evaluated. The following two chapters will utilize these methods to understand the deposition of two dielectric materials essential to micro- and nanoscale device manufacturing, silicon dioxide and silicon nitride.

Chapter 4: Silicon Dioxide Deposition

As discussed previously in **Chapter** 1, silicon dioxide thin films can be deposited using a wide variety of methods. The choice of a particular method largely depends on the end-use for the film, as well as any constraints imposed by previous and future steps in the fabrication method. ICP-CVD occupies a unique position amongst the other SiO_2 deposition techniques, offering significantly lower deposition temperatures than thermal oxidation, LPCVD, and PECVD, faster deposition rates than thermal oxidation and LPCVD, and better film quality than PECVD. Even with these advantages, in order to be a useful processing tool, an ICP-CVD system must also be able to produce uniform, consistent films both intra-wafer and inter-wafer, and be flexible enough to produce films with properties tailored to the desired application. To verify that these characteristics and capabilities could also be achieved in the 1" Fab ICP-CVD (IFIC) system, a series of experiments were performed to explore the parameter space, establish a reliable processing window, understand how each of the input parameters affect the films, develop a quantitative model for predicting the output characteristics of the films, and finally, validate that model. This chapter describes the results and insights gained from these experiments.

4.1 Early Testing

The SiO_2 characterization process began by examining the literature for recipes utilized in existing systems. These recipes were catalogued and analyzed to establish a range of reasonable parameters for SiO_2 deposition. Most of the recipes found use 100% SiH_4 for the silicon feedstock (recipes using the liquid precursor TEOS are not considered here), but one set of papers described films produced using 5% SiH_4 (diluted in He) using a Sentech SI 500 D ICP-CVD reactor [32], [71]–[73], which is much closer to the 1.5% SiH_4 (diluted in He) mixture used in the IFIC system. The parameters found in these papers were very helpful in establishing a reasonable starting point for SiO_2 depositions.

4.1.1 Stabilizing Deposition Parameters

The initial deposition tests revealed several important pieces of information about the 1" Fab ICP-CVD's performance. Firstly, they provided essential information about plasma striking and matching conditions (ICP powers greater than 250 W and an adjustment of the shunt capacitance range of the automatic matching network were needed to maintain a stable discharge). Secondly, the initial tests alleviated the initial concern that the large amount of helium diluent in the silane mixture might screen out or hinder the transport of the other process gases to the substrate, and lead to very slow deposition rates. The earliest films showed deposition rates between 30 and 40 nm/min, which was well above the goal of 20 nm/min.

The third discovery from the initial tests was that the recipes being used were producing very Si-rich SiO_2 films, which was determined by measuring the films' index of refraction (n) using variable-angle spectroscopic ellipsometry (see **Section 3.2.2** for the ellipsometry procedure). Index values at 632-633 nm (the typical wavelength used for reporting n) ranged from 1.61 to 1.66, compared to the ~1.45-1.46 typically seen in stoichiometric oxide films [74], [75]. The ratio of O_2 to SiH_4 is the primary parameter by which the index of refraction can be modulated (see **Section 4.3.2.2**), and follow up tests showed that by increasing this ratio from 1.5-2.0:1 to > 2.5:1 restored the index to ~1.46. The minimum O_2/SiH_4 ratio of ~2.5:1 for producing films with $n \approx 1.46$ matches the ratio reported in [50], but several other sources have reported lower ratios (~1.25:1 in [6], ~1.23:1 in [71], ~2.0:1 in [76]) for $n \approx 1.46$. One possible explanation is a difference in the concentration of reactive O* species created by the ICP source in the IFIC versus other systems. This could stem from the use of N_2O versus O_2, or from larger or more efficient power coupling into the reaction chamber. Optimization of the two-turn helical ICP source used in the IFIC system could potentially lower this ratio to be more in line with existing systems, but there

has been no evidence uncovered that would suggest shifting this ratio would have any positive effect other than lowering the already very small amount of O_2 used for deposited[21].

4.1.2 Chasing Uniformity

The final major discovery from early tests was significant spatial non-uniformity in the deposited film thickness. This non-uniformity was evident from variations in the color of the film, and confirmed with ellipsometry and SEM measurements. Films were thickest in the center of the wafer, and traveling radially from the center gradually became thinner. Near the edge of the alumina clamp, the thickness dropped off quickly to zero. **Figure 4.1a** shows a photo of a sample with this non-uniformity. Several different tests were undertaken to try and identify the source of this non-uniformity. Possible culprits included edge or shadowing effects from the mechanical substrate clamps, temperature variations on the substrate, spatial variation in the process gases in the chamber, or spatial variation of the reactive species generated in the plasma discharge itself. Each of these possibilities were explored.

4.1.2.1 Possible Causes

First, the effect of the alumina mechanical clamp ring was tested by carefully running samples without this ring (unclamped). Without the clamp, backside helium flow was not possible, and so extra time (20 minutes) was allowed after the sample was loaded from the load lock into the process chamber for the temperature to fully equilibrate. (Process-induced temperature variations could not, of course, be mitigated during these tests, but the goal was to isolate the effect of the clamp). Visually inspecting the samples showed that while the clamp has a dramatic short range effect in the first 2-4mm from the clamp edge, the longer range non-uniformity still remained. (Quantitative measures of this non-uniformity are presented in **Figure 4.5** and **Figure 4.6**). **Figure 4.1** shows a comparison of clamped versus unclamped samples.

---

[21] In fact, lowering the amount of O_2 needed for depositions could actually increase the cost of the system as mass flow controllers tend to increase in price at ultra-low full-scale flow (typically < 20 sccm) values.

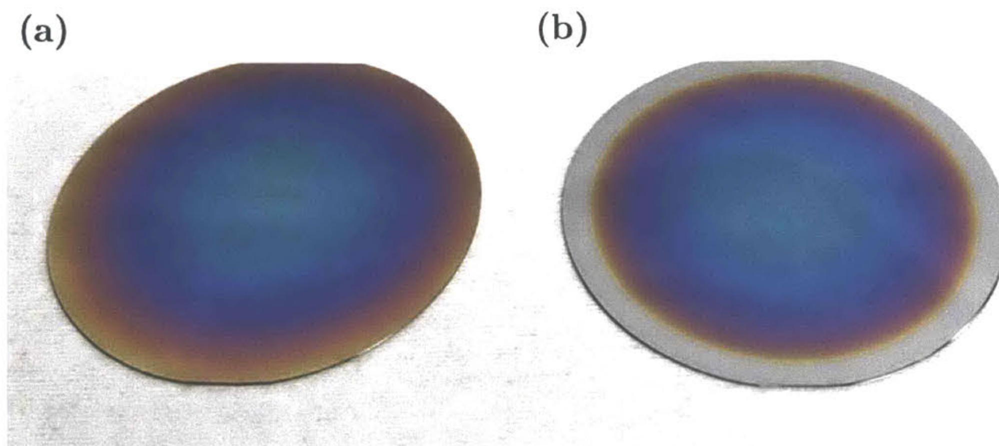

Figure 4.1: (a) SiO_2 deposition without mechanical clamp; (b) SiO_2 deposition with mechanical clamp (1.75" (44.5 mm) diameter aperture).

Two further tests, in which the samples were directly clamped to a large aluminum thermal mass (~100 g, roughly 3 times largely than the standard puck chuck) using small 2-56 PEEK pan-head screws were carried out to reduce the effect of any deposition process-induced heating of the samples. The first test featured the wafer clamped in the middle of thermal mass, and the second clamped the wafer in an off-center position. The wafers after deposition are shown in **Figure 4.2**. The centered wafer (**Figure 4.2a**) shows the same long-range non-uniformity seen in the unclamped sample of **Figure 4.1b**, while the off-center wafer exhibits a similar uniformity profile but centered toward the center of thermal mass and chuck (and thus the center of the vacuum chamber).

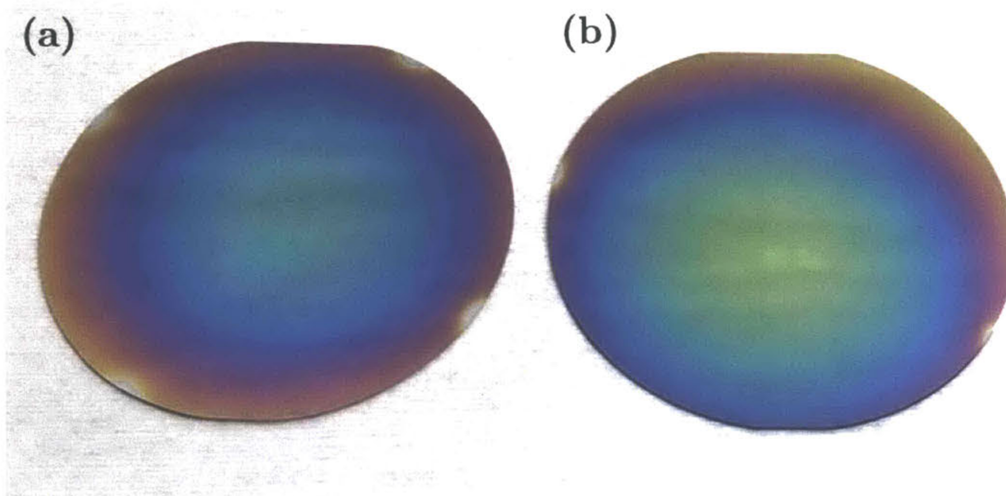

Figure 4.2: (a) SiO_2 deposition on wafer centered on large thermal mass; (b) SiO_2 deposition of wafer placed off-center on large thermal mass.

The results of **Figure 4.1** and **Figure 4.2** indicate that while there is a shadowing effect from masking elements, there exists a more prevalent effect related to either the plasma or process gas spatial distribution.

The upper flange installed in the UCA (see **Section 2.3.2**) for early testing featured a single, centrally-located gas entry point. To test whether this single gas entry point was causing the non-uniformity, the upper flange was replaced with one containing a gas distribution showerhead attached to the underside of the flange. This showerhead divided the incoming precursor gas into six evenly spaced injection points at a radius of 1" (25.4 mm) from the center of the flange. This spatial distribution of the precursor gas did not, however, lead to any noticeable improvement in the radial uniformity of the deposited film. While this was a negative result in terms of determining the cause of the radial non-uniformity, it actually provided a confirmation that the installed showerhead was producing a spatial gas distribution that did not significantly alter the otherwise good axial symmetry of the deposited film[22]. There was no similarly straightforward way of testing the SiH_4 gas ring for uniformity, but again the axial symmetry of the deposited films suggest that this distribution was unlikely to be a major cause of the radial non-uniformity.

With the other causes ruled out, spatial variation in the plasma discharge itself then remained as the source of the non-uniformity. Radial non-uniformity in the density of reactive species of a plasma discharge is a well-known phenomenon [77]–[79], and a variety of different methods to counteract this are found in both the literature and in commercial systems. Two of these methods, magnetic multipole confinement and aperture plates, were explored as solutions for the non-uniformity observed in the IFIC system.

[22] Having a gas showerhead installed in the upper flange has the additional advantage of freeing up the central portion of the flange. This area was fabricated with a 1.33" CF pattern, which allows an additional monitoring or diagnostic accessory such as a viewport (for sample imaging or OES), Langmuir probe, or pressure transducer to be easily incorporated into the system.

4.1.2.2 Magnetic Multipole Confinement

Magnetic multipole confinement (MMC) is a technique used in plasma-based processing tools to increase the plasma density and radial uniformity [78], [80]. MMC involves adding a ring of permanent magnets around the chamber with alternating north and south poles. This forms what is known as a "line cusp" configuration, which results in a strong magnetic field near the walls of the chamber that is essentially axially symmetric, but decays radially in intensity away from the walls (see Figure 5.6 in [78] or Figure 6 in [79]). This strong magnetic field limits the diffusion of charged particles to the chamber walls, effectively reflecting these particles back toward the center of the chamber, increasing both the density and the uniformity of the plasma discharge [77]–[79], [81]. An example of the results of implementing of an MMC configuration in an ICP-based plasma system is shown in Figure 2 of [80], reproduced below as **Figure 4.3**.

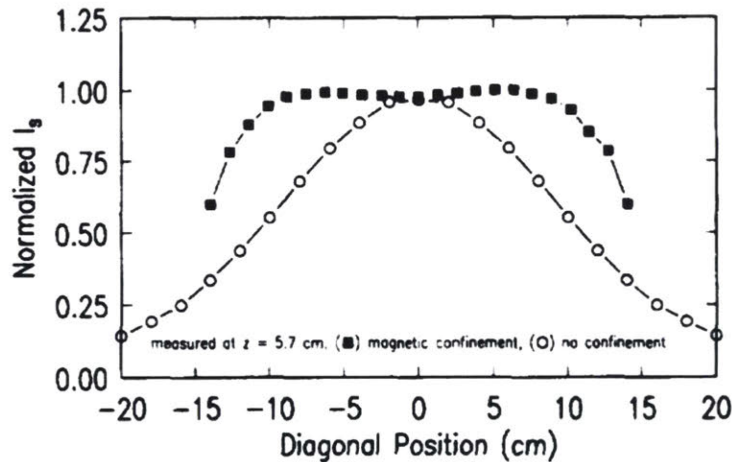

Figure 4.3: Demonstration of the effect of MMC on the ion saturation current (which is proportional to the plasma density [78]). Both the density and uniformity are improved. Figure reproduced from [80].

In a typical commercial ICP-based processing chamber implementing some form of MMC, the dimensions of the chamber (particularly the diameter) are significantly larger than the maximum substrate size it is designed to process. This extra size is necessary to account for the width of the diffusion barrier region induced by the MMC configuration, which has a very low plasma density. The region in the middle of the chamber where the plasma is more uniform (the MMC "field-free" region), can be increased by sharpening the transition between it and the diffusion

barrier region (by optimizing the size, strength, and number of magnets used in the line cusp geometry [81], [82], but the width of the diffusion barrier remains. This can be seen in **Figure 4.3**, as the density is more uniform in the middle ~200 mm of the chamber, but rolls off dramatically as the diffusion barrier region is breached. Experimental [81] and simulation [82] results also show that there is a steep roll-off at the barrier.

The minimum barrier width found in the literature was 20 mm [82], which is approximately three times larger than the extra space available between the IFIC chamber wall (diameter ~73 mm) and the edge of the SCA (diameter ~61 mm). Even in the SCA diameter matched that of the 2" (50.8 mm) wafers used for testing, this would only leave 10.5 mm of extra space for the diffusion barrier. Despite this dimensional hurdle, several different MMC configurations featuring a wide variety of different magnet sizes and strengths were tested to see if they improved deposition uniformity, but no quantitative advantages were observed for any of the tested configurations. It was thus concluded that the current dimensions of the IFIC UCA are too small to make an effective MMC configuration feasible. If future revisions of the UCA expand the chamber diameter, MMC will be revisited as a potential uniformity solution.

4.1.2.3 Aperture Plates

The second method for rectifying the plasma density uniformity problem (and the one ultimately implemented in the IFIC) uses what have been called aperture or baffle plates to control the distribution of reactive species seen by the substrate [83]–[86]. The plates have both solid and open regions that block and permit flux, respectively, and the regions are carefully positioned to produce the optimal deposition profile. This approach has the advantages of being very simple and inexpensive to implement, but since the plates operate by obstructing flux to particular regions, their use does come at the cost of a reduced overall deposition rate. Fortunately however, achieving the maximum possible deposition rate is nearly always secondary in importance to producing films with a uniform thickness profile. Like other helical ICP sources, the IFIC plasma discharge is densest in the center of the chamber (which, in **Section 4.1.2.1**, was suggested to be the most likely cause of the non-uniform film profile of early depositions),

and so the IFIC aperture plates have less open area in the middle of the plate and more open area near the edge to counteract this density non-uniformity and help equalize the spatial distribution of reactive precursor gases seen by the substrate. The actual plate design used can be seen in **Figure 4.4**.

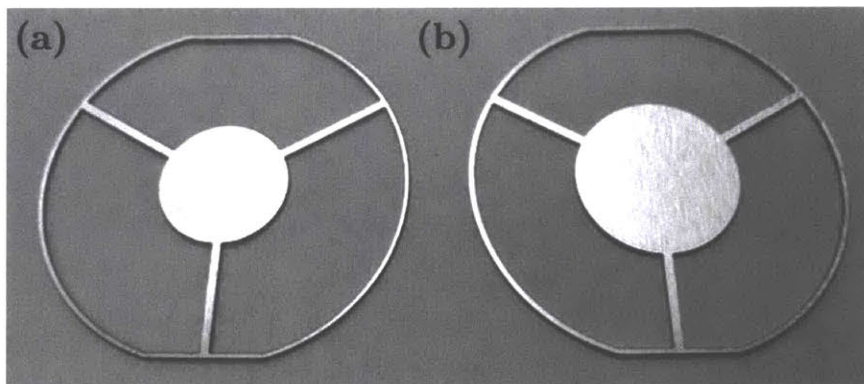

Figure 4.4: Aperture plates with varying center diameters. (a) AP0.75; (b) AP1.25.

Design goals for this plate were to have something that was both easy to fabricate and simple to insert and remove from the system. The plates were cut from 0.04" (1 mm) thick 6061 aluminum using a waterjet cutter and cleaned using the standard cleaning process outlined in **Appendix A**. A single plate takes less than 5 minutes to fabricate, between cutting on the waterjet and sanding to remove any remaining burs or surface roughness. The flats on the sides of the plate allow it to be inserted vertically from the bottom of the UCA and then rotated 90 degrees to rest horizontally on the "ledge" provided by the lower flange, ~0.25" (6.35 mm) above the integrated silane gas ring[23]. The three legs supporting the central circle are very thin (0.08" (2 mm)) to minimize the amount of flux they block. The size of the central circle was a primary variable used in optimizing the aperture plate design, along with its spacing relative to the substrate. Data from this optimization process can be seen below in **Figure 4.5** and **Figure 4.6**.

[23] Specifically, it sits on top of the inner wall of the O-ring groove that seals the quartz cylinder to the lower flange. Spacer rings can be similarly fabricated and added in the same manner as the aperture plate to adjust its height, but no spacers are used in the current design.

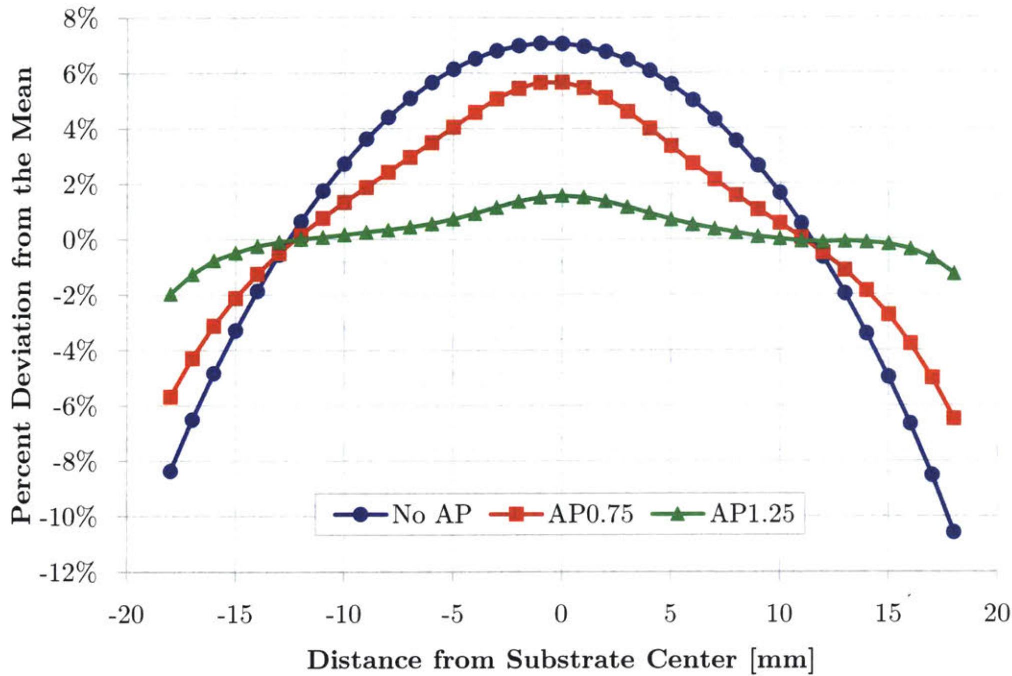

Figure 4.5: Percent deviation from the mean film thickness across the wafer as a function of the central dimension of the aperture plate. The edge exclusion is 4 mm in each scans.

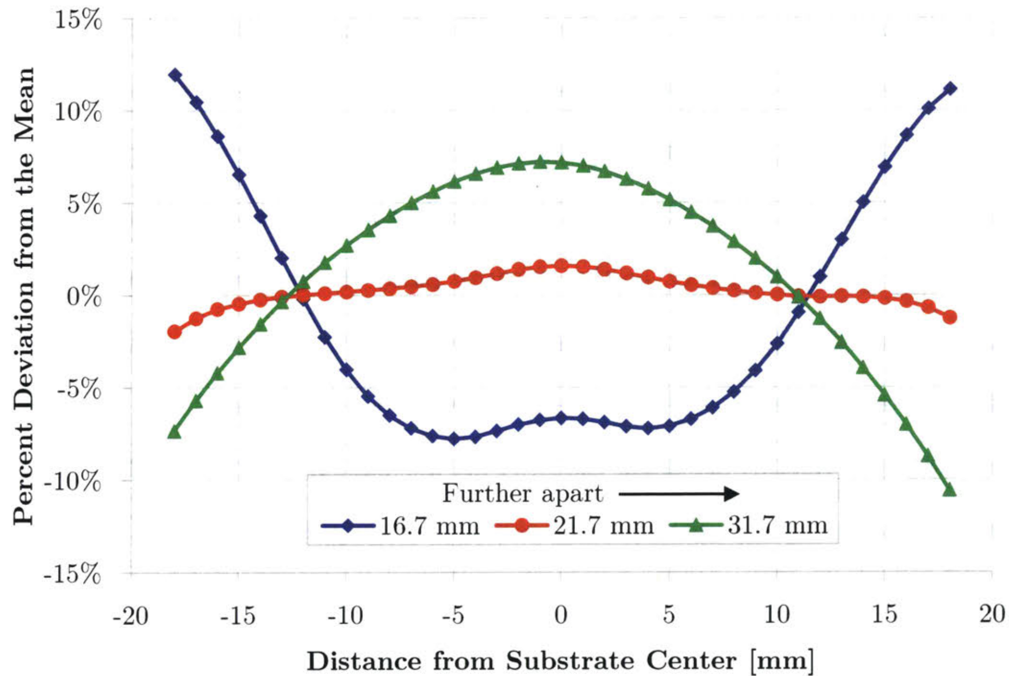

Figure 4.6: Percent deviation from the mean film thickness across the wafer as a function of the spacing between the wafer and aperture plate (AP1.25, 1.25" center diameter). The edge exclusion is 4 mm in each scan.

Figure 4.5 shows uniformity profiles for samples with and without aperture plates. This data was taken using spectral reflectometry, using the process outlined in **Section 3.2.4**. The

spatial data produced by these scans is often reduced in the literature to a single value known eponymously as "uniformity", and capitalized as "Uniformity" from this point forward. Uniformity is essentially a worst case metric that takes the difference between the thickest and thinnest sections of the film and divides by twice the mean film thickness to produce a number in the form of ±X% that described the full variation in film thickness.

$$Uniformity = \left(\frac{height_{max} - height_{min}}{2 \times (height_{mean})}\right)$$

It is clear that the plate with a 1.25" diameter central circle (AP1.25) is a dramatic improvement over both the 0.75" (AP0.75) and no aperture plate cases, reducing the deposition Uniformity to ~2.8%, markedly better than the AP0.75 (9.3%) and no-plate cases (11.4%)[24]. Using the AP1.25 plate, further tests were then run to fine-tune the uniformity by modulating spacing between the plate and the substrate. These tests were very quick to perform as the design of the LCA's lift assembly allows the spacing to be set continuously in-situ by translating the SCA up and down along the system's vertical axis which, unlike changing aperture plates, does not require venting the chamber, can be completed in just a few seconds, and is easily automatable. When the substrate is too far away, the profile begins to look like the no-plate case (although the overall the deposition rate remains much lower), while placing the substrate to close to the aperture causes the thickness profile to invert, as the aperture plate blocks too much of the O_2, reducing the deposition rate relatively to the edge region. The spacing resulting in the least non-uniformity (lowest Uniformity value) for SiO_2 after this testing was found to be 21.7 mm (see **Figure 4.6**), which can be easily and reliably set using the SCA lift mechanism (**Section 2.3.1**), and was kept constant throughout the tests described in the rest of this chapter.

[24] The Uniformity values were calculated from a full 2D scan of the film (4 mm exclusion zone). Line scans are shown in **Figure 4.5** and **Figure 4.6** to more easily compare the results from different tests.

4.2 Establishing a Process Window

With the index of refraction and uniformity problems resolved, the next step in understanding the operation of the IFIC was establishing a reliable window of operation for all of the relevant adjustable parameters in the SiO_2 deposition process. Parameters tested included the relative spacings of the precursor gas showerhead, ICP coil, aperture plate, silane gas ring, and substrate, the flow rates and ratios of SiH_4 and O_2, the applied ICP power and substrate power, the substrate temperature, and the process pressure. The output characteristics used to assess the effects of these parameters were deposition rate, index of refraction, average film stress, etch rate in 7:1 BOE, and film thickness uniformity. The standard characterization sequence in which these data were gathered for each samples was outlined in **Section 3.3.2**. The trends uncovered from these experiments (along with subsequent testing) populate **Table 4.1**.

	Deposition Rate	Index of Refraction	Average Film Stress	BOE Etch Rate Ratio	Uniformity
↑ ICP Power	↑	↓	↑	↓	—
↑ Bias Power	↓	—	↑	↓	—
↑ O_2/SiH_4 Ratio	↑	↓	varies	↑	—
↑ Temperature	↓	—	↑	↓	—
↑ Pressure	—	—	↓	↑	—
↑ Substrate-to-AP gap	↓	varies	↓	↑	↓

Table 4.1: The effect of increasing input parameters on output SiO_2 film characteristics. A dash indicates a small or negligible effect over the range tested.

Valuable information was also gained about the reasonable range of parameter values for films of good quality. These ranges and the explanations for their values are summarized in **Table 4.2**.

Parameter	Process Window	Below This Range	Above This Range
ICP Power	200 – 350 W	Plasma discharge difficult to maintain	Excess chamber heating
Bias Power	0 – 5 W	n/a	High average film stress
O_2/SiH_4 Ratio	2.5:1 – 5:1	Si-rich films, $n > 1.5$	Low-density films
Temperature	25°C – 150°C	n/a	Reduced material compatibility
Pressure	5 – 100 mTorr	Plasma discharge difficult to maintain	Low-density films, pressure control difficult
Substrate-to-Aperture Plate Gap	21 – 24 mm	Poor uniformity	Low deposition rate, poor uniformity

Table 4.2: Process window for stable SiO_2 depositions.

With the basic understanding of the IFIC system's performance now acquired, a more thorough, quantitative understanding was pursued through the use of statistical design-of-experiments techniques.

4.3 Response Surface Testing

Having a qualified recipe is great, but it is even better to have a predictive model that can produce custom recipes that need little or no optimization, particularly in multi-user, R&D-type settings where film requirements frequently vary dramatically. To construct such a model for SiO_2 depositions in the IFIC, a design-of-experiments (DOE) technique known as the response surface method (RSM) was employed. A primer on RSM testing and the particular sub-type used here (the central composite design) can be found in **Section 3.2.1**.

4.3.1 RSM Parameter Selection

As demonstrated in **Section 4.2**, the IFIC has a large number of potential factors that affect the characteristics of produced SiO_2 films, and could be used in a potential circumscribed CCD test sequence. **Table 4.3** shows how the number of factors included in a circumscribed CCD

affects the total number of tests needed, as well as the α values needed for rotatable or orthogonal designs.

Factors	**Cube Block**	**Star Block**	**Center Point (varies)**	**Total Tests**	α **Rotatable**	α **Orthogonal**
2	4	4	4	12	1.414	1.414
3	8	6	6	20	1.682	1.633
4	16	8	6	30	2.000	2.000
5 (half-factorial)	16	10	7	33	2.000	2.000
5 (full-factorial)	32	10	10	52	2.378	2.428
6 (half-factorial)	32	12	10	54	2.378	2.366
6 (full-factorial)	64	12	14	90	2.828	2.828

Table 4.3: Number of experiments needed and α values for CCD RSM sequences of various sizes.

As **Table 4.3** shows, even using the fractional factorial configurations allowed by CCD RSM designs, the number of experiments required quickly accelerates as the number of factors being tested increases. Given the time required to carry out and analyze the data, an RSM sequence including all of the factors affecting the SiO_2 films was simply not feasible. After scrutinizing the results of the process window tests, a CCD design using four factors was selected. The four factors chosen were the O_2 flow, the RF power applied to the substrate, the system pressure, and the substrate temperature. Each of these four factors play a significant in the properties of the deposited SiO_2 films, and are each can be very easily and reliably adjusted. For the RSM sequence, the other input parameters were kept at constant values near the middle of the range established by the process window tests. These values are shown in **Table 4.4**.

Parameter	Value	Notes
ICP Power	300 W	This value was found to reliably sustain a plasma discharge, produce reasonable deposition rates, and did not induce excessive chamber heating.
SiH_4/He Flow	100 sccm	1.5 sccm of SiH_4 equivalent. This value was kept constant and the O_2 flow was varied to adjust the film parameters.
Aperture Plate	AP1.25	This aperture plate has a 1.25" diameter center circle and was found to produce the most uniform films.
Substrate-Aperture Plate Spacing	21.7 mm	This distance produced the most uniform films.
Substrate Backside Helium Pressure	20 torr	This pressure provides sufficient heat transfer from the SCA to the substrate and does not cause a He leak to from the SCA to the chamber.
Test Time	10 minutes	This value was chosen to produce films with sufficient thickness for post-processing measurements while not requiring large amounts of processing time.

Table 4.4: Constant parameters used for the SiO_2 RSM test sequence.

The actual RSM test sequence was generated using R, an open-source statistical analysis platform, and the RSM package for R developed by Russell Lenth [87]. This software package allows a variety of RSM-style DOE sequences to be generated and analyzed quickly. Using the *ccd.pick* and *ccd* functions from this package, a four factor CCD design with 30 total tests was selected. **Table 4.5** shows the full list of parameters and their values for the test sequence.

Standard Order	Run Order	Block	Test Type	(Coded Values) F1	F2	F3	F4	(F1) O_2 Flow [sccm]	(F2) Pressure [mTorr]	(F3) Temperature [°C]	(F4) Bias Power [W]
1	8	1	Cube	-1	-1	-1	-1	4	36	75	0
2	17	1	Cube	1	-1	-1	-1	6	36	75	0
3	11	1	Cube	-1	1	-1	-1	4	60	75	0
4	2	1	Cube	1	1	-1	-1	6	60	75	0
5	14	1	Cube	-1	-1	1	-1	4	36	125	0
6	6	1	Cube	1	-1	1	-1	6	36	125	0
7	18	1	Cube	-1	1	1	-1	4	60	125	0
8	12	1	Cube	1	1	1	-1	6	60	125	0
9	16	1	Cube	-1	-1	-1	1	4	36	75	3
10	10	1	Cube	1	-1	-1	1	6	36	75	3
11	9	1	Cube	-1	1	-1	1	4	60	75	3
12	1	1	Cube	1	1	-1	1	6	60	75	3
13	13	1	Cube	-1	-1	1	1	4	36	125	3
14	4	1	Cube	1	-1	1	1	6	36	125	3
15	19	1	Cube	-1	1	1	1	4	60	125	3
16	5	1	Cube	1	1	1	1	6	60	125	3
17	3	1	CP	0	0	0	0	5	48	100	1.5
18	7	1	CP	0	0	0	0	5	48	100	1.5
19	15	1	CP	0	0	0	0	5	48	100	1.5
20	20	1	CP	0	0	0	0	5	48	100	1.5
21	27	2	Star	-2	0	0	0	3	48	100	1.5
22	25	2	Star	2	0	0	0	7	48	100	1.5
23	24	2	Star	0	-2	0	0	5	24	100	1.5
24	23	2	Star	0	2	0	0	5	72	100	1.5
25	29	2	Star	0	0	-2	0	5	48	50	1.5
26	30	2	Star	0	0	2	0	5	48	150	1.5
27	22	2	Star	0	0	0	**-.5**	5	48	100	**0.75**
28	26	2	Star	0	0	0	2	5	48	100	4.5
29	21	2	CP	0	0	0	0	5	48	100	1.5
30	28	2	CP	0	0	0	0	5	48	100	1.5

Coding Formulas

$CP_{O_2} = 5$ sccm	$\Delta_{O_2} = 1$ sccm	$O_2\ Flow = (\text{Coded Value})\Delta_{O_2} + CP_{O_2}$
$CP_{Press} = 48$ mTorr	$\Delta_{Press} = 12$ mTorr	$Pressure = (\text{Coded Value})\Delta_{Press} + CP_{Press}$
$CP_{Temp} = 100$°C	$\Delta_{Temp} = 25$°C	$Temperature = (\text{Coded Value})\Delta_{Temp} + CP_{Temp}$
$CP_{BP} = 1.5$ W	$\Delta_{BP} = 1.5$ W	$Bias\ Power = (\text{Coded Value})\Delta_{BP} + CP_{BP}$

Table 4.5: RSM test sequence for SiO_2. Also shown are the equations and valued needed to convert factors from coded to actual units.

This design features the standard 16 (2^4) axial tests and the 8 (2×4) star tests, plus 6 center point tests to test for repeatability and curvature in the fitted models. Conveniently, the alpha (α) value for this design is 2.0 for both a rotatable and orthogonal design. In the RSM package, the factor values for design sequences are coded to a general 0, +1, -1, +α, -α format, and so to convert between these coded values and the factor values in their respective units of measure, the formulas found at the bottom of **Table 4.5** can be used.

The methodology behind the selection of the center point and delta values was to be broad enough that each of the output responses could provide statistically significant and useful results, but not so broad as to include too many tests that were either not possible or known to produce films with undesirable characteristics. For the values chosen, only one test falls into that latter category, the -α test for bias power. Using the given center point and delta values produces a bias power value of -1.5 W for this test, which is not possible since only positive power values can be delivered to the substrate electrode. The process window tests showed that bias power has a significant effect on the average film stress observed in the SiO_2 films, and that applying no power (0 W) was a very good way to keep the film stress below the 300 MPa threshold often used to delineate low-stress SiO_2 films [6], [50]. However, it was also determined in these early tests that applying bias power could improve the BOE etch rate of films. It was thus desirable to construct the test sequence such that multiple samples would be run both with zero and non-zero bias power settings (instead of picking either a large center point bias value and having only the -α test reach 0 W, or removing bias power as a factor altogether). As a result, it was decided that the -α bias power test would be replaced with a test using a bias power of 0.75 W (coded form: +0.5Δ). This change is highlighted in the RSM test sequence shown in **Table 4.5**. The table is shown in the "standard order" for clearness, but the tests were carried out in the randomized order shown by the second column. Tests were split into two blocks, which were run on consecutive days. Block effects were considered in the analysis but found to be small relative to the other factors. The absence of major block effects was also corroborated by the repeatability study discussed later in **Section 4.3.3.3**.

4.3.2 RSM Results

After completing the 30 RSM tests, each of the samples were thoroughly characterized using the sequence described in **Section 3.3.2**. The quantitative results from the tests are shown in **Table 4.6**.

Standard Order	Deposition Rate [nm/min]	Index of Refraction	Average Film Stress [MPa]	Coefficient of Variation [%]	Uniformity [%]	BOE Etch Rate Ratio
1	28.60	1.444	-283.6	1.54%	3.32%	3.13
2	41.37	1.457	-282.6	1.63%	2.74%	16.43
3	30.23	1.464	-282.2	1.55%	2.63%	6.01
4	41.19	1.461	-208.3	1.82%	3.06%	16.73
5	27.98	1.425	-225.7	1.72%	4.22%	2.05
6	35.96	1.445	-356.9	1.47%	2.54%	13.86
7	28.38	1.450	-187.6	1.45%	3.16%	2.51
8	36.03	1.462	-292.5	1.75%	3.08%	14.55
9	31.61	1.435	-526.9	1.36%	2.67%	1.60
10	38.80	1.457	-510.3	1.44%	2.44%	9.28
11	30.48	1.464	-417.9	1.60%	3.13%	1.98
12	39.64	1.467	-431.5	1.65%	2.87%	15.28
13	28.58	1.440	-463.5	1.50%	2.89%	1.31
14	35.40	1.448	-654.9	1.50%	2.68%	2.94
15	29.90	1.454	-469.3	1.76%	3.77%	1.64
16	35.63	1.467	-549.5	1.69%	3.06%	8.47
17	33.94	1.455	-468.3	1.50%	2.71%	5.78
18	33.81	1.455	-513.4	1.42%	2.62%	5.54
19	34.36	1.458	-476.3	1.44%	2.69%	5.27
20	35.98	1.455	-457.6	1.41%	2.50%	5.63
21	23.09	1.539	-276.7	1.47%	2.58%	0.87
22	41.68	1.463	-341.6	1.75%	3.06%	17.01
23	31.51	1.441	-676.3	1.55%	3.78%	2.24
24	35.21	1.468	-456.6	1.73%	3.12%	9.46
25	39.93	1.466	-432.5	1.57%	2.79%	14.14
26	31.79	1.450	-610.9	1.41%	2.87%	2.35
27	35.55	1.458	-455.5	1.39%	2.33%	8.84
28	35.03	1.464	-675.6	1.38%	2.46%	3.06
29	34.97	1.462	-493.7	1.35%	2.47%	5.46
30	35.23	1.456	-526.5	1.33%	2.49%	5.62

Table 4.6: Raw results for each sample in the SiO_2 RSM test sequence

This dataset was loaded in R and fitting algorithms were applied to each of the measured response variables using the *rsm* function. First-order, second-order, and two-factor interaction terms can be included in these fits. Data on the quality of the fit, including an ANOVA table, is generated automatically alongside the coefficients. In the following sections, these results and fits will be analyzed.

4.3.2.1 Deposition Rate

The early tests and the process window tests indicated a strong positive relation between the SiO_2 deposition rate and the input O_2 flow, and a moderate negative relation with the substrate temperature. These trends agree with the existing literature [21], [50], and were also seen in the RSM results. A second order model including two-factor interactions was found to fit the RSM data very well (lack of fit p-value = 0.49). The coefficients for this fit are below[25], followed by surface/contour plots showing the parameter relationships. The average residual between the collected data and the fitted model is 0.55 nm/min, with an average percent error of 1.65%. The standard residual deviation is 0.66 nm/min.

O_2 Flow	Pressure	Temperature	Bias Power	$\left(O_2\ \text{Flow}\right)^2$	$(\text{Pressure})^2$	$(\text{Temperature})^2$	$\left(\text{Bias Power}\right)^2$
4.352	0.483	-1.639	0.054	-0.679	-0.435	0.190	-0.027

$O_2 \cdot$ Press	$O_2 \cdot$ Temp	$O_2 \cdot$ BP	Press · Temp	Press · BP	Temp · BP	Block	Intercept
-0.016	-0.681	-0.591	-0.009	-0.104	0.064	0.537	34.068

Table 4.7: Fit coefficients for second-order model for deposition rate.

[25] The function produced by the coefficients in **Table 4.7** takes coded parameter values as inputs.

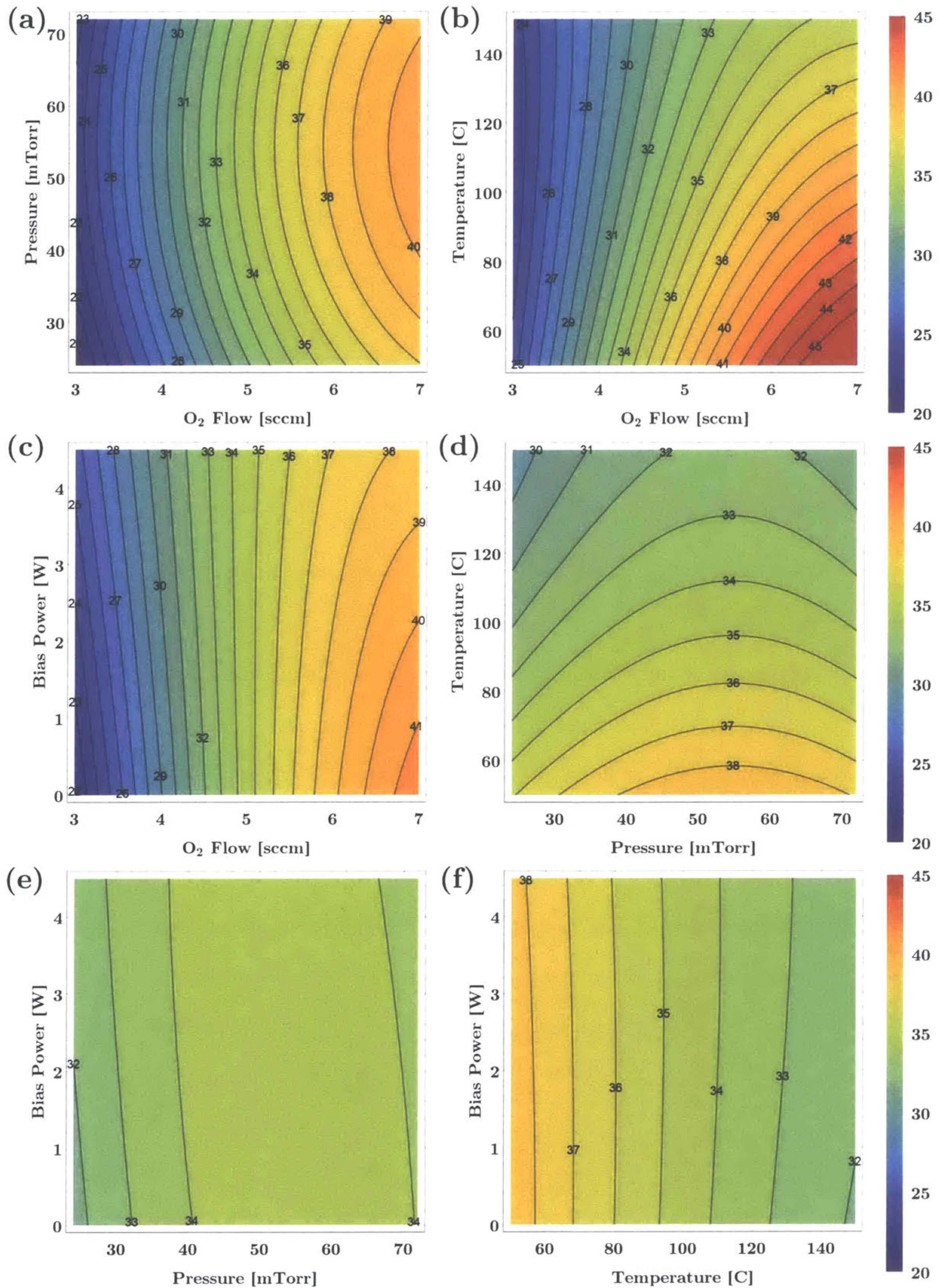

Figure 4.7: Contour plots showing deposition rate vs. pairs of input factors. Each graph is evaluated at the center point values of the factors not shown. Contours are equal across all plots.

The matched color scales seen in **Figure 4.7** makes it easy to see that the O_2 flow plays the largest role in determining the deposition rate. The gradual slopes in the temperature axes of **Figure 4.7b**, **4.7d**, and **4.7f** also show the slight negative effect of increasing temperature. Compared to higher temperature SiO_2 processes like LPCVD and oxidation, the low temperatures of ICP-CVD are not sufficient to cause thermal dissociation of SiH_4. In this lower-temperature regime, an increasing substrate temperature serves to decrease the likelihood of adsorption of reactive species [21], [88]. Once on the surface, an increased temperature helps overcome the activation energy for the deposition reaction, but also improves the surface mobility, which leads to overall denser films (i.e. a lower thickness deposition rate for an equivalent mass deposition rate).

The relatively flat surface of the contour plot featuring the other two factors, pressure and bias power (**Figure 4.7e**), shows the smaller impact these factors have on deposition rate. This small effect also holds for other evaluation points. An accurate prediction of the deposition rate for a particular process is one of the most important things to know when planning out a fabrication sequence, but as noted previously, it is not typically something that needs to be maximized for non-production applications. For a relatively large film thickness of 1 μm, the range of rates observed in these tests leads to a difference of at most 19 minutes (~43 minutes vs. ~24 minutes). Considering the time needed for sample preparation, loading/unloading, and thermal equilibration, this difference is minor. If faster depositions are necessary, turning up the O_2 flow or reducing the substrate temperature will produce larger rates, but, as will be discussed in the following sections, this can also lead to deficiencies in other film qualities[26].

[26] As discussed in **Table 4.1**, if the absolute deposition rate must be raised, the ICP Power or overall gas flow can be increased, but the full effect of these changes on all of the output parameters was not explored as part of the RSM sequence described here.

4.3.2.2 Index of Refraction

The generally accepted index of refraction (at 632-633 nm) value for stoichiometric, thermally-grown SiO_2 films is ~1.45-1.46 [74], [75]. The early testing of the IFIC (**Section 4.1**), produced Si-rich films with larger indexes (1.55-1.65), but it was quickly discovered that this could be rectified by increasing the ratio of O_2 flow to SiH_4/He flow. As the ratio increases above 2:1, the index deposited films decreases to ~1.46 and remains near that level for increasing ratios (ratios up to 5:1 have been tested). This fast drop followed by relative steadiness in the index of refraction for increasing O_2/SiH_4 ratios is well-known in the literature [6], [19]. For the RSM test sequence, the O_2/SiH_4 ratios ranged from 2.67:1 to 4.0:1 for the cube block (3.33:1 for the center point tests), and the star tests for O_2 flow had ratios of 2.0:1 ($-\alpha$) and 4.67:1 ($+\alpha$). As a result, the measured indexes did not show much variation, and a statistically significant model for the RSM data was not found. The lone exception was the low-ratio $-\alpha$ test for O_2 flow (3 sccm O_2, ratio: 2.0:1), which had an index of 1.54, which was in line with previous tests at this low O_2/SiH_4 ratio. **Figure 4.8** combines data from the RSM test sequence with data from follow-up testing (see **Section 4.3.3.1**) to show the independence between O_2/SiH_4 flow ratio and index of refraction for ratios > 2:1. All of the RSM tests are included in this data, showing the relative independence of refractive index from other input factors (i.e. pressure, temperature, bias power).

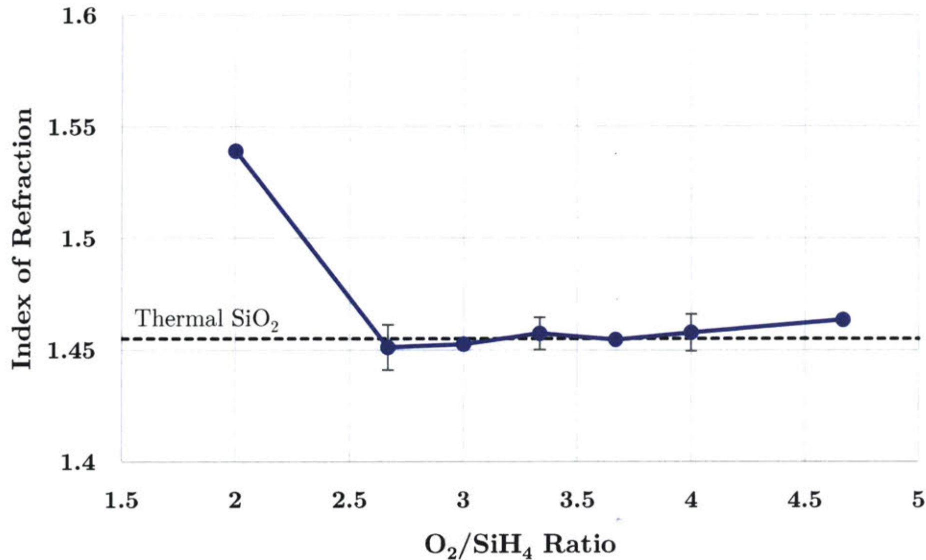

Figure 4.8: Index of Refraction vs. O_2/SiH_4 ratio. Included are data from both the RSM sequence and follow-up testing (Section 4.3.3.1), containing tests at several different pressures, temperatures, and bias powers. The error bars show the standard deviation.

4.3.2.3 Average Film Stress

The ability to predict and control the film stress in CVD processes is extremely important. Film stresses induce bow in the underlying substrate, which, if unaccounted for, can lead to large variations or even material failure in devices with thin membranes such as microphones and pressure sensors. Both thermally-grown[27] [89]–[91] and CVD-deposited SiO_2 films are nearly always compressive [13], and the typical threshold for "low-stress" films is less than 300MPa (or ≥-300MPa using the standard convention of negative values for compressive stress and positive values for tensile stress) [6], [50]. The average film stress for the RSM samples was measured using a Tencor FLX-2320 Film Stress Measurement System using the process described in **Section 3.2.3**. The 2" wafers used for the RSM came from two 25-wafer cassettes from the same lot, and the initial bow measurement was used to filter out wafers with unusual curvature that could potentially skew the post-deposition stress measurement.

[27] As long as the growth temperature is below the flow temperature for oxide (~975°C for wet oxide [91]).

The results of the RSM sequence showed that each of the four factors tested play an important role in determining the output stress of the film, and that "low-stress" films can be reliably achieved using an appropriate combination of parameters. A second-order model with two-factor interactions was found to fit well with the RSM data (lack-of-fit p-value = 0.20), and the coefficients for this fit are shown below along with the surface/contour plots showing the parameter relationships. The average residual between the collected data and the fitted model is 19.2 MPa, with an average percent error of 4.74%. The standard residual deviation is 23.9 MPa. This percent error is larger than the one seen for the deposition rate, but, as discussed in **Section 3.2.3**, the stress measurement technique is also not as precise as the ellipsometry measurement for film thickness, displaying an average 1σ repeatability of ~15 MPa, or ~3.5% of the average stress measured across the all the samples in the RSM sequence.

O_2 Flow	**Pressure**	**Temperature**	**Bias Power**	**$\left(O_2\ \text{Flow}\right)^2$**	**$(\text{Pressure})^2$**	**$(\text{Temperature})^2$**	**$\left(\text{Bias Power}\right)^2$**
-23.322	37.705	-25.555	-120.81	56.785	-7.532	3.647	27.178

$O_2 \cdot$ Press	**$O_2 \cdot$ Temp**	**$O_2 \cdot$ BP**	**Press · Temp**	**Press · BP**	**Temp · BP**	**Block**	**Intercept**
11.254	-36.607	-6.736	-3.839	6.826	-15.290	-63.335	-403.67

Table 4.8: Fit coefficients for second-order model for average film stress.

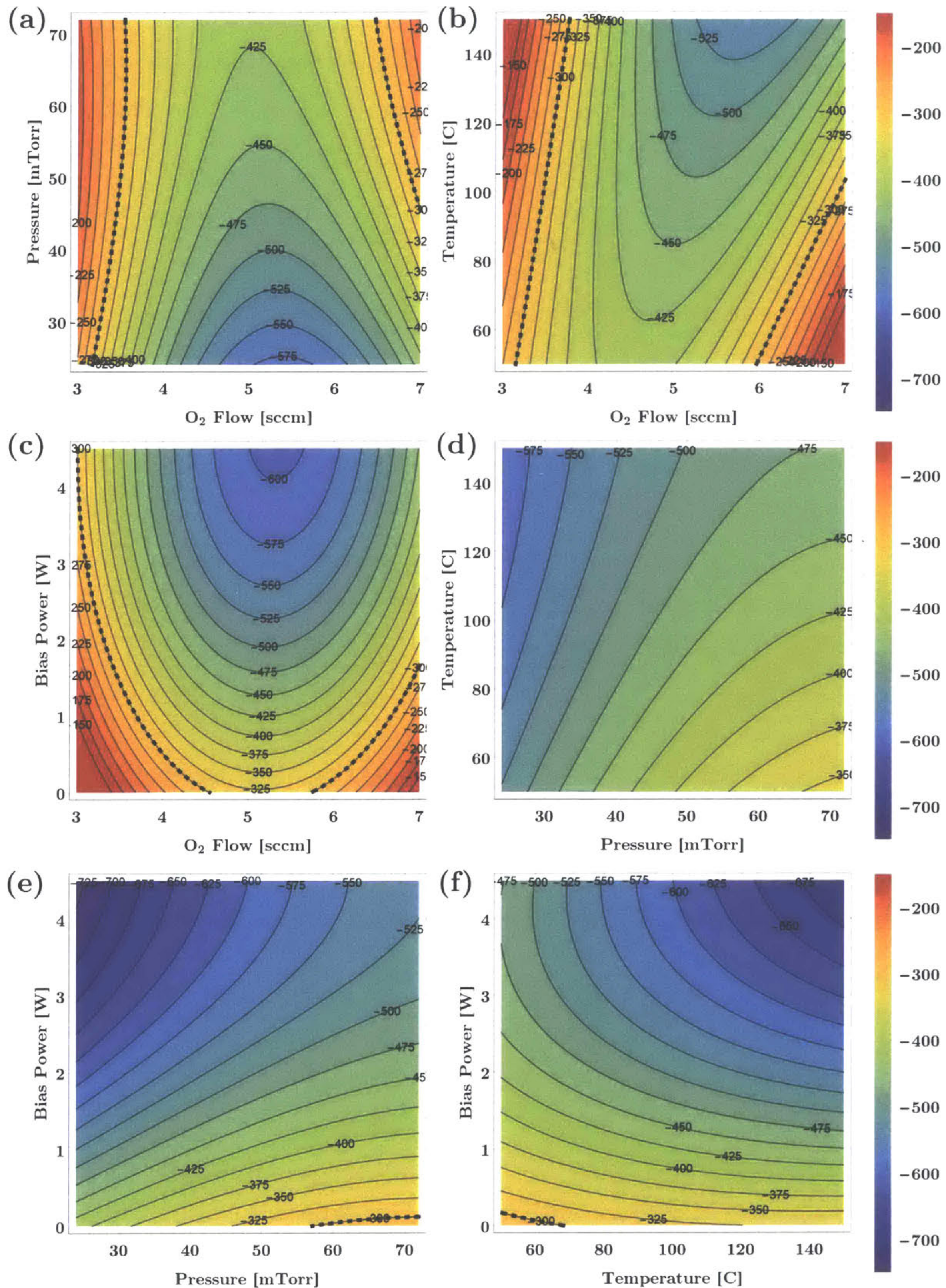

Figure 4.9: Contour plots showing average film stress vs. pairs of input factors. The dotted line marks the -300 MPa contour. Each graph is evaluated at the center point values of the factors not shown.

Examining the trends shown in **Figure 4.9**, it is apparent that the average film stress depends on each of the four tested factors. There is a very pronounced effect from the applied bias power, with increasing power leading to more compressive stress. This is due to the increased energy and level of ion bombardment caused by the negative DC voltage developed on the substrate electrode from the applied bias power. Decreases in the chamber pressure also lead to more compressive films, likely due also to an increase in ion bombardment energy stemming from the longer mean free paths at lower pressures [92]. The substrate temperature and O_2 have non-monotonic effects on the film stress, with increasing temperature generally increasing the stress, except at low O_2 levels, where the trend reverses slightly. The large coefficient for the O_2 flow quadratic term leads to a prediction of reduced compressive stress at both high and low O_2 values (relative to the 5 sccm center point) in the process window. There are examples in the literature of reduced compressive stress for both increasing [6][28] and decreasing [50] O_2 flows.

The presence of a dotted line in the graphs of **Figure 4.9** denotes when the predicted stress crosses the -300 MPa "low-stress" threshold. This line is not present in **Figure 4.9d**, indicating that, at the center point values of 5 sccm and 1.5 W, achieving a "low-stress" film is not possible within the RSM process window. Observing the other model data, however, it is clear that less compressive films happen when the bias power approaches 0 W, and when the O_2 flow is either above or below the center point of 5 sccm. Taking these observations into account, if **Figure 4.9d** (reproduced as **Figure 4.10a**) is re-evaluated at 0 W (**Figure 4.10b**), a window of low stress operation appears at high pressures and low to medium temperature. If the model is run with O_2 flow also reduced to 4 sccm (**Figure 4.10c**), the window widens substantially to predict that most pressure and temperature combinations (within the RSM process window) will now produce a film with less than 300 MPa of compressive stress.

[28] The actual plotted data in [6] appears to show a bit of curvature in line with what the RSM model predicted, but it was not discussed in that work.

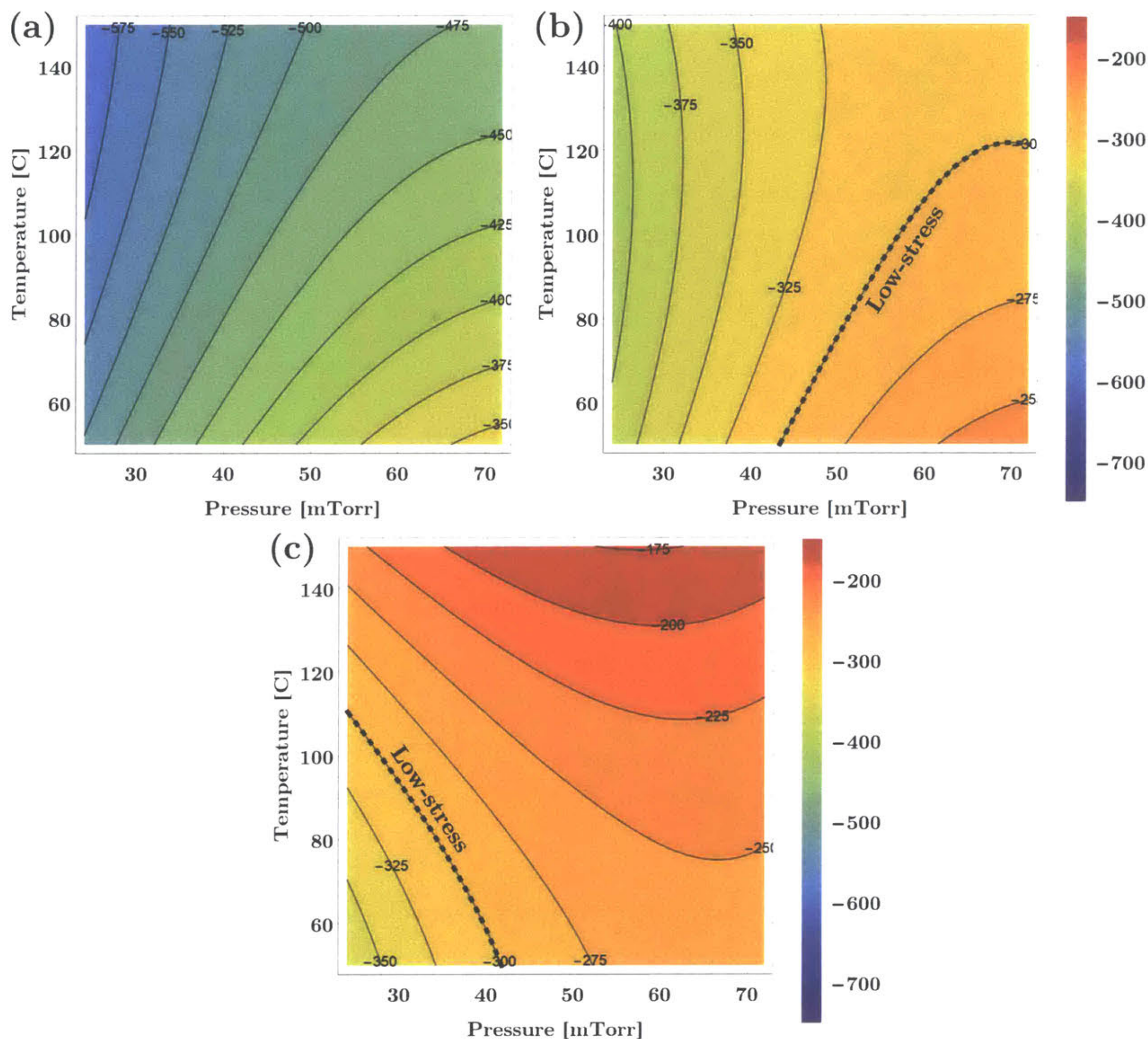

Figure 4.10: Contour plots of average film stress vs. pressure and temperature. (a) Evaluated at 5 sccm O_2, 1.5 W; (b) Evaluated at 5 sccm O_2, 0 W; (c) Evaluated at 4 sccm O_2, 0 W. The -300 MPa threshold for "low-stress" SiO_2 films is denoted with a dotted black line.

The progression of **Figure 4.10** demonstrates some of the real utility of RSM models for predicting system performance. The initial center point for the RSM sequence was not ideal for producing low-stress films, but the produced model has suggested a new operating point around which recipes can be developed. Using the RSM results to predict and produce a film with specific qualities will be revisited below at the end of this chapter.

4.3.2.4 Uniformity

Achieving a uniform film thickness across a substrate is one of the most important characteristics of a deposition process. Uniformity was one of the challenges discovered during the initial testing of the IFIC, and was ultimately solved using the aperture plate concept discussed in **Section 4.1.2.3**. For the RSM test sequence, uniformity was measured using spectral reflectometry as described in **Section 3.2.4**, with a 4 mm exclusion zone from the edge of the deposition region (providing a 36 mm diameter measurement region)[29]. **Figure 4.11** shows three contour plots generated from the first, middle, and last tests of the RSM sequence, which conveniently also includes a cube, center point, and star test (in the standard order, the test numbers are 12, 19, and 26). The black dotted line indicates the mean film thickness and the white dotted lines indicate plus or minus one standard deviation.

[29] Officially the exclusion zone used was 4.225 mm, calculated from the 1.75" (44.45mm) diameter aperture defined by the alumina clamp.

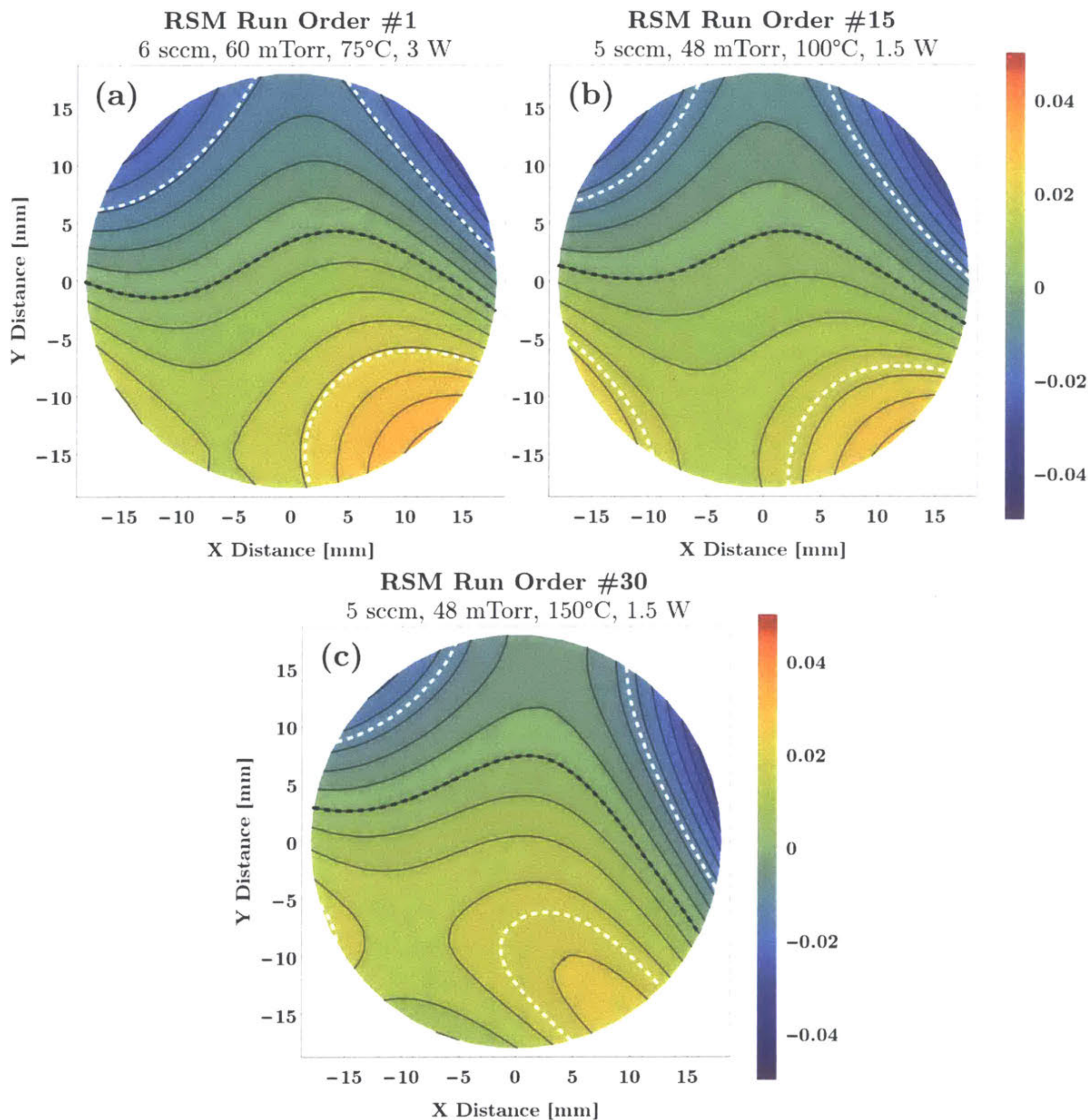

Figure 4.11: Contour plots of film uniformity (percent deviation from the mean). (a) Test #1 from the cube block; (b) Center point test (overall test #15); (c) Test #30 from the star block. The black lines indicate the mean film thickness, while the white lines show one standard deviation.

The plots of **Figure 4.11** are representative of the rest of the RSM sequence and show that IFIC depositions are quite uniform and maintain that uniformity across a wide variety of process parameters. The data does show that the film thickness profile is slightly tilted, with the mean thickness line roughly running through the center of the deposition (parallel to the wafer flat, which is at the bottom of these plots), and the bottom half showing a 1-2% larger thickness. The most likely explanation for this small thickness asymmetry is a small non-uniformity in the gas

flow rate through the SiH_4 gas ring or the precursor gas showerhead. These items were carefully designed and simulated to produce a uniform gas injection profile, but do require tight tolerances, which may have been slightly deviated from during fabrication, or changed slightly as a result of wall deposition during processing. Nevertheless, the non-uniformity is still on the same order as other commercial systems, which will be directly addressed at the end of this section.

To directly compare uniformity across samples, two values were calculated from the UV1250 data. The first measure was Uniformity, which was introduced in **Section 4.1.2.3** when discussing the effect of aperture plates. The second measure calculated was the coefficient of variation (CV), sometimes also referred to as the relative standard deviation, which is the ratio of the standard deviation to the mean thickness (i.e. $CV = \sigma/\mu$). This metric is in fact automatically calculated as part of the UV1250 data set, and is useful in moderating the effect of outlier measurements, which in the case of the RSM samples happen exclusively near the edge of the film, as shadowing effects from the alumina clamp begin to dominate. These effects could be removed simply by increasing the measurement exclusion zone, but this would eliminate some valuable knowledge about the limits and capabilities of the IFIC system as described here. **Figure 4.12** shows data from a center point test run at various edge exclusion distances.

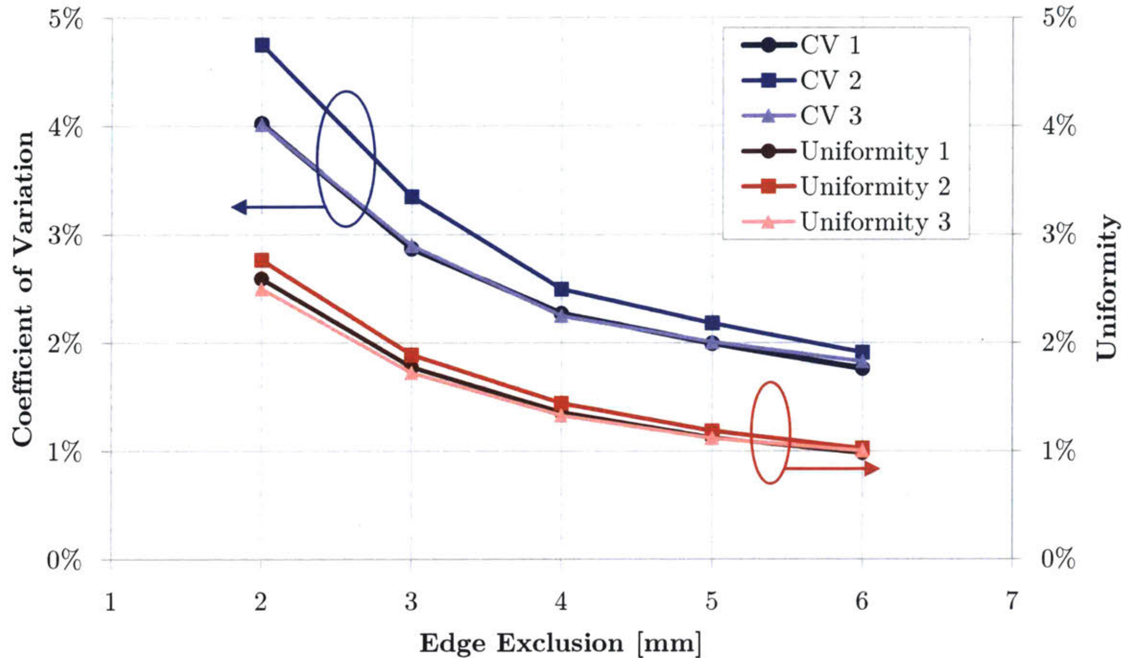

Figure 4.12: CV and Uniformity as a function of edge exclusion distance for three different samples. A 4 mm edge exclusion was used for the RSM test sequence.

These data show how the Uniformity and CV metrics can be affected by the choice of edge exclusion. The choice of 4 mm for the RSM data provides a 36 mm diameter measurement region and is a good compromise that does not fully wash out the effect of the mechanical wafer clamping, and still captures any non-uniformity inherent to the chamber or the process.

Like the index of refraction, the raw data collected on the film thickness uniformity does not vary much across the RSM samples, with the Uniformities ranging from 2.33% to 4.22% (average: 2.89%), and the CV values ranging from 1.33% to 1.83% (average: 1.54%). The relative homogeneity (...or uniformity) of the Uniformity and CV data made fitting to a statistical model not possible, but it does suggest that the uniformity is very repeatable and independent of the four factors tested in the RSM sequence. This matches up with the observations from the early testing, which showed that uniformity was very closely tied to the relative geometric spacing of the components in the chamber (most notably the aperture plate geometry and the substrate-aperture plate spacing, as seen in **Figure 4.5** and **Figure 4.6**) and largely independent on other input parameters.

Uniformity is one of the most commonly quoted statistics for commercially available ICP-CVD systems. To provide a frame of reference for the Uniformity results gathered here, **Table 4.9** shows a compilation of values found in the literature, along with context about the systems they come from.

SiO_2 Reference	Uniformity	Substrate Size	Exclusion Zone	Additional Information
IFIC	±2.9%	50.8 mm	4 mm	Inch Fab ICP-CVD system
[50]	±3%	100 mm	not provided	Oxford Instruments ICP180 Source
[93]	±3%	100 mm	7 mm	Oxford Instruments ICP180 Source
[66]	±5%	50 mm (GaAs)	5 mm	Oxford Instruments
[6]	±2.5%	100 mm	not provided	PlasmaTherm Versalock
[71]	±3.2%	100 mm	not provided	Sentech SI 500 D

Table 4.9: Published Uniformity values for SiO_2 depositons in commercial ICP-CVD systems. The average Uniformity from the SiO_2 RSM sequence is included in green for reference.

The Uniformity of SiO_2 films produced by the IFIC (2.89%, 4 mm edge exclusion) compares well with the existing commercial options, and with further optimization of the aperture plate design could certainly be improved even more. The consistency of the results shown in the RSM sequence however, do provide a great validation of the system as tested and suggest that its performance is at a level that would make it attractive to the low-volume R&D and production market.

4.3.2.5 BOE Etch Rate Ratio

The final measurement carried out on each of the wafers in the SiO_2 RSM test sequence was a timed etch in a buffered HF etching solution (known as BOE or BHF). This test is commonly used for CVD-deposited SiO_2 as a way of assessing the density of the film. A commercially mixed 7:1 BOE (7 parts 40% ammonium fluoride in water, 1 part 49% hydrofluoric acid in water) solution was used to etch the 30 RSM samples, following the procedure outlined in **Section 3.2.5**. The specific etch rate data was gathered using a stylus profilometer. Because the etch rate of BOE is largely tied to the ambient conditions [66] (etch rates can increase up to 100% for each 10°C increase in temperature [65]), in each etch run a piece of silicon with thermally-grown oxide (cleaved from a single 150mm wafer) was included. The gathered etch rates were then normalized

to the etch rate of the thermal oxide piece to help control for any difference in experimental conditions. Even with this control in place, the etch rate observed can still vary appreciably due to conditions like uneven flow or currents over the samples in the BOE dish or small differences in time between a sample's removal from the BOE dish and immersion in DI water to stop the etch. Other investigators have estimated a ±10% error for timed etch tests [32], [67] and internal repeatability tests showed an average variation of ~7.1%. Those caveats aside, the data gathered still indicated that O_2 flow, substrate temperature, and bias power have significant impacts on the films' etch rate. A statistical model including all four factors that passed the lack-of-fit p-test ($p > 0.05$) could not be found, but a second order model did show significant parameter effects that were corroborated in single factor analysis, and the residuals from this model were normally distributed, although they are larger (relatively) than those in the deposition rate and average film stress models. This model was therefore deemed acceptable to provide rough predictions of the BOE etch rate for a given operating point. The model's average residual was 0.94, with a standard residual deviation of 1.23. The coefficients for this model and the standard contour plots are shown below.

O_2 Flow	Pressure	Temperature	Bias Power	$\left(O_2\ \text{Flow}\right)^2$	$(\text{Pressure})^2$	$(\text{Temperature})^2$	$\left(\text{Bias Power}\right)^2$
4.566	1.292	-1.946	-2.127	0.738	-0.033	0.565	0.373

$O_2 \cdot$ Press	$O_2 \cdot$ Temp	$O_2 \cdot$ BP	Press · Temp	Press · BP	Temp · BP	Block	Intercept
0.529	-0.794	-1.152	-0.160	0.495	-0.279	0.363	5.323

Table 4.10: Fit coefficients for second-order model for normalized etch rate.

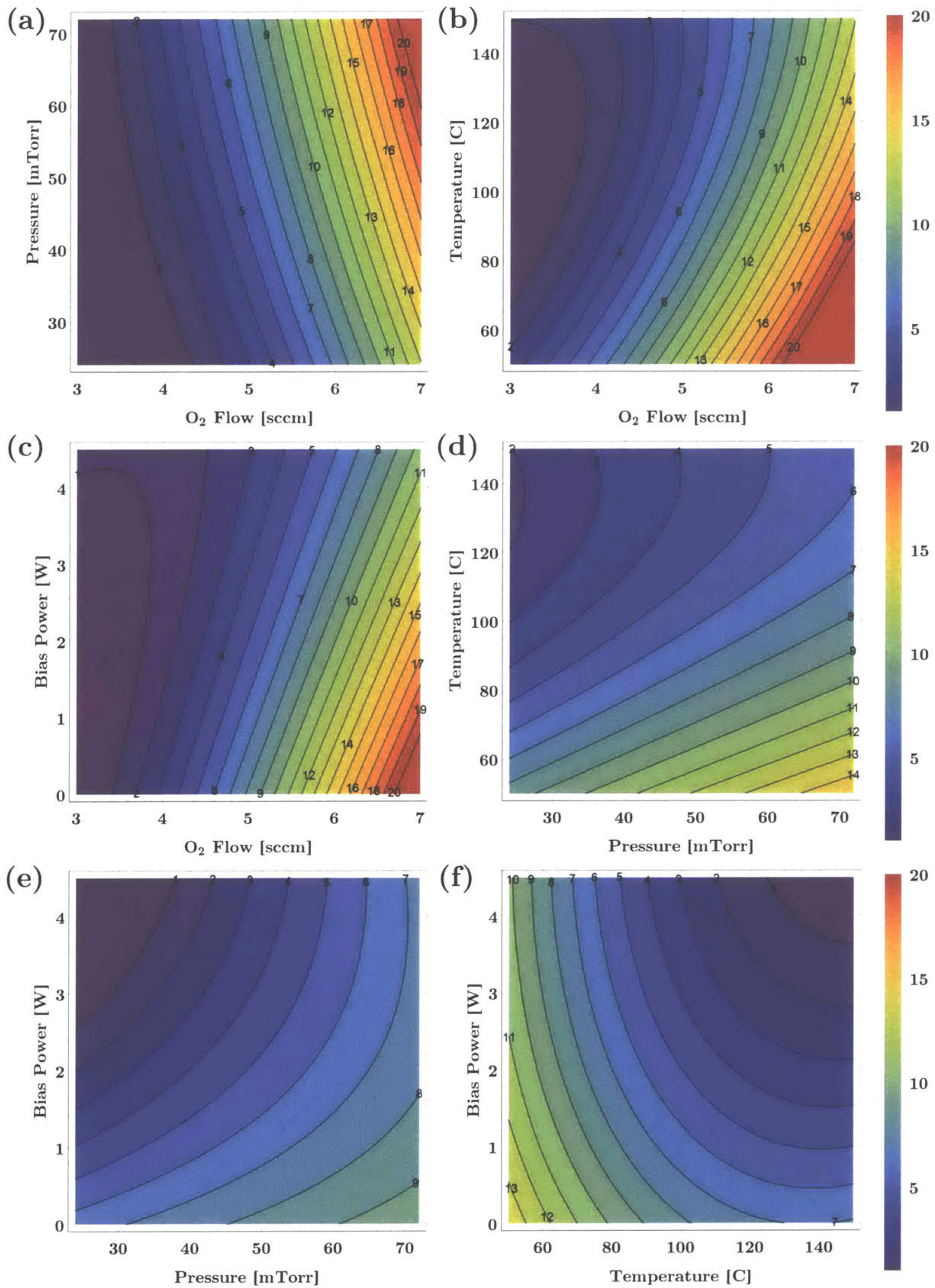

Figure 4.13: Contour plots showing the normalized BOE etch rate vs. pairs of input factors. Each graph is evaluated at the center point values of the factors not shown.

The trends in the data show that increasing the bias power reduces the etch rate in nearly all circumstances, which can be ascribed to an increase in ion bombardment [28], [94], [95], which serves to densify the film as it grows [66]. Increasing the substrate temperature, which is also known to increase the film density [6], [50], [96], also results in a significant decrease in etch rates. Reducing the O_2 flow produces the most dramatic effect seen in the model and data, drastically decreasing the predicted etch rate. If O_2 flows are low enough that films become Si-rich, they will exhibit lower etch rates [6], [13], [19]. This was observed in the RSM data, as the only Si-rich sample (from the -α (3 sccm) O_2 flow test) showed the lowest etch rate. The 4 sccm O_2 samples however, which each had near-stoichiometric indexes of ~1.45, also showed much lower etch rates than their 6 sccm O_2 partner tests (which were also near-stoichiometric). This crossover region, where films deposited with low O_2 flow feature indexes near 1.45 and also much lower etch rates than films deposited with more O_2 has also been identified and utilized in commercial tools [6]. The lower etch rates can be attributed to the fact that the films, which showed lower deposition rates, are likely denser than their higher deposition rate 6 sccm O_2 counterparts [13].

Drawing back to the discussion of **Section 1.2.5**, which compared the capabilities of ICP-CVD versus parallel-plate PEVCD, all of the etch rates shown here are substantially better than what would be expected from a PECVD system operating at the same temperature. Data comparing the etch rates between PECVD and ICP-CVD systems is presented in [50] and [6]. These data show that in order to obtain comparable film etch rates (and by extension, film densities), PECVD systems must heat the substrate ~250-300°C hotter than in ICP-CVD systems. This temperature-density shift between PECVD and ICP-CVD is also corroborated in [20], which notes that films deposited at 70°C in ICP-CVD reactors have comparable density to PECVD-deposited films at 350°C. This gives ICP-CVD systems like the IFIC much more flexibility in the types of substrates and film stacks they can process, widening the potential market for these systems.

4.3.3 Validation of RSM results

The data gathered during the SiO_2 RSM test sequence provided a great level of understanding about the capabilities of the IFIC system. The data and models fit very well with the literature's understanding of how different input parameter should affect the properties of SiO_2 films, but it is critically important that the model predictions and observed trends continue to fit with results beyond those taken during the RSM sequence. That is to say, the true validation of a model comes from not only fitting the data used to generate itself, but also accurately predicting results for new tests and parameter combinations.

4.3.3.1 Post-RSM Testing

To test the models' validity, five films were deposited using parameter values not tested during the RSM sequence, and then analyzed using the same measurement sequence. The results were then compared to the predictions made by the RSM model. The parameter values, measured results, and comparison to model predictions are shown in **Table 4.11-Table 4.13**.

Run Order	Test Type	(Coded Values) F1	F2	F3	F4	(F1) O_2 Flow [sccm]	(F2) Pressure [mTorr]	(F3) Temperature [°C]	(F4) Bias Power [W]
1	Follow-up	-1	0.5	-0.4	-1	4	54	90	0
2	Follow-up	-1	0	0	-1	4	48	100	0
3	Follow-up	-1	0	1	-1	4	48	125	0
4	Follow-up	-0.5	0	1	-1	4.5	48	125	0
5	Follow-up	0.5	0	1	-1	5.5	48	125	0

Table 4.11: Input parameters for the RSM follow-up tests

Run Order	Deposition Rate [nm/min]	Index of Refraction	Average Film Stress [MPa]	Coefficient of Variation [%]	Uniformity [%]	BOE Etch Rate Ratio
1	30.08	1.460	-266.0	1.52%	3.22%	4.45
2	29.43	1.450	-250.8	1.38%	3.16%	3.69
3	27.82	1.448	-186.5	1.42%	3.50%	2.42
4	30.99	1.453	-301.4	1.35%	2.94%	6.30
5	35.57	1.455	-301.2	1.35%	2.52%	13.19

Table 4.12: Measured results for the RSM follow-up tests

Run Order	Deposition Rate Estimate [nm/min]	Deposition Rate Difference [nm/min]	Deposition Rate Diff. [%]	Average Film Stress Estimate [MPa]	Average Film Stress Difference [MPa]	Average Film Stress Diff. [%]	BOE Etch Rate Ratio Estimate	BOE Etch Rate Ratio Difference	BOE Etch Rate Ratio Diff. [%]
1	29.54	0.54	1.84%	-246.9	-19.1	7.73%	3.80	0.65	17.11%
2	28.90	0.53	1.83%	-245.7	-5.1	2.10%	3.21	0.49	15.22%
3	28.07	-0.25	-0.89%	-215.7	29.2	-13.54%	2.90	-0.47	-16.33%
4	30.71	0.28	0.91%	-284.8	-16.6	5.82%	4.81	1.50	31.15%
5	34.97	0.60	1.71%	-338.0	36.8	-10.88%	9.73	3.46	35.53%

Table 4.13: Comparison of RSM follow-up results to model predictions

The data in **Table 4.13** show that the characteristics measured for the follow-up tests match well with the derived RSM models. The follow-up tests' average deviation from the model predictions for the deposition rate (0.44 nm/min) is just below the RSM value (0.55 nm/min). For the average film stress, the average deviation is a little larger (21.4 vs. 19.2 MPa) in the follow-ups, and for the BOE etch rate ratio the follow-ups' average deviation is (1.31 vs. 0.94) larger, but just ~0.3σ away for this admittedly noisier and less well-fit parameter. The refractive indexes for the five samples all indicate near stoichiometric films (this data is actually included as part of **Figure 4.8**), and the average Uniformity (3.07%) and CV (1.41%) values also compare well with the expectations from the RSM dataset (average Uniformity: 2.89%, average CV: 1.54%). The good correlation across the measured film characteristics of the follow-up tests to the predictions provided by the RSM models speak to their overall robustness.

4.3.3.2 Pre-RSM Testing

As a further validation, the data from the depositions prior to the RSM (running back to the previous chamber clean and conditioning[30]) were also compared to model predictions. Excluding the samples with different values for the static parameters in the RSM sequence (e.g. ICP power, substrate spacing), this adds an additional 14 samples for assessment. A summary of these results are shown in **Table 4.14**.

---

[30] Before this chamber cleaning most of the samples were being run with a different aperture plate and a different substrate-to-aperture-plate spacing.

	Deposition Rate [nm/min]	Average Film Stress [MPa]	BOE Etch Rate Ratio
Average Deviation from Model Prediction	0.4410	24.5710	1.2395
Average % Deviation from Model Prediction	1.28%	5.35%	27.82%

Table 4.14: Summary of the model fits for the 14 qualified pre-RSM experiments.

Like the results from the post-RSM tests, the above data confirm that the models generated by the RSM sequence are very competent at predicting the characteristics of output films. The average deviations/residuals for deposition rate, average film stress, and BOE etch rate ratio are each very near to the values seen for the both the RSM sequence and the 5 follow-up tests. For all 14 samples, the O_2/SiH_4 ratios were between 2.67 and 4, and the index of refraction was very stable, averaging 1.458. The uniformity metrics were not taken before BOE etching on 5 samples, but the remaining 9 showed an average Uniformity of 2.75% and an average CV of 1.54%. These numbers all correspond well with the data from RSM and follow-up tests. An additional dimension that can be considered with the inclusion of this test data is the long-term stability or predictability of the IFIC. The short term predictability was established through the RSM sequence, where a large number of samples were run in a short period of time. A tool such as the IFIC may however, be installed in an environment where its overall utilization is small or sporadic. In this scenario, producing predictable results for many samples in a row is less important, and the ability of the system to perform as expected over the long term or after being dormant for days is essential. The pre-RSM data being discussed in this section includes processing gaps of 8 and 6 days, and together with the RSM sequence, follow-up tests from the previous section, and the center point tests discussed in the following section, span a total length of time of more than a month, during which all of the eligible tests were well predicted by the models. This long term predictability over not just a single process, but many different process conditions, is also extremely important to recognize. The following section extends this look into the IFIC's predictability by looking closely at the system's performance on a single recipe, the RSM center point, over time.

4.3.3.3 Single Recipe Repeatability

The ability to correctly predict the output characteristics of a deposited film relies on the assumption that every time a process is run with the same input parameters it will return the same results. Repeatability is a crucial trait for all semiconductor fabrication processes, and to test how repeatable SiO_2 depositions are in the IFIC, the center point test from the RSM sequence (5 sccm O_2, 48 mTorr, 100°C, 1.5 W) was performed a total of 14 times (including the 6 tests from the RSM sequence) over a period of two weeks. In some instances, the test was the only test performed on that day, and in other cases sometimes it occurred within a sequence of several tests. This was purposefully done to potentially reveal any carry-over effects from differing deposition processes or variations stemming from differing chamber conditions. Wafers from four different cassettes, including both N and P-type, were also used to see check for any variation stemming from substrate differences. Fortunately, none of these changes in the experimental setup had an observable effect in the gathered data, which is displayed in **Figure 4.14** in terms of the percent deviation from the mean value. **Table 4.15** summarizes this data into the average percent deviation from the mean, and also adds the average percent deviation from the values predicted by the RSM models and the uniformity measurements for each sample.

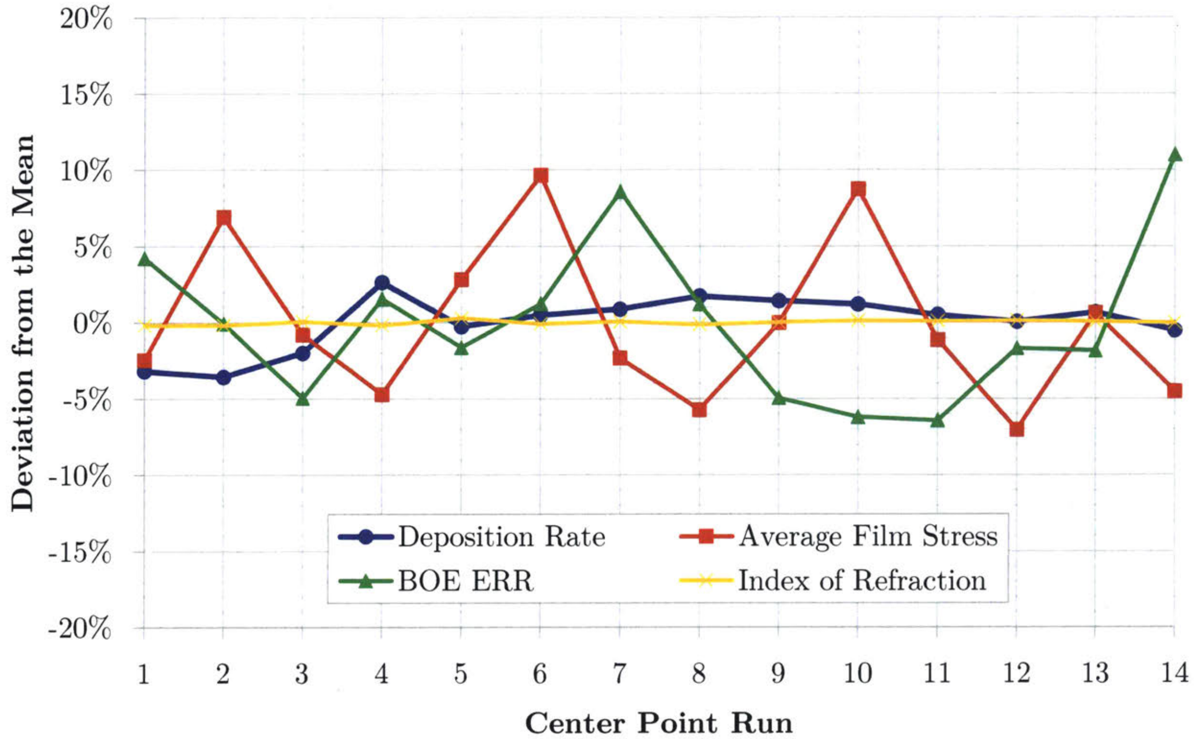

Figure 4.14: RSM center point deviation from the mean for each measured parameter.

	Deposition Rate [nm/min]	Index of Refraction	Average Film Stress [MPa]	CV [%]	Uniformity [%]	BOE Etch Rate Ratio
Mean	35.06	1.458	-480.2	1.37%	2.50%	5.68
Standard Deviation	0.63	0.002	25.4	0.07%	0.12%	0.27
Coefficient of Variation	1.80%	0.14%	5.29%	4.92%	4.90%	4.83%
Average Deviation from Mean	0.48	0.002	19.7	0.06%	0.10%	0.21
Average % Deviation from Mean	1.36%	0.11%	4.11%	4.22%	3.82%	3.64%
Average % Deviation from Model Prediction	2.02%	–	4.44%	–	–	2.36%

Table 4.15: Summary of results from center point repeatability tests.

The above data indicates that SiO_2 depositions in the IFIC system are indeed quite repeatable. As discussed in previous sections (and in more depth in **Section 3.2**) the larger magnitudes in the percent error for the average film stress and BOE etch rate numbers are likely attributable to the inherent error present in the respective measurement methods. Literature data showing ICP-CVD repeatability measurements for any film parameter are sparse, and especially so for anything besides deposition rate and refractive index, but the few results that have been reported do show

a significantly larger run-to-run deviation for stress (~±10% in [50], ~±8% in [6]) than for deposition rate (±2% in [50]) or refractive index (±0.3% in [50]). The numbers shown here for the IFIC system outpace all of these values, reinforcing the repeatability conclusions suggested above.

4.4 Additional Tests

The SiO_2 RSM test sequence and the follow-up tests were extremely useful in understanding and confirming the relationship in the IFIC between the input parameters for a process and the output characteristics of the film it produces. To further understand the properties of deposited SiO_2 films deposited by the IFIC system, three additional types of tests, FTIR spectroscopy, electrical breakdown measurements, and white light interferometry, were performed on select samples to learn more about their chemical, electrical, and surface properties.

4.4.1 FTIR

FTIR measurements were performed in a ThermoFisher Nicolet iS50 FTIR system in transmission mode. A blank wafer was first measured to provide a background signal (lightly-doped silicon is transmissive in the IR range), and then a wafer with a deposited SiO_2 film (from the same cassette) was measured. The background wafer signal was subtracted from this scan, followed by atmospheric and baseline corrections, and then conversion to the standard absorbance format. Spectra for two different samples, run using the RSM center point parameters (Test #9 and #10 from the center point repeatability data shown in **Figure 4.14**) are shown in **Figure 4.15**.

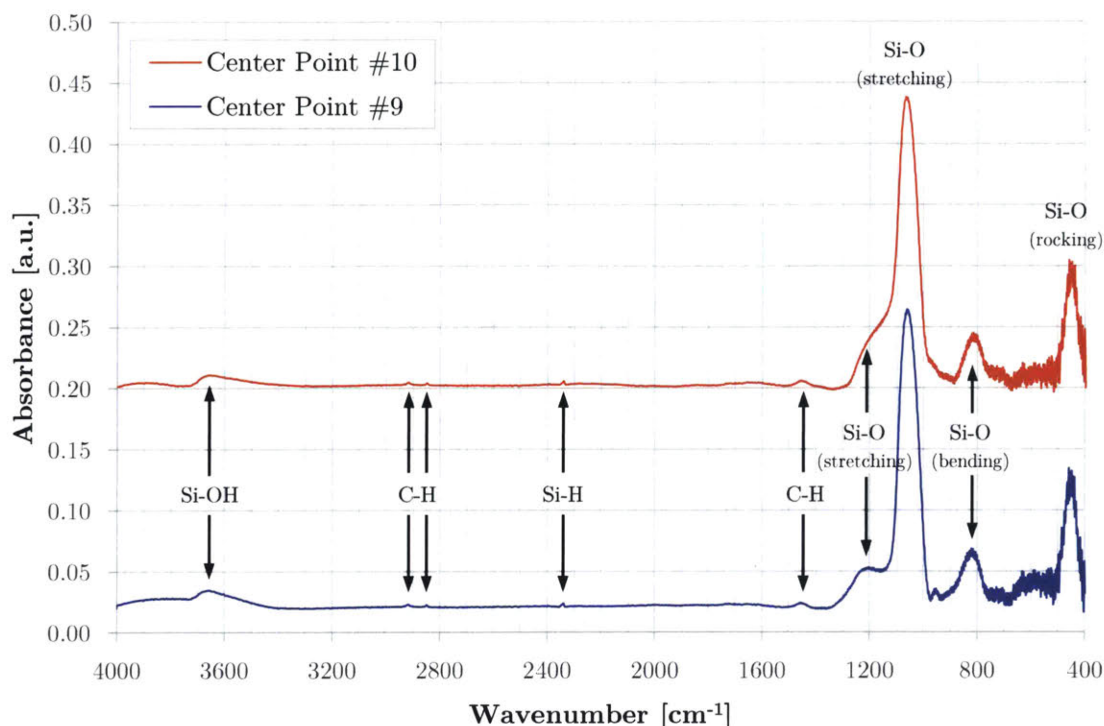

Figure 4.15: FTIR spectra for 2 RSM center point samples. The spectra are offset for clarity. The observable peaks are labeled. The faint C-H peaks are likely from surface contamination, and were not observed in other IFIC samples.

The rocking, bending, stretching (in-phase), and stretching (out-of-phase) peaks associated with SiO_2 at ~450, ~805, ~1075, and ~1180 cm^{-1}, respectively, are all prominently present in both spectra. The peaks seen at 1450, 2850, and 2920 cm^{-1} correspond to hydrocarbon bonds, which were persistent as a background signal in the FTIR system. The peaks associated with Si-H (~2230 cm^{-1}) and Si-OH (~3660 cm^{-1}) bonds can both be seen, but they are very weak compared to the levels usually seen in films deposited by traditional, parallel-plate PECVD reactors [31]. This indicates that the IFIC films have a very low hydrogen content, which is desirable for many applications because it implies tight chemical bonding and a high density film [68][31]. The high density of the films compared to those made using parallel-plate PECVD also fits with the results

[31] Although there are some applications in which large hydrogen incorporation is desirable, such as passivation for PV devices [117].

shown in **Section 4.3.2.5**, which showed the substantially lower BOE etch rates achieved by the IFIC, even at lower temperature depositions, compared to those seen in PECVD films.

4.4.2 Electrical Breakdown

To assess the electrical quality of the SiO_2 films deposited in the IFIC, breakdown voltage measurements were taken using a probe station and high voltage SMUs. The films for these tests were deposited on highly-doped P-type wafers (0.001-0.005 $\Omega \cdot$cm) and prepared using the process laid out in **Section 3.2.7**. To measure the breakdown characteristics, voltage sweeps were then carried out on contact pads in a variety of locations on the sample until total electrical breakdown was achieved. The voltage was swept in 2 V increments from 0 to -400 V, with each step lasting ≥50 ms, and the current at each strep was recorded. The recorded data was then converted to the traditional current density vs. electric field strength format using the measured pad sizes and film thickness values. The results for two samples (BV1 and BV2) measured are shown in **Figure 4.16** and **Figure 4.17**.

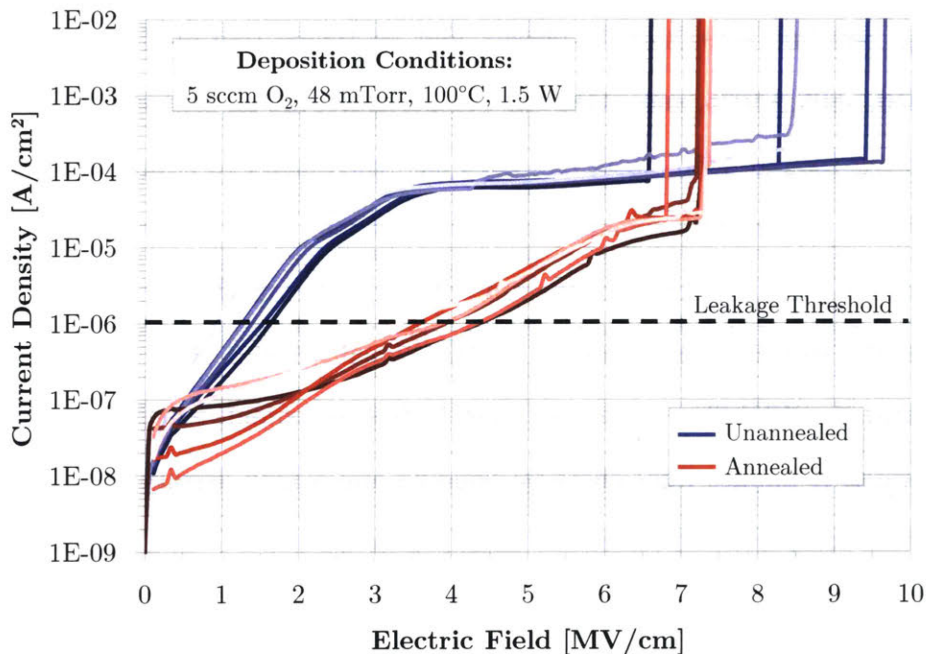

Figure 4.16: J-E plot for SiO_2 sample deposited at 100°C and 1.5 W bias power.

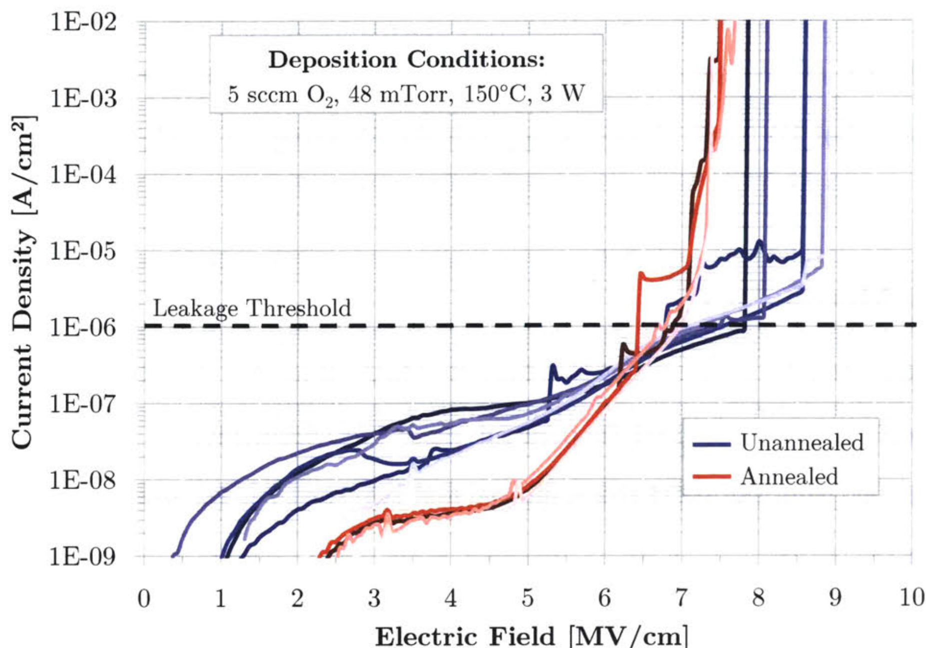

Figure 4.17: J-E plot for SiO_2 sample deposited at 150°C and 3 W bias power.

There are two main ways in which "electrical breakdown" is reported. The first is the applied field strength at which the measured leakage current density crosses a certain threshold. A threshold of 1 μA/cm² is commonly used in the CVD literature [71], [96], [97] and marked in both of the above plots. The second breakdown condition is the field strength at which a conducting pathway is permanently formed (an electrical "short") between the two measurement points, causing the measured current to rise rapidly to the compliance limit of the SMU. This is sometimes known as irreversible breakdown. Irreversible breakdown can be seen beginning near 7 MV/cm for all four plots. Thermal SiO_2 generally undergoes irreversible breakdown at ~8-10 MV/cm [97], [98], while PECVD SiO_2 deposited at 300C breaks down at 5-6 MV/cm [50]. Comparing **Figure 4.16** and **4.17**, it is clear that the 1 μA/cm² breakdown threshold is dramatically different, occurring at ~1.5 MV/cm for Sample BV1, and at ~7.5 MV/cm for Sample BV2. This large difference can be attributed to the differences in deposition parameters between the samples. BV1 was deposited using the RSM center point parameters (5 sccm O_2, 48 mTorr, 100°C, 1.5 W), whereas BV2 was deposited using a higher substrate temperature and bias power (5 sccm O_2, 48 mTorr, 150°C, 3 W), which, from the discussion in **Section 4.3.2.5**, are values known to produce very dense films. Denser films are known to have fewer charge traps (due to

fewer dangling bonds or H atom incorporation), which reduces the leakage current [99], [100]. For the annealed halves of the samples, there is a definite improvement seen compared to the unannealed halves, but BV2 still shows an appreciable advantage at 1 µA/cm², ~7MV/cm to ~4 MV/cm.

4.4.3 Surface Morphology

The final characteristic explored for the deposited SiO_2 films was their surface morphology. A white light interferometer was used to perform these measurements, as described in **Section 3.2.8**. Two samples from the RSM test sequence and two center point tests were measured, and surface plots of the results are shown in **Figure 4.18**, along with the average roughness from measurements at three location on each sample. The particular RSM samples measured were chosen because they represented the high and low end of the stress values observed, and could potentially feature surface cracking or film delamination.

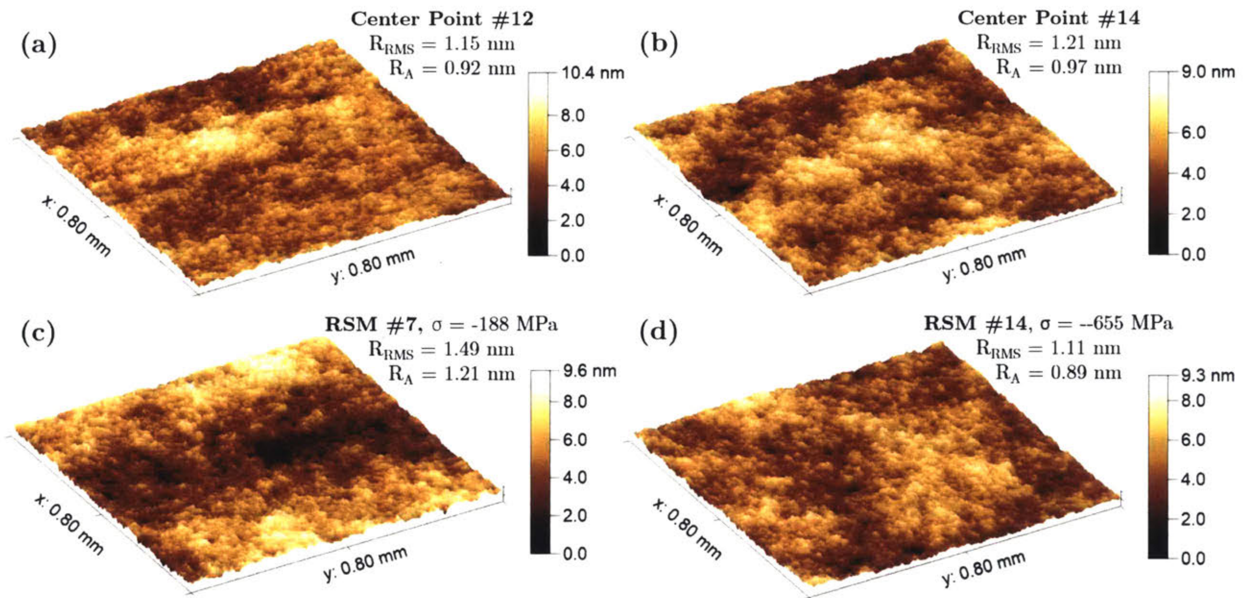

Figure 4.18: Surface roughness maps. (a-b) Center point tests; (c) Film with low compressive stress; (d) Film with high compressive stress.

All of the surfaces measured did not exhibit any unexpected phenomena, and showed very similar roughness values to one another. No data has been found in the literature for the surface roughness of ICP-CVD SiO_2, but R_a values from 1.5 nm [101] up to 7.9 nm [102] have been

reported for SiO_2 films deposited PECVD systems, which compares favorably to the results observed here.

4.5 Summary of Results

As mentioned at the beginning of this chapter, the specific characteristics needed for a film depend on its functional purpose as well as its compatibility with previous and future processes in the fabrication sequence. In the previous sections, parameter effects on output characteristics were primarily discussed independently, but when planning a process sequence for a device, they all need to be considered together. By using the models derived for the IFIC for deposition rate, average film stress, and BOE etch rate ratio, along with the trends observed for index of refraction and film uniformity, a complete picture of the film characteristics can be predicted and tailored to the desired application. This can drastically reduce the amount of time needed for process refinement and integration into a fabrication sequence.

Two scenarios showing how the models derived in this chapter can be used to work backward from a specific film goal to predict the input parameters needed to realize that film are explored below.

Scenario 1 Requirements	**Scenario 2 Requirements**
Deposition Rate > 40 nm/min	Deposition Rate > 28 nm/min
Average Film Stress > -250 MPa	Average Film Stress > -300 MPa
BOE Etch Rate Ratio < 20:1	BOE Etch Rate Ratio < 3:1
	Index of Refraction < 1.48

Table 4.16: Desired film properties for two sample scenarios.

In the first scenario, the goal is to produce a thick SiO_2 film that will ultimately reside on a thin membrane. The requirements for such a film are that it can be deposited quickly (at greater than 40 nm/min), but that it also has a very low stress (less than 250 MPa compressive), such that it will not cause the membrane to bow or warp excessively. An extra requirement might be to have a BOE etch rate ratio < 20:1 as a proxy to ensure that the film is sufficiently dense. For the second scenario, the film is to be used as an KOH etch mask, so it needs to be very dense (BOE etch rate ratio < 3:1), not be Si-rich (index of refraction < 1.48), have a relatively low

stress to avoid inducing bow in the etched substrate (less than 300 MPa compressive), and finally, be able to be deposited reasonably quickly if a thicker mask is required (>28 nm/min). **Figure 4.19** shows overlay plots based on the RSM data to show how films with these constraints can be deposited.

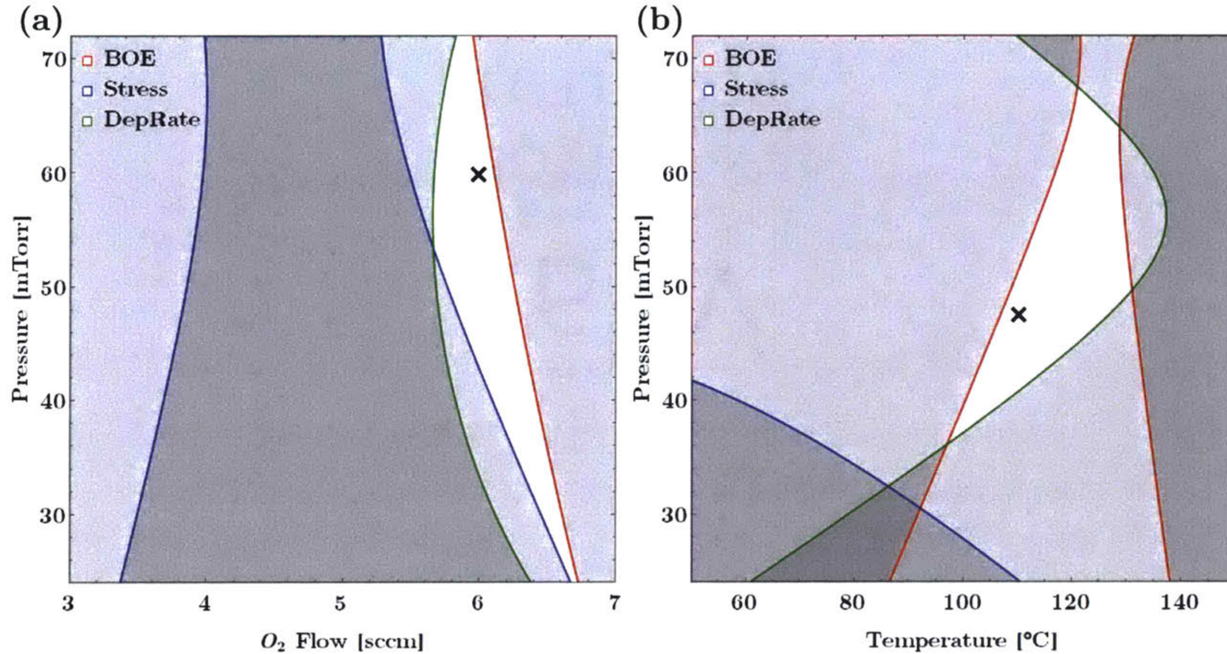

Figure 4.19: Overlay plots for the two film scenarios described in Table 4.16. The white region indicates the remaining available process window. The black Xs show the locations of actual tests. The plot in (a) was evaluated at 75°C and 0 W bias power. The plot in (b) was evaluated at 4 sccm O_2 and 0 W bias power.

The unshaded regions of Figure OO show the process where the films described for each scenario can be achieved. The black **X** symbols within this region indicate the position of a test that was actually performed and met all of the stated requirements (RSM test #4 for Scenario 1, and follow-up test #3 for Scenario 2). These scenarios provide a great summary of the knowledge gained through the characterization of SiO_2 deposition in the IFIC system, and demonstrate how the derived process-property relationships can be utilized to produce films with the desired characteristics with little to no iteration needed.

In this chapter, more than 50 SiO_2 depositions spanning a wide range of parameters have been carefully analyzed and found to fit well with a series of RSM models describing their characteristics. The robustness of these results offer a very optimistic picture of an ultra-low cost

tool that offers the process flexibility, run-to-run repeatability, and intra-wafer uniformity that end users currently expect from other commercially available tools. Future testing can build on this work to expand the understanding of how changes in input parameters affect the precise chemical composition and surface morphology of films, as well as explore additional system optimizations to further improve film uniformity.

The insights gained through the system and process design discussed in this chapter were not only useful to SiO_2 depositions, but also laid the groundwork for the characterization of silicon nitride (SiN_x) depositions, which is discussed in detail in the following chapter.

Chapter 5: Silicon Nitride Deposition

Silicon nitride is a very versatile material for micro- and nanoscale fabrication, with uses ranging from final device encapsulation and passivation to anti-reflection coatings to mechanical structures [103], [104]. As reviewed in **Chapter 1**, SiN_x films can be deposited using LPCVD and plasma-based CVD methods. LPCVD SiN_x is typically grown at 600-900°C is typically used for thinner films due its low deposition rate (~2-5 nm/min) compared to plasma-based methods [16], [103]. The films produced using LPCVD are very dense, exhibit good conformality, and have low hydrogen content [104]. LPCVD-deposited SiN_x films do however, typically have high tensile stresses unless their stoichiometry is adjusted to be silicon-rich (compared to the 0.75 Si:N ratio of Si_3N_4), which is generally accomplished by reducing the ratio of the NH_3 to SiH_4 or SiH_2Cl_2 [104]–[106]. In MEMS devices in particular, the ability to control the stress of a deposited SiN_x film can be crucial to achieving a particular geometry like a bowed cantilever [107] or avoiding a particular failure mode such as the excessive warpage of thin membranes or cracking [104]. Compared to stoichiometric films however, silicon-rich SiN_x has lower etch resistant to KOH etching, which can be problematic [16]. Parallel-plate PECVD is often used over LPCVD for SiN_x deposition because of its higher deposition rate (up to 150 nm/min) and lower deposition temperature (250-400°C) [16]. PECVD also offers an improved ability to tune the stress of deposited films all the way from very compressive to moderately tensile while maintaining a similar stoichiometry. PECVD SiN_x films are however, less dense than LPCVD films and have larger H_2 incorporation. The high ion energies produced by the parallel plate sources can also lead to damage in sensitive electronic devices like AlGaN HFETs [108] and other III-V devices [95].

ICP-CVD of SiN_x combines many of the advantages of both LPCVD and PECVD, offering highly dense films with low hydrogen incorporation, low ion bombardment, moderate deposition rates, compressive-to-tensile stress control, and achieves all of this using much lower deposition temperatures (as low as room temperature, but typically at temperatures between 50 and 150°C), which makes it compatible with a wider variety of materials. As a further advantage, the higher

dissociation power of the ICP source allows N_2 to be used instead of NH_3 as the source of nitrogen atoms for the deposited films. NH_3 is corrosive and requires much more expensive abatement and flow control equipment, and tends to produce films with higher H_2 content [16].

This chapter focuses on the experiments undertaken in the IFIC system to verify whether these superlatives could be achieved in a tool with a much smaller physical and financial footprint. As was done with SiO_2, the characterization process began with an exploration of the parameter space and the establishment of a reliable process window for depositions, followed by a series of tests designed to produce a quantitative response surface models of the output film properties, and lastly, follow-up testing to confirm the consistency of the system's performance and the accuracy of the derived models.

5.1 Early Testing

The understanding of the IFIC's behavior/dynamics/capabilities provided by the SiO_2 experiments of the previous chapter were immensely useful and greatly accelerated the path to stable SiN_x processes. Before beginning actual depositions, recipes and trends from the literature were gathered and used to establish a reasonable starting point for each of the parameters. Once again the papers describing depositions using the Sentech SI 500 D ICP-CVD system and 5% SiH_4/He were very helpful [32], [72], [73], as were technical reports from Plasma-Therm [6] and Oxford Instruments [50].

5.1.1 Chamber Spacing

The first experimental steps taken in the SiN_x characterization process were to confirm that the chamber geometry-specific effects uncovered during the SiO_2 depositions still held for SiN_x. This began with tests to confirm that plasma discharges using the new SiH_4/He/N_2/Ar deposition chemistry could be attained and stably maintained with the same ICP coil position used for SiO_2. Even though the ICP coil can be moved relatively easily up and down along the main axis of the UCA, the process still takes multiple steps and would not be convenient for end-users to check or

carry out before each process. Fortunately, these early tests confirmed that there were no stability problems at the 300W ICP power used for most depositions.

Another set of early tests were run without the aperture plates devised to improve the SiO_2 deposition uniformity, and the depositions resulting from these tests showed a similar radial non-uniformity pattern (the films were thickest in the middle and thinnest along the edges). Therefore, the same aperture plate found to work best for SiO_2 (the plate denoted as AP1.25 in Figure 4.4b) was reintroduced to the system, which, as expected, improved the uniformity significantly. These tests were run using the ideal aperture plate-to-substrate spacing of 21.7 mm found for SiO_2 (see **Figure 4.6**). While it was very clear that this spacing plus the AP1.25 was a marked improvement, the spatial thickness profile of the showed a noticeably W-shaped profile similar to what was seen in the SiO_2 tests when the substrate was too close to the aperture plate. Therefore, several new spacing tests were undertaken. A spacing of 23.7 mm, 2 mm lower than the SiO_2 case, was found to produce films with the best Uniformity values. Profiles from a selection of these tests are shown in **Figure 5.1**.

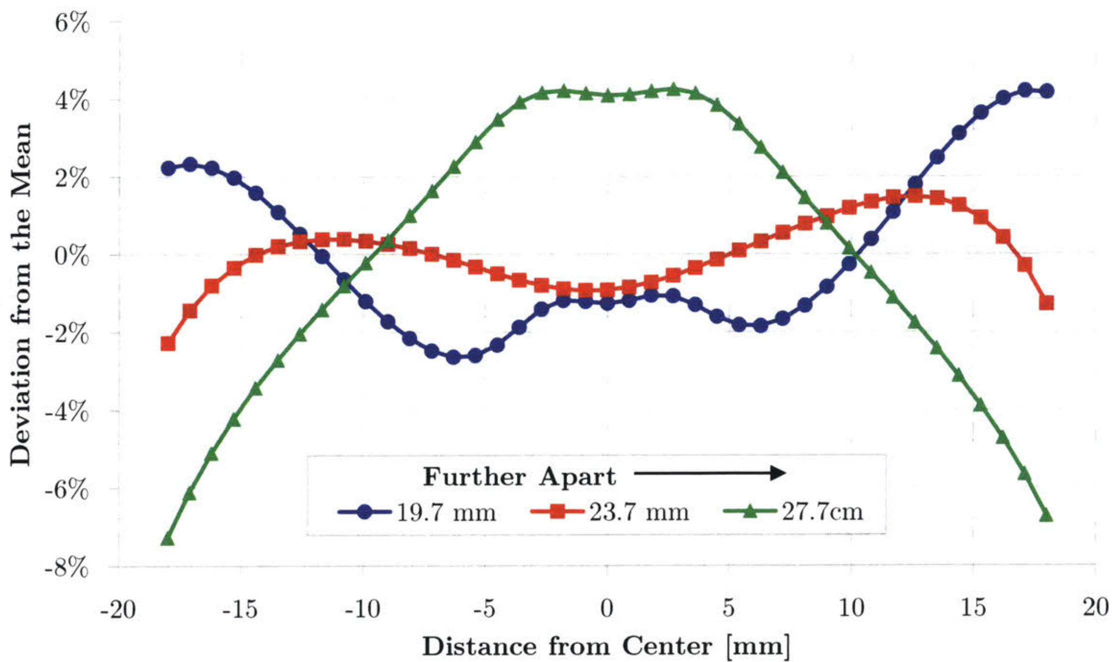

Figure 5.1: Percent deviation from the mean SiN_x film thickness across the wafer as a function of the spacing between the wafer and aperture plate (AP1.25, 1.25" center diameter). The edge exclusion is 4 mm in each scan.

As the above data shows, the resulting thickness profile at the 23.7 mm spacing has a slight M-shaped profile, but the Uniformity and coefficient of variation (CV) values (at the standard 4 mm edge exclusion) are much improved at this spacing. Specific uniformity values and the reasoning behind the profile shape will be discussed in **Section 5.3.2.4**.

While the ideal scenario for the IFIC would be to have a single, unified set of spacings that apply for all materials being deposited, the fact that achieving good film thickness uniformity for both SiO_2 and SiN_x requires changing only the height to which the substrate is raised for after being loaded into the chamber should not be overlooked. Other commercial ICP-CVD tools that use forms of aperture plates for uniformity control actually require different aperture plate geometries [50], [93] for SiO_2 and SiN_x. Swapping these plates requires opening the process chamber, which means that a significant amount of time is required to switch between depositing SiO_2 and SiN_x in these tools. In a high-volume production environment where a single tool is used only to deposit a specific film, this is not an issue, but for the prototyping and low-volume, high process variety environments for which the Inch Fab initiative tools are best suited, this would be a serious drawback. Changing the substrate height on the other hand is something that happens external to the processing chamber, and the substrate always has to be raised from the loading/unloading position (~100 mm away from the aperture plate) to the processing position. A very simple mechanical solution using slide-in spacers (the SiN_x spacer being 2 mm thicker than the SiO_2 version) on the LCA lift assembly can be used to reliably set the appropriate height for the material being deposited, and a more closed loop solution can be implemented using a linear slide potentiometer that measures the height of SCA support plate in the lift assembly and compares it to the correct height stored in the control system for the desired material.

5.1.2 Stress Reduction

After confirming the required geometrical parameters for uniform film thicknesses, the output characteristics of deposited films were addressed. The earliest films deposited using the recipes derived from the published literature produced acceptable deposition rates and indices of refraction, but the films all showed large levels of compressive stress (as high as -4 GPa). From

this point, single factor testing quickly showed that increasing the deposition pressure and the Ar flow drastically reduced the amount of compressive stress seen in the films. The increases together were actually enough to produce tensile films.

Decreasing film stress by increasing the process pressure is a method acknowledged and utilized by many in the literature [50], [72], [109]. The shorter mean free paths at higher pressure reduce the ion bombardment energy seen by the growing film, which in turn reduces the amount of compressive stress [72]. No reports however, have been found that specifically document the effect of Ar flow on stress (or its effects on any other output parameter). A probable mechanism can be inferred though by stitching together results from several different sources. Typical Ar/N_2 ratios seen in ICP-CVD SiN_x recipes are 2-4 [6], [7], [93] for low-stress films. This is vastly different from the 5% SiH_4/He papers, which report ratios of 7-20 for low-stress films [32], [72], [73]. So it would seem that the addition of significant amounts of He to the deposition environment require the addition of appreciably more Ar to keep the film stress low. Adding substance to this theory are results presented in [95], which show that the addition of He to PECVD SiN_x depositions significantly increases the compressive stress of the films. The mechanism suggested for this is that He catalyzes the creation of N^+ ions in the plasma discharge, which leads to a large increase in the concentration of nitrogen bonds in the film and a resulting stress increase [110]. The addition of Ar then, which assists in the dissociation of SiH_4 [7], [50], and has been observed to preferentially sputter N atoms (over Si) from SiN_x films [7] likely serves to bring the deposition back into balance and curb the stress increase caused by the increased He. This effect of argon flow on the SiN_x film stress, as well as on the other film properties will be examined further in the response surface test sequence.

5.2 Establishing a Process Window

Following the sequence used for the SiO_2 characterization, after the initial substrate spacing and high average film stress were resolved, the rest of the input parameter space was explored to establish a reliable process window for SiN_x depositions. The parameters tested were the total

and relative flows of SiH_4/He, N_2, and Ar, the ICP power, bias power, chamber pressure, and substrate temperature. The parameters measured for each sample were deposition rate, index of refraction, thickness uniformity, average film stress, and etch rate in 7:1 BOE. The methods and procedures used to carry out these measurements were detailed in **Section 3.2.5**. The results from these exploratory tests are shown in **Table 5.1**, which relates each input parameter to the output film characteristics, and **Table 5.2**, which provides the reasonable operating range for each input parameter and comments on what happens above and below these ranges. This represents the process window for quality SiN_x depositions in the IFIC system.

	Deposition Rate	**Index of Refraction**	**Average Film Stress**	**BOE Etch Rate Ratio**	**Uniformity**
↑ ICP Power	↑	↓	↑	↓	–
↑ Bias Power	↓	–	↑↑	↓	–
↑ Total Gas Flow	↑	–	–	–	–
↑ N_2/SiH_4 Ratio	↑	↓	↓	↑	–
↑ Ar/SiH_4 Ratio	↓	↓	↓	**varies**	–
↑ Temperature	↓	↑	↑	↓	–
↑ Pressure	↓	↓	↓	**varies**	–
↑ Substrate-to-AP gap	↓	**varies**	↓	↑	↓

Table 5.1: The effect of increasing input parameters on output SiN_x film characteristics. A dash indicates a small or negligible effect over the range tested.

Parameter	Process Window	Below This Range	Above This Range
ICP Power	250 – 350 W	Plasma discharge difficult to maintain	Excess chamber heating
Bias Power	0 W	n/a	Excess compressive film stress
Total Gas Flow	105 – 270 sccm	Low deposition rate	Turbo throughput-limited
N_2/SiH_4 Ratio	0.5:1 – 1:1	Very Si-rich films: $n > 2.3$, high compressive film stress	Very N-rich films: $n < 1.8$, high tensile stress
Ar/SiH_4 Ratio	1.5:1 – 4:1	High compressive film stress	High tensile film stress
Temperature	25°C – 150°C	n/a	Reduced material compatibility
Pressure	30 – 100 mTorr	High compressive film stress	Low-density films, pressure control difficult
Substrate-to-Aperture Plate Gap	22 – 25 mm	Poor uniformity	Low deposition rate, poor uniformity

Table 5.2: Process window for quality SiN_x depositions

As a result of the tests performed to generate the above tables, two important changes to the standard deposition process were made. The first change was increasing the total gas flow used for depositions. This change was made for two reasons. The first was to increase the overall deposition rate, which was, on average, about 16 nm/min when using flows of 150 sccm SiH_4/He, 1.5 sccm N_2, and 6 sccm Ar. Increasing these flows by a third to 200/2/8 raised the average deposition rate ~25% to ~20 nm/min. Reported literature values for ICP-CVD SiN_x deposition rates vary significantly with the tool and recipe parameters chosen, but the 20 nm/min value represents half of the rate reported by investigators using the 5% SiH_4/He mixture [32], which is the roughly same fraction that was observed for SiO_2 (35 nm/min vs. 75 nm/min with 5% SiH_4/He [71]). No adverse effects on film quality were observed with along with rate increase, and a higher overall deposition rate is useful for most situations.

The second reason behind the flow increase was to increase the pressure control sensitivity in the chamber. The throttle valve system used to control the pressure operates by changing the conductance of the foreline with a rotating butterfly mechanism. The butterfly mechanism moves

in discrete steps, with ~250 steps[32] between fully open and fully closed. As the valve becomes more closed and the conductance decreases, the effect of each additional step on the pressure increases. At the higher average process pressures of SiN_x depositions (75 mTorr as compared to 48 mTorr for SiO_2 depositions), the valve is more closed, which increases the pressure sensitivity, and small changes to the pressure become more difficult. Adding more process gas serves to bias the valve back into a less sensitive operating window, allowing finer adjustment of the process pressure.

The second change made to the standard SiN_x deposition process was to forgo using substrate bias power in any of the future characterization experiments. The effects of adding bias power can be seen in the single factor testing results shown in **Figure 5.2**.

[32] This is an empirical observation. When directly controlling the position of the valve, the input is in the form of percent closed from 0-100. Non integer values are accepted, but small changes (e.g. 75.3% to 75.5% closed) do not always result in an updated valve position.

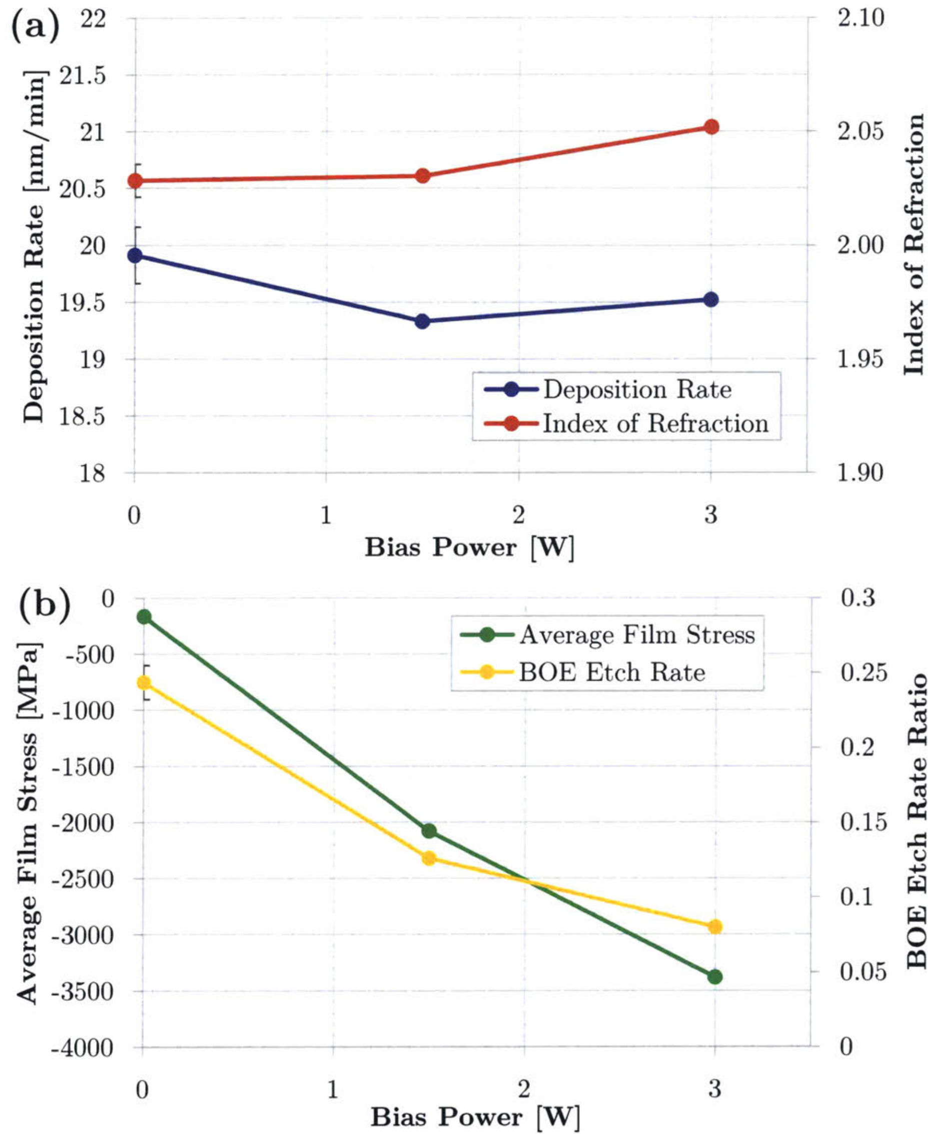

Figure 5.2: Bias power effects on film characteristics. Non-uniformity increases slightly with increasing base power (3.2% to 3.5%). Error bars for 0 W points indicate one standard deviation. Constant parameter values: 300W ICP Power, 2 sccm N_2, 8 sccm Ar, 75 mTorr, 100°C substrate temperature.

Looking at the data displayed in the above figure, it is clear that by far the largest effect of adding bias power is dramatically increasing the compressive stress in the films. This relationship is much more pronounced than what was observed in in SiO_2, and in practice too coarse to be of significant use, as the fine control of very low bias power is already difficult based on the available equipment (see **Section 2.4.3**). The bias power effect on deposition rate and index of refraction are minor in comparison to what can be achieved by modulating the other input parameters, and

BOE etch rate effect is of a similar order to what can be achieved. Given that the average film stress can be modulated using several other parameters, this essentially obviates the need to use bias power as an input. This is positive in the sense that it reduces the number of knobs that need to be tuned for quality SiN_x depositions, but the real potential value comes from recalling that the results of the SiO_2 response surface testing also showed that the effects of bias power could generally be subsumed by the other inputs, except for perhaps the rare case in which SiO_2 films with large compressive stresses are required. If bias power is not needed for SiO_2 or SiN_x, the associated RF generator and impedance matching network are no longer necessary. As discussed in the cost analysis section (**Section 2.5**), RF equipment is very expensive and, particularly in the case of substrate bias power, not well matched to the ultra-low output power requirements of the IFIC. Even the least expensive commercial RF generator options require the addition of an attenuator to force their outputs to a more stable operating point. Eliminating this RF generator and matching network would significantly reduce the cost of the IFIC, which for many potential users would be well worth the slight loss of functionality. The bias power connection in the SCA is not expensive or complex, so it could be left in place, which would allow users the option of adding the bias power back if needed.

5.3 Response Surface Testing

In order to expand on the knowledge gained from the process window testing and develop a predictive model for the deposition characteristics of SiN_x films produced in the IFIC, the response surface method (RSM) was employed. The mechanics of RSM testing were explained in **Section 3.2.1**. As was done for the SiO_2 characterization process, a circumscribed central composite design (CCD) was chosen for the SiN_x test format. The specifics of the design, the resulting response surface models, and validation of those models are discussed in the following sections.

5.3.1 RSM Parameter Selection

Like the SiO_2 characterization process, there are many more parameters ("factors" in RSM terminology) available that affect the film properties than can reasonably be tested in a CCD

design. A three factor circumscribed CCD design was sought for logistical reasons. The results of the process window testing identified the relative gas flows (SiH_4/He, N_2, Ar), the process pressure, and the substrate temperature as the factor candidates which had the most significant effects on the measured film characteristics. Of these, the N_2 flow (or the relative N_2/SiH_4 ratio) has the largest effect on most of the parameters, and the effects of varying Ar flow hold particular interest because they have not been reported on, despite being included as process gas (and in very different quantities) in nearly all of the recipes found in the literature. Process pressure and temperature were both scrutinized for the third factor slot, and ultimately process pressure was chosen because as a factor it can be quickly and easily controlled to a finer degree than temperature, and because its effect on film characteristics (within the process window) is less pronounced than temperature. In this way, it was theorized that as a factor it could serve as a fine tuning knob to dial in specific film characteristics which had first been set by the coarse tuning N_2 knob. The RSM results shown in the next section do appear to bear this hypothesis out. The effect of substrate temperature was investigated using single factor testing, and the results are presented in **Section 5.4.1** following the discussion of the RSM testing.

The CCD design used for the three factors is shown in **Table 5.3**, along with the formulas needed to convert between the coded and actual factor values. The alpha value of 1.682 for the design provides rotatability (and happens to be nearly orthogonal, but blocking factors were not used in the calculation of any resulting models). The test sequence includes 6 center point tests to check for repeatability was completed over the course of two experimental sessions.

Standard Order	Run Order	Block	Test Type	(Coded Values) F1	F2	F3	(F1) N_2 Flow [sccm]	(F2) Ar Flow [sccm]	(F3) Pressure [mTorr]
1	8	1	Cube	-1	-1	-1	1.7	6.5	60
2	17	1	Cube	1	-1	-1	2.3	6.5	60
3	11	1	Cube	-1	1	-1	1.7	9.5	60
4	2	1	Cube	1	1	-1	2.3	9.5	60
5	14	1	Cube	-1	-1	1	1.7	6.5	90
6	6	1	Cube	1	-1	1	2.3	6.5	90
7	18	1	Cube	-1	1	1	1.7	9.5	90
8	12	1	Cube	1	1	1	2.3	9.5	90
9	16	1	CP	0	0	0	2	8	75
10	10	1	CP	0	0	0	2	8	75
11	9	1	CP	0	0	0	2	8	75
12	1	1	CP	0	0	0	2	8	75
13	13	2	Star	-1.682	0	0	1.5	8	75
14	4	2	Star	1.682	0	0	2.5	8	75
15	19	2	Star	0	-1.682	0	2	5.48	75
16	5	2	Star	0	1.682	0	2	10.52	75
17	3	2	Star	0	0	-1.682	2	8	49.8
18	7	2	Star	0	0	1.682	2	8	100.2
19	15	2	CP	0	0	0	2	8	75
20	28	2	CP	0	0	0	2	8	75

Coding Formulas			
	$CP_{N_2} = 2$ sccm	$\Delta_{N_2} = 0.3$ sccm	$N_2\ Flow = (\text{Coded Value})\Delta_{N_2} + CP_{N_2}$
	$CP_{Ar} = 8$ sccm	$\Delta_{Ar} = 1.5$ sccm	$Ar\ Flow = (\text{Coded Value})\Delta_{Ar} + CP_{Ar}$
	$CP_{Press} = 75$ mTorr	$\Delta_{Press} = 15$ mTorr	$Pressure = (\text{Coded Value})\Delta_{Press} + CP_{Press}$

Table 5.3: RSM test sequence for SiN_x. Also shown are the equations and valued needed to convert factors from coded to actual units.

Table 5.4 provides the values used for each of the constant, non-factor parameters during the RSM sequence. These values are at or near the center of the process window defined in the previous section to maintain a stable deposition environment for the RSM testing.

Parameter	Value	Notes
ICP Power	300 W	This value was found to reliably sustain a plasma discharge, produce reasonable deposition rates, and did not induce excessive chamber heating.
SiH_4/He Flow	200 sccm	3.0 sccm of SiH_4 equivalent. This value was kept constant and the N_2 and Ar flow were varied.
Substrate Temperature	100°C	This temperature is sufficiently high to produce high quality films, but still low enough to accommodate many different substrate materials.
Bias Power	0 W	Even small bias powers were found to induce large compressive stresses, so none was applied.
Aperture Plate	AP1.25	This aperture plate has a 1.25" diameter center circle and was found to produce the most uniform films.
Substrate-Aperture Plate Spacing	23.7 mm	This distance produced the most uniform films.
Substrate Backside Helium Pressure	20 torr	This pressure provides sufficient heat transfer from the SCA to the substrate and does not cause a He leak to from the SCA to the chamber.
Test Time	10 minutes	This value was chosen to produce films with sufficient thickness for post-processing measurements while not requiring large amounts of processing time.

Table 5.4: Constant parameters used for the SiN_x RSM test sequence.

5.3.2 RSM Results

Once the RSM test sequence was completed, the film characteristics of each of the samples were measured using the standard sequence laid out in **Section 3.3.2**. The quantitative results from these tests are summarized in **Table 5.5**.

Standard Order	Deposition Rate [nm/min]	Index of Refraction	Average Film Stress [MPa]	Coefficient of Variation [%]	Uniformity [%]	BOE Etch Rate Ratio
1	18.16	2.248	-799.8	1.76%	3.61%	0.19
2	24.36	1.958	74.5	1.53%	3.07%	0.39
3	16.57	2.195	-600.6	1.66%	3.40%	0.18
4	22.46	1.960	261.6	1.36%	2.75%	0.35
5	16.61	2.208	-613.9	2.49%	4.41%	0.16
6	22.23	1.976	169.1	1.85%	3.34%	0.30
7	15.56	2.149	-500.5	2.27%	3.88%	0.15
8	20.99	1.947	276.6	1.89%	3.40%	0.38
9	19.53	2.034	-173.6	1.69%	3.31%	0.23
10	19.82	2.023	-171.9	1.63%	3.13%	0.25
11	19.72	2.034	-158.0	1.66%	3.19%	0.24
12	19.55	2.044	-185.6	1.66%	3.36%	0.24
13	15.72	2.334	-887.0	2.57%	4.51%	0.20
14	23.98	1.931	347.0	1.81%	3.05%	0.59
15	20.86	2.068	-363.8	1.69%	3.06%	0.23
16	18.84	2.009	-45.5	1.73%	3.36%	0.23
17	20.86	2.046	-305.3	1.20%	2.32%	0.22
18	18.68	2.013	-119.8	2.19%	3.78%	0.25
19	20.27	2.025	-166.9	1.64%	3.10%	0.24
20	19.65	2.035	-181.6	1.65%	3.16%	0.24

Table 5.5: Raw results for each sample in the SiN_x RSM test sequence

Using the same framework established during the SiO_2 RSM sequence, the above SiN_x dataset was loaded in ***R*** and the *rsm* library [87] was used to build and assess various model fits to each of the measured response variables. The standard fitting procedure considers first-order, second-order, and two-factor interaction terms, and subsets thereof. Data on the quality of the fits, including an ANOVA table, were generated with each fit, which allowed the goodness of fit to be examined and compared across models. The upcoming sections will discuss these fits and the overall results from the RSM sequence.

5.3.2.1 Deposition Rate

The average deposition rate observed during the RSM sequence was 19.7 nm/min, but the spread of values measured was quite large, reaching as high as 24.4 nm/min and dipping to 15.6 nm/min depending on the factor values, specifically the flow of N_2.

The fitting process in ***R*** produced a second-order model with two-factor interactions that fit the data well (lack-of-fit p-value = 0.19). The average residual between the collected data and the fitted model is 0.20 nm/min, with an average percent error of 1.07%. The standard residual deviation is 0.25 nm/min. The model coefficients can be seen in **Table 5.6**, and contour plots for each pair of factors follow in **Figure 5.3**.

N_2 Flow	Ar Flow	Pressure	$N_2 \cdot$ Ar	$N_2 \cdot$ Press	Ar $\cdot$ Press
2.712	-0.672	-0.720	-0.0625	-0.130	0.150

$(N_2$ Flow$)^2$	(Ar Flow$)^2$	(Pressure$)^2$	Intercept
-0.011	-0.011	-0.040	19.763

Table 5.6: Fit coefficients for second-order IFIC SiN_x deposition rate model.

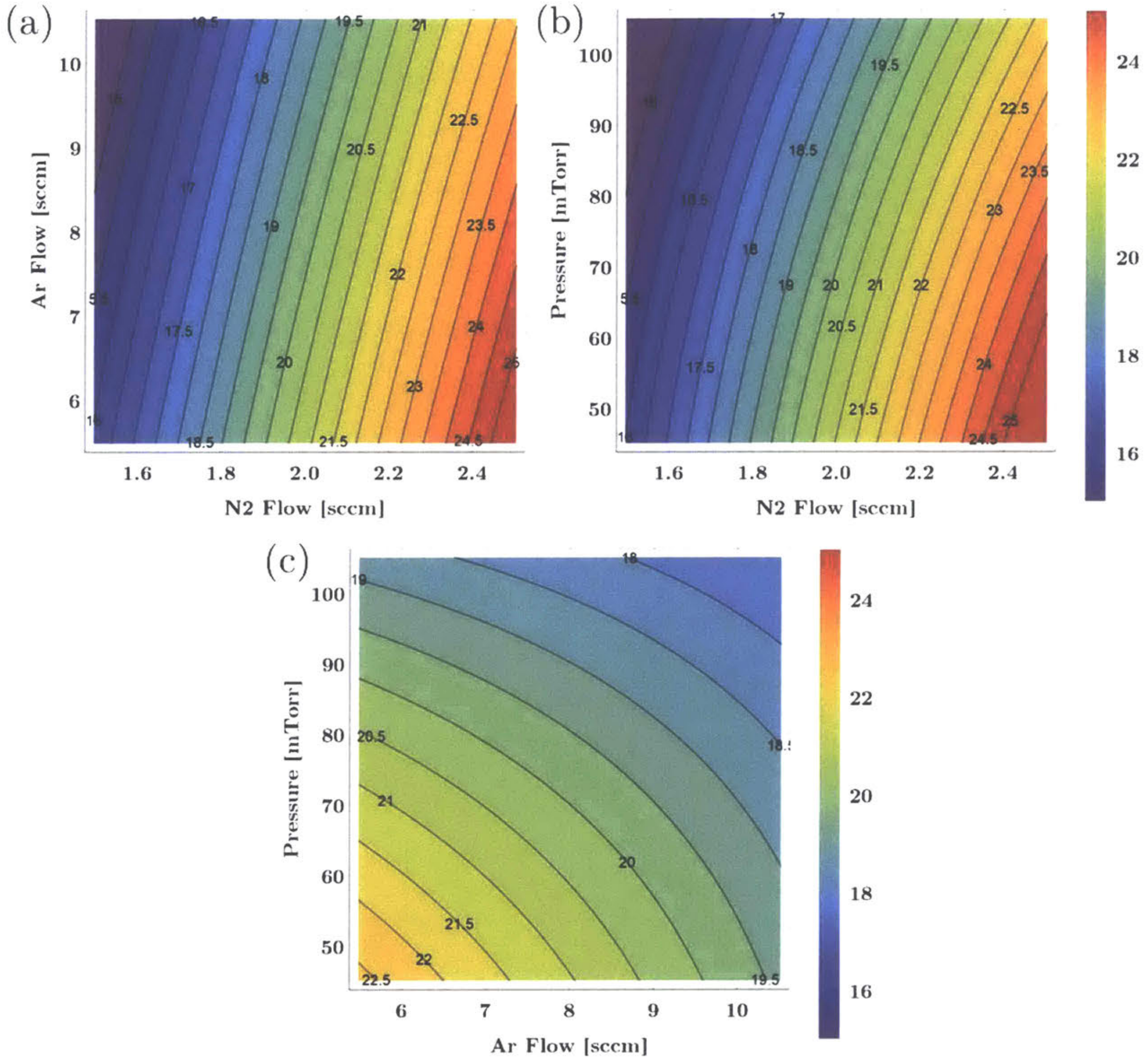

Figure 5.3: Contour plots showing the RSM model-predicted SiN_x deposition rate vs. pairs of input factors. Each graph is evaluated at the center point value of the factor not shown. Contours are equal across all plots.

The data of **Figure 5.3** shows a clear positive correlation between N_2 flow and deposition rate, which fits with the observations from early depositions and with literature expectations [25], [32], [66]. The influence of Ar flow and process pressure is smaller than that of N_2, but have a very similar magnitude compared to one another. The decrease in deposition rate with increasing Ar flow can be attributed to increased sputtering of the deposited film, but the pressure effect is not as straightforward. Several investigators have documented increasing deposition rates with increasing pressure [50], [109], but the articles using 5% SiH_4/He report the same decrease in

deposition rate with increasing pressure [32], [72]. One big difference between these sides is the actual pressure range used during deposition. In [50], [109] the process pressure ranges from 3-10 mTorr, as compared to 38-113 mTorr in [32], [72] (and 50-100 mTorr in the IFIC RSM sequence discussed here). An explanation for this different behavior between pressure ranges may relate to the large amount of diluent He included in the high pressure ranges. For the systems using non-diluted SiH_4, the partial pressures of SiH_4 and N_2 comprise a large fraction of the total pressure, and therefore are significantly increased when the process pressure increases (e.g. from ~2 to ~4 mTorr for both SiH_4 and N_2 when the process pressure rises from 4 to 8 mTorr in [109]), providing a higher concentration of potential reactive species and increasing the deposition rate. For the IFIC and 5% SiH_4/He system, increasing the process pressure still raises the partial pressures, but to a much smaller absolute amount (e.g. from ~0.7 to ~1.4 mTorr for SiH_4 and ~0.5 to 1.0 mTorr for N_2 for a pressure rise from 50 to 100 mTorr in the IFIC RSM). The He in the system, which accounts for more than 90% of the total pressure, has its partial pressure rise from ~46.9 to 93.8 mTorr when the system pressure rises from 50 to 100 mTorr. This much larger absolute difference may, in effect, screen out some of the reactive species from reaching the substrate, causing the deposition rate to decrease.

5.3.2.2 Index of Refraction

Unlike the SiO_2 RSM sequence, which did not feature much variation in the index of refraction, the SiN_x RSM showed that the index of refraction can be precisely tuned by the input factors. The ability to control the index of refraction is very important for optical applications and as a proxy for determining a film's other characteristics, such as KOH etch resistance [16]. A second-order model with two-factor interactions resulted in a very good fit to the gathered data (lack-of-fit p-value = 0.27) and smallest residual deviation of any of the RSM models for SiO_2 or SiN_x. The average index residual was just 0.005, or 0.27%. The standard residual deviation is 0.006. The model coefficients and factor-pair contour plots can be seen below.

N_2 Flow	Ar Flow	Pressure	$N_2 \cdot$ Ar	$N_2 \cdot$ Press	Ar $\cdot$ Press
-0.120	-0.018	-0.010	0.011	0.011	-4.7×10^{-3}

$(N_2\text{ Flow})^2$	$(\text{Ar Flow})^2$	$(\text{Pressure})^2$	Intercept
0.038	4.4×10^{-3}	1.4×10^{-3}	2.032

Table 5.7: Fit coefficients for second-order IFIC SiN_x index of refraction model.

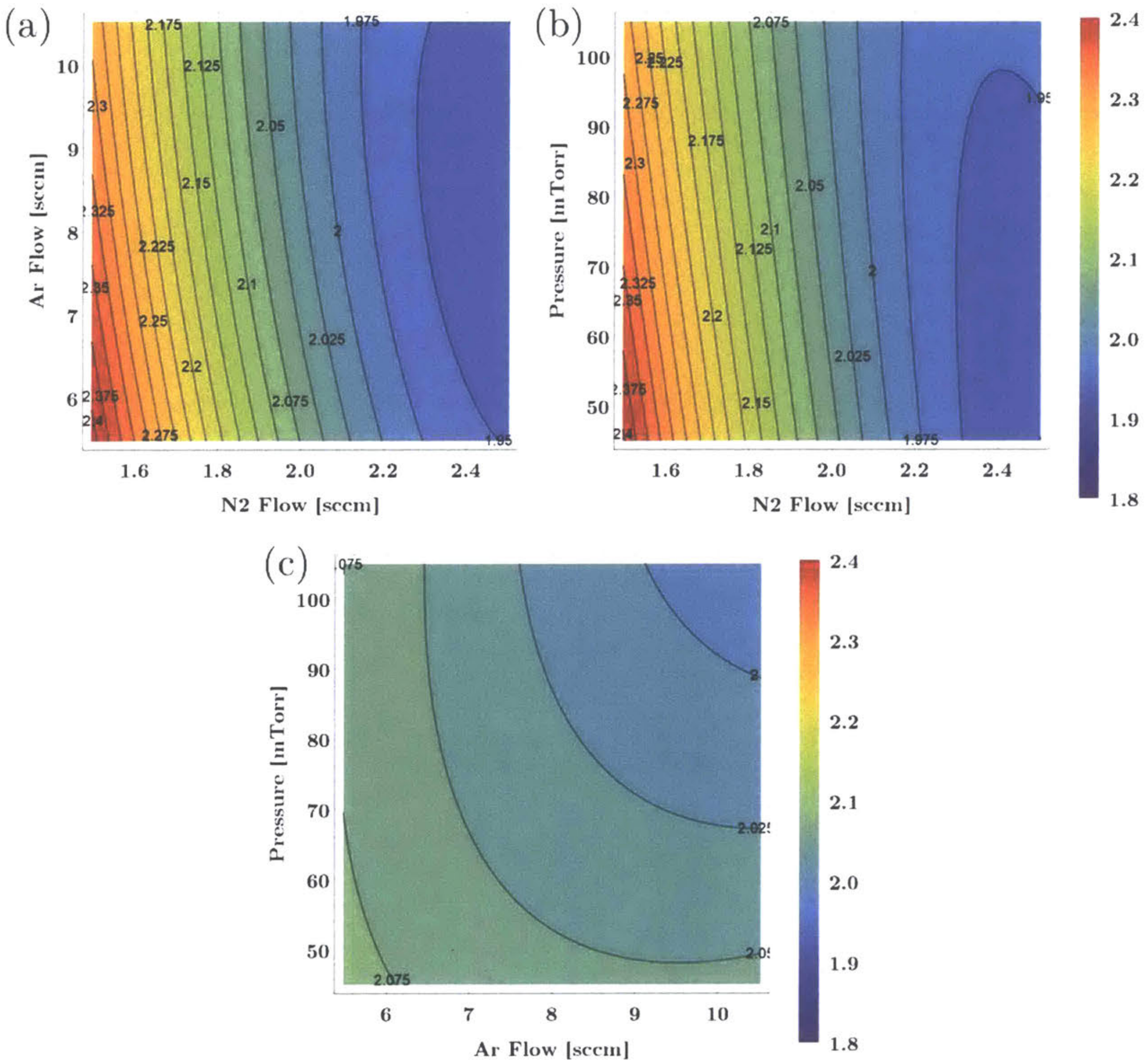

Figure 5.4: Contour plots showing the RSM model-predicted SiN_x index of refraction vs. pairs of input factors. Each graph is evaluated at the center point value of the factor not shown. Contours are equal across all plots.

Once again the plots show that the N_2 flow plays the largest role, decreasing the index of refraction with increasing flow. At the center point values for Ar flow and pressure, the model predicts indexes from 1.936 to 2.340 over the tested process window (the observed values at these N_2 flows (the $\pm\alpha$ tests) were very close: 1.931 and 2.334). Ar flow and process pressure have similar effects, generally increasing the index with increasing values, and serve as fine-tuning knobs for the index. For index-sensitive applications, it is important to have a fine tuning knob from a practical perspective. The N_2 flow is set by mass flow controllers, which have a high level of precision, but do drift out of calibration (accuracy) over time[33]. If the index of refraction for a process begins to drift, the Ar flow and pressure, with their lower overall index-sensitivity, can be used to compensate for this drift until it shifts back or re-calibration is deemed necessary.

As mentioned earlier, the index of refraction for a SiN_x film, which is relatively easy to measure (see **Section 3.2.2**) can be used as a proxy for determining other film characteristics. In [111]–[113], the index of refraction was used to develop a formula for estimating the Si:N ratio in a film. This formula is below.

$$Si\!:N\ Ratio\ in\ film = \frac{Si}{N} = \frac{3}{4}\left(\frac{n_{film} - 2 * n_{Si_3N_4} + n_{Si}}{n_{Si} - n_{film}}\right) \quad (5.1)$$

Using this formula with the standard $n_{Si_3N_4} = 2.0$ and $n_{Si} = 3.85$, the the Si/N ratios for the deposited RSM films can be estimated. Combined with the RSM model results, the Si:N ratio for a SiN_x film deposited in the IFIC can be predicted just from its input parameters. An example of this is shown in **Figure 5.5**, which plots the model-predicted ratio and measured data points (at 8 sccm Ar, and 75 mTorr) versus the input N_2 flow. Similar curves or contour maps can easily be generated for any other input factors within the process window.

---

[33] The Alicat MFCs used in the IFIC have a post-calibration accuracy of 0.8% of the setpoint flow plus 0.2% of the full scale flow value. For the 10 sccm full scale N_2 MFC, this leads to range of 2±0.036 sccm for the center point value. Higher accuracy could be gained by going to a smaller full scale value, but this also increases the price of the MFC.

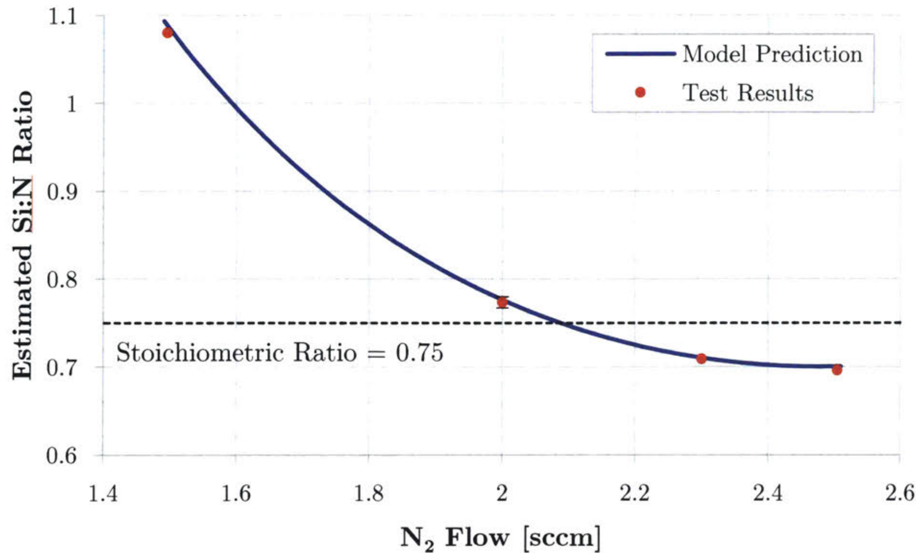

Figure 5.5: Estimated Si:N ratio vs. N2 flow (at 8 sccm Ar and 75 mTorr). The error bar barely visible on the 2 sccm N_2 point represents one standard deviation.

5.3.2.3 Average Film Stress

Achieving the desired stress level in SiN_x film layers is essential to the performance of many micro-and nanoscale devices. The wide range of stress levels achievable using plasma-based CVD SiN_x processes is one of the largest reasons it is used over LPCVD. ICP-CVD, like PECVD, has been shown to be able to tune film stress from compressive to tensile, while maintaining an index of refraction near the stoichiometric value of 2. The RSM results shown below confirm that the IFIC is also capable of this level of control. Using the standard fitting procedures in R, a second-order fit with two-factor interactions produced a reasonable fit to the data ($R_{adj}^2 = 0.992$, average residual = 16.9 MPa), but a significant lack-of-fit ($p = 0.003$). When examining the residuals for this fit, a clear cubic dependency was seen (rather than the expected normal distribution for a good fit). By adding in third-order terms for each of the three factors (just the cubic terms, no higher two- or three-factor interactions), the lack-of-fit became non-significant ($p = 0.09$), and the residuals returned to being normally distributed with an average value of 7.4 MPa. The resulting model coefficient and factor-pair contour plots are provided in **Table 5.8** and **Figure 5.6**.

N_2 Flow	Ar Flow	Pressure	$N_2 \cdot$ Ar	$N_2 \cdot$ Press	Ar · Press
436.7	65.67	46.33	-2.256	-22.04	-20.68

$(N_2\text{ Flow})^2$	$(\text{Ar Flow})^2$	$(\text{Pressure})^2$	$(N_2\text{ Flow})^3$	$(\text{Ar Flow})^3$	$(\text{Pressure})^3$	Intercept
-30.98	-7.871	-10.66	-24.72	10.24	3.122	-173.4

Table 5.8: Fit coefficients for simple third-order IFIC SiN_x average film stress model.

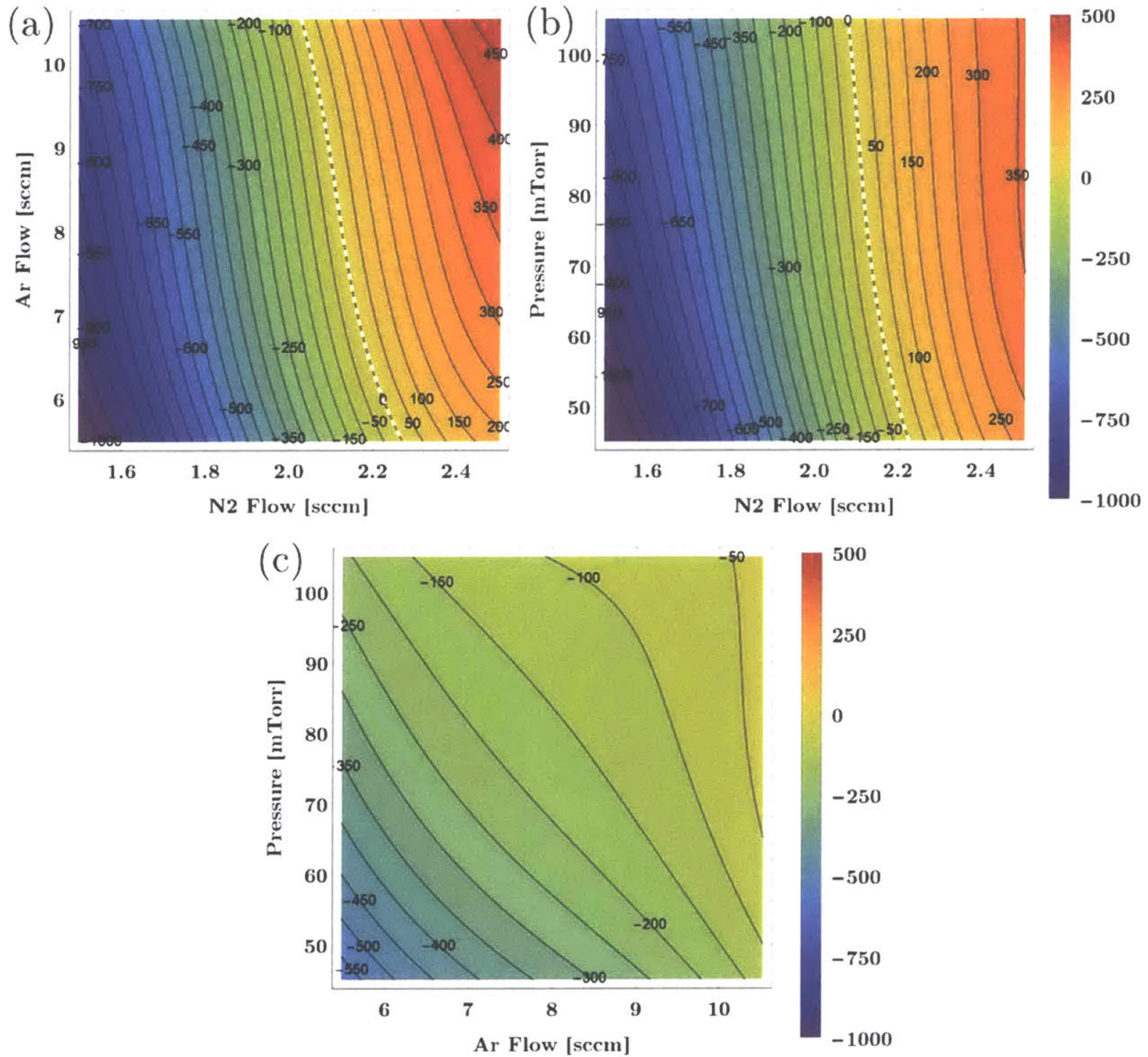

Figure 5.6: Contour plots showing the RSM model-predicted SiN_x average film stress vs. pairs of input factors. Each graph is evaluated at the center point value of the factor not shown. Contours are equal across all plots.

As the contour plots indicate, the N_2 flow again plays the role of the coarse knob when predicting the average film stress of a deposition, with increasing flows pushing the stress into the

tensile region. More than 1 GPa of stress can be modulated with the adjustment of just 1 sccm of N_2 over a wide range of Ar flow and pressure setpoints. With decreasing N_2 flow, the film becomes more Si-rich, which leads to more compressive stress, just as is seen with the nitrogen source (NH_3) in LPCVD [104]–[106], and other plasma-based CVD systems [32], [50], [66], [95]. Examining the model coefficients, the Ar flow and pressure have similar effect magnitudes for low to moderate N_2 values where the stress of compressive, but the pressure effect levels off for higher pressure values as the stress becomes neutral to tensile with increasing N_2 and Ar flow. This can be seen in **Figure 5.7**, which plots the stress vs. pressure at several operating points. Measured data points are shown where available. This matches up with several observations in the literature [32], [66].

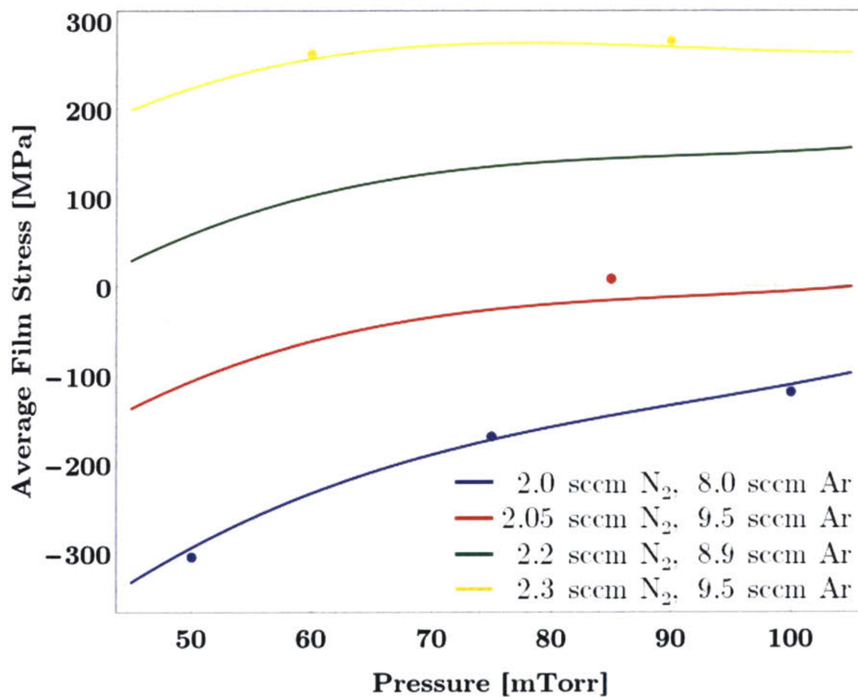

Figure 5.7: Evolution of pressure effect on film stress for several scenarios. Dots indicate data from a measured test.

As was stated in the index of refraction section, there is definite value to the smaller Ar flow and pressure effects observed here. The ability to fine-tuning the stress of a SiN_x film can be particularly important in MEMS and chip-stacking processes where bonding of substrates is a key part of the fabrication process, and wafer bow needs to be compensated for.

5.3.2.4 Uniformity

The film thickness uniformity across the substrate is a crucial metric by which CVD systems and process are compared. The largest uniformity challenges with the IFIC were met and mitigated in the early stages of the SiO_2 deposition characterization (see **Section 4.1.2**). With the optimization of the substrate-to-aperture plate spacing discussed in **Section 5.1.1**, the SiN_x uniformity was greatly improved. Uniformity measurements were taken for each of the SiN_x RSM samples (with 4 mm exclusion zone) using spectral reflectometry as described in **Section 3.2.4**, and the coefficient of variation and the (capital U) Uniformity were calculated[34].

The results were largely very consistent, with the CV values ranging from 1.20% to 2.57% (average: 1.80%), and the Uniformities from 2.32% to 4.51% (average: 3.36%). The 2D height data for each sample was also examined, particular for the samples at each end of the ranges. **Figure 5.8** shows the 2D heights for the first and last sample of the RSM sequence, and the $\pm\alpha$ tests for pressure (50 mTorr and 100 mTorr), which showed some of the most and least uniformity, respectively.

---

[34] The use of variable angle spectroscopic ellipsometry to gather the index of refraction data prior to the reflectometry measurements proved especially useful for SiN_x samples, which featured a much larger spread of indexes compared to the SiO_2 samples. For each sample, the precise index data gathered by ellipsometry was used to build a custom material model in the reflectometry system. This greatly improved the accuracy of the collected data (as determined by the goodness of fit calculated for each measurement point).

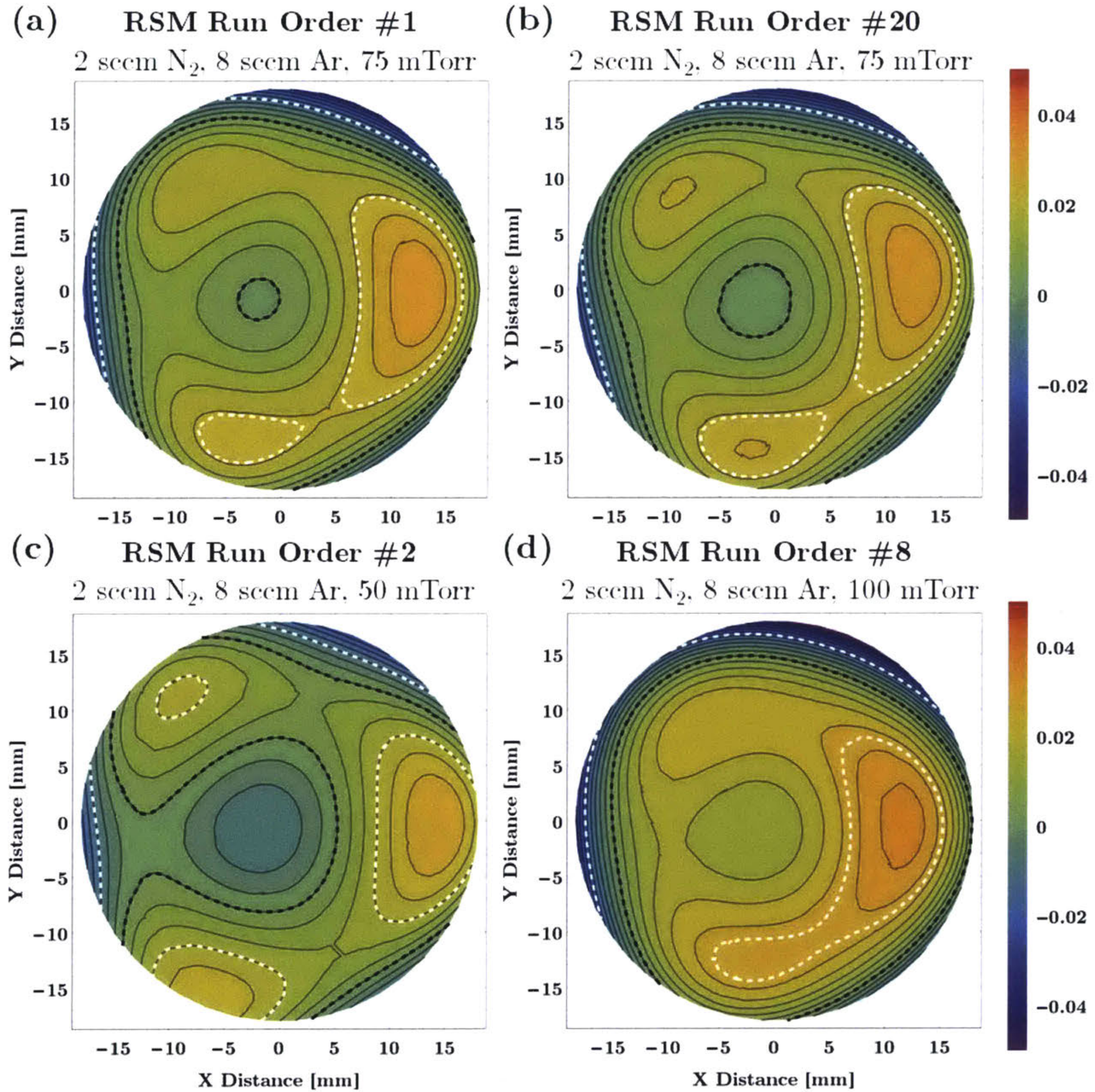

Figure 5.8: Contour plots of film uniformity (percent deviation from the mean). The black lines indicate the mean film thickness, while the white lines show one standard deviation. (a) CV: 1.64%, Uniformity: ±3.10%; (b) CV: 1.66%, Uniformity: ±3.36%; (c) CV: 1.20%, Uniformity: ±2.32%; (d) CV: 2.19%, Uniformity: ±3.78%;

Before discussing the specifics of the patterns seen above, it should be noted that the uniformity values measured across the RSM sequence compares extremely well with published numbers from commercial systems. These numbers are relatively scarce and often come with very little context, but are still very useful for benchmarking the performance of SiN_x depositions in the IFIC. The available numbers are summarized below in **Table 5.9**.

SiN_x Reference	Uniformity	Substrate Size	Exclusion Zone	Additional Information
IFIC	±3.4%	50.8 mm	4 mm	Inch Fab ICP-CVD system
[50]	±6%	50 mm	not provided	Oxford Instruments ICP65 Source
	±3%	100 mm	not provided	Oxford Instruments ICP180 Source
	±5%	150 mm	not provided	Oxford Instruments ICP180 Source
	±5%	200 mm	not provided	Oxford Instruments ICP380 Source
[93]	±4%	100 mm	7 mm	Oxford Instruments ICP180 Source
[96]	±4-7%	100 mm	not provided	Oxford Instruments ICP180 Source
[66]	±4%	50 mm (GaAs)	5 mm	Oxford Instruments
[6]	±4%	100 mm	not provided	PlasmaTherm Versalock
[114]	±3%	100 mm	~5 mm	Sentech SI 500 D, exclusion zone estimated from graph

Table 5.9: Published Uniformity values for SiN_x depositions in commercial ICP-CVD systems. The average Uniformity from the SiN_x RSM sequence is included in green for comparison.

Each of the thickness contour maps in **Figure 5.8** show a distinct triangular three-lobe pattern, with a slight dip in the middle of the substrate. Based on the orientation, this was determined to be an artifact of the aperture plate, which has three legs that support the center disk (**Figure 4.4b** shows a picture of the exact AP1.25 design used in both the SiO_2 and SiN_x optimized depositions). **Figure 5.9** shows a rendering of the aperture plate overlaid (in the actual orientation used in the system) on the thickness contour map from **Figure 5.8a**. This rendering represents the actual orientation of the plate legs relative to the substrate in the system, and matches well with the three-lobe pattern seen in the contour plot[35].

[35] The specific orientation of the legs of the aperture plate was not monitored during the SiO_2 depositions (which did not exhibit any noticeable lobed profiles), but once the three-lobed profile was observed in the SiN_x depositions and confirmed to be caused by the plate legs, the plate orientation was noted and maintained across all future depositions.

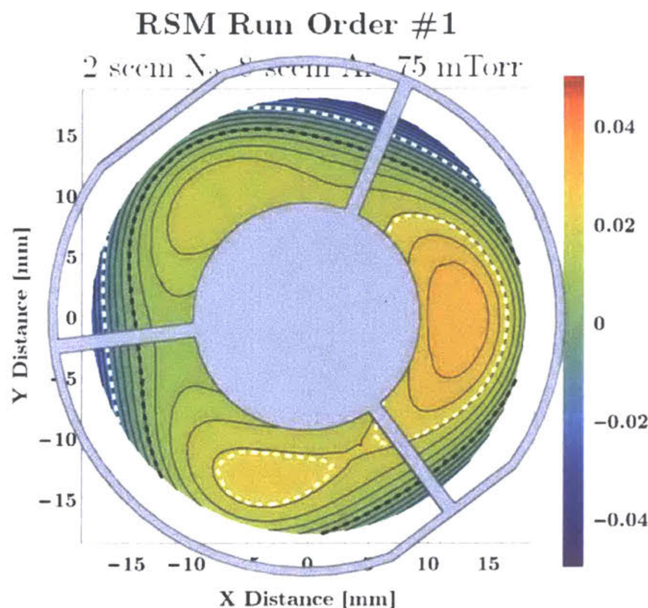

Figure 5.9: Sample contour plot of film uniformity with AP1.25 aperture plate overlaid in the same orientation used in the IFIC during the SiN_x tests.

This three-lobe pattern is visible in all of the samples processed with the AP1.25 plate and 23.7 mm substrate-to-aperture plate spacing, and the pattern becomes more pronounced at lower pressures (see the black line denoting the mean thickness in **Figure 5.8c**), although this does not hurt the Uniformity numbers, which still are influenced in most part by the thickness roll-off at the edge of the deposition. The pressure relationship can be explained by considering the mean free path, which is largest at the lowest pressures, suggesting that the process gas molecules which pass through the openings in the aperture plate do not experience enough collisions in the 23.7 mm between the plate and substrate to re-homogenize. This is an interesting phenomena that could be investigated more through the use of different aperture plate geometries that could include things like holes in the central region[36] or thinner or fewer legs on the aperture plate. The latter idea is potentially more promising, as the overall weight of central section is very small (~2.7 grams) and could potentially be supported by a single ultra-thin leg, which would minimize the amount of flux blocked outside of the central region of the aperture plate while maintaining the overall simplicity of the aperture plate design. If needed, the stiffness of the support leg could

---

[36] This is the method used in Oxford Instruments Plasmalab ICP-CVD systems, but in an aperture plate designed specifically for SiN_x deposition (a different plate is used for SiO_2) [50], [93].

be increased by increasing its thickness while maintaining a very small width (the leg stiffness is proportional to its thickness cubed, but only scales linearly with its width).

It would be important of course to consider how these changes would affect deposition of SiO_2 though, which shows excellent uniformity using the AP1.25 plate as designed. As discussed in **Section 5.1.1**, using different plate designs for different deposition materials is not ideal, especially for a tool like the IFIC that will likely be used for depositing different films regularly.

5.3.2.5 BOE Etch Rate Ratio

The last measurement performed on the SiN_x RSM samples was wet etching in 7:1 BOE solution. The buffered oxide etch (BOE) etch rate of SiN_x provides information about the film's density and by proxy its hydrogen concentration. The process used for performing and measuring the etches is described in **Section 3.2.5**. As is discussed in that section, BOE etch rates are very sensitive to environmental conditions, so a piece of thermally-grown SiO_2 (cleaved from a single 150 mm wafer used) was included with each batch of samples to provide a reference etch rate[37] that the measured SiN_x samples could be normalized to. The etch rate ratio is the measurement used to fit the response surface models. Like the SiO_2 RSM sequence, a statistical model with a lack-of-fit p-value greater than the normal 0.05 threshold could not be constructed, but a second-order fit with two-factor interactions did provide a model that fit the RSM data with normally distributed residuals and an $R_{adj}^2 = 0.926$. The average residual deviation for this was actually just 5.8% from the measured values, which, given the observed 5.7% repeatability error for SiN_x BOE tests determined through the tests also described in **Section 3.2.5**, was taken as more than acceptable for a coarse prediction model. The model coefficients and factor-pair contour maps are included below.

[37] The etch rates observed for the thermal SiO_2 reference pieces were between 80 and 85 nm/min for the SiN_x RSM tests.

N_2 Flow	Ar Flow	Pressure	$N_2 \cdot$ Ar	$N_2 \cdot$ Press	Ar $\cdot$ Press	$(N_2\ \text{Flow})^2$	$(\text{Ar Flow})^2$	$(\text{Pressure})^2$	Intercept
0.102	-3.2×10^{-4}	-4.4×10^{-3}	6.4×10^{-3}	-1.8×10^{-3}	0.015	0.049	-7.8×10^{-3}	-8.0×10^{-3}	0.240

Table 5.10: Fit coefficients for second-order IFIC SiN_x BOE etch rate ratio model.

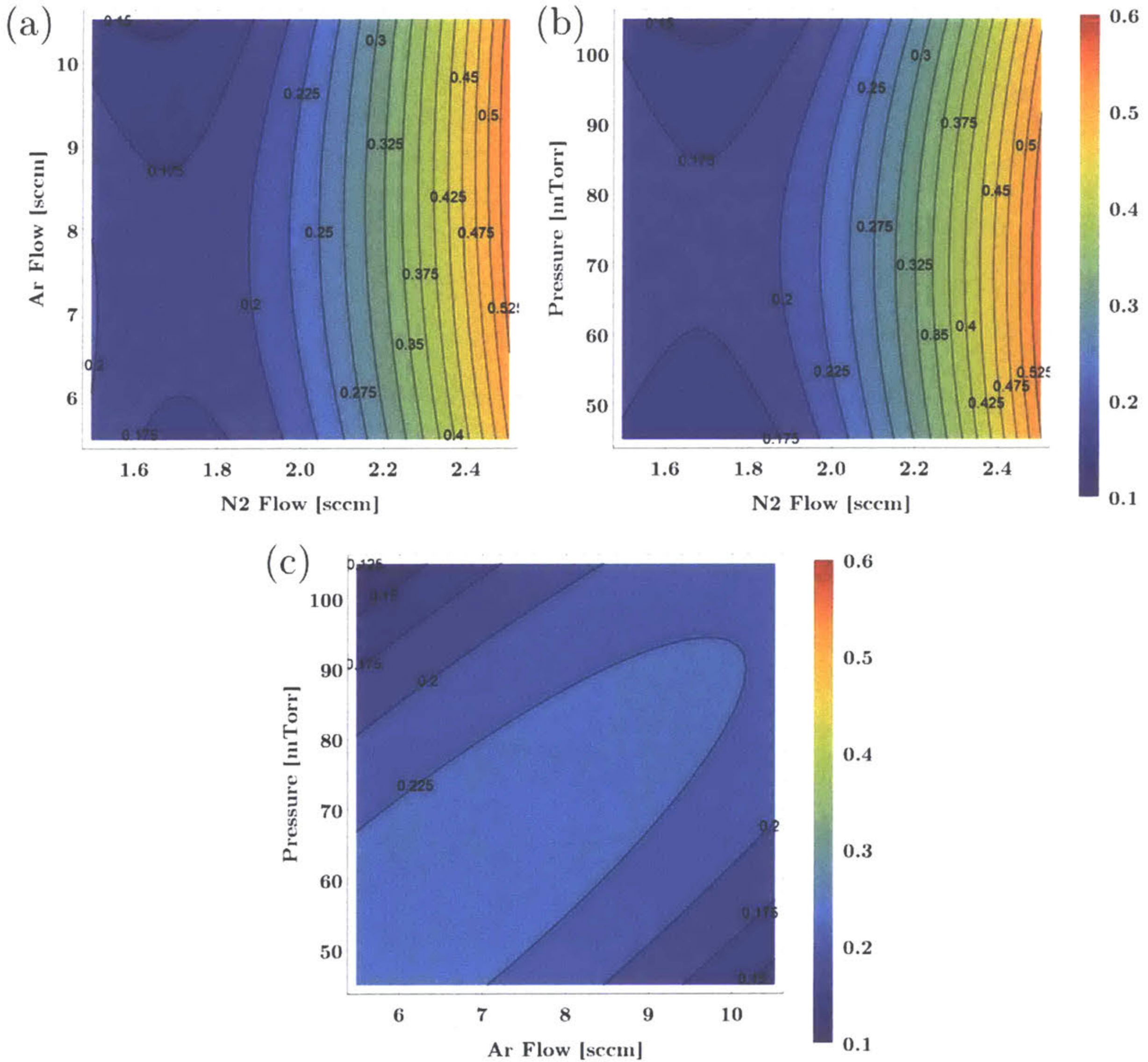

Figure 5.10: Contour plots showing the RSM model-predicted SiN_x BOE etch rate ratio vs. pairs of input factors. Each graph is evaluated at the center point value of the factor not shown. Contours are equal across all plots.

The plots show a similar trend, with the N_2 flow producing the largest variation, and the Ar flow and pressure exhibiting smaller but similarly shaped effects. The mechanisms at work are relatively straightforward, with the N-rich, low refractive index films resulting from large N_2 flows exhibiting larger etch rates due to their decreased density (as indicated by the increased deposition rate) and higher hydrogen concentration [31], [32]. As the N_2 flow decreases and the index returns to near-stoichiometric and then moves to slightly Si-rich, the etch rate begins to level off as less hydrogen is incorporated and the film becomes denser [7]. Some investigators have reported etch rate minima beginning at near stoichiometric indexes [32], [66], [72], and others have shown it occurring at Si-rich indexes [6], [115].

Unfortunately, there are many different BOE ratios and deposition conditions used in the literature which makes it difficult to directly compare etch rates or etch rate ratios observed in the IFIC with other systems, but broadly speaking the median 7:1 BOE etch rates observed here (~0.18-0.30:1 in ratio form and ~150-250 nm/min in raw form) are in the same range as other values reported in the literature under similar conditions. Several of the values are included in **Table 5.11**.

Reference	Etch Rate [nm/min]	Deposition Technique	Etchant	Temperature [°C]	Other Conditions
IFIC	150-250	ICP-CVD	7:1 BOE	100	22-24°C etch
[6]	100	ICP-CVD	7:1 BOE	100	n=2.0, 20°C etch
[66]	200	ICP-CVD	7:1 BOE	80	n=2.0, 23°C etch
[29]	275	ICP-CVD	7:1 BOE	100	n=2.03
[116]	150	ICP-CVD	6:1 BOE	100	
[6]	1100	PECVD	7:1 BOE	100	n=2.0, 20°C etch
[66]	134	PECVD	7:1 BOE	300	23°C etch
[116]	200-300	PECVD	6:1 BOE	300	

Table 5.11: Published BOE etch rate values for ICP-CVD and PECVD SiN_x depositions. The average etch rate range from the SiN_x RSM sequence is included for comparison.

Table 5.11 also includes several etch rates for PECVD SiN_x depositions. As these data show, the BOE etch rate seen in the IFIC is significantly lower than PECVD films deposited at the

same temperature, and is comparable to the rates seen for PECVD films deposited using a 200°C higher substrate temperature.

5.3.3 Validation of RSM Results

The SiN_x RSM results presented in the previous sections provided the important confirmation that the IFIC system is fully capable of not only producing high quality SiO_2 films, but also high quality SiN_x films with characteristics comparable to those achieved using larger and more expensive commercial systems. While each of the models generated were shown to agree with the gathered data and the literature's general understanding of how input parameters affect the output characteristics of SiN_x films, it is critically important that the observed trends and model predictions continue to fit with data generated outside the RSM test sequence. To this end, the following sections describe the results of two studies designed to test the validity of the RSM models and the longer term repeatability of processes in the IFIC.

5.3.3.1 Follow-Up Tests

To confirm that the response surface models generated from 20-test CCD sequence still held for new film depositions not included in their generation, a set of five follow-up tests were carried out using parameters values not tested during the RSM sequence. The factor values for the first three tests were selected to simply test points in-between those used in the RSM sequence, while the factors values for the fourth and fifth tests were specifically chosen to try and produce films with an average film stress near zero and a stoichiometric index of refraction ($n \approx 2$). As noted in the previous sections, the coarse N_2 flow factor knob and the fine Ar flow and pressure factor knobs make it possible to achieve these desired film characteristics using multiple combinations of factor values. The factor values selected for these tests are shown in **Table 5.12**. All other input parameter values were kept at their RSM values. The measured film characteristics for each of the five follow-up tests are shown in **Table 5.13**, and are compared to the model predictions in **Table 5.14**.

Run Order	Test Type	(Coded Values) F1	F2	F3	(F1) N_2 Flow [sccm]	(F2) Ar Flow [sccm]	(F3) Pressure [mTorr]
1	Follow-up	1	0	0	2.3	8	75
2	Follow-up	0	1	0	2	9.5	75
3	Follow-up	0	0	-1	2	8	60
4	Follow-up	0.333	0.5	0	2.1	8.75	75
5	Follow-up	0.167	1	0.5	2.05	9.5	82.5

Table 5.12: Input factor values for the SiN_x RSM follow-up tests.

Run Order	Deposition Rate [nm/min]	Index of Refraction	Average Film Stress [MPa]	Coefficient of Variation [%]	Uniformity [%]	BOE Etch Rate Ratio
1	22.92	1.948	208.4	1.75%	3.53%	0.373
2	19.38	2.011	-74.2	1.63%	3.27%	0.214
3	20.44	2.040	-218.3	1.42%	2.96%	0.207
4	20.61	1.988	55.9	1.65%	3.26%	0.262
5	19.26	1.991	7.5	1.78%	3.35%	0.237

Table 5.13: Measured results for the SiN_x RSM follow-up tests.

Run Order	Deposition Rate: Estimate [nm/min]	Deposition Rate: Difference [nm/min]	Index of Refraction: Estimate	Index of Refraction: Difference	Average Film Stress: Estimate [MPa]	Average Film Stress: Difference [MPa]	BOE Etch Rate Ratio: Estimate	BOE Etch Rate Ratio: Difference
1	22.46	0.46	1.950	-0.002	204.9	3.5	0.391	-0.018
2	19.08	0.30	2.019	-0.008	-81.7	7.5	0.232	-0.018
3	20.44	0.00	2.044	-0.004	-220.0	1.7	0.236	-0.029
4	20.32	0.29	1.990	-0.002	9.6	46.3	0.279	-0.016
5	19.22	0.04	1.996	-0.005	-6.2	13.7	0.254	-0.017

Table 5.14: Comparison of SiN_x RSM follow-up results to model predictions.

Apart from one stress measurement, the results from the follow-up tests agree very well with the model predictions. The observed deposition rates were between 0 and 2% higher than predicted by the model, averaging 1.06%, which is nearly identical to the 1.07% average seen during the RSM sequence. A similarly high level of agreement is seen for the index of refraction values, which ranged from 0.1-0.4% lower than predicted. The average 0.21% deviation is very close to the 0.27% average residual deviation observed in the RSM sequence. The residuals for the first three of the five average film stress measurements agree very well with the model

predictions, showing residuals near or below the average 7.4 MPa residual from the RSM test. The fifth residual is still within one standard deviation (13.7 MPa vs. 15.7 MPa) and the measured 7.5 MPa stress value is still very near to the neutral stress goal identified during the factor selection process. The 55.9 MPa of tensile stress measured in the fourth follow-up sample was unfortunately not as near to the neutral stress goal. One potential explanation for this difference may be a fluctuation in the N_2 flow during the deposition. This stress value would be expected for N_2 flow of ~2.138 sccm rather than the 2.1 sccm desired, which is within the reasonable range given for accuracy of the Alicat MFCs used. The surrounding tests did not show any signs of N_2 drift, so this seems a bit unlikely, but not impossible. Another explanation could be an inaccurate measurement of the initial wafer curvature. Additional testing around this operating point could determine whether this specific sample was an aberration or if the model needs to be updated to include a new piece of curvature.

Moving on to the uniformity metrics, the values calculated from the 2D thickness profiles are very much in line with the averages seen during the RSM (~0.1% smaller than the RSM average for both metrics). The last measured value, the BOE etch rate ratio, showed residual deviations of 4.7-12.5% (average 7.5%), which is larger than the 5.8% percent observed during the RSM sequence, but even the 12.5% variation seen for the third sample still falls within one standard deviation (13.6%). The larger residuals seen for the BOE tests here and in the RSM sequence are again likely attributable to the variation inherent in the etch rate process.

Taken together, the results from the five follow-up tests agreed quite well with the predictions of the RSM-derived models. This speaks well to the validity of the models themselves and of the stability of the IFIC system itself. A more rigorous examination of this stability is provided in the next section.

5.3.3.2 Single Recipe Repeatability

The ability to correctly predict the output characteristics of a film deposited using a new set of input parameters is extremely important, but of equal or greater importance for a micro- and

nanoscale fabrication process is that each time an existing recipe is run, it produces the same outcome. To confirm that this could be accomplished for SiN_x films in the IFIC, the center point recipe from the RSM sequence (2 sccm N_2, 8 sccm Ar, 75 mTorr) was run 14 times (including the 6 tests from the RSM sequence) over a period of 2.5 weeks. Just as was done for the similar SiO_2 repeatability test sequence, these tests were sometimes carried out alone and sometimes as part of a long sequence of tests. The data from these tests is shown in **Figure 5.11** and in **Table 5.15**.

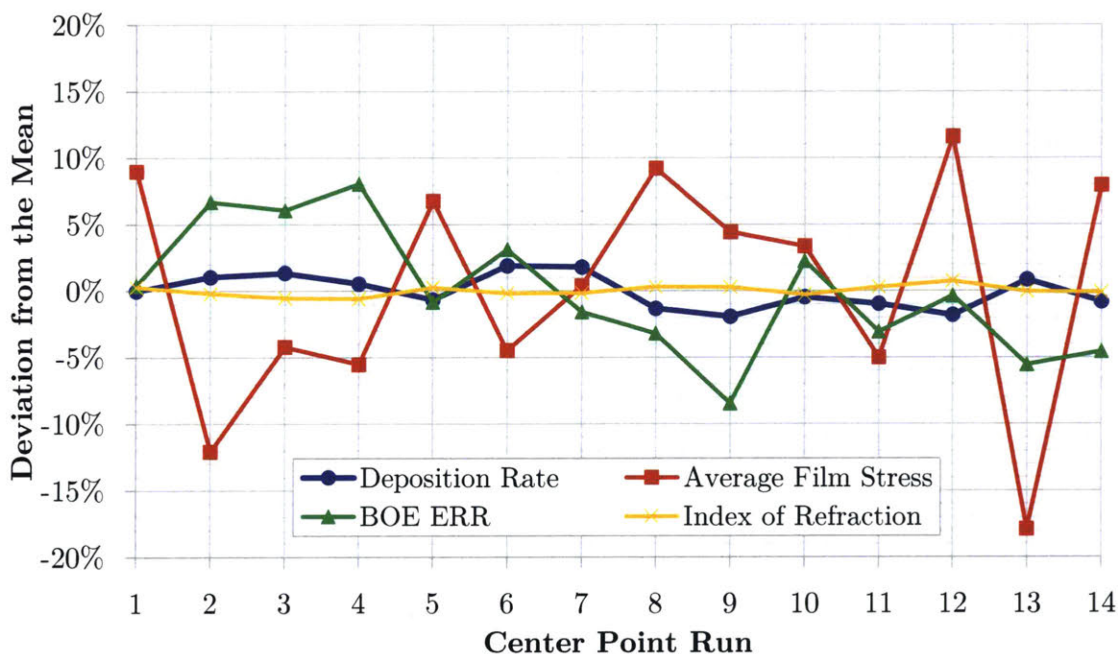

Figure 5.11: SiN_x center point deviation from the mean for each measured parameter.

	Deposition Rate [nm/min]	Index of Refraction	Average Film Stress [MPa]	CV [%]	Uniformity [%]	BOE Etch Rate Ratio
Mean	19.91	2.028	-166.7	1.65%	3.19%	0.24
Standard Deviation	0.26	0.007	14.6	0.04%	0.09%	0.01
Coefficient of Variation	1.29%	0.37%	8.75%	2.23%	2.85%	4.69%
Average Deviation from Mean	0.22	0.006	12.0	0.03%	0.07%	0.01
Average % Deviation from Mean	1.10%	0.30%	7.22%	1.54%	2.29%	3.87%
Average % Deviation from Model Prediction	1.16%	0.33%	7.06%	–	–	3.96%

Table 5.15: Summary of results from SiN_x repeatability tests.

The data shown above provide an excellent proof of the repeatability of SiN_x depositions in the IFIC. The average deviations for deposition rate, index of refraction, and uniformity are small and do not appear to be trending in any direction. The average magnitudes of the larger deviations observed for average film stress are still within the one standard deviation range of repeatability (~15 MPa) established in **Section 3.2.3** for the stress measurement itself[38], and the BOE measurement deviations also fall below that same threshold established from the tests of **Section 3.2.5**.

As mentioned in the SiO_2 repeatability section, the run-to-run repeatability for ICP-CVD processes is very rarely reported on in the literature, but the data that is publically available shows comparable run-to-run deviation for average film stress (~±10% in [50], ~±8% in [6]), deposition rate (±2% in [50]), and refractive index (±0.3% in [50]), suggesting that repeatability of SiN_x depositions in the IFIC are on par with those in currently available commercial systems.

5.4 Additional Testing

To round out the understanding of SiN_x depositions in the IFIC, two additional measurements and one additional set of tests were carried out. Chemical composition and surface morphology were examined for select samples tested using FTIR and white light interferometry, respectively. The additional testing performed was a 5-level, single-factor test investigating the effect of substrate temperature on SiN_x film properties. The results from these tests are presented below.

5.4.1 Substrate Temperature

Substrate temperature was identified in the early SiN_x testing as having a moderate effect on a variety of SiN_x film properties, was very nearly included in the RSM sequence. To specifically quantify its effect, depositions were performed at 50°C, 75°C, 125°C, and 150°C, in addition to the multiple runs already completed at 100°C. The results of these tests shown in **Figure 5.12**.

---

[38] The percent deviations are higher than seen in SiO_2 because the stress values are much lower for SiN_x (-166 MPa vs. -480 MPa).

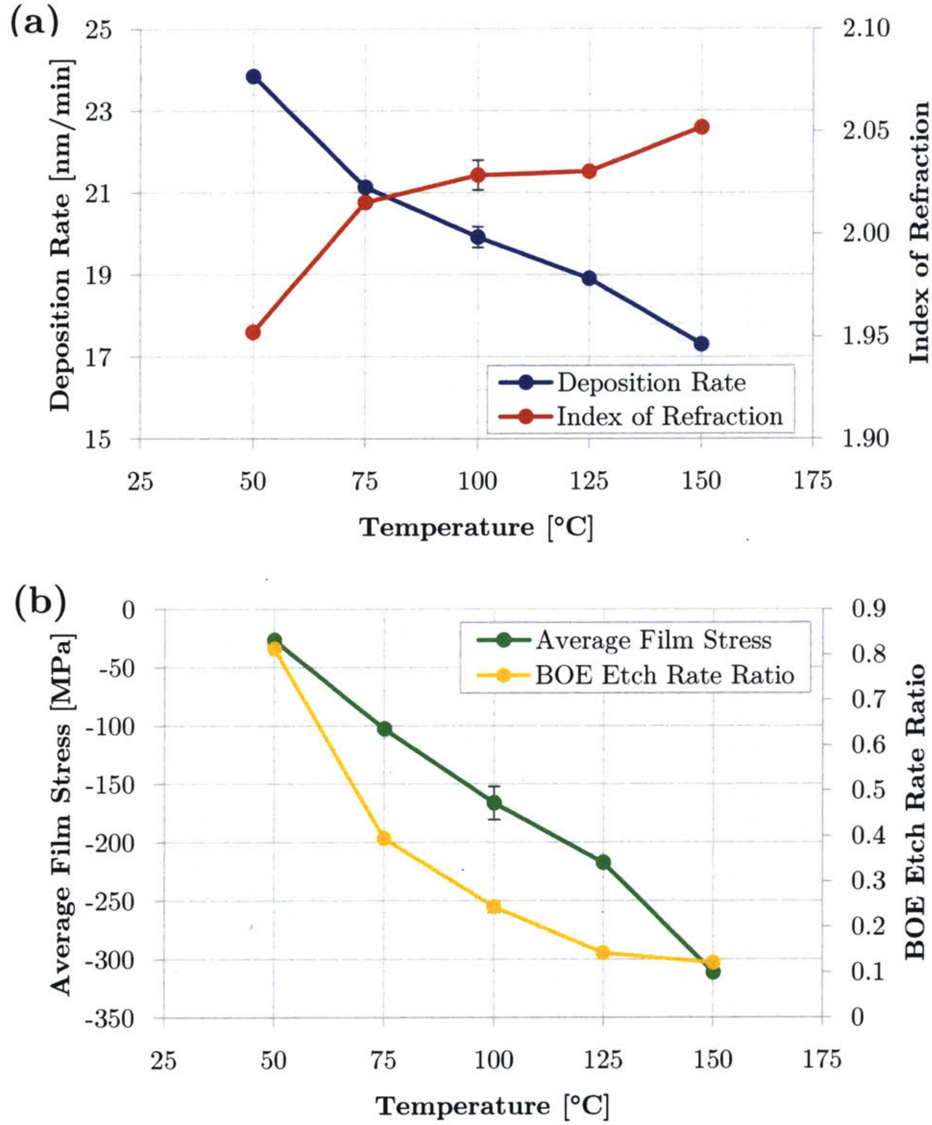

Figure 5.12: Results from single-factor temperature testing. (a) Deposition rate and index of refraction; (b) Average film stress and BOE etch rate ratio. The error bars on the 100°C data points represent one standard deviation. Tested were performed using the SiN_x RSM center point values.

The results shown in the above plots are consistent with trends reported throughout the literature [66], [116]. The Uniformity and CV values were also measured and found to decrease slightly with increasing temperature, likely due to increased surface mobility. Hydrogen content is known to decrease with increasing temperatures, causing the film density to increase as fewer Si-H and N-H increases [25], [116]. The increase in density leads to a drop in BOE etch rate and also contributes to the decreased overall deposition rate, which (as discussed in **Section 4.3.2.1**) is also due to decreased adsorption of reactive species. The increase in index to slightly Si-Rich

values at temperatures above 100°C is also known [29], [66], as is the relationship between Si-Rich films and more compressive stress discussed in previous sections. In instances where the desired film characteristics cannot be attained using the processing window described by the RSM model predictions, the trends confirmed through these tests provide another knob that can be adjusted to meet the desired film goal.

5.4.2 FTIR

To assess the relative concentrations of different bond types in SiN_x films deposited in the IFIC, Fourier transform infrared (FTIR) spectroscopy was used. Transmission mode measurements were accomplished by first measuring the background signal of an unprocessed wafer (lightly-doped silicon is transmissive in the IR range), and then subtracting this background from subsequent measurements of the wafers with SiN_x films to leave just the signal originating from the film. Three sets of SiN_x films were measured: a group of three center point tests, a series of three samples with increasing N_2 flows, and a series of three samples deposited at different substrate temperatures. The center point scans are shown first in **Figure 5.13**.

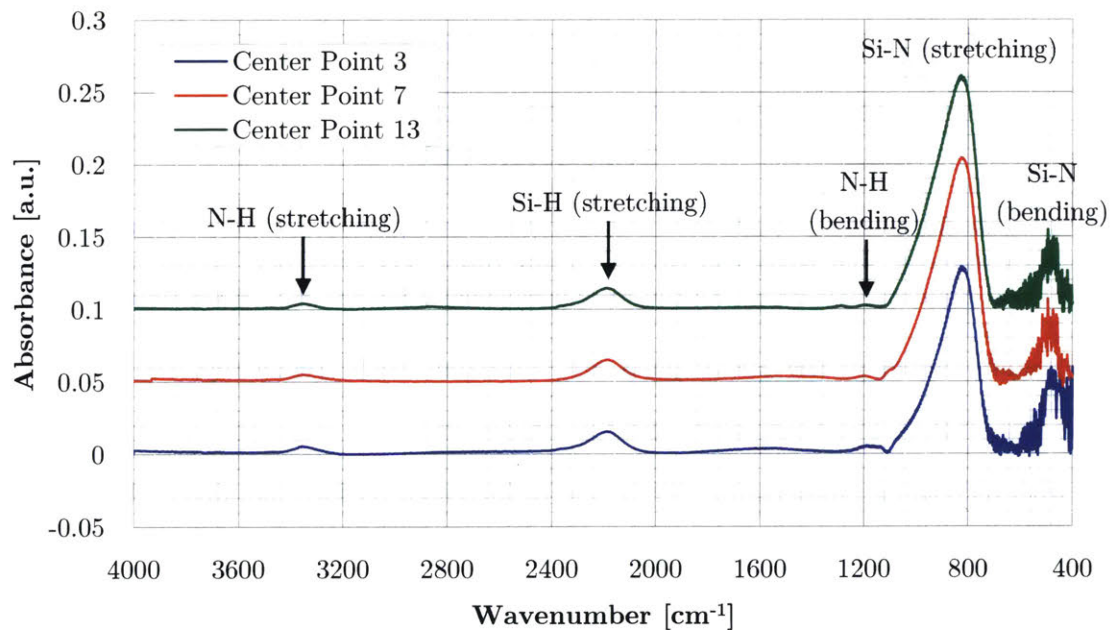

Figure 5.13: FTIR scans of three SiN_x RSM center point tests.

The first thing of note about the three above scans are their similarity. As was shown in the previous section, depositions using the same recipe in the IFIC are very consistent, and these data show that consistency extends to their chemical composition. The labeled peaks show the dominant Si-N stretching band (~850 cm^{-1}), smaller Si-N bending (~480 cm^{-1}) and Si-H stretching mode (~2200 cm^{-1}), and small amounts of N-H stretching (~3400 cm^{-1}) and bending modes (~1200 cm^{-1}). The relative size of the Si-H and N-H peaks are on par with those reported in the ICP-CVD literature using similar deposition conditions [24], [28], [116], [117], and are similar to those seen for 300°C PECVD films [94], [113]. The next set of scans show the effect of changing the N_2 flow, which was seen throughout the RSM sequence to have the largest effect on a film's properties.

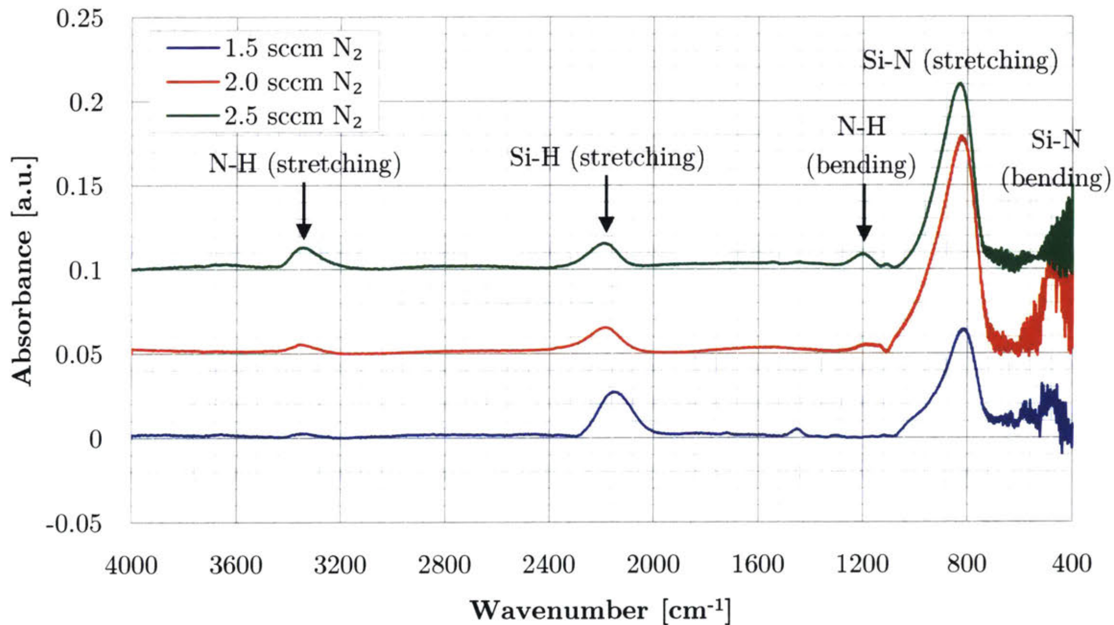

Figure 5.14: FTIR scans of three SiN_x samples deposited with increasing N_2 flow levels. All other parameters were kept at the RSM center point values.

The scans in **Figure 5.14** show the relative concentrations of Si-H and N-H bonds is closely tied to the N_2 flow during the deposition process, with N-H bond concentration rising with increasing and the Si-H bond concentration falling initially from 1.5 to 2 sccm N_2, then remaining roughly the same at 2.5 sccm N_2. This inversion of the N-H and Si-H peaks for changing N_2 flow has been observed in [27], [117], [118] and was quantified in [25]. As observed during the RSM testing, when the N_2 flow increases, the SiN_x films become less dense (higher BOE), which is linked

to higher H incorporation [31], [66], and can be seen here with the larger N-H peaks and still moderate Si-H peaks for the highest N_2 levels. The relative bond concentrations are also known to change with deposition temperature, which was the independent variable for the last set of scans, which are shown in **Figure 5.15**.

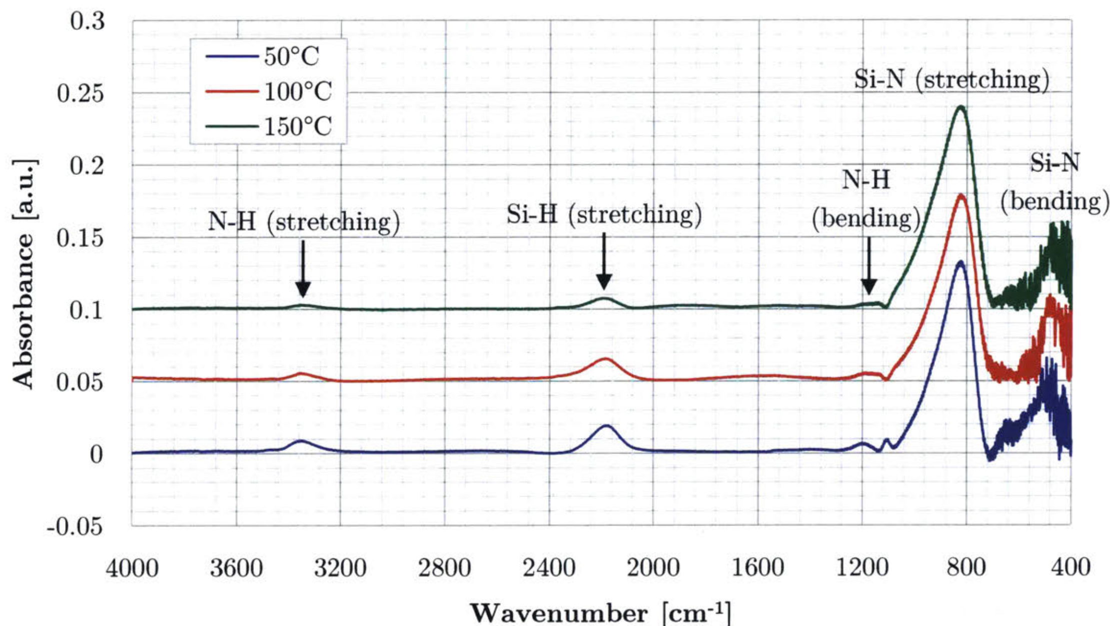

Figure 5.15: FTIR scans of three SiN_x samples deposited at different substrate temperatures. All other parameters were kept at the RSM center point values.

The data from this final set of scans shows that a film's hydrogen content in the form of both Si-H and N-H bonds decreases with increasing temperature. This has also been observed specifically for ICP-CVD depositions [25], but the relationship is well-known to hold for PECVD and LPCVD as well [104], [119]. The advantage of the ICP-CVD technique is the ability to realize this decreased hydrogen concentration at low deposition temperatures. As was shown in **Table 5.11**, the etch rates for SiN_x films (linked to the H concentration) deposited in the IFIC at 100°C are comparable to those of PECVD at 300°C. This ~200°C advantage observed here and by other investigators [6], [50] opens up many new possibilities for materials and devices with low thermal budgets.

5.4.3 Surface Properties

The surface morphology of SiN_x films deposited in the IFIC was the final characteristic measured. Surface roughness measurements were carried out on specific samples using a white light interferometer as described in **Section 3.2.8**. Samples from the RSM test sequence with the highest compressive and tensile stresses were chosen to investigate whether any surface cracking, delamination, or other abnormalities could be detected. Two samples from the center point repeatability sequence were also measured. The resulting surface plots are show below in **Figure 5.16**. The surface roughness values shown alongside each plot are the average of measurements taken at three locations on each sample.

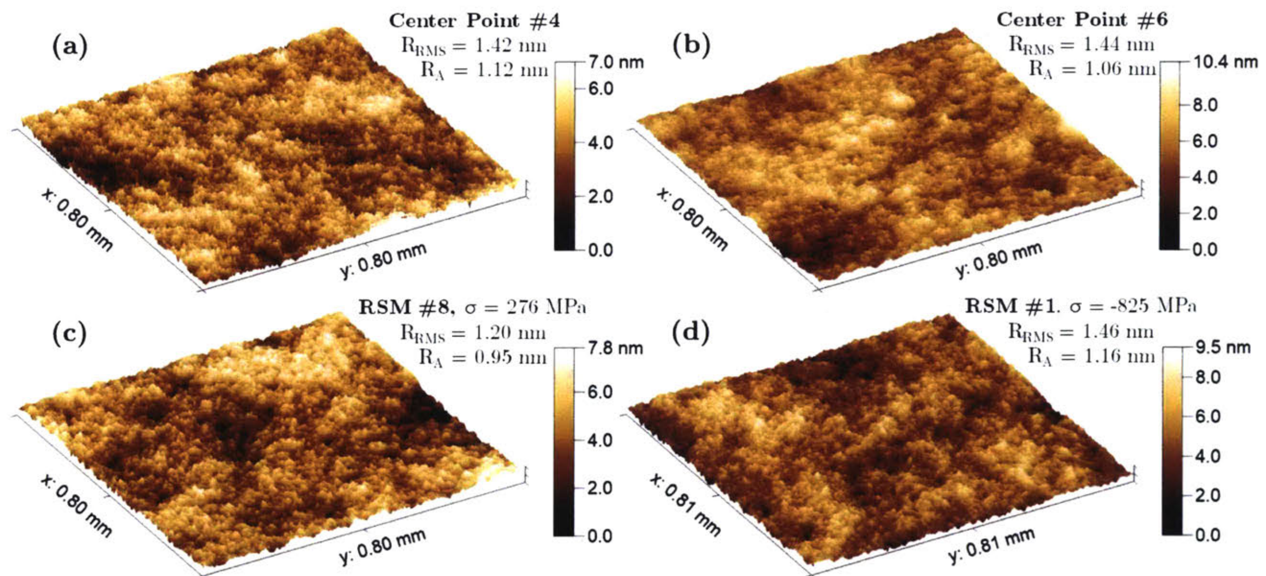

Figure 5.16: Surface roughness maps. (a-b) Center point tests; (c) Film with high tensile stress; (d) Film with high compressive stress.

The surfaces displayed above are otherwise unremarkable, with very similar roughness values and total height variation, even across samples with large stress differences, suggesting the film cracking or delamination is not present. RMS roughness ranges of 0.16-0.59 nm [120], 1.6-2.0 nm [116], and 1.6-2.2 nm [28] have been reported for ICP-CVD SiN_x films, which are similar to the IFIC values presented here. It has been suggested that the lower deposition temperatures of ICP-CVD compared to PECVD result in smaller grain sizes and therefore lower roughness values [28].

Surface roughness is an important factor for SiN_x films used in optical applications, where excess roughness can lead to scattering and propagation losses [113].

5.5 Summary of Results

The results presented in this chapter demonstrates that the IFIC system is well suited to depositing high-quality silicon nitride films and controlling their properties to fit particular applications. Models have been generated that can predict a film's deposition rate, index of refraction, average film stress, and BOE etch rate over a large range of useful values, and these films can be consistently deposited with a high level of uniformity across the substrate, which can be any of a wide variety of materials due to the low deposition temperature. When coupled with the similarly positive results from the SiO_2 deposition characterization and the ultra-low price point, it is easy to be optimistic about the future Inch Fab ICP-CVD system.

Chapter 6: Conclusions and Future Efforts

The design, fabrication, and characterization process of the Inch Fab ICP-CVD system, as described in the previous chapters of this thesis, has demonstrated that a high-performance ICP-CVD fabrication tool can be created while still maintaining an ultra-low capital cost and small physical footprint.

The deposition of SiO_2 and SiN_x films in the IFIC has been thoroughly characterized and models have been generated that allow the properties of the deposited film to be accurately predicted based on the input parameter choices. The information from these models can also be used in the other direction, starting from a list of desired properties and generating a list of input parameter values that can be used to create the needed film. The range of output film properties achievable for SiO_2 and SiN_x depositions in the IFIC are summarized in **Table 6.1**.

	SiO_2	SiN_x
Deposition Rate [nm/min]	23 – 42	15 – 25
Index of Refraction	~1.46	1.90 – 2.35
Average Film Stress [MPa]	-700 to -180	-900 to +300
Coefficient of Variation	~1.5%	~1.8%
Uniformity	~2.9%	~3.4%
7:1 BOE Etch Rate Ratio	0.9 – 17.0	0.15 – 0.60
RMS Roughness [nm]	~1.2	~1.4

Table 6.1: Range of film properties achievable for SiO_2 and SiN_x films deposited in the IFIC. The values provided are based on the process windows used for the RSM test sequences for each film type.

As was noted in **Chapter 4** and **Chapter 5**, the values shown above are comparable to those seen in existing commercial ICP-CVD tools in every parameter except deposition rate. This lower deposition rate is largely due to one of the differentiating features of the IFIC—its use of a highly dilute, non-pyrophoric 1.5% SiH_4/He mixture. One of the goals of the Inch Fab initiative is to minimize or eliminate the use of hazardous gases in its tools, and the demonstration through this

work that high-quality SiO_2 and SiN_x films, which traditionally require not only pyrophoric SiH_4, but also corrosive NH_3 (for SiN_x), can be generated without these hazards shows that upholding such a goal does not have to hinder the performance of Inch Fab tools.

While the testing performed to characterize the IFIC was thorough, there are still additional experiments and measurements that can be carried out to build a more complete understanding of its operation. The first of these is a more thorough analysis of the chemical composition of the deposited films, particularly looking at the precise level of hydrogen incorporation in the films, and how this is modulated by the choice of deposition parameters. Observing how this level, as well as the levels of silicon and oxygen or nitrogen in the films evolve over their depth [31], [116], [121] would also provide useful insights into the dynamic behavior of the IFIC during a single deposition process. The bulk composition of a film can be inferred using FTIR spectroscopy data that has been calibrated with a secondary measurement such as elastic recoil detection (ERD) [122], but techniques such as secondary ion mass spectroscopy (SIMS) or Rutherford backscattering spectroscopy (RBS) can provide more accurate, depth-sensitive measurements (that can then be used to calibrate the easier-to-collect FTIR data [94]).

One characteristic that is known to be a strength of ICP-CVD but has only been briefly explored in the IFIC is the conformality of deposited films. Conformality is extremely important in applications like shallow trench isolation (STI), where SiO_2 is used to fill gaps etched in between active device regions. In order to fill these small trenches without leaving voids, conformality is a must. Structured films for conformality testing can be created using etch techniques (in a tool like the Inch Fab DRIE) or simple photoresist structures, due to the very low deposition temperatures in the IFIC. In **Figure 6.1**, cross-sectional images are shown of two samples that were patterned with photoresist and then covered with ~200 nm SiN_x (deposited at 75°C) using the IFIC. The good conformality shown by these initial test samples suggests that the IFIC could readily be optimized for use in gap fill and device encapsulation applications.

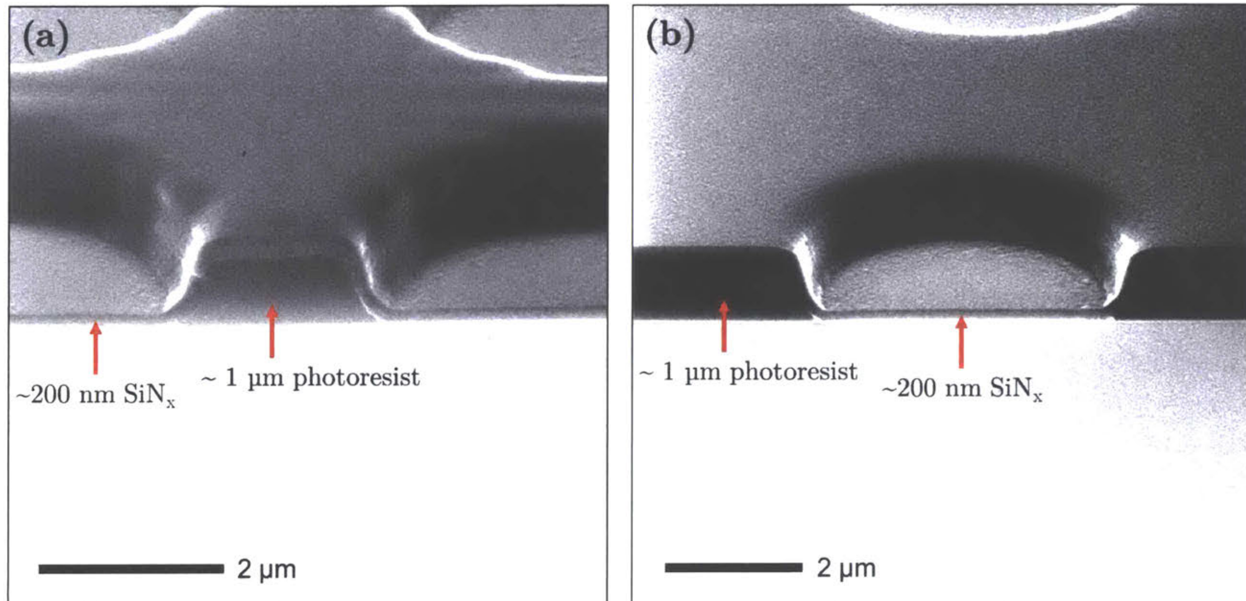

Figure 6.1: Cross-sectional images of ~200 nm of SiN_x deposited at 75°C on top of ~1 µm of patterned photoresist. The SiN_x films show good conformality.

Another set of future experiments in the IFIC should investigate the existence and persistence of process history or memory effects. These tests, which could involve alternating between SiO_2 and SiN_x depositions (both within a single sample and across samples), would confirm whether there are any carry-over effects from previous deposition conditions on the current operating environment. This is important to understand because many of the places where Inch Fab tools are likely to be adopted are multi-user facilities where process requirements can vary widely. Establishing guidelines, if necessary, for conditioning the chamber[39] between changes in the type of film being deposited would be critically important for those potential users. Along these same lines, new and varied substrate materials should also be tested in the IFIC, as all of the substrates used during this work were silicon wafers. Popular flexible and organic substrate materials like polyethylene terephthalate (PET) and polyethylene naphthalate (PEN), which cannot withstand the substrate temperatures required for quality films in other CVD techniques, would be great candidates for such further testing.

---

[39] Although, as posited in Section 2.5.1, the very low cost of the IFIC's upper chamber assemblies (UCAs) may make it such that the best solution is simply swapping UCAs when switching to a new film material.

Additional film materials can and should also be tested in the IFIC. With no additional gases or equipment, amorphous silicon (a-Si) and silicon oxynitrides (SiO_xN_y) can be deposited in the IFIC. SiO_xN_y films are very useful in optical applications as their range of refractive indexes can be tuned from that of SiO_2 to SiN_x ($n \approx 1.46$-2.0) [123]. Low-temperature a-Si films deposited with ICP-CVD are important in photovoltaic applications [124], [125], thin-film transistors [126], [127], and in optical and MEMS devices [128].

In addition to these new substrate and film materials, periodic testing should also continue for SiO_2 and SiN_x, if for no other reason than providing data on the long term stability of the deposition recipes. This information will be extremely important to provide to potential Inch Fab early adopters.

Along with the positive results gathered during the SiO_2 and SiN_x characterization processes, there were also several observations made about aspects of the IFIC that can be improved upon, and several features that can be added to further enhance the IFIC's performance and value proposition as an ultra-low cost fabrication tool. In **Section 3.3.1** the standard operating protocol for processing samples was provided. Among the early steps of this protocol are the description of the procedure used to warm up or prime the chamber for deposition. Without this warm-up sequence, the first sample run will generally show a ~5-7% higher deposition rate than the derived models would predict. The 7 minute warm-up sequence prevents this overshoot, but including the loading/unloading process, it does add 10-15 minutes to the time needed to process the first substrate (which may be the only sample required). To eliminate this requirement, the chamber could be continually heated, as is done in many commercial tools, or a system could be devised whereby the chamber can be remotely heated prior to processing. In a multi-user facility, the remote heat-up could be integrated with the facility's scheduling system such that the heat-up process automatically begins prior to a reserved time slot.

In this same mode, the time it takes for a loaded substrate to be heated to its deposition temperature is also an area where time efficiency could be improved. No significant efforts have been made to improve the PID tuning process and accelerate the warm-up, but this most certainly

can be done, in addition to other potential tactics like preheating the SCA (with no substrate loaded) to a slightly higher temperature than will be used for the next deposition, such that when the substrate is loaded the immediate heat transfer does not drop the SCA temperature below the setpoint temperature.

Another area for improvement also relates to the start-up process in the IFIC after a long period of inactivity. The proportional valves used in the MFCs to control the output mass flow provide a moderate seal to vacuum when they are not in use (0 sccm setpoint), but some gas is still able to leak through. This gas is confined effectively by the small electronic solenoid valves in the manifold, but the "dead volume" between the MFC outlet and the solenoid valve input will slowly rise in pressure due to the leak-through. If several days pass without the solenoid being opened, enough pressure will build up in the dead volume such that when the solenoid valve is opened, there system will be exposed to a pressure spike, which can reduce the lifetimes of the vacuum pumps (particularly the turbo pump). There are two potential ways this can be solved. The first is to add another valve to the gas manifold that can route the built-up pressure around both the process chamber and turbo pump and direct it near the inlet of the rotary vane pump. The other solution is based around trying to minimize amount of dead volume between the MFC and solenoid valve, which will diminish the effect of a spike. A new manifold that minimizes this dead volume by directly coupling to the outlet of the MFCs has been designed and built, but not yet tested[40].

Two additional features that can be added to the IFIC to improve its functionality are a more robust system of interlocks that allow or prevent certain actions based on the state of the system, and remote process control and monitoring. The former, which actually should not require much additional hardware, is mostly about fully integrating all of the existing setpoint relays, position indicators, user settings, and other related sensor or status inputs to create a complete state

[40] This new design also features an extra valve position so that the preemptive exhausting solution can also be employed.

machine that can, for instance, only allow a process to start if the substrate is at the right correct processing height, or prevent the isolation gate valve between the LLA and LCA from being opened unless the load lock pressure is below a certain threshold. Some interlocks of this nature have already been integrated into the system, but a full map of all the possible states needs to be created so that all the common and edge cases can be considered.

The second feature that would provide a great boost to the functionality (and potentially competitive advantage) of the IFIC is a remote process control and monitoring system. Such a system would not only include the ability to track what the current system conditions are, but also be able to report on any aberrations that occur between processes or track trends across processes. The models developed from the RSM sequences could be integrated into such a system so that a user could input their desired film characteristics rather than recipe parameters, and the monitoring system would use the model data and its own observations on the recent trajectory of performance to dynamically create a recipe using machine learning techniques. Post-deposition measurement data taken periodically from samples could also be fed back into such a system to improve the recipe recommendations. From a hardware perspective, this does not necessarily require any new equipment or electronics (the control system has plenty of extra processing bandwidth) and would primarily require just the appropriate software engineering and integration.

The future success and market adoption of the ideas of the Inch Fab initiative relies on the continued development of high-quality, ultra-low cost tools like the IFIC. The DRIE system, this ICP-CVD system, and the magnetron sputtering system (being developed concurrently), provide a great start to the realization of a full fabrication platform. It is firmly believed that the availability of a radically lower-cost solution for micro- and nanoscale fabrication will help to drastically increase access to micro- and nanofabrication capabilities and provide anyone with a novel device idea the opportunity to have that idea built, tested, and iterated upon in an economical way.

References

[1] McKinsey & Company, "Creating value in the semiconductor industry," 2011.

[2] P. A. Gould and M. D. Hsing, "Design, fabrication, and characterization of a compact deep reactive ion etching system for MEMS processing," Massachusetts Institute of Technology, 2014.

[3] P. A. Gould, M. D. Hsing, H. Q. Li, K. K. Gleason, and M. A. Schmidt, "An ultra-low cost deep reactive ion etching (drie) tool for flexible, small volume manufacturing," in *2015 Transducers - 2015 18th International Conference on Solid-State Sensors, Actuators and Microsystems (TRANSDUCERS)*, 2015, pp. 2268–2271.

[4] F. Laermer and A. Schilp, "Method for anisotropic plasma etching of substrates," US 5498312A, 17-May-1994.

[5] F. Laermer and A. Schilp, "Method of anisotropically etching silicon," US 5501893, 26-Mar-1996.

[6] K. Mackenzie, J. Lee, and D. Johnson, "Inductively-Coupled Plasma Deposition of Low Temperature Silicon Dioxide and Silicon Nitride Films for III-V Applications," *Proc. Symp. 30th State-of-the-Art Progr. Compd. Semicond.*, vol. 99, no. 4, pp. 1–12, 1999.

[7] J. W. Lee, K. D. Mackenzie, D. Johnson, J. N. Sasserath, S. J. Pearton, and F. Ren, "Low Temperature Silicon Nitride and Silicon Dioxide Film Processing by Inductively Coupled Plasma Chemical Vapor Deposition," *J. Electrochem. Soc.*, vol. 147, no. 4, pp. 1481–1486, 2000.

[8] Oxford Instruments, "PlasmaPro 100 Etch and deposition tools for wafer processing," 2018.

[9] E. M. Sherwood and J. M. Blocher, "Vapor deposition: The first hundred years," *JOM*, vol. 17, no. 6, pp. 594–599, Jun. 1965.

[10] R. K. Waits, "Edison's vacuum coating patents," *J. Vac. Sci. Technol. A Vacuum, Surfaces, Film.*, vol. 19, no. 4, pp. 1666–1673, Jul. 2001.

[11] A. C. Jones and M. L. Hitchman, "Chapter 1. Overview of Chemical Vapour Deposition," in *Chemical Vapour Deposition*, A. C. Jones and M. L. Hitchman, Eds. Cambridge: Royal Society of Chemistry, 2008, pp. 1–36.

[12] L. A. Chow, "Equipment and Manufacturability Issues in Chemical Vapor Deposition Processes," in *Handbook of Thin Film Deposition*, 4th ed., K. Seshan and D. Schepis, Eds. Cambridge: Elsevier, 2018, pp. 269–316.

[13] J. Foggiato, "3 – Chemical Vapor Deposition of Silicon Dioxide Films," in *Handbook of Thin Film Deposition Processes and Techniques*, 2001, pp. 111–150.

[14] A. Rockett, "Chemical Vapor Deposition," in *The Materials Science of Semiconductors*, 2008.

[15] E. Chen, "II. Thin Film Deposition (Lecture Slides)." Harvard University, pp. 1–34, 2004.

[16] Plasma-Therm, "Silicon Nitride for MEMS Applications: LPCVD and PECVD Process Comparison (Whitepaper)," 2014.

[17] Oxford Instruments, "Basic PECVD Plasma Processes (SiH4 based)," 2003.

[18] C. Iliescu, F. E. H. Tay, and J. Wei, "Low stress PECVD-SiNx layers at high deposition rates using high power and high frequency for MEMS applications," *J. Micromechanics Microengineering*, vol. 16, no. 4, pp. 869–874, Apr. 2006.

[19] T. V. Herak, T. T. Chau, D. J. Thomson, S. R. Mejia, D. A. Buchanan, and K. C. Kao, "Low-temperature deposition of silicon dioxide films from electron cyclotron resonant microwave plasmas," *J. Appl. Phys.*, vol. 65, no. 6, pp. 2457–2463, Mar. 1989.

[20] M. Shearn, X. Sun, M. David, A. Yariv, and A. Scherer, "Advanced Plasma Processing: Etching, Deposition, and Wafer Bonding Techniques for Semiconductor Applications," in *Semiconductor Technologies*, InTech, 2010.

[21] R. G. Andosca, W. J. Varhue, and E. Adams, "Silicon dioxide films deposited by electron cyclotron resonance plasma enhanced chemical vapor deposition," *J. Appl. Phys.*, vol. 72, no. 3, pp. 1126–1132, Aug. 1992.

[22] M. J. Hernandez, J. Garrido, J. Martinez, and J. Piqueras, "Compositional and electrical properties of ECR-CVD silicon oxynitrides," *Semicond. Sci. Technol.*, vol. 12, no. 7, pp. 927–932, Jul. 1997.

[23] D. G. Farber, S. Bae, M. Okandan, D. M. Reber, T. Kuzma, and S. J. Fonash, "Pathway to Depositing Device-Quality 50°C Silicon Nitride in a High-Density Plasma System," *J. Electrochem. Soc.*, vol. 146, no. 6, p. 2254, Jun. 1999.

[24] B. F. Hanyaloglu and E. S. Aydil, "Low temperature plasma deposition of silicon nitride from silane and nitrogen plasmas," *J. Vac. Sci. Technol. A Vacuum, Surfaces, Film.*, vol. 16, no. 5, pp. 2794–2803, Sep. 1998.

[25] S.-S. Han, B. Jun, K. No, and B. Bae, "Preparation of a-SiNx Thin Film with Low Hydrogen Content by Inductively Coupled Plasma Enhanced Chemical Vapor Deposition," *J. Electrochem. Soc.*, vol. 145, no. 2, pp. 652–658, 1998.

[26] D. V. Tsu and G. Lucovsky, "Silicon nitride and silicon diimide grown by remote plasma enhanced chemical vapor deposition," *J. Vac. Sci. Technol. A Vacuum, Surfaces, Film.*, vol. 4, no. 3, pp. 480–485, May 1986.

[27] G. H. Gweon, J. H. Lim, S. P. Hong, and G. Y. Yeom, "Effect of DC Bias Voltage on the Characteristics of Low Temperature Silicon Nitride Films Deposited by Internal Linear Antenna Inductively Coupled Plasma Source," *Jpn. J. Appl. Phys.*, vol. 49, no. 5, p. 056505,

May 2010.

[28] Q. Xu, Y. Ra, M. Bachman, and G. P. Li, "Characterization of low-temperature silicon nitride films produced by inductively coupled plasma chemical vapor deposition," *J. Vac. Sci. Technol. A Vacuum, Surfaces, Film.*, vol. 27, no. 1, pp. 145–156, Jan. 2009.

[29] D. Kim *et al.*, "Innovative Low damage Silicon Nitride Passivation of 100nm In0.45AlAs/In0.4GaAs Metamorphic HEMTs with Remote ICPCVD," in *ECS Transactions*, 2007, vol. 6, no. 3, pp. 577–589.

[30] D. K. T. Ng *et al.*, "Exploring High Refractive Index Silicon-Rich Nitride Films by Low-Temperature Inductively Coupled Plasma Chemical Vapor Deposition and Applications for Integrated Waveguides," *ACS Appl. Mater. Interfaces*, vol. 7, no. 39, pp. 21884–21889, Oct. 2015.

[31] J. Yota, J. Hander, and A. A. Saleh, "A comparative study on inductively-coupled plasma high-density plasma, plasma-enhanced, and low pressure chemical vapor deposition silicon nitride films," *J. Vac. Sci. Technol. A Vacuum, Surfaces, Film.*, vol. 18, no. 2, pp. 372–376, Mar. 2000.

[32] R. Wolf, K. Wandel, and B. Gruska, "Low-temperature ICPECVD of silicon nitride in SiH4–NH3–Ar discharges analyzed by spectroscopic ellipsometry and etch behavior in KOH and BHF," *Surf. Coatings Technol.*, vol. 142–144, pp. 786–791, Jul. 2001.

[33] Plasma-Therm, "Plasma-Therm: VERSALINE," 2018. [Online]. Available: http://www.plasma-therm.com/versaline.html. [Accessed: 30-Aug-2018].

[34] Meyer Tool & Manufacturing Inc., "VACUUM TECHNOLOGY – Material Choices Based on Vacuum Range." [Online]. Available: https://www.mtm-inc.com/av-20140529-vacuum-technology-ndash-material-choices-based-on-vacuum-range.html. [Accessed: 20-Aug-2018].

[35] A. Itoh, Y. Ishikawa, and T. Kawabe, "Reduction of outgassing from stainless-steel surfaces by glow discharge cleaning," *J. Vac. Sci. Technol. A Vacuum, Surfaces, Film.*, vol. 6, no. 4, pp. 2421–2425, Jul. 1988.

[36] H. F. Dylla, "Glow discharge techniques for conditioning high-vacuum systems," *J. Vac. Sci. Technol. A Vacuum, Surfaces, Film.*, vol. 6, no. 3, pp. 1276–1287, May 1988.

[37] Parker Hannifin Corp., "Parker O-Ring Handbook ORD 5700," 2007.

[38] J. A. Theil, "Gas distribution through injection manifolds in vacuum systems," *J. Vac. Sci. Technol. A Vacuum, Surfaces, Film.*, vol. 13, no. 2, p. 442, Mar. 1995.

[39] R. G. Livesey, "Method for calculation of gas flow in the whole pressure regime through ducts of any length," *J. Vac. Sci. Technol. A Vacuum, Surfaces, Film.*, vol. 19, no. 4, pp. 1674–1678, Jul. 2001.

[40] R. G. Livesey, "Solution methods for gas flow in ducts through the whole pressure regime," *Vacuum*, vol. 76, no. 1, pp. 101–107, Oct. 2004.

[41] R. G. Livesey, “Flow of Gases Through Tubes and Orifices,” in *Foundations of Vacuum Science and Technology*, J. M. Lafferty, Ed. New York: John Wiley & Sons, 1998, pp. 81–140.

[42] Minco Products Inc., “Estimating Power Requirements of Etched-Foil Heaters,” 2008.

[43] Minco Products Inc., “Flexible Heaters Design Guide,” 2016.

[44] M. L. Huber and A. H. Harvey, “Thermal Conductivity of Gases,” *CRC Handb. Chem. Phys.*, vol. 92nd Ed., 2011.

[45] C. M. Horwitz and Electrogrip, “Electrostatic Chucks: Thermal Transport,” 1997.

[46] Alicat Scientific Inc., “Gas mass flow controllers,” 2018. [Online]. Available: https://www.alicat.com/product/gas-mass-flow-controllers/. [Accessed: 25-Aug-2018].

[47] Clippard Instruments Laboratory Inc., “Clippard Analytical Series Electronic Valves,” 2018. [Online]. Available: http://www.clippard.com/cms/wiki/clippard-analytical-series-electronic-valves. [Accessed: 25-Aug-2018].

[48] Leybold GmbH, “Turbovac i(X) Manual,” Cologne, Germany, 2017.

[49] Pfeiffer Vacuum, “Turbomolecular pumps: Design / Operating principle,” 2018. [Online]. Available: https://www.pfeiffer-vacuum.com/en/know-how/vacuum-generation/turbomolecular-pumps/design-operating-principle/. [Accessed: 30-Aug-2018].

[50] O. Thomas, “Inductively coupled plasma chemical vapour deposition (ICP-CVD),” Oxford, UK, 2010.

[51] A. Al Bastami *et al.*, “Dynamic Matching System for Radio-Frequency Plasma Generation,” *IEEE Trans. Power Electron.*, vol. 33, no. 3, pp. 1940–1951, Mar. 2018.

[52] “Vacuum Helium Leak Testing Services | Meyer Tool & Mfg.” [Online]. Available: https://www.mtm-inc.com/helium-leak-testing.html. [Accessed: 11-Aug-2018].

[53] K. Zapfe, “Leak Detection,” in *CERN Accelerator School on Vacuum in Accelerators*, 2007, pp. 227–240.

[54] MKS Instruments, “HPS Series 901 Plus Micropirani/Piezo Loadlock Transducer,” 2018.

[55] Inficon, “SKY® CDG045D 0.05 ... 1000Torr / mbar - INFICON.” [Online]. Available: https://products.inficon.com/en-us/nav-products/product/detail/sky-cdg04d/. [Accessed: 11-Aug-2018].

[56] D. C. Montgomery, *Design and Analysis of Experiments*, 8th ed. New York: John Wiley & Sons, 2013.

[57] G. E. P. Box and K. B. Wilson, “On the Experimental Attainment of Optimum Conditions,” *J. R. Stat. Soc. Ser. B*, vol. 13, no. 1, pp. 1–45, Jan. 1951.

[58] G. E. P. Box and D. W. Behnken, “Some New Three Level Designs for the Study of Quantitative Variables,” *Technometrics*, vol. 2, no. 4, pp. 455–475, Nov. 1960.

[59] NIST-SEMATECH, "NIST/SEMATECH e-Handbook of Statistical Methods," 2012. [Online]. Available: https://www.itl.nist.gov/div898/handbook/index.htm. [Accessed: 01-Aug-2018].

[60] "STATISTICA Help | Central Composite and Non-Factorial Response Surface Designs - Alpha for Rotatability and Orthogonality." [Online]. Available: http://documentation.statsoft.com/STATISTICAHelp.aspx?path=Experimental/Doe/Overview/CentralCompositeandNonFactorialResponseSurfaceDesignsAlphaforRotatabilityandOrthogonality. [Accessed: 03-Aug-2018].

[61] "Ellipsometry Measurements - J.A. Woollam." [Online]. Available: https://www.jawoollam.com/resources/ellipsometry-tutorial/ellipsometry-measurements. [Accessed: 12-Aug-2018].

[62] J. A. Woollam, B. D. Johs, C. M. Herzinger, J. N. Hilfiker, R. A. Synowicki, and C. L. Bungay, "Overview of variable-angle spectroscopic ellipsometry (VASE): I. Basic theory and typical applications," 1999, vol. 10294, p. 1029402.

[63] G. G. Stoney, "The tension of metallic films deposited by electrolysis," *Proc. R. Soc. London. Ser. A*, vol. 82, no. 553, pp. 172–175, May 1909.

[64] Tencor, "FLX-2320 Thin Film Stress Measurement User Manual," 1995.

[65] "BOE Buffered Oxide Etchants | Transene." [Online]. Available: https://transene.com/sio2/. [Accessed: 01-Aug-2018].

[66] S. Jatta, K. Haberle, K. Singh, B. Koegel, H. Halbritter, and P. Meissner, "Bulk-micromachined dielectric tunable optical filter realized with inductively coupled plasma chemical vapour deposition," in *Proc. SPIE 7101, Advances in Optical Thin Films III*, 2008, vol. 7101, p. 71011D.

[67] G. Gulleri, C. Carpanese, C. Cascarano, D. Lodi, R. Ninni, and G. Ottaviani, "Deposition temperature determination of HDPCVD silicon dioxide films," *Microelectron. Eng.*, vol. 82, no. 3–4, pp. 236–241, Dec. 2005.

[68] S. V Nguyen, "High-density chemical vapour deposition High-density plasma chemical vapor deposition of silicon- based dielectric films for integrated circuits," *IBM J. Res. Dev.*, vol. 43, no. 1, pp. 1–19, 1999.

[69] Y. Nishimoto, N. Tokumasu, and K. Maeda, "Low Temperature Chemical Vapor Deposition of High Quality SiO2 Film Using Helicon Plasma Source," *Jpn. J. Appl. Phys.*, vol. 34, pp. 762–766, Feb. 1995.

[70] Gwyddion, "Gwyddion – Free SPM (AFM, SNOM/NSOM, STM, MFM, ...) data analysis software," 2018. [Online]. Available: http://gwyddion.net/. [Accessed: 30-Aug-2018].

[71] T. Chen, R. Ishihara, and K. Beenakker, "High Quality SiO2 Deposited at 80°C by Inductively Coupled Plasma Enhanced CVD for Flexible Display Application,"

Electrochem. Solid-State Lett., vol. 13, no. 8, pp. J89–J91, 2010.

[72] R. Wolf, K. Wandel, and C. Boeffel, "Moisture Barrier Films Deposited on PET by ICPECVD of SiNx," *Plasma Process. Polym.*, vol. 4, no. S1, pp. S185–S189, Apr. 2007.

[73] J. Zhang *et al.*, "Investigation of ICPECVD Silicon Nitride Films for HgCdTe Surface Passivation," *J. Electron. Mater.*, vol. 44, no. 9, pp. 2990–3001, Sep. 2015.

[74] W. A. Pliskin and R. P. Esch, "Refractive Index of SiO2 Films Grown on Silicon," *J. Appl. Phys.*, vol. 36, no. 6, pp. 2011–2013, Jun. 1965.

[75] A. Yasunas, D. Kotov, V. Shiripov, and U. Radzionay, "Low-temperature deposition of silicon dioxide films in high-density plasma," *Semicond. Physics, Quantum Electron. Optoelectron.*, vol. 16, no. 2, pp. 216–219, 2013.

[76] Stanford Nanofabrication Facility, "Labmembers Wiki - HDP_SiO2," 2018. [Online]. Available: https://snf.stanford.edu/SNF/equipment/chemical-vapor-deposition/pecvd/plasmatherm-versaline-hdpcvd/hdpecvd-recipes/hd_sio. [Accessed: 01-Aug-2018].

[77] K. N. Leung, T. K. Samec, and A. Lamm, "Optimization of permanent magnet plasma confinement," *Phys. Lett. A*, vol. 51, no. 8, pp. 490–492, May 1975.

[78] M. A. Lieberman and A. J. Lichtenberg, *Principles of plasma discharges and materials processing.* Wiley-Interscience, 2005.

[79] H. Nihei, H. Enomoto, and J. Morikawa, "Magnetic Multipole Field Generated by Columns of Permanent Magnets Arranged on a Cylindrical Surface," *Jpn. J. Appl. Phys.*, vol. 31, pp. 1885–1889, Jun. 1992.

[80] J. Hopwood, C. R. Guarnieri, S. J. Whitehair, and J. J. Cuomo, "Langmuir probe measurements of a radio frequency induction plasma," *J. Vac. Sci. Technol. A Vacuum, Surfaces, Film.*, vol. 11, no. 1, pp. 152–156, Jan. 1993.

[81] N. Tomozeiu and W. I. Milne, "Magnetic multipole confinement used in amorphous hydrogenated carbon films deposition," *J. Non. Cryst. Solids*, vol. 249, no. 2, pp. 180–188, 1999.

[82] M. Hosseinzadeh and H. Afarideh, "Numerical simulation for optimization of multipole permanent magnets of multicusp ion source," *Nucl. Instruments Methods Phys. Res. Sect. A Accel. Spectrometers, Detect. Assoc. Equip.*, vol. 735, pp. 416–421, Jan. 2014.

[83] O. Thomas, A. Griffiths, and M. Cooke, "Surface Processing Apparatus," 09-Aug-2007.

[84] S. Y. Choi *et al.*, "Plasma uniformity control by gas diffuser hole design," US 2016/0056019 A1, 2015.

[85] G. Balasubramanian, J. C. Rocha-Alvarez, T. K. Cho, and D. Raj, "Uniformity control for low flow process and chamber to chamber matching," US 7622005 B2, 2005.

[86] Q. Wang *et al.*, "Gas distribution uniformity improvement by baffle plate with multi-size

holes for large size pecvd systems," US 2008/0178807 A1, 2008.

[87] R. V. Lenth, "Response-Surface Methods in R, Using rsm," *J. Stat. Softw.*, vol. 32, no. 7, pp. 1–17, Oct. 2009.

[88] J. H. de Boer, *The Dynamical Character of Adsorption*, 2nd ed. Oxford, UK: Oxford University Press, 1968.

[89] E. Kobeda and E. A. Irene, "SiO2 film stress distribution during thermal oxidation of Si," *J. Vac. Sci. Technol. B Microelectron. Nanom. Struct.*, vol. 6, pp. 574–578, Mar. 1988.

[90] E. Kobeda and E. A. Irene, "Intrinsic SiO2 film stress measurements on thermally oxidized Si," *J. Vac. Sci. Technol. B Microelectron. Process. Phenom.*, vol. 5, pp. 15–19, 1987.

[91] E. P. Eernisse, "Stress in thermal SiO2 during growth," *Appl. Phys. Lett.*, vol. 35, pp. 8–10, 1979.

[92] A. Boogaard *et al.*, "Langmuir-probe Characterization of an Inductively-Coupled Remote Plasma System intended for CVD and ALD," in *ECS Transactions*, 2007, vol. 2, no. 7, pp. 181–191.

[93] Nanoelectronics Centre ITT Bombay, "Oxford Plasmalab System100 ICP180," Bombay, India.

[94] F. Karouta, K. Vora, J. Tian, and C. Jagadish, "Structural, compositional and optical properties of PECVD silicon nitride layers," *J. Phys. D. Appl. Phys.*, vol. 45, no. 44, p. 445301, Nov. 2012.

[95] K. Mackenzie *et al.*, "Stress control of Si-based PECVD dielectrics," in *Proceedings of the 207th Electrochemical Society Meeting*, 2005, vol. PV2005-01, no. 9, pp. 148–159.

[96] H. Zhou, C. Sim, A. Glidle, C. Hodson, R. Kinsey, and C. D. W. Wilkinson, "Chapter 6. Properties of Silicon Nitride by Room-Temperature Inductively Coupled Plasma Deposition," in *Plasma Processes and Polymers*, Wiley, 2005, pp. 77–86.

[97] J. Sim Jung *et al.*, "SiO2 Film Formed by Inductivity Coupled Plasma Chemical Vapor Deposition at Low Temperature for Poly-Si TFT," *J. Korean Phys. Soc.*, vol. 4530, Jan. 2005.

[98] Virginia Semiconductor, "The General Properties of Si, Ge, SiGe, SiO2, and Si3N4," 2002.

[99] A. Kovalgin, A. Boogaard, I. Brunets, T. Aarnink, and R. Wolters, "Electrical Properties of Plasma-Deposited Silicon Oxide Clarified by Chemical Modeling," in *ECS Transactions*, 2009, vol. 25, no. 8, pp. 23–32.

[100] A. Boogaard *et al.*, "Characterization of SiO2 films deposited at low temperature by means of remote ICPECVD," *Surf. Coatings Technol.*, vol. 201, no. 22–23, pp. 8976–8980, Sep. 2007.

[101] S. Majee, D. Barshilia, S. Kumar, P. Mishra, and J. Akhtar, "Signature of growth-

deposition technique on the properties of PECVD and thermal SiO2," *AIP Conf. Proc.*, vol. 1989, p. 020023, 2018.

[102] C. S. Tan, A. Fan, K. N. Chen, and R. Reif, "Low-temperature thermal oxide to plasma-enhanced chemical vapor deposition oxide wafer bonding for thin-film transfer application," *Appl. Phys. Lett.*, vol. 82, no. 16, pp. 2649–2651, Apr. 2003.

[103] C. Yang and J. Pham, "Characteristic Study of Silicon Nitride Films Deposited by LPCVD and PECVD," *Silicon*, pp. 1–7, Apr. 2018.

[104] A. Stoffel, A. Kovács, W. Kronast, and B. Müller, "LPCVD against PECVD for micromechanical applications," *J. Micromechanics Microengineering*, vol. 6, no. 1, pp. 1–13, Mar. 1996.

[105] B. Zheng, C. Zhou, Q. Wang, Y. Chen, and W. Xue, "Deposition of Low Stress Silicon Nitride Thin Film and Its Application in Surface Micromachining Device Structures," *Adv. Mater. Sci. Eng.*, vol. 2013, pp. 1–4, Oct. 2013.

[106] P. Temple-Boyer, C. Rossi, E. Saint-Etienne, and E. Scheid, "Residual stress in low pressure chemical vapor deposition SiN x films deposited from silane and ammonia," *J. Vac. Sci. Technol. A Vacuum, Surfaces, Film.*, vol. 16, no. 4, pp. 2003–2007, 1998.

[107] C. Abels *et al.*, "Nitride-Based Materials for Flexible MEMS Tactile and Flow Sensors in Robotics," *Sensors*, vol. 17, no. 5, p. 1080, May 2017.

[108] W. S. Tan, P. A. Houston, G. Hill, R. J. Airey, and P. J. Parbook, "Influence of dual-frequency plasma-enhanced chemical-vapor deposition Si3N4 passivation on the electrical characteristics of AlGaN/GaN heterostructure field-effect transistors," *J. Electron. Mater.*, vol. 33, no. 5, pp. 400–407, May 2004.

[109] S. Jatta, K. Haberle, A. Klein, R. Schafranek, B. Koegel, and P. Meissner, "Depositon of Dielectric Films with Inductively Coupled Plasma-CVD in Dependence on Pressure and Two RF-Power-Sources," *Plasma Process. Polym.*, vol. 6, no. S1, pp. S582–S587, Jun. 2009.

[110] M. J. Loboda and J. A. Seifferly, "Chemical influence of inert gas on the thin film stress in plasma-enhanced chemical vapor deposited a-SiN: H films," *J. Mater. Res.*, vol. 11, no. 02, pp. 391–398, Feb. 1996.

[111] E. Bustarret, M. Bensouda, M. C. Habrard, J. C. Bruyère, S. Poulin, and S. C. Gujrathi, "Configurational statistics in a-SixNyHz alloys: A quantitative bonding analysis," *Phys. Rev. B*, vol. 38, no. 12, pp. 8171–8184, Oct. 1988.

[112] H. Mäckel and R. Lüdemann, "Detailed study of the composition of hydrogenated SiNx layers for high-quality silicon surface passivation," *J. Appl. Phys.*, vol. 92, no. 5, pp. 2602–2609, Sep. 2002.

[113] T. Domínguez Bucio *et al.*, "Material and optical properties of low-temperature NH3-free PECVD SiNx layers for photonic applications," *J. Phys. D. Appl. Phys.*, vol. 50, no. 2, p.

025106, Jan. 2017.

[114] Sentech Instruments GmbH and M. Arens, “Plasma Prozess-Technologie bei SENTECH Instruments,” 2013.

[115] D. Dergez, J. Schalko, A. Bittner, and U. Schmid, “Fundamental properties of a-SiNx:H thin films deposited by ICP-PECVD for MEMS applications,” *Appl. Surf. Sci.*, vol. 284, pp. 348–353, 2013.

[116] H. Kim, Y. Lee, Y. Ra, G. P. Li, and J. Yota, “Low Temperature Silicon Nitride Deposition by Inductively Coupled Plasma CVD for GaAs Applications,” in *ECS Transactions*, 2007, vol. 6, no. 3, pp. 531–547.

[117] H. P. Zhou *et al.*, “Low temperature SiNx:H films deposited by inductively coupled plasma for solar cell applications,” *Appl. Surf. Sci.*, vol. 264, pp. 21–26, 2013.

[118] L. da Silva Zambom, R. Domingues Mansano, and R. Furlan, “Silicon nitride deposited by inductively coupled plasma using silane and nitrogen,” *Vacuum*, vol. 65, no. 2, pp. 213–220, 2002.

[119] Plasma-Therm, “Current Trends with DRIE/DSE Processing for MEMS Devices and Structures (Whitepaper),” 2012.

[120] A. Kshirsagar, P. Nyaupane, D. Bodas, S. P. Duttagupta, and S. A. Gangal, “Deposition and characterization of low temperature silicon nitride films deposited by inductively coupled plasma CVD,” *Appl. Surf. Sci.*, vol. 257, no. 11, pp. 5052–5058, 2011.

[121] H. Zhou, K. Elgaid, C. Wilkinson, and I. Thayne, “Low-hydrogen-content silicon nitride deposited at room temperature by inductively coupled plasma deposition,” *Jpn. J. Appl. Phys.*, vol. 45, no. 10S, pp. 8388–8392, 2006.

[122] V. Verlaan, C. H. M. van der Werf, W. M. Arnoldbik, H. D. Goldbach, and R. E. I. Schropp, “Unambiguous determination of Fourier-transform infrared spectroscopy proportionality factors: The case of silicon nitride,” *Phys. Rev. B*, vol. 73, no. 19, p. 195333, May 2006.

[123] K. Wörhoff, L. T. H. Hilderink, A. Driessen, and P. V. Lambeck, “Silicon Oxynitride,” *J. Electrochem. Soc.*, vol. 149, no. 8, p. F85, Aug. 2002.

[124] C. Jeong, S. Boo, M. Jeon, and K. Kamisako, “Characterization of intrinsic a-Si:H films prepared by inductively coupled plasma chemical vapor deposition for solar cell applications.,” *J. Nanosci. Nanotechnol.*, vol. 7, no. 11, pp. 4169–4173, Nov. 2007.

[125] V. A. Dao *et al.*, “Hydrogenated Amorphous Silicon Layer Formation by Inductively Coupled Plasma Chemical Vapor Deposition and Its Application for Surface Passivation of p-Type Crystalline Silicon,” *Jpn. J. Appl. Phys.*, vol. 48, no. 6, p. 066509, Jun. 2009.

[126] M. Goto, H. Toyoda, M. Kitagawa, T. Hirao, and H. Sugai, “Low Temperature Growth of Amorphous and Polycrystalline Silicon Films from a Modified Inductively Coupled

Plasma," *Jpn. J. Appl. Phys.*, vol. 36, pp. 3714–3720, Jun. 1997.

[127] S. K. Kim, Y. J. Choi, K. S. Cho, and J. Jang, "Coplanar amorphous silicon thin film transistor fabricated by inductively coupled plasma chemical vapor deposition," *J. Appl. Phys.*, vol. 84, no. 7, pp. 4006–4012, Oct. 1998.

[128] D. K. Tripathi *et al.*, "Optimization of ICPCVD Amorphous Silicon for Optical MEMS Applications," *J. Microelectromechanical Syst.*, vol. 24, no. 6, pp. 1998–2007, Dec. 2015.

[129] Swagelok Company, "Thread and End Connection Identification Guide," 2012.

[130] VAT Group AG, "VAT | Insertable gate valve." [Online]. Available: http://www.vatvalve.com/business/valves/catalog/A/081_1_V. [Accessed: 21-Aug-2018].

[131] K. R. Williams, K. Gupta, and M. Wasilik, "Etch rates for micromachining processing-part II," *J. Microelectromechanical Syst.*, vol. 12, no. 6, pp. 761–778, Dec. 2003.

Appendix A: Standard Cleaning Protocol

After fabrication, any parts made for the IFIC were cleaned using the following protocol before being installed in the system.

1. Clean parts thoroughly by hand with degreaser, removing any large chips. Use compressed air to blow out any blind threaded holes. Dry completely.
2. Use ultrasonic cleaner to clean parts in a 10% solution of Brulin 815 GD (in deionized water) for 30 minutes at 40°C.
3. Upon removal of parts from ultrasonic cleaner, immediately wash with deionized water to remove excess Brulin 815 GD solution.
4. Dry completely with N_2, paying special care to any small threaded holes.
5. Bake in vacuum oven at 90°C for at least 12 hours.
6. After cooling in oven, immediately install parts or place in a new zippered cleanroom bag in the laminar flow hood for temporary storage until installation.

Appendix B: Gas Delivery and Vacuum Generation System